LONG-TERM REMOTE SINGLE-DISH OBSERVATIONS OF BLAZAR RADIO VARIABILITY.

Steven James Bramley Carter
B.Sc. (Physics), Toronto
B.Sc. (Civil Eng.), Manchester
Ph.D. (Engineering), Tasmania
FIEAust, CPEng

Submitted in fulfilment of the requirements for the degree of

Doctor of Philosophy

University of Tasmania
Faculty of Science and Engineering

May 2008

This thesis is dedicated to

Three old friends

Simon Davis, Stephen Wilcock, and Susan Wild

The Mole Creekers

Mike, Sallie, Katie, Melissa, and Margaret

Rosie & Daisy

Semper Furry Fidelis

Tisha

Love always

Statements

This thesis contains no material which has been accepted for the award of any other degree or diploma in any University or other institution. To the best of my knowledge, it contains no material previously published or written by another person, except where due reference has been made in the text.

In particular, all the software procedures relied on in this thesis for data processing and analysis were written by me without assistance, except for guidance from Dr Jean-Pierre Macquart on the modelling of annual cycles in variability time scales, based on software written by Professor Barney Rickett; and ISS modelling software provided by PhD student Jamie McCallum (Section 4.6).

Signed.....…… Date.....
Steven J.B. Carter

I consent to this copy of my thesis, when deposited in the University Library, being available for loan and limited photocopying, in accordance with the *Copyright Act (1968).*

Signed.....…… Date.....
Steven J.B. Carter

Abstract

This research has demonstrated that a small, remotely operated radio telescope can perform well enough to monitor blazar radio variability over periods of months to years. Such observations are not possible using premier telescope facilities, given observing time demands, and they enable scintillation effects intrinsic to the source to be disentangled from scintillation due to scattering of radio waves by the interstellar medium. This exercise provides insight into the nature of the source, and also provides a probe of turbulence in the interstellar medium.

The University of Tasmania's 30 m antenna near Ceduna in South Australia was converted to a radio telescope facility in 1997 from its former use as an Earth station. The COntinuous Single dish Monitoring of Intraday variables at Ceduna (COSMIC) campaign started in March 2003, and extended to early 2005. It observed a number of blazars, with the telescope remotely operated from Tasmania. The blazars were divided into groups lying south and north of the zenith at Ceduna, with each group served by a calibrator source and observed in turn for periods of 10-15 days.

A source scanning strategy was developed, and semi-automatic software procedures were written to process raw data into calibrated flux density data sets, corrected for gain-elevation and pointing, and subject to quality control tests. The consistency in calibrator observations over the ~2 year period shows that a 30 m antenna can carry out long term monitoring of blazars with strengths ≥ ~1 Jy to the accuracy needed to identify variability on time scales of days, and better performance is expected in future campaigns The antenna's $1/f$ noise is ~1% of the total flux density, and is likely due to electronic gain fluctuations. It is about 2½ times greater than thermal noise at the integration times relevant to the Ceduna flux density measurements.

COSMIC campaign data contain ±0.15 Jy systematic flux density fluctuations, that have a thermal origin. These fluctuations were initially believed to be genuine variability, and are most evident on diurnal time scales. The raw data processing exercise cannot be adjusted to remove the fluctuations for the blazars of interest to this research, PKS B1622-253 and PKS B1519-273, but the genuine variability in these two blazars occurs on time scales of ~1-10 days. A method of filtering and correcting the flux density data was developed, the strategy being to smooth through the diurnal systematic effects, remove longer term flux density trends, correct for systematic effects on weekly and seasonal time scales, and hence isolate the genuine variability.

A suite of variability analysis tools appropriate for Ceduna data was developed, using the scintle peak-to-peak period, T_{period} , to define the characteristic variability time scale. Values of $T_{0.5}$ or $T_{1/e}$ can also be estimated, enabling examination of decorrelation timescales, but with caveats due to the peculiarities of the Ceduna data sets, whose data gaps and other characteristics provide challenges to an analysis of variability on a time scale of days.

T_{period} values are determined for each 10-15 day observing period by spectral analysis, using a power spectral density function obtained as the Fourier transform of a discrete autocorrelation function. Empirical scintle counting and data folding exercises cross-check the T_{period} values. Scintle periods are well modelled as Gaussian distributions that are similar for the two blazars, since both sources are large enough to band-limited the scintillation process in similar ways.

The statistical properties of the scintle periods provide empirical error bars estimates for the T_{period} values. Also, the 95% confidence interval error bars for T_{period} values calculated from a typical set of scintles are comparable to the $2\sigma \sim 10\%$ upper limit of the stochasticity in T_{period} values that Monte Carlo modelling predicted would enable T_{period} to be computed with fair accuracy.

For both PKS B1622-253 and PKS B1519-273, the T_{period} values computed for each observing period over the COSMIC campaign exhibit clear annual cycles, which unequivocally proves that in both cases the observed scintillation is primarily due to scattering by the interstellar medium. Multi-frequency observations of PKS B1519-273 have shown that its scintillation is associated with the weak scattering régime at the 6.7 GHz Ceduna observing frequency, and this is also believed to be the case for PKS B1622-253.

The annual cycles in the variability time scales (i.e. T_{period} values) of the two blazars are well fitted by the standard model of interstellar scintillation. T_{period} values for PKS B1622-253 and PKS B1519-273 range from about 2 – 10 days and about 1-5 days respectively. The strength of PKS B1519-273 fell below ~½ Jy in mid-2004, precluding accurate determination of T_{period} values in the final months of the COSMIC project.

For both sources, the best annual cycle model fit is for highly anisotropic scintles and large velocity offsets of the scattering screen with respect to the Local Standard of Rest. This is unsurprising, since scintillation on time scales of days is associated with distant scattering screens, typically hundreds of parsecs from Earth, which are often in motion with respect to the LSR.

The annual cycle model fits to the PKS B1622-253 and PKS B1519-273 T_{period} values have reduced chi-square values of 2.12 and 0.83 respectively, confirming that the empirically determined error bar estimates are appropriate, and that the annual cycle model credibly describes the variation in the variability time scales of the two blazars.

The variability characteristics of PKS B1519-273, and the annual cycle in its variability time, agree well with previous analyses of this source based on more limited data, but data recorded by much better telescopes. This agreement confirms the success of the COSMIC project. An annual cycle in the variability time scale of PKS B1622-253 has not previously been observed. The main follow-on research tasks are to study the implications of the variability characteristics of both PKS B1622-253 and PKS B1519-273, with consideration of anisotropy; eliminate the problem of systematic fluctuations; and examine the other blazars monitored in the COSMIC campaign.

Acknowledgements

Somewhere a doctoral thesis may exist which was produced without the benefit of support and helpful suggestions from numerous people. Not this one!

I am first and foremost very grateful to Tisha, my wife, for her support.

And I also thank the following people:

- My supervision team: Dr Simon Ellingsen, Dr Jean-Pierre Macquart, and Dr Jim Lovell;

- Dr Hayley Bignall, Dr Giuseppe Címò, Jamie McCallum, and Cliff Senkbeil for their help and for fun along the way; and

- Professor John Dickey, Emeritus Professor Peter McCulloch and Dr Dave Jauncey for their useful comments.

Supporting Work and Publications

This research spanned the five-plus year period from mid-2002 to late 2007. Although the focus is on processing data, I gained hands-on experience of radio astronomy work through use of the University of Tasmania's 30 m radio telescope at Ceduna in South Australia. I have also used the University's 29 m antenna near Hobart; and I attended observing sessions at the Australia Telescope Compact Array at Narrabri in New South Wales in September, 2002 and July 2003.

The thesis is supported by the following publications.

McCulloch, P.M., Ellingsen, S.P., Jauncey, D.L., **Carter, S.J.B**., Cimò, G., Lovell, J.E.J., & Dodson, R.G. 2005, AJ, 129, 2034-2040. [*COSMIC: Microarcsecond resolution with a 30 meter radio telescope*]. This paper was written by Dr Simon Ellingsen with assistance from myself and others, and draws on the work presented in Chapter 3 of this thesis. Professor McCulloch and Dr Jauncey are co-authors primarily because of their involvement with the Ceduna conversion work.

Bignall, H.E., Jauncey, D.L., Lovell, J.E.J., Kedziora-Chudczer, Macquart, J-P., Tzioumis, A.K., Rickett, B.J., Ojha, R., **Carter, S.,** Cimo, G., Ellingsen, S., & McCulloch, In Proc. 7th EVN Symposium, Bachiller, R., Colomer, F., Desmurs, J.F., & de Vincente, P. Eds., October 12-15 2004, Toledo, Spain. [*Interstellar scintillation as a probe of microarcsecond scale structure in quasars*]. This paper presented some initial COSMIC results.

This research has been dogged by concerns about the presence of systematic fluctuations in the Ceduna data. In was only in mid-2007 that it finally became clear that the research methodology had been successful, at least for the two blazars that are the focus of this research, with annual cycles found in the characteristic variability time scales of both sources. A full analysis of this variability is a follow-on research task that will require consideration of anisotropy, described in Chapter 8, and it is planned to publish the findings once this analysis is completed.

LONG-TERM REMOTE SINGLE-DISH OBSERVATIONS OF BLAZAR RADIO VARIABILITY.

Page

1.0 INTRODUCTION

1.1 Research Motivation

In the 1980s, I completed an honours physics degree at the University of Toronto, which included courses in astrophysics and astronomy. In the subsequent decades great progress has been made in understanding the Universe, and the research presented in this thesis was largely motivated by a desire to learn about the advances in these subjects, and to participate in the ongoing adventure of discovery.

The space program has provided high quality observational data across the electromagnetic spectrum, for example through the *Hubble, Compton, Chandra,* and *Spitzer* telescopes. At the same time, computer technology and software improvements have greatly benefited ground-based astronomy. For example, the use of interferometry has been facilitated, and premier facilities such as the Australia Telescope Compact Array now use interferometry as their principal mode of operation, and most radio telescopes routinely participate in Very Long Baseline Interferometry studies.

In 2002, Dr David Jauncey and Dr Jim Lovell, of CSIRO's Australia Telescope National Facility (ATNF), visited the University of Tasmania and lectured on the variability of radio signals from Active Galactic Nuclei (AGNs). I decided that I wanted to better understand the fascinating arena of extreme physics that is the AGN central engine model, especially since I took courses in general relativity and high energy physics while at the University of Toronto, but my lecture notes confirm that the central engine model was never mentioned. In addition, I have a fair working knowledge of geophysical fluid dynamics, and wanted to learn more of the interstellar medium, which is so similar and yet so different to the Earth's atmosphere and oceans.

Becoming involved in AGN radio variability research seemed a good way to do this. In particular:

- AGNs are so distant that *any* information about the sizes of their emission regions is invaluable. Variability in AGN radio signals, whether intrinsic or due to scintillation, offers a way to probe the structure of AGNs at ultra-fine (microarcsecond) resolution.
- Variability in AGN radio signals that is due to scintillation has the potential to probe the electron density and turbulence structure of the local interstellar medium (ISM).

The radio astronomers told me that work to analyse the variability of AGN radio signals has led to an appreciation of the benefits of monitoring radio-loud AGNs quasi-continuously for periods of months to years.

The bad news, they said, was that dedicated long-term observing campaigns are not possible using a premier radio telescope facility, which is subject to intense demand for its usage. The good news was that the University of Tasmania and the CSIRO ATNF had just finished converting a 30 m antenna near Ceduna in South Australia for radio astronomy usage after closure in 1995 of an earth-satellite telecommunications station. The "new" radio telescope greatly enhanced Australia's VLBI capability, and initially it was heavily involved in the VSOP survey program, typically carrying out one 8 hour VLBI experiment each week. But by 2003 the VSOP satellite had failed, decreasing usage of the telescope for VLBI work. It seemed possible that Ceduna's availability might solve the problem of long-term AGN radio variability monitoring, although this was far from certain.

Sign on to the team, the radio astronomers urged. Perhaps it was the challenge of climbing another mountain. My wife believes I realised that radio astronomers believe beer drinking aids research. Anyway, I learned the secret handshake and decided that following the PhD route was a good way to ensure that I stuck to my commitment.

1.2 Research Goals and Thesis Outline

The following principal research goals were set in mid-2002.

- Develop an understanding of AGN central engine theory and AGN observational characteristics, together with an understanding of interstellar scintillation modelling.

- Establish whether the Ceduna radio telescope, remotely operated, could perform well enough to monitor variability in blazars for periods of months to years. The work included determining an appropriate observing strategy, and developing a suite of specialised data processing software specific to the monitoring program.

- Gather sufficient data that annual cycles in the signal variability could be detected if present, since this phenomenon establishes scattering by the interstellar medium as the principal cause of signal variability. The data presented in this thesis were gathered from early 2003 to early 2005, a period of about two years. Processing the observed data to produce calibrated flux density data necessitated developing a suite of software routines.

- Analyse data from selected sources. This necessitated developing an additional suite of specialised data analysis software, because the analysis of long term radio variability data holds challenges that are different from the analysis of shorter term time series.

The research strategy pursued these goals in a linear fashion, and in addition I was a minor participant in observing campaigns at the Australia Telescope Compact Array at Narrabri, and the Mount Pleasant radio telescope near Hobart.

An overview of the structure of this thesis is as follows.

1. **Research goals and AGN theory (Chapter 1).** This chapter to date has outlined my research motivation and goals. It goes on to review AGN classifications, central engine theory, and the proposed unification of AGN types according to this theory.

2. **AGN radio variability theory (Chapter 2).** This chapter reviews explanations for AGN radio signal variability on time scales of hours to days, including interstellar scintillation. It discusses annual cycle and time delay tests to determine the cause of radio variability, and sets out the need for long term observation records.

3. **Ceduna and the COSMIC project (Chapter 3**). This chapter describes the Ceduna radio telescope and the work to establish it as a continuous-operation remote-mode facility able to provide the long term data needed to study variability in AGN signals. Work on this task started in mid-2002, with development of an observing strategy and data processing software appropriate for Ceduna Data.

   The COntinuous Single dish Monitoring of Intraday variables at Ceduna (COSMIC) campaign started in March 2003, targeting blazars with flux densities ≥~1 Jy, and the monitoring period that provides the basis for this thesis continued until early 2005.

   The first COSMIC results were presented in July 2003 by me at the Parkes workshop *The Variable Radio Universe*, and subsequently by Dr Dave Jauncey in a discussion session at the 2003 IAU General Assembly. The demonstration that a remotely operated 30 m telescope could achieve the performance needed for blazar radio variability monitoring, together with the earlier conversion project, won an Engineering Excellence Award from Engineers Australia in late 2003.

4. **Data analysis tools (Chapter 4).** The long term radio signal time series recorded by the Ceduna telescope contain systematic fluctuations, primarily on diurnal time scales. Fortunately, the two blazars of interest to the present research, PKS B1519-273 and PKS B1622-253 both display variability only on time scales longer than a day. Chapter 4 describes a data filtering and correction method that isolates the genuine variability in the flux density time series for these two blazars.

The chapter also presents variability analysis tools based on spectral analysis, scintle counting, data folding, appropriate for analysis of variability in Ceduna's data, which have gaps and other characteristics that provide a significant challenge to a variability analysis.

5. **Telescope performance (Chapter 5).** This chapter examines the performance of the Ceduna telescope, benchmarked by calibrator observations. The antenna's $1/f$ noise and thermal noise characteristics are examined, particularly at the integration times relevant to the Ceduna flux density measurements. The chapter also provides a detailed study of the PKS B1519-273 and PKS B1622-253 data sets, and establishes that in both cases the diurnal time scales contain no genuine variability.

6. **Variability analysis of PKS B1622-253 and PKS B1519-273 (Chapters 6 & 7).** These chapters present the data gathered by the COSMIC program for these blazars, supported by material presented in appendices to this thesis, and present the variability analyses of the data. Both sources have flux densities that vary greatly over the course of months, assumed due to processes intrinsic to the source. However both also exhibit annual cycles in their variability time scales, a clear fingerprint of variability that is primarily due to radio wave scattering by the interstellar medium.

7. **Conclusions and future research (Chapter 8).** This chapter concludes that the Ceduna blazar radio variability monitoring program has demonstrated that a 30 m telescope can provide valuable long-term data sets. The variability analyses of PKS B1622-253 and PKS B1519-273 are consistent with previous work, and extend that work. Concurrent and follow on research initiatives are outlined, and eliminating the problem of systematic effects is expected to enable Ceduna to examine variability on times scales of hours in sources with flux densities less than ~1 Jy, which is roughly the present limit.

The two appendices present the flux density time series for both blazars, together with all the supporting variability analysis plots.

1.3 The Nature and Classification of Active Galactic Nuclei

Active galactic nuclei (AGN) are associated with only a few percent of the estimated 40 billion galaxies in the observable universe (Chaisson & McMillan, 2002). Their defining characteristic is the generation of large amounts of non-thermal radiation from a small region of space. The botanical nature of AGN terminology reflects their apparently disparate characteristics, which are now largely explained by AGN unification schemes.

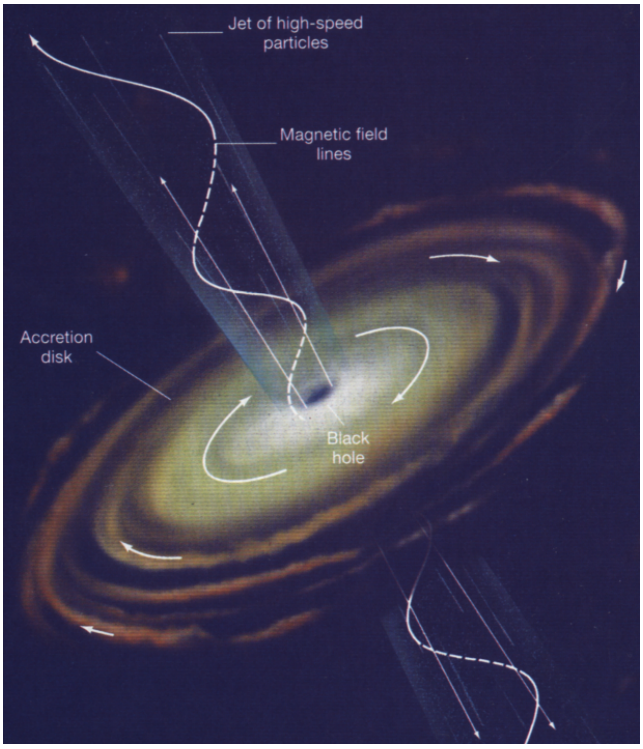

Figure 1.1 shows the central engine model that underpins the most widely accepted AGN unification scheme, in which gas and dust accrete onto a rotating massive black hole near the center of a galaxy.

This produces powerful and highly variable non-thermal emissions, both from the accretion disc and also from the plasma jet outflows perpendicular to the accretion disc.

Figure 1.1 The classic central engine with axial plasma outflow jets. From Chaisson & McMillan (2002).

About 20% of AGN are radio loud, commonly defined as having 5 GHz fluxes greater than 10 times their optical (B-band) fluxes (Urry & Padovani; 1995). *Seyfert galaxies* are characterised by intense radio and infra-red radiation from an AGN (e.g. De Young, 2002), although they are radio quiet by the above definition. They are usually spiral galaxies, and comprise ~1% of all spiral galaxies.

Radio galaxies are characterised by radio emissions from lobes whose structure can extend far beyond the visible component of the host galaxy, fed by high energy plasma jets that emerge from the AGN. Fanaroff & Riley (1974) divided radio galaxies into FR-I types, with relatively weak jets and diffuse radio lobes; and FR-II types, with stronger jets that terminate in hot-spots within the lobes. The FR-I and FR-II galaxies are oriented such that their radio lobes and AGN jets are visible from Earth, and have narrow emission lines in their optical spectra. Core-halo radio galaxies are radio galaxies viewed along a jet axis, and have broader emission lines in their optical spectra.

Quasars typically lie at high redshifts, and have very broad emission lines. As discussed by Urry & Padovani (1995), quasars radiate across the spectrum from radio to X-rays, and occasionally gamma-rays. Radio quiet quasars are similar to many Seyfert galaxies while the less numerous radio loud quasars are basically very luminous core-halo radio galaxies.

Synchrotron emission constitutes the dominant radiation in radio loud quasars and other compact radio sources (e.g. Ulrich et al., 1997). This leads to their classification on the basis of their spectral characteristics, which are represented as power laws or combinations of power laws of the form $S_\nu = \nu^{-\alpha}$, where S_ν is the flux density (Jy) at frequency ν (GHz).

The principal radio loud quasar types are flat-spectrum radio quasars (FSRQs), with a GHz range spectral index of $\alpha < 0.5$, and steep-spectrum radio quasars (SSRQs), with $\alpha \geq 0.5$.

BL Lac objects have characteristics similar to radio loud quasars, but their spectral lines are very faint when they are detectable at all. Like radio loud quasars, their emissions are highly variable and they are interpreted as AGN seen along the line of the jet, but in the case of BL Lac objects the effect is so strong that the synchrotron radiation swamps the stellar (thermal) radiation from the host galaxy.

FSRQs and BL Lac objects are collectively referred to as *blazars*. They have high apparent luminosities caused by Doppler boosting of the radiation, with the illusion of superluminal transverse motion if the source is moving almost along the line of sight (Blandford et al., 1977). Figure 1.2 shows the double-humped spectral energy distribution that is characteristic of blazars. The low energy peaks are associated with synchrotron radiation, and the higher energy peaks with inverse Compton scattering of lower energy photons. Padovani & Giommi (1995) divided BL Lac objects into high frequency peaked (HBL) and low frequency peaked (LBL) groups. FSRQs have similar emission spectra to LBLs.

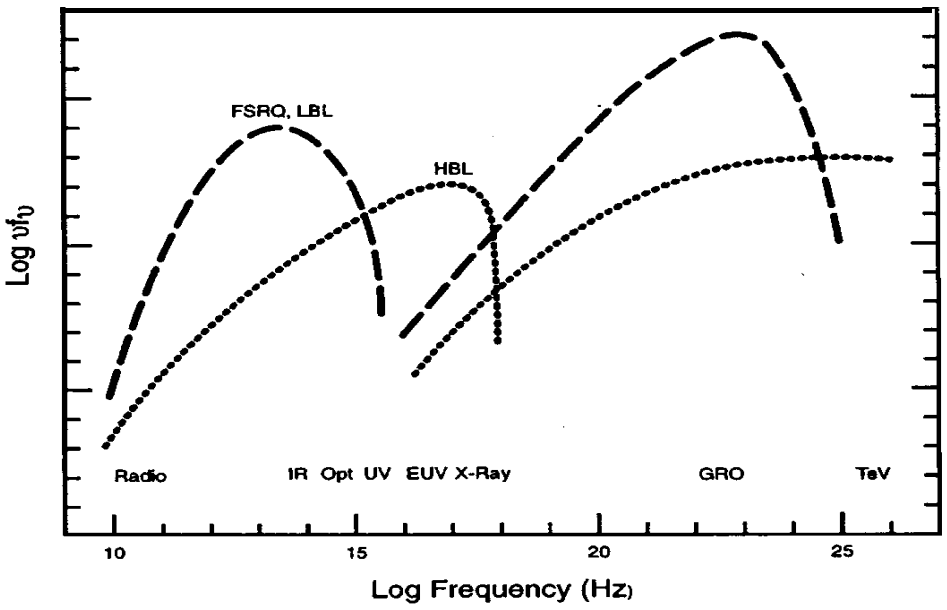

Figure 1.2 Typical blazar spectral energy distribution. The vertical axis is log (νS_ν) and multiplying the intensity power law model by ν gives $\nu S_\nu = \nu^{1-\alpha}$. A flat spectrum with $\alpha = 0$ appears as a rising spectral energy distribution. From Ulrich et al. (1997).

Blazars often exhibit radio variability on time scales of hours or days in both their total and polarised flux densities (Fuhrmann et al., 2002). Blazars are very compact sources, with cores typically less than 0.25″ at 5 GHz, the resolution of the VLA (Punsly, 2001). Indeed, "compact" used to be a synonym for "unresolved", although many compact sources are now associated with host galaxies, even if they are only indistinct fuzzy halos as in the case of many quasars (De Young, 2002).

Nearly 40% of compact radio sources do not neatly fit into the above AGN classification scheme, notably Compact Steep Spectrum (CSS) sources, and Gigahertz Peaked Spectrum (GPS) sources. O'Dea (1998) and Tornikoski et al. (2001) discuss these sources, whose typical sizes are less than ~ 15 kpc and ~ 1 kpc respectively (Urry & Padovani, 1995).

Figure 1.3 shows the canonical spectrum for 72 GPS sources, presented by de Vries et al. (1997), with the observed frequencies and flux densities for each source normalised with respect to the peak (turn-over) frequency and peak flux density.

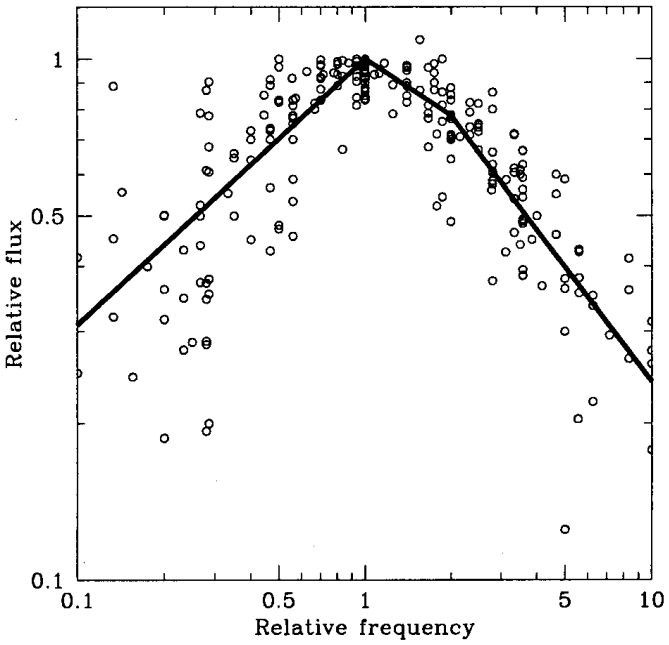

The turn-over is believed to be due to synchrotron self-absorption or free-free absorption (O'Dea, 1998). The best fit has spectral indices α = -0.51, 0.36 and 0.73 for the regions $\nu \leq \nu_T$, $\nu_T < \nu \leq 2\nu_T$ and $\nu > \nu_T$ respectively, where ν_T is the turn-over frequency.

Figure 1.3 The canonical GPS spectrum (de Vries et al., 1997).

Some blazars and radio galaxies have received secondary classifications as CSS or GPS sources (Urry & Padovani, 1995). O'Dea (1998) concluded that most evidence favours the hypothesis that CSS and GPS sources are young radio sources, with GPS sources evolving through a CSS stage en route to becoming larger scale radio sources (see also Fanti et al., 1990). It is also important to note that, while some CSS and GPS sources are characterised by radio variability, many are not: indeed, the primary flux density calibrator used by many Australian radio telescopes, PKS B1934-638, was the first GPS source discovered, in 1963.

1.4 The AGN Central Engine

AGN radio variability studies provide insight into details of AGN central engines, and it is thus appropriate to review basic central engine theory, which is a rapidly evolving field. Punsly (2001) is a good text, while Begelman & Rees (1998) and Blandford (2002) give excellent non-mathematical treatments of the topic. Shu (1992) is one of many good texts on magnetohydrodynamics (MHD) and plasma physics, and Battaner (1996) is an excellent graduate text on astrophysical fluid and plasma physics.

The central engine AGN unification scheme holds that observational differences between various AGN types are primarily due to viewing the central engine and its outflow jets from different lines of sight from Earth; to the different amounts of gas & dust available to fuel a central engine at a given time; and to minor variations in the nature of the central engine. Much AGN radio variability research – including the present Ceduna work – focuses on blazars, which are thought to be AGNs whose outflow jets are viewed almost along the line of sight, with emissions subject to relativistic beaming, as discussed in Section 1.5.

AGNs are characterised by high luminosity compared to stellar sources, and high variability across the electromagnetic spectrum. The Eddington luminosity, L_E , of an object is that for which radiation pressure balances gravitational attraction and limits accretion (assuming a spherically symmetric accretion flow). It is given approximately by (Battaner, 1996):

$$L_E \approx 30{,}000 \left(\frac{M_{AGN}}{M_{Sun}} \right) L_{Sun}$$

This can be used to place a lower limit on an AGN's mass, M_{AGN} . As an example, for an AGN luminosity of $L_{AGN} \sim 10^{14} L_{Sun}$, requiring that $L_{AGN} < L_E$ gives $M_{AGN} \sim 10^8$ solar masses. Further, if AGN emissions are observed to vary over time Δt, then causality limits the size of the emission region to $\sim \gamma \, c \, \Delta t$, where γ is the Lorentz factor. X-ray emission fluctuations on the order of minutes indicate that a typical AGN emission region is less than 10^{13} m across (Battaner, 1996). These arguments suggest the central engine of a typical AGN is a black hole, and Rees (2004) notes there is evidence that most galaxies host black holes of up to billions of solar masses. Sgr A*, the compact radio source at the center of our Galaxy is believed to be associated with a black hole of 3-4 x 10^6 solar masses (Eckart et al., 2002).

The power of most AGNs is likely due to viscous energy dissipation of the accretion flow onto the black hole, a highly effective energy production mechanism (Blandford, 2002). Begelman & Rees (1998) note that up to 42% of the infalling mass can be converted to energy, which is far more efficient than nuclear fission or fusion.

Most AGNs are radio quiet, with ultraviolet and x-ray wavelength emissions dominating their spectra (Ulrich et al., 1997). Radio loud AGNs are associated with plasma jets along the accretion disk's axis of rotation, which typically lead to extended radio lobes, and a unified central engine theory must explain the production and collimation of these outflows. These AGNs, notably blazars, often have such extraordinary luminosities that release of accretion material binding energy is insufficient to power them.

The required additional power may be being obtained by tapping the black hole's rotational energy (Blandford, 1994; 2002). A mechanism to achieve this was first proposed by Penrose (1969) and requires a spinning black hole with the surrounding space-time described by the Kerr metric. A Kerr black hole has no detailed features – the "no hair" theorem – and is defined only by its mass, angular momentum, and charge. Kerr black holes are described by Penrose & Floyd (1971), Misner et al. (1973) and Birrell & Davies (1982); and in the context of AGNs by Punsly (2001) and Blandford (2002).

The Kerr hole's ergosphere is defined to lie between its oblate static limit, inside which frame dragging must occur, and its event horizon, as shown in Figure 1.4 (Begelman & Rees, 1998; De Young, 2002).

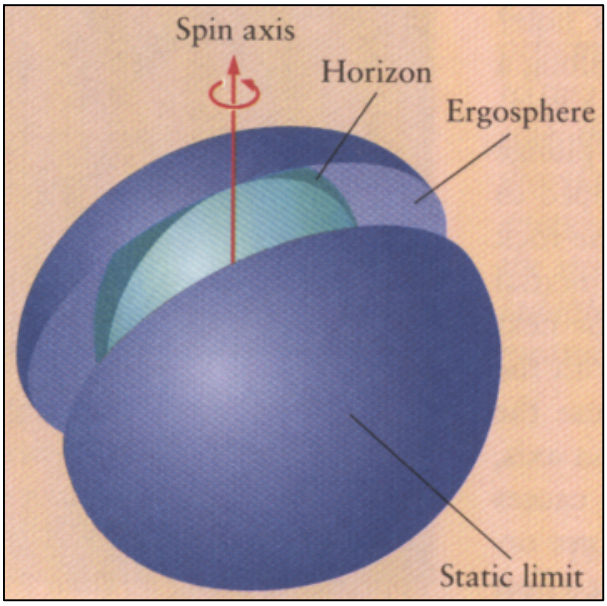

Figure 1.4 A Kerr black hole ergosphere (Begelman & Rees, 1998).

The Penrose mechanism has similarities to the Hawking radiation process, but the latter is a quantum mechanical effect, while the Penrose mechanism is an electromagnetic effect: if a particle in the ergosphere splits into two charged particles (an electron-positron pair), one with negative mass energy that falls through the event horizon and the other with positive energy that escapes to the external world, then the escaped particle has more energy than the original particle (Penrose & Floyd, 1971).

The Penrose particle is not coupled dynamically to the external world (Thorne & Blandford, 1982; De Young, 2002). However, building on pulsar research, Blandford & Znajek (1977) showed that rotational energy and angular momentum can be extracted electromagnetically from a Kerr hole if the event horizon is threaded by magnetic field lines supported by external currents in the accretion disc. The model parameters are the black hole's mass, angular momentum, accretion rate, and the near-hole magnetic field strength (Punsly, 2001).

Alternative energy channels are possible. Blandford & Payne (1982) proposed a process whereby accretion could power outflow winds, and Punsly & Coroniti (1990) extended this idea to situations in which ergospheric frame-dragging enables an indirect way to extract the Kerr hole's rotational energy. The magnetic flux tubes are forced to rotate and are stripped of their plasma, some of which enters negative energy orbits to spin down the hole in a Penrose-type process.

Outflow winds from the central engine can also be launched and collimated in several ways. One popular theory is that a plasma outflow wind is driven by magnetic pressure, and basic MHD theory suggests the plasma will be characterised by Alfvén waves, similar to the process whereby a Faraday wheel attached to a plasma-filled waveguide acts as a piston to drive Alfvén waves (e.g. Shu, 1992).

Detailed numerical simulations suggest that Alfvén outflow winds are a general feature of rapidly rotating, gravitationally confined plasmas, threaded by frozen magnetic field lines (Meier et al., 2001). The outflow winds are often relativistic with strong magnetic fields, as shown in Figure 1.5. The magnetic fields are helical, having been coiled by their forced rotation, which causes the plasma that follows the field lines to produce broadband self-absorbed synchrotron radiation. The pinch effect (e.g. Shu, 1992) applied to the poloidal magnetic field lines collimates the outflow into a jet.

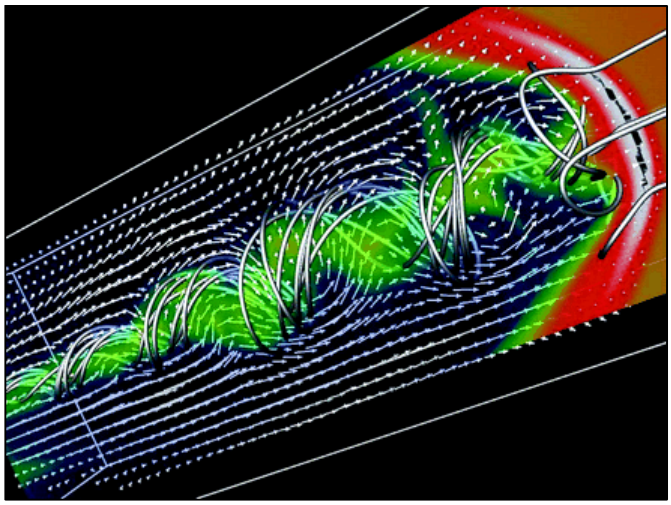

Figure 1.5 An Alfvénic jet with a bow shock wave at its leading edge, and an instability that distorts the jet's shape. High energy particles accelerated in the twisting magnetic field emit synchrotron radiation. From Meier et al. (2001).

Meier (2003) argues that jet production is an integral part of the accretion process, not a central engine model extension. He notes that the spine-sheath model of jets may be quite common, whereby the central engine produces two plasma jets in each outflow, as shown in Figure 1.6. The fact that jets are such common astrophysical phenomena, appearing for example in connection with star formation, tends to support Meier's position.

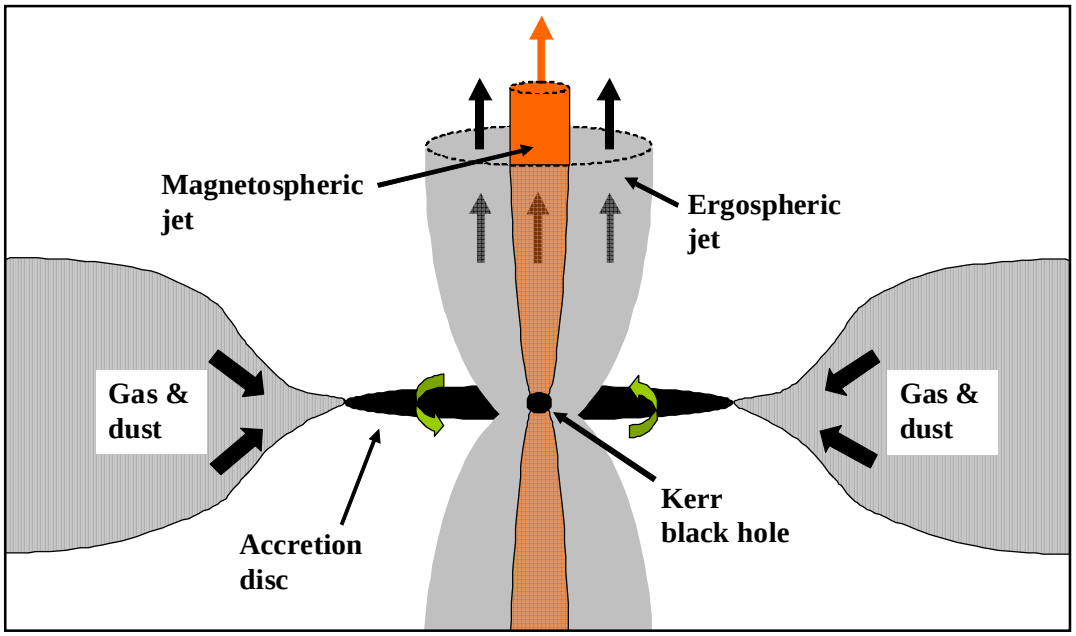

Figure 1.6 AGN central engine outflows: a bright inner jet nested within an outer jet. Adapted from Punsly (2001), and Burke & Graham-Smith (2002).

In Figure 1.6, the inner jet is driven by the magnetosphere, and its emission spectrum tends to peak at millimeter wavelengths. It has a high Lorentz factor (see Section 1.5) compared to the surrounding jet that is driven by the ergosphere, whose spectrum tends to peak at centimeter wavelengths (Meier, 2003; Punsly, 2001). Radio loud quasars and FR-II galaxies are therefore proposed to be associated with magnetospheric jets, while BL Lacs and FR-I galaxies are associated with ergospheric jets (Punsly, 2001).

1.5 Relativistic Radiative Processes

Understanding observations of radiation from blazars requires consideration of the effects associated with relativistic speeds, and with the cosmological distances at which blazars lie. These two factors are best considered separately.

Consider a jet moving towards Earth at high speed, close to the line of sight to Earth. Blazar radio emissions are believed to be incoherent synchrotron radiation from electrons in the jet as they spiral out along the magnetic field lines. The relativistic aspects of this effect can be isolated by examining the radiation observed just outside the jet region.

The frame of reference co-moving with the electrons producing the radiation moves at speed β at angle ϕ with respect to the observing frame of reference on the Earth. The angle ϕ is between the jet axis and the line of sight to Earth, and for blazars ϕ is small. The emitted and observed radiation frequencies are related by (e.g. Lightman et al., 1975):

$$\frac{\nu_{emit}}{\nu_{obs}} = D^{-1}$$

where $D = \gamma\left(1 - \beta\cos\phi\right)^{-1}$ is the Doppler factor and (as before) $\gamma = \left(1-\beta^2\right)^{-1/2}$ is the Lorentz factor. This expression can also be obtained as the Lorentz transform of the 4-wavenumber's time component, $k^0 = \omega/c = 2\pi\nu/c$, where $k^\mu = \left\{k^0,\ k^i\right\}$, and $k_i\, k^i = \omega/c$ in a vacuum (e.g. Rybicki & Lightman, 1979):

$$\omega_{obs} \equiv k^0_{obs} = \Lambda^0_\alpha\ k^\alpha_{emit} = \gamma\left(k^0_{emit} - \beta\, k^1_{obs}\right) = \omega_{emit}\,\gamma\left(1-\beta\cos\theta\right)$$

where Λ^0_α is the time component of the Lorentz transformation matrix, Λ^μ_α . In addition to a frequency shift, the synchrotron emissions experience relativistic beaming, such that if isotropic emissions are assumed then half the emitted photons are projected forward into an angle ~1/γ (Rybicki & Lightman, 1979). Vermeulen & Cohen (1994) note that AGN jet plasma may be associated with a wide range of Lorentz factors, but it is usually assumed that the jet is characterised by a bulk Lorentz factor, and it is with this value that the radiation is Doppler boosted.

Beaming greatly increases the intensity of the blazar radiation measured by an observer on Earth, typically swamping stellar radiation from the host galaxy. It is possible that blazar emission region velocities can boost the apparent brightness temperature by a factor of ~1,000 or more (Readhead, 1994).

Two principal radiative quantities of interest in radio variability studies are:

- The flux density at frequency ν, denoted by S_ν and measured in Jy (10^{-26} W m^{-2} Hz^{-1}).
- The specific intensity, $I_\nu = S_\nu / \Omega$ W m^{-2} Hz^{-1} sr^{-1} is the flux density at frequency ν per unit solid angle Ω subtended by the source(e.g. Peterson, 1997). If the source is spherically symmetric, the expression becomes $I_\nu = 4S_\nu / \pi\ \theta_s^2$ where θ_s (rad) is the angular diameter of the source.

Relativistic transformations of expressions involving these quantities can be derived using the fact that I_ν / ν^3 is Lorentz invariant (P5.10 in Lightman et al., 1975; Rybicki & Lightman, 1979). However, S_ν / ν^3 is *not* Lorentz invariant.

The cosmological distances at which blazars lies must also be considered. Over the time that radiation takes to reach Earth from a blazar at redshift *z*, the space-time metric expands, so that the radiation's wavelength increases by a factor of 1 + *z*. If specific intensity measurements are of radiation that has travelled from the blazar without being scattered by the interstellar medium, then:

$$I_\nu^{obs} = \left(\frac{\nu_{obs}}{\nu_{emit}} \right)^3 I_\nu^{emit} \quad = (1+z)^{-3} \; I_\nu^{emit}$$

In terms of Doppler factors the transformation is $I_\nu^{obs} = D^3 \, I_\nu^{emit}$ and similarly $S_\nu^{obs} = D^3 \, S_\nu^{emit}$. More generally, $S_\nu^{obs} = D^n \, S_\nu^{emit}$ where *n* depends on the beaming model. An optically thin emission sphere model is often assumed, for which $n = 3 - \alpha$, where α is the spectral index in the emission power law, $S_\nu = \nu^{-\alpha}$ (e.g. Blandford & Königl, 1979). The relativistic correction for this model can be decomposed into a factor D^2 due to aberration, a factor D due to time dilation, and a factor $D^{-\alpha}$ due to blue shifting. This last factor is usually set to unity, since blazars have flat ($\alpha \approx 0$) spectra.

The continuous jet or a "string of bullets" model requires $n = 2 - \alpha$. Vermeulen & Cohen (1994) examined the performance of four beaming models applied to a set of 25 quasars, and concluded that $1.8 \leq n \leq 2.3$ appeared to best fit the observations.

A third radiative quantity of interest is the apparent brightness temperature of the emission source. This quantity is of great importance to radio variability studies, and is discussed in Chapter 2.

2.0 VARIABILITY OF BLAZAR RADIO EMISSIONS

2.1 Historical Perspective

Understanding the origin of fluctuations in emissions from astronomical objects has been an active research field since the early years of astronomy. A key goal is to determine how much variation is intrinsic to the source, and how much is due to propagation effects caused by the medium between the source and the receiver.

If this disentanglement can be accomplished, then:

a) Intensity variations intrinsic to the source limit the linear size of its emission region, *L*, since intensity changes over a period Δt imply that, at most, $L \approx \gamma c \, \Delta t$.

b) Intensity variations due to scattering by the medium, known as *scintillation*, constrain the angular size of the emission region ("planets don't twinkle"). Scintillation also provides a tool to probe the density structure and turbulence properties of the medium.

The disentanglement problem arises because intensity variations on time scales of hours to days can be caused by many processes intrinsic to a source. However, the above causality argument requires such variations to be associated with a compact emission source, in which case its emissions can also undergo scattering by the interstellar medium at centimeter wavelengths (Narayan, 1992), leading to observation of scintillation. Such scattering is associated with variations in the electron density of the interstellar plasma.

[Electrons within the plasma have far smaller masses than protons or ions, but the same charge. By Newton's second law, they react most to the electric field of a radio wave, oscillating and re-radiating at the wave frequency: contributions of other plasma components to radio wave perturbations can be ignored (Rohlfs & Wilson, 2000).]

Astronomers first encountered variability in radio signals in the 1940s, when signals from Cygnus A were found to fluctuate in intensity on a time scale of ~10 s. An intrinsic process required Cygnus A to be comparable in size to a star, but it was soon determined that the signal fluctuations were caused by the ionosphere (Ryle & Hewish, 1950). Ionospheric plasma, created by solar ultraviolet radiation, contains turbulence that causes electron density variations, resulting in signal intensity fluctuations (Tatarskii, 1961).

The solar wind and the interplanetary medium within the solar system are also plasmas whose electron density irregularities influence the propagation of radio waves. In the 1960s, as radio astronomy methods became more sophisticated, variations in radio emissions from Jupiter and from the Sun provided opportunities to probe both the structure of these radio emission sources, and the nature of the solar wind and interplanetary medium.

A brilliant demonstration of the use of radio signal variations to probe source structure came in the 1960s, when Anthony Hewish argued that signal pulses discovered by Jocelyn Bell could be explained only by a very compact and rapidly rotating source, which they identified as a neutron star (Hewish et al., 1968). Scheuer (1968) and Rickett (1969) recognised that secondary variations in pulsar signal intensity could be explained as diffractive scintillation due to scattering by the interstellar medium (ISM), and this has been a fruitful research field.

In the 1980s, fluctuations were observed in cm-wavelength radio signals from some Active Galactic Nuclei (AGNs). For example, Heeschen (1984) reported signal "flickering" in many observations during a 9 cm survey of 226 compact flat-spectrum sources. Much of the variability occurs on time scales of hours, and is known as *Intraday Variability*. The Ceduna program is generally considered to be IDV research, but the Ceduna sources analysed by the author actually vary on time scales longer than a day, so this term is avoided in this thesis.

2.2 Evidence for Intrinsic Causes of Blazar Radio Variability

By the early 1990s, radio variability on time scales of a day or so had been observed in several AGNs, notably by the Bonn group using the 100 m Effelsberg telescope. Reviews of AGN variability are provided by Wagner & Witzel (1995), and Ulrich et al. (1997).

It was believed in the mid-1990s that almost all blazar radio variability was intrinsic to the source, and for good reason. AGNs exhibit variability across the electromagnetic spectrum, on time scales from minutes to years. Much of this variability is dramatic and broadband in nature, such that it must be intrinsic to the source, and blazars in particular exhibit violent variability due to flaring events.

Arguments supporting an intrinsic explanation for observations of blazar variability at radio wavelengths are that:

- If the central engine model of AGNs is correct, then its emissions will be characterised by variability that simply reflects the many variable processes that are associated with the model. These process include accretion feed rate changes, plasma instabilities, the explosive reconnection of magnetic flux lines, and shock waves propagating in the jet plasma (Wagner & Witzel, 1995; Punsly, 2001).
- The observed variability of blazar emissions has a broadband nature, which strongly suggests a common and intrinsic production process (Wagner & Witzel, 1995).
- Scintillation due to scattering by the interstellar medium is a phenomenon that is highly wavelength-dependent. The effect should fade at higher frequencies, so the presence of signal variability at mm and sub-mm wavelengths is evidence of an intrinsic process (Fuhrmann et al., 2002).

2.3 Relativity and the Brightness Temperature Constraint

The *brightness temperature*, T_b ,of a source with specific intensity I_ν is the temperature of a blackbody radiating with the same specific intensity. The *source brightness* is the specific intensity at the source, which is the same as I_ν in the absence of emission or absorption processes along the ray path. The Rayleigh-Jeans approximation is appropriate for radio frequencies, giving $T_b = c^2 I_\nu / 2 k_B \nu^2$, where k_B is the Boltzmann constant.

From Section 1.5, the brightness temperature transforms as ν given that I_ν / ν^3 is Lorentz invariant, so the brightness temperature in the rest frame of the source is:

$$T_b^{\text{rest}} = D^{-1} \frac{c^2}{2 k_B \nu_{obs}^2} I_\nu^{obs}$$

where $D = \gamma \left(1 - \beta \cos\phi\right)^{-1}$ is the Doppler factor, and $\gamma = \left(1 - \beta^2\right)^{-1/2}$, with β = v/c. However, the observed quantity is the flux density, S_ν , not the specific intensity, I_ν , so an appropriate angular diameter must be included, since $I_\nu = 4 S_\nu / \pi\, \theta_s^2$ (see Section 1.5).

Brightness temperatures can be inferred from blazar radio variability, but the expression for the apparent brightness temperature, and extent to which relativistic corrections are needed to obtain the brightness temperature in the source rest-frame, both depend on whether the flux density variability is intrinsic or due to ISM scintillation.

If blazar radio variability is due to scattering by the interstellar medium, no additional relativistic corrections are needed, and the angular diameter is given by scintillation theory, which is set out later in this chapter. However, the brightness temperature inferred from scintillation depends on the distance to the scattering plasma, and on the level of intensity modulation observed, in addition to the variability time scale (Rickett et al., 2002).

If blazar radio variability is intrinsic to the source, then the minimum angular diameter of the emission region corresponds to the light travel time across the region, and hence $\theta_s \geq c\, \tau_{\text{rest}} \,/\, d_A$, where τ_{rest} is the variability time scale and d_A is the angular distance to the source. Since $\tau_{\text{rest}} = D\, \tau_{obs}$, this gives:

$$T_b^{\text{rest}} = D^{-1} \frac{c^2}{2 k_B \nu_{obs}^2} \frac{S_\nu^{obs}}{\pi \left(c\, D\, \tau_{obs} / 2 d_A\right)^2} = D^{-3} \frac{2 d_A^2}{\pi k_B \tau_{obs}^2 \nu_{obs}^2} S_\nu^{obs}$$

In summary: $T_{\text{b}}^{\text{rest}} = D^{-1}\, T_b^{\text{apparent}}$ ISM scintillation

$T_{\text{b}}^{\text{rest}} = D^{-3}\, T_b^{\text{apparent}}$ Intrinsic variations

where $T_{\text{b}}^{\text{apparent}}$ refers to the brightness temperature determined by an observer on Earth.

Some workers incorrectly suggest T_b^{apparent} may scale as higher powers of the Doppler factor under some source-intrinsic emission scenarios, such as the shock-in-jet model in which a shock wave moves along an oscillating jet (e.g. Qian et al., 1991). Begelman et al. (1994) disagree, and assert that T_b^{apparent} scales exactly as D^3 in accord with the above derivation.

Kellermann & Pauliny-Toth (1969) first showed that the radio brightness temperatures of blazars should be limited by inverse Compton scattering, whereby the relativistic electrons spiralling outwards along the AGN jet's magnetic field lines produce synchrotron radiation and are then scattered from these lower energy photons, which causes their catastrophic cooling. Inverse Compton scattering occurs when the radiation energy density exceeds the magnetic field energy density, and gives an upper limit of (Melrose, 2002):

$$T_b^{\text{rest}} \approx A\left(\mathrm{B} / \mathrm{B}_{\text{ref}}\right)^{-1/7}. \qquad \text{where } A = 1.0 \times 10^{12} \text{ K and } \mathrm{B}_{\text{ref}} = 10^{-4} \text{ Tesla.}$$

Readhead (1994) pointed out that inverse Compton scattering requires the blazar emissions to be far from the equipartition and minimum energy conditions, and that an equipartition brightness temperature limit of $T_b^{\text{rest}} \approx 4.7 \times 10^{10}$ K agrees well with the observational data, which had grown greatly subsequent to Kellermann & Pauliny-Toth's original work.

2.4 Evidence for Blazar Radio Variability due to ISM Scattering

By the end of the 1990s, evidence was accumulating to swing the argument regarding the cause of blazar variability at radio wavelengths away from source-intrinsic processes (which has been well established for decades), towards scattering by the interstellar medium. This was not totally unexpected, given the point made by Narayan (1992), that variability on timescales of hours to days due to a source intrinsic process required such a small source that its radio emissions should also undergo scattering in the interstellar medium.

As noted above, observations of signal "flickering" were first reported by Heeschen (1984). Several subsequent IntraDay Variability (IDV) surveys have been carried out. Kedziora-Chudczer et al. (2001) found 22 IDV sources in a 1997-2000 southern sky survey of 118 blazars. The survey was carried out in a series of ~ 48 hour sessions, with the Australia Telescope Compact Array, observing at 1.4, 2.4, 4.8 and 8.6 GHz. Bignall (2003) reports on a program to monitor the radio variability of 22 southern sky blazars, using the ATCA between 1997 and 2000.

A northern sky *Microarcsecond Scintillation-Induced Variability Survey* was carried out at 4.9 GHz, using the VLA in four sessions between January 2002 and January 2003. Lovell et al. (2003) report results from the first epoch, in which IDV was found in 85 of 710 compact

flat-spectrum sources (a conservative cut-off was applied to classify sources as variable. Lovell et al. (2007) analysed data from all four epochs, and found that 56% of 482 compact sources showed significant IDV in at least one epoch.

Blazar radio variability analyses include B0917+624, reported by Rickett et al. (1995) and Jauncey & Macquart (2001); and PKS B1519-273, reported by Macquart et al. (2000) and Jauncey et al. (2003). These studies concluded that the radio variability on time scales of hours to days is due mainly to interstellar scintillation, and model fitting exercises provided scattering screen distance estimates of ~200 pc and ~390 pc, and source angular diameter estimates of ~60 μas at 5 GHz and ~37 μas at 4.8 GHz respectively.

J1819+3845, PKS 1257-326 and PKS B0405-385 are the most remarkable IDV sources found to date, exhibiting rapid radio variability of ~0.1 day. Analyses of J1819+3845 are reported in de Bruyn & Dennett-Thorpe (2001), Dennett-Thorpe & de Bruyn (2000; 2003) and more recently in (Macquart & de Bruyn 2006; 2007). PKS 1257-326 is reported by Bignall et al. (2003); and PKS B0405-385 is reported by Kedziora-Chudczer et al. (1997) and Rickett et al. (2002). These rapid scintillators are all associated with ISM scattering screens less than ~30 pc from Earth, which leads to the suggestion that rapid IDV may be a potential tool to assist mapping the electron density structure of the local ISM.

Two tests, described in Section 2.5, can decide whether blazar radio variability is source intrinsic, or due to the Earth moving through a scintillation pattern in space generated by scattering in the interstellar medium. First, time delays in IDV signals received at different radio telescopes are expected if the variability is due to scattering, and have been found in all the rapid scintillators, which are ideal for such experiments. Second, the presence of an annual cycle in the variability time scale is expected if the variability is due to scattering, and have been detected in J1819+3845, PKS 1257-326, PKS B1519-273, and B0917+624.

Most IDV surveys have understandably examined small numbers of strong sources, with flux densities typically ~1 Jy. However, the rapid scintillators J1819+3845 and PKS 1257-326 both have quite low flux densities (~0.2 Jy at 5 GHz), and this motivated the 2002 MASIV survey goal of identifying a larger (100 to 150) set of IDV sources, including weak sources, to better understand the statistics of the scintillation phenomenon.

Consideration of apparent brightness temperatures inferred from the variability time scales generally leads to the conclusion that some beaming is necessary to reduce the rest frame brightness temperatures to less than the upper limits imposed by the inverse Compton effect, or the slightly more stringent limit associated with the equipartition brightness temperature.

In the case of the three rapid scintillators, a source-intrinsic interpretation corresponds to $T_b^{\text{apparent}} \sim 10^{21}$ K. Coherent emission mechanisms such as electron cyclotron masar emissions and plasma emissions exist, and would account naturally for such high T_b^{apparent} values. However, Melrose (2002) has concluded that the emissions probably are synchrotron in origin. In this case, a source-intrinsic interpretation requires Doppler factors greater than 2,000 if T_b^{rest} is to be $\sim 10^{11}$ K. Ultra-relativistic AGN outflow jets may be possible, but Begelman et al. (1994) highlight the difficulties of explaining radio variability of blazars in terms of a source-intrinsic scenario involving such jets emitting incoherent synchrotron radiation. The jets would have very small synchrotron radiative efficiencies, and would have to carry large fluxes of electromagnetic and kinetic energy to produce the intraday variability, which in turn limits the bulk Lorentz factors to perhaps 100 or less. However Begelman et al. (1994) also note that this does not rule out a source-intrinsic scenario, if some other process is producing the incoherent synchrotron radiation.

Initially, a non-intrinsic interstellar scintillation (ISS) explanation of high T_b^{apparent} values did not appear more attractive. For example, Kedziora-Chudczer et al. (1997) found that, if ISS causes the variability in PKS B0405-385, then a bulk Doppler factor of $D > 10^3$ is needed to explain the observed $T_b^{\text{apparent}} \sim 5 \times 10^{14}$ K. However, a detailed analysis of PKS B0405-385 by Rickett et al. (2002) associated a peak value of $T_b^{\text{apparent}} \sim 2 \times 10^{13}$ K with the scintillating component of the emissions, with a much closer scattering screen of 25 pc compared to the previously assumed 500 pc, needing a Doppler factor of only ~75.

Rickett (2004) provides a good review of the state of IDV knowledge, and concludes that most IDV observations can be explained mainly by scattering in the interstellar scintillation. However, there is clearly much still to be learned, and it would be naïve to think that blazar radio variability does not include some source intrinsic effects. This research explores the potential of a program of long-term continuous monitoring of IDV sources to add to our understanding of blazar radio variability.

2.5 Interstellar Scintillation

2.5.1 The Interstellar Medium

Kaplan & Pikelner (1970) provide an excellent review of early knowledge of the interstellar medium (ISM). Good recent reviews of the nature of the ISM are given by Bland-Hawthorn & Reynolds (2000), and Ferrière (2001). Galactic geometry is reviewed by most astronomy texts (e.g. Zeilik & Gregory, 1998), and in brief the main Galactic disc of gas and stars is roughly circular, ~0.5 kpc thick, with a diameter of ~50 kpc.

The ISM consists mainly of molecular hydrogen (H_2), neutral atomic hydrogen (HI), and ionized hydrogen (HII). Table 2.1, taken from Reynolds (2002), shows the hydrogen exists mainly in warm neutral (HI) and warm or hot ionised (HII) phases, and helium accounts for 30% of the ISM's mass, and 9% of its number density.

Ionised regions constitute two-thirds by volume of the ISM, and radio wave scattering by this ISM component causes several phenomena in addition to scintillation, including dispersion, temporal broadening of pulsar signals, and angular broadening of radio images (e.g. Lyne & Graham-Smith, 1998). Measurements of these effects form the basis for modelling the large scale distribution of ISM free electron density. Figure 2.7 shows the results of the model developed by Cordes & Lazio (2006a; 2006b).

	H_2 Clouds	**HI Clouds**	**Warm HI**	**Warm HII**	**Hot HII**
Temperature (K)	15	120	8,000	8,000	~10^6
Midplane density (cm^{-3})	200	25	0.3	0.15	0.002
Thickness of layer (pc)	150	200	1,000	2,000	6,000
Volume fraction (%)	0.1	2	35	20	43
Mass fraction (%)	18	30	30	20	2

Table 2.1 ISM components (after Reynolds, 2002).

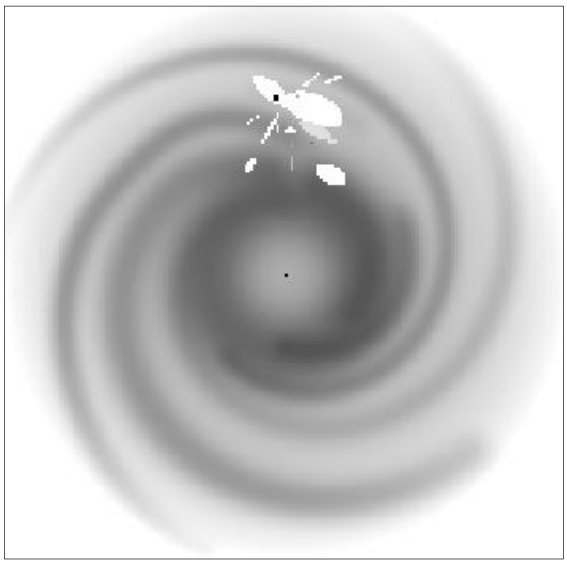

Figure 2.7 Model distribution of the Galaxy's ISM free electron density on a 30 x 30 kpc plane. The light patches are local ISM features, whose lower than average density enables the model to predict certain pulsar distances that are known independently. From Cordes & Lazio (2006a).

The average vertical electron density, $\langle n_e \rangle$, away from the Galactic Bulge can be described as (Reynolds, 1991):

$$\langle n_e \rangle \approx 0.025 \exp\left(-\frac{|z|}{900 \text{ pc}}\right) + 0.015 \exp\left(-\frac{|z|}{70 \text{ pc}}\right) \quad \text{cm}^{-3}$$

where the 900 pc and 70 pc scale heights account for electron density contributions from the diffuse warm $H_{II,}$ and the bulk effect of discrete hot H_{II} regions respectively. The equation is only a bulk description of the vertical electron density structure, and it is not valid near the Sun, which resides in a region of hot (~10^6 K) H_{II} gas known as the Local Bubble (e.g. Maíz-Apellániz, 2001). The Local ISM consists of the Local Bubble and its surrounding region, sometimes termed the Local Cavity, and soft X-ray data indicate it extends 50-100 pc in the Galactic Plane, and 200-300 pc perpendicular to the Plane (e.g. Snowden et al., 1998).

The Sun is located outside the Galactic Bulge at $z \approx 15$ pc above the Galactic Plane, for which the above equation predicts $\langle n_e \rangle \approx 0.037$ cm^{-3}. The electron density distribution in the Local ISM is not well known, (Bhat et al., 1998), but the mean electron density is believed to be $\langle n_e \rangle \approx 0.005$ cm^{-3} (Ferrière, 2001). However, patchiness probably characterises much of the Galaxy's ISM, and is not likely to be the purely local effect suggested by Figure 2.7.

Cordes & Lazio (2006a; 2006b) incorporated four distinct local ISM features into their electron density model, as shown in Figure 2.8, in which the Sun is located at {X,Y} = {0 8.5} kpc. The features are a local hot bubble (LHB), the "Loop 1" component, a local superbubble (LSB), and a low density region (LDR). The Gum Nebula and Vela pulsar are modelled as spherical regions of enhanced electron density.

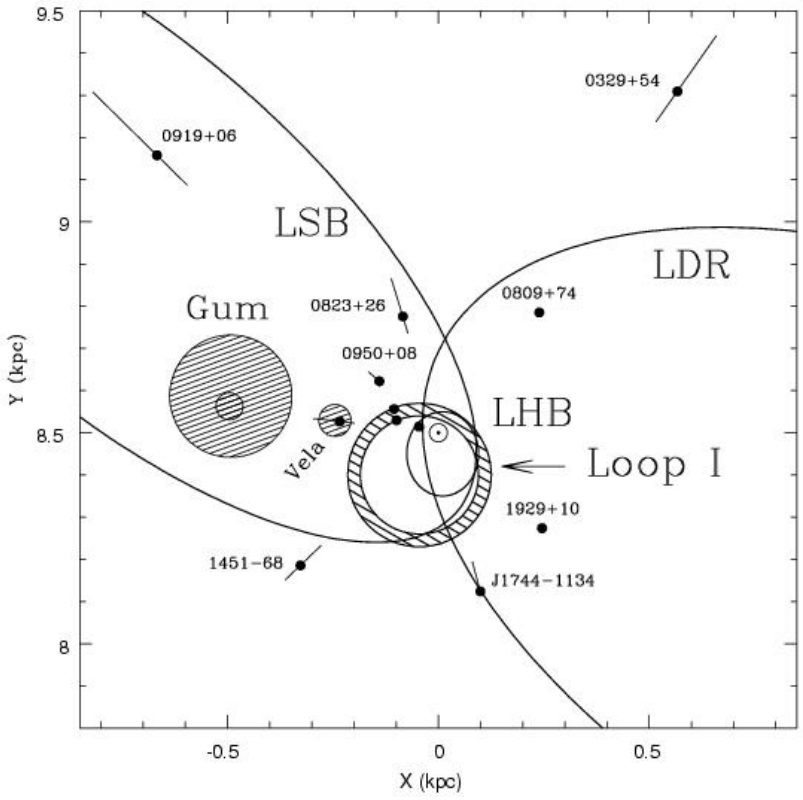

Figure 2.8 Features of the Local Bubble in the Cordes & Lazio (2006b) model. See text for details.

The distribution of neutral gas density in the Local ISM is better known than its electron density distribution, through surveys of NaI absorption. Figure 2.9 from Maíz-Apellániz (2001) shows a Galactic Plane map of neutral gas density within ~150pc of the Sun (Figure 2.8 only shows the region within ~1 kpc of the Sun). NaI absorption is mainly associated with cold (< 1,000 K) regions, so Figure 2.9 maps a different component of the ISM from that mapped by electron density distributions. In Figure 2.9, the darker shading denotes high gas density areas, while the red circle defines the region within 100 pc of the Sun. The hot Local Bubble's extent is indicated by the solid / dashed line, dashed where uncertain.

The local ISM is of central importance to understanding AGN radio signal variability due to interstellar scintillation. As discussed in Section 2.4, scattering material is usually expected to be within ~200 pc of the Sun, and often within ~50 pc. Fuhrmann et al. (2002) discuss attempts to detect evidence of scattering material in the local ISM along lines of sight to AGNs in which radio signal variability is observed. They report the discovery of molecular clouds ~100 pc distant, very close to the lines of sight to the scintillators 0917+624 and 0954+658. They suggest that, if these clouds are associated with enveloping shells of ionized material, they are attractive candidates for the sites of scattering material.

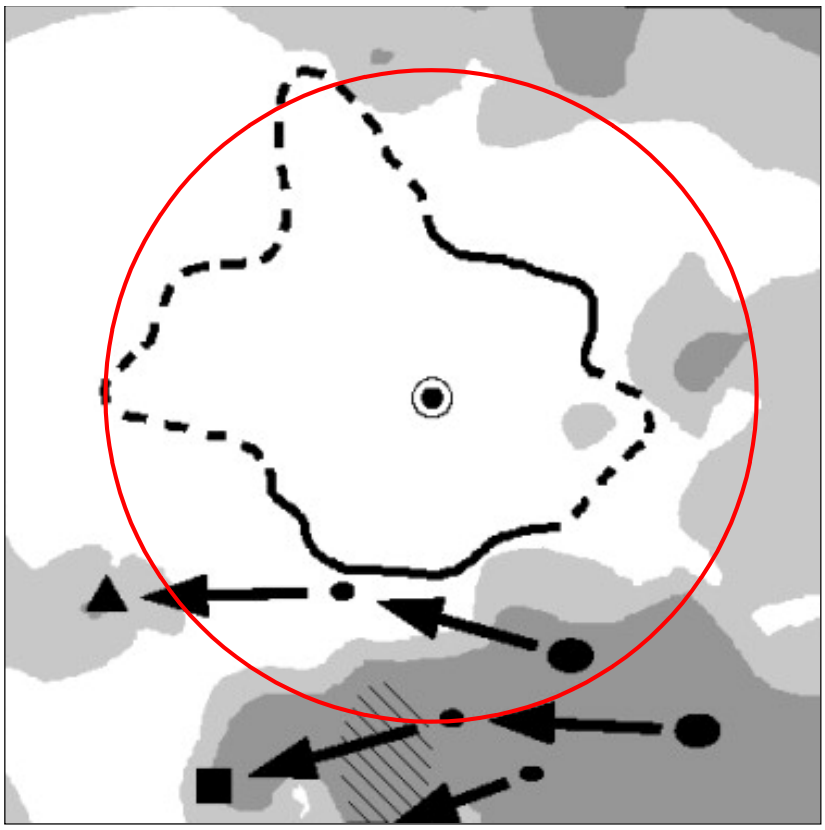

Figure 2.9 Distribution of neutral gas density in the Local ISM. Dark shading indicates high density gas. The red circle defines the region within 100 pc of the Sun (Maíz-Apellániz, 2001).

There is every reason to expect the local ISM to have plasma features able to cause radio signal scintillation. The Local Bubble is believed to be the result of several supernova explosions within the last 10 million years (Cox, 1998; Maíz-Apellániz, 2001), and it is a widely believed that supernovae cause ISM turbulence. In addition to shock waves, plasma structures may be produced by turbulent wakes from molecular clouds (Norman & Ferrara, 1996), and by elongation of plasma along magnetic field lines (Cordes & Lazio, 2001).

Blazar radio variability due to interstellar scintillation has the potential to probe the local ISM's electron density microstructure, with rapid scintillators associated with closer ISM scattering screens. Scintillation effects associated with pulsar radio variability are subtlety different, since pulsars are effectively point sources, while AGNs are extended sources. Bhat et al. (1998) examined the scintillation of 20 pulsars, and found scattering effects that they suggested may be explained by the solar neighbourhood being surrounded by a shell of much higher electron density fluctuations, embedded in the large scale ISM.

2.5.2 The Interstellar Scintillation Mechanism

A glossary of ISS modelling symbols is provided in Section 2.9. Figure 2.10 shows the standard ISS model, in which a plane wave passes through a thin screen of ISM plasma which contains electron density irregularities (Rickett 1977; 1990; 2004), Narayan (1992), and the presentations at IAU workshop 182 edited by Strom et al. (2001).

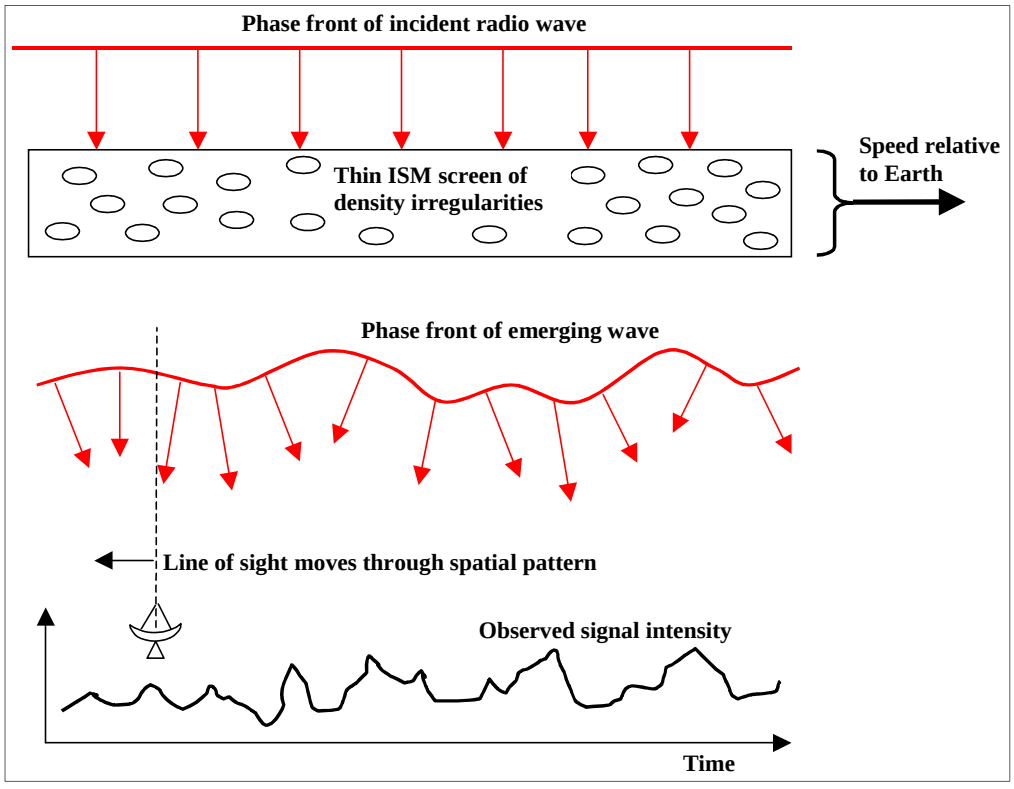

Figure 2.10 The thin-screen scattering and scintillation model.

An electron density irregularity of thickness *a*, with an excess density of Δn_e compared to the mean density, produces a phase shift of $\Delta\phi_a = r_e\ \lambda\ a\ \Delta n_e$ in a plane wave of wavelength λ, where r_e = 2.82 x 10^{-15} m is the classical electron radius (e.g. Thompson et al., 2001). Different parts of the wave pass through different parts of the scattering material, producing random phase fluctuations in the emerging wave front. These phase fluctuations interfere, and are converted to transverse spatial fluctuations of the amplitude of the radio waves at distance *R* from the scattering screen (Rickett, 2001).

In general, the Earth has a relative transverse motion with respect to the scattering screen, which causes a telescope's line of sight to move through the spatial intensity modulation pattern. For pulsar emissions, the line of sight passes through the spatial fluctuations quickly compared to the evolution time scale of the ISM electron density irregularities that produce the fluctuations (Chandran & Backer, 2002). This assumption is also usually made for AGN emissions, although it may not always be valid.

The telescope therefore moves transversely through a spatial modulation pattern that is essentially frozen for the observing period, and it observes a time series of intensity fluctuations that is the phenomenon of scintillation (e.g. Rickett, 2001). Emissions from nearby point sources, such as pulsars, are modelled as spherical waves. AGNs are so distant that they can often be treated as distant point sources whose radio signals are best modelled as plane waves, as shown in Figure 2.10. Emissions from AGNs with extended structure are modelled as a sum of mutually incoherent plane waves incident upon the ISM over a range of angles equal to the angular size of the source.

Radio wave scattering can be described using classical diffraction theory. Figure 2.11 shows the geometry of radio wave diffraction by an ISM region of anomalous electron density (a plasma "blob"). The incident wave is ψ_{inc}, and the scattering angle is θ_{scatt}. The Fresnel-Kirchhoff integrals predict the wave observed on Earth, ψ_{Earth}. For the cases of a point source at distance r_o, producing a spherical wave, and a distant point source producing a plane wave, these integrals are (e.g. Marion & Heald, 1980):

Spherical wave $\quad \psi_{inc} = A\dfrac{e^{ikr_o}}{r_o} \qquad \psi(P) = i\dfrac{Ak}{4\pi}\int \dfrac{e^{ik(r+r_o)}}{r\,r_o}(\hat{e}_r - \hat{e}_o).\hat{n}\,da$

Plane wave $\quad \psi_{inc} = \psi_o \qquad \psi(P) = -i\dfrac{\psi_o}{2\lambda}\int \dfrac{e^{ikr}}{r}(1+\cos\theta)\,da$

where the plane wave front is assumed to be parallel to the scattering screen, so that $\hat{e}_o\ \hat{n} = 1$ and $\hat{e}_r\ \hat{n} = -\cos\theta$.

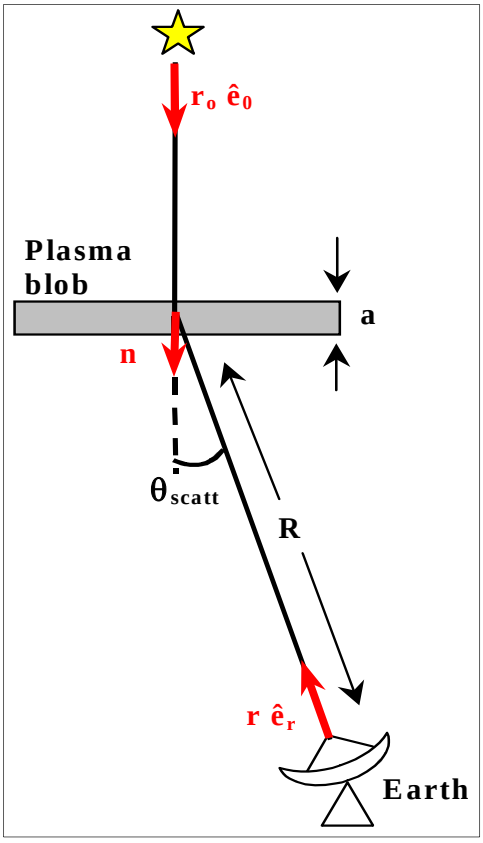

Figure 2.11 Scattering geometry.

In the case of a plane wave incident on a scattering screen, Fresnel diffraction occurs near the scattering screen, and generates a spatial modulation pattern that is translated by the Earth's passage through the pattern into the phenomenon of scintillation. Fraunhofer diffraction characterises the far-field situation, which is also well known to astronomers: it leads to Rayleigh's criterion, which says that a telescope at wavelength λ can only resolve two point sources at distance d if they are separated by angle $\theta \geq 1.22\ \lambda / d$.

Fresnel parameters

As noted above, scintillation is essentially a near field phenomenon in spite of the parsec scale distances between the ISM scattering screen and the Earth (although the limit of strong scintillation is equivalent to the far-field limit). Fresnel zones are used in studies of on-axis Fresnel diffraction problems, and the first Fresnel zone is a benchmark parameter in scintillation studies. Its linear size is the *Fresnel scale*, $L_F = \sqrt{R/k}$, where R is the distance to the scattering screen, and the radio signal has wavenumber k. The angular size of the first Fresnel zone is $\theta_F \approx L_F / R$, and the Fresnel time scale, τ_F, is the time for the telescope's line of sight to cross the Fresnel zone (Rickett, 1990).

Phase structure function and coherence scale

The observed electric field, *E*, varies as the telescope's line of sight to the source moves through the spatial intensity modulation pattern generated by the ISM scattering screen. For observations at times *t* and $t+\Delta t$, and locations separated by distance *s*, the electric field amplitude and phase are given by (e.g. Chandran & Backer, 2002): $E(\bar{r},t)\,E^{*}(\bar{r}+\bar{s},t+\Delta t)$.

Two observation records can be autocorrelated by taking their ensemble average over a sufficient time, τ, and assuming that the observing frequency, ν ,is greater than the ISM plasma frequency. The result is the visibility of the electric field. In the common interferometric situation in which observations are taken at the same time, but at locations separated by distance *s*, the visibility of the electric field is (e.g. Gupta, 2001):

$$V_{\nu}(\bar{s})=\left\langle E_{\nu}(\bar{r})\,E_{\nu}^{*}(\bar{r}+\bar{s})\right\rangle=\exp\left[-0.5\,D_{\phi}(\bar{s})\right]$$

where $D_{\phi}(\bar{s})$ is the *phase structure function,* which defined as the ensemble averaged (over time τ) square phase difference between the two observations.

$$D_{\phi}(\bar{s})=\left\langle\left[\phi(\bar{r}+\bar{s})-\phi(\bar{r})\right]^{2}\right\rangle_{\tau}$$

The *coherence scale* , also known as the decorrelation scale, s_o, is defined as $D_{\phi}(s_o)=1$. This is the length at which the visibility function falls to exp(-½), or alternatively the length at which the scattering material produces phase variations of 1 radian (Rickett, 1990).

From Section 2.3, the source brightness, B_{ν}, at frequency ν, is the specific intensity at the source. The fundamental relationship between B_{ν} and the measured visibility, V_{ν}, is:

$$V_{\nu}(\bar{r})=\int\exp\left[-i\,k\,\hat{\theta}.\bar{r}\right]B_{\nu}(\theta)\;\mathrm{d}^{2}\theta$$

where $\mathrm{d}^{2}\theta$ denotes the solid angle, $\hat{\theta}$ is the unit vector defining the direction of the wave, and $\bar{r}=\bar{V}_{rel}\,\Delta t$ where $\bar{V}_{rel}$ is the scintillation pattern velocity transverse to line of sight, which is considered in detail in Section 2.7. [In Figure 2.11, $\hat{\theta}=\hat{e}_r$, and $\bar{r}$ has a different meaning]. The scattering angle θ_{scatt} measures the width of the brightness spectrum, and the coherence scale, s_o, measures the width of the visibility, which motivates linking the two quantities (Rickett, 1990):

$$\theta_{scatt}=1/(k\,s_o).$$

2.5.3 Scintillation Régimes

Two scintillation régimes are distinguished by a scattering strength parameter, $u = L_F / s_o$, which compares the coherence scale, s_o, to the Fresnel scale, L_F (Rickett 1990; 2001).

Strong scattering ($u > 1$)
Strong scattering induces significant phase fluctuations (> 1 rad) in the radio wave front on scales smaller than the Fresnel scale ($s_o < L_F$), and is associated with relatively distant ISM scattering screens, and low observing frequencies. There are two strong ISS phenomena: *diffractive interstellar scintillation* (*DISS*) and *refractive interstellar scintillation* (*RISS*).

DISS is the diffraction pattern that results from interference between components of the scattered wave spectrum. The spatial scale of the phase fluctuations induced in the radio wave emerging from the scattering screen is effectively the coherence scale, $s_d \approx s_o$, and the spatial intensity pattern produced at the observer has peaks that occur on the same scale as the phase fluctuations (Rickett, 1990). This is a narrow band effect, with the intensity peaks corresponding to interference fringes with a characteristic frequency band (Walker, 1998).

In contrast to this, RISS is a broad band effect. It occurs when wave front fluctuations cause focusing and defocusing of the radio signal. The *scattering disc* is the region of radio wave above an observer that influences the signal intensity, and its radius sets the RISS spatial scale, s_r, which is thus larger than the DISS spatial scale, s_d (Rickett, 1990).

The strong scattering spatial pattern for a point source thus has peaks at scales of s_d, due to DISS, with peaks grouped into clumps at scales of s_r, due to RISS. These scales are related to the Fresnel scale through the relation $s_d\, s_r = (L_F)^2$ (e.g. Rickett, 1990).

Weak scattering ($u < 1$)
As the observing frequency increases, the DISS and RISS effects steadily converge, and become equal at the *transition frequency*, discussed in the next section. Higher frequencies are associated with the weak scattering régime, which leads to *weak interstellar scintillation* (WISS), a broad band effect which for sources off the Galactic plane is associated with scattering screens less than ~500 pc from Earth, and observing frequencies above ~3 GHz (Rickett, 2001), at least for lines of sight off the Galactic plane.

In WISS, the phase coherence scale is larger than the Fresnel scale ($s_o > L_F$), since the ISM induces only small phase changes (< 1 rad) in the wave front on scales comparable to L_F. Physically, large scale electron density fluctuations focus and defocus radio waves to produce a spatial intensity pattern observed on Earth (e.g. Beckert et al., 2002). However, although $s_o > L_F$, the focusing and defocusing action sets L_F as the size of a coherent patch of wave front, so $s_w \approx L_F$ (Narayan, 1992).

Scintillation Angular Scales and Cut-Offs

Table 2.2 summarises the characteristic spatial and angular scales for WISS, DISS, and RISS (e.g. Rickett, 2004).

	Spatial scale	**Angular scale**
DISS	$s_d \approx 1/(k\,\theta_{scatt})$	$\theta_d \approx s_d/R = 1/(R\,k\,\theta_{scatt})$
RISS	$s_r \approx R\,\theta_{scatt} = R/(k\,s_d)$	$\theta_r \approx s_r/R = \theta_{scatt}$
WISS	$s_w \approx L_F = \sqrt{R/k}$	$\theta_w \approx \theta_F = s_w/R = \sqrt{1/Rk}$

Table 2.2 Characteristic interstellar scintillation scales.

In Table 2.2, θ_{scatt} is the scattering angle, *k* is the wavenumber, and $s_r\ s_d = L_F^2 = R/k$. The scintillation scales vary with scattering screen distance, *R*, and with observing frequency, $\nu = k\,c/2\,\pi$. The form of the variation depends on the ISM free electron density fluctuation spectrum, which is responsible for inducing phase fluctuations in radio waves that translate into the scintillation phenomenon.

The electron density fluctuation spectrum is usually assumed to follow the Kolmogorov power law that describes a turbulence (i.e. eddy) spectrum across the inertial range of scales that lies between the outer scale at which energy is input to the ISM, and an inner energy dissipation scale (Kolmogorov, 1941; Pope, 2000). Armstrong et al. (1995) show that a Kolmogorov power law is consistent with local ISM observations over a wavenumber range of 10^{-13} to 10^{-8} m^{-1}, although at a fine level of detail the local ISM is quite patchy.

A key assumption is that density is a passive tracer for turbulence, so the electron density fluctuation spectrum is similar to the ISM turbulence spectrum, whereby the inertial range between the inner and outer scales is characterised by large eddies breaking into smaller ones. This assumption is good for modelling ocean turbulence (Dr Trevor McDougall, CSIRO, pers. comm., 2003), but it is not an obvious assumption since turbulence can occur in an incompressible fluid in the absence of density variations. Since much ISM turbulence is generated by violent processes such as supernovae (Elmegreen & Scalo, 2004), it might be expected that ISM plasma compressibility should be assumed when modelling turbulence, and departures from the Kolmogorov spectrum are known to exist along some lines of sight from the Earth (Cordes & Lazio, 2006b). However, it is generally believed that Alfvén turbulence in incompressible magnetohydrodynamics is able to explain the ISM turbulence spectrum and aspects of interstellar scintillation such as the anisotropic nature of the scattering structures (Norman & Ferrara, 1996; Goldreich & Sridhar, 1995; 1997; Spangler, 1999; Chandran & Backer, 2002; Luo & Melrose, 2006).

Cordes & Lazio (2006b) concluded that a Kolmogorov ISM free electron density spectrum appears to be a reasonable assumption overall, and it is a good starting point for predicting how angular scattering parameters vary with screen distance, R, and observing frequency, ν.

If the Kolmogorov spectrum is combined with the cold plasma dispersion relation, then (Narayan, 1992):

$$s_o \propto \lambda^{-1.2} R^{-0.6}$$

Substituting this into the expressions set out in Table 2.2 gives the scaling relationships, summarised in Table 2.3.

	$\theta_d \propto \lambda^{-1.2} R^{-1.6}$	$\theta_r \propto \lambda^{2.2} R^{0.6}$	$\theta_w \propto \lambda^{0.5} R^{-0.5}$
or	$\theta_d \propto \nu^{1.2} R^{-1.6}$	$\theta_r \propto \nu^{-2.2} R^{0.6}$	$\theta_w \propto \nu^{-0.5} R^{-0.5}$

Table 2.3. Variation of angular scattering sizes with screen distance and observing wavelength or frequency, for a Kolmogorov ISM electron density spectrum.

The scaling relationships in Table 2.3 define angular cut-off sizes for the various modes of scintillation. Figure 2.12 shows the angular cut-off sizes varying with observing frequency, ν, with the relationships linearised by the log-log scale. The gradients of the θ_d , θ_r , and θ_w cut-off lines are 1.2, -2.2, and -0.5 respectively.

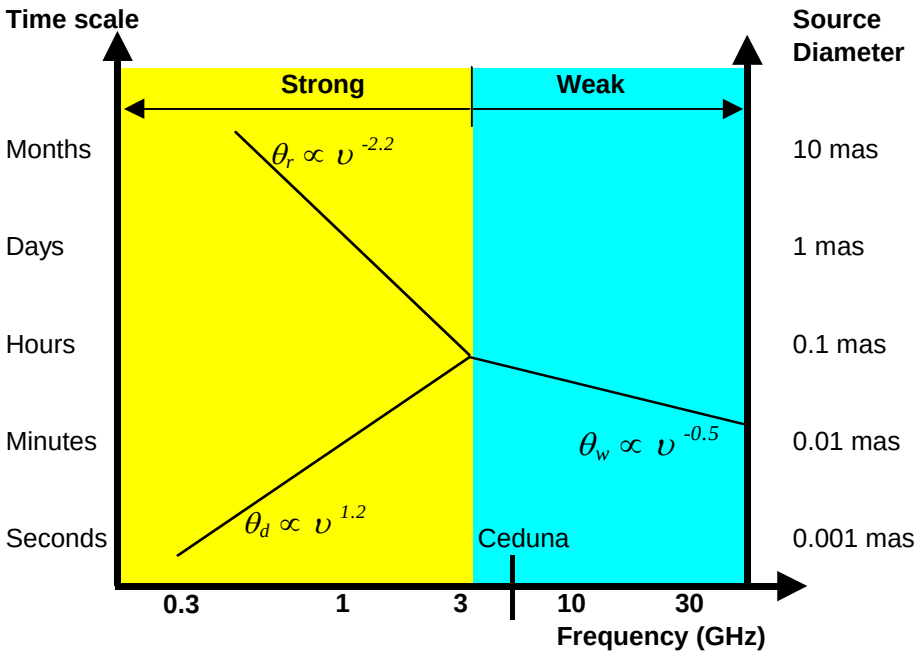

Figure 2.12 Typical ISS angular cut-offs, after Rickett(2004). Example: If WISS is present in emissions observed at 10 GHz, for a source with a transition frequency of ~ 3 GHz, the source size must be less than ~ 0.05 mas.

Figure 2.12 supports the saying that *pulsars scintillate, but AGN may not,* counterpart to the adage *stars twinkle, planets don't.* Pulsars are effectively point emission sources, and ISS in all forms has been observed in pulsar radio signals (e.g. Gupta, 2001). However, AGN emission regions have extended angular structure which restricts the ISS effects that an ISM scattering screen can generate from an AGN's radio emissions.

The restrictions occur because a source of angular size θ blurs the scintillation pattern at distance R over a spatial scale $\sim R\theta$. This quenches ISS when θ is large enough that ISS patterns due to emissions from different parts of the source overlap and smear each other out (e.g. Rickett 1990; 2001; Narayan, 1992). Thus WISS is quenched when θ is comparable to the characteristic angular scale, θ_w, and similarly for DISS and RISS (Rickett, 2004).

Figure 2.12 also shows that AGNs are associated with WISS and RISS. DISS requires sources of smaller angular size than WISS, since $s_d < L_F$, and AGN angular sizes almost always blur out DISS. But $s_r > s_d$ so the cut-off for RISS is less stringent than for DISS. Thus a source of angular size $\theta_d < \theta < \theta_r$ quenches DISS effects at the small scale on which strong scattering induces diffractive phase perturbations, but the source is still small enough to exhibit the RISS effects associated with the larger scattering disc size (Rickett, 1990).

2.5.4 The Transition Frequency

A critical input to Figure 2.12 is its assumption of a transition frequency of $\upsilon_o \sim 3$ GHz, between the weak and strong scattering régimes, which depends in large part on the nature of the ISM plasma that scatters the radio emissions.

The scaling relationships of Table 2.3 assume the plasma (free electron) density *fluctuations* follow a Kolmogorov spectrum. However, the actual distribution of the plasma density on the line of sight from Earth to the AGN must also be estimated, using one of the empirical models described in Section 2.5.1. The key parameter is the scattering measure, *SM*, which for extragalactic sources is (Taylor & Cordes, 1993):

$$SM = \int C_N^2 \, ds \quad = \left(\frac{\theta_{scatt}}{128 \text{ mas}} \right)^{5/3} \nu_{\text{GHz}}^{11/3} \qquad \text{kpc / m}^{\,20/3}$$

where C_N^2 is the spectral coefficient of the free electron density spectrum, discussed in Section 2.5.6, and the integral is along the line of sight through the Galaxy in the direction of the AGN. θ_{scatt} is measured as the Full Width Half Maximum value.

The distance from Earth to an "equivalent scattering screen", R, is defined as:

$$R_{\mathrm{kpc}} = \frac{1}{SM}\int \left(s\, C_N^2\right) ds$$

The Taylor & Cordes (1993) and Cordes & Lazio (2006a; 2006b) models provide values for *SM* and *R* along a specified line of sight, and knowing these values enables the scattering strength, *u*, for the line of sight to be determined as function of observing frequency. Using the Taylor & Cordes (1993) model, this gives Walker (1998; 2001):

$$u = L_F\; k\; \theta_{scatt} \quad = 15800\; \xi\; SM^{\,0.6}\; R_{\mathrm{kpc}}^{0.5}\; \nu_{\mathrm{GHz}}^{-1.7}$$

$$\nu_{\mathrm{o\ GHz}} = \left(15800\; \xi\right)^{10/17}\; SM^{\,6/17}\; R_{\mathrm{kpc}}^{5/17}$$

where the transition frequency, ν_o , occurs at $u = 1$. The equivalent expressions using the Cordes & Lazio (2006a) model have a numerical factor of 17950 instead of 15800. The ξ factor modifies the expression according to the preferred Fresnel scale definition. Walker (1998) defines $u = 1$ to correspond to phase fluctuations of $\xi \approx 0.5$ radians at the Fresnel scale, while a $\xi \approx 1$ radian definition is used herein.

The Cordes & Lazio (2006a) model, with $\xi = 1$, gives the υ_o values shown in Table 2.4, for the main blazar sources monitored by Ceduna at 6.7 GHz.

Source	**Galactic Long. & Lat. (°)**	**υ_o (GHz)**
PMN J1326-5206	{308.4, +10.40}	26.2
PKS B1144-379	{289.2, +22.95}	10.2
PSK B1519-273	{339.6, +24.41}	12.5
PKS B1622-253	{352.1, +16.32}	17.5

Table 2.4 Indicative transition frequencies for Ceduna IDV sources, assuming an ISM electron density distribution of the Cordes & Lazio (2006a; 2006b) model.

The Cordes & Lazio model was calibrated using pulsar data. The transition frequency for an AGN should be the same as for a distant pulsar on the same line of sight, but the predictions in Table 2.4 are too high. This may reflect a need to include additional distant pulsars in the model calibration, and certainly the spectral coefficient, C_N^2 , is quite variable (Taylor & Cordes, 1993); or there may be a bias towards observing AGN scintillation through nearby scattering material which has a lower transition frequency than a more distant screen. The more distant scattering material contributes to the total scattering measure determined from pulsar observations, but makes little contribution to the AGN variability because the source size exceeds the angular size cut-off for ISS in the more distant screens.

The transition frequency for a blazar is therefore best established by examination of multi-frequency data rather than from the predictions of the Cordes & Lazio model, or any other electron distribution model. For example, ATCA data presented in Chapter 7 show PKS B1519-273 to have a transition frequency of $\nu_o \approx$ 3-5 GHz, close to the Ceduna observing frequency of 6.7 GHz. This source therefore lies in the weak scattering régime at 6.7 GHz, not in the strong scattering régime associated with the Table 2.4 prediction.

2.5.5 Modulation Indices and Variability Time Scales

The fundamental features of a scintillation time series are its characteristic variability time scale, $T_{\rm char}$, and its modulation index, *m*, as discussed in Chapter 4. In brief, when the variability is due to interstellar scintillation, then $T_{\rm char}$ for Ceduna data is best measured as the scintillation period, which refers to the mean peak-to-peak interval that characterises a set of scintles, since scintillation is essentially a random phenomenon. [A scintle is a characteristic element – a fluctuation – in the spatial modulation field].

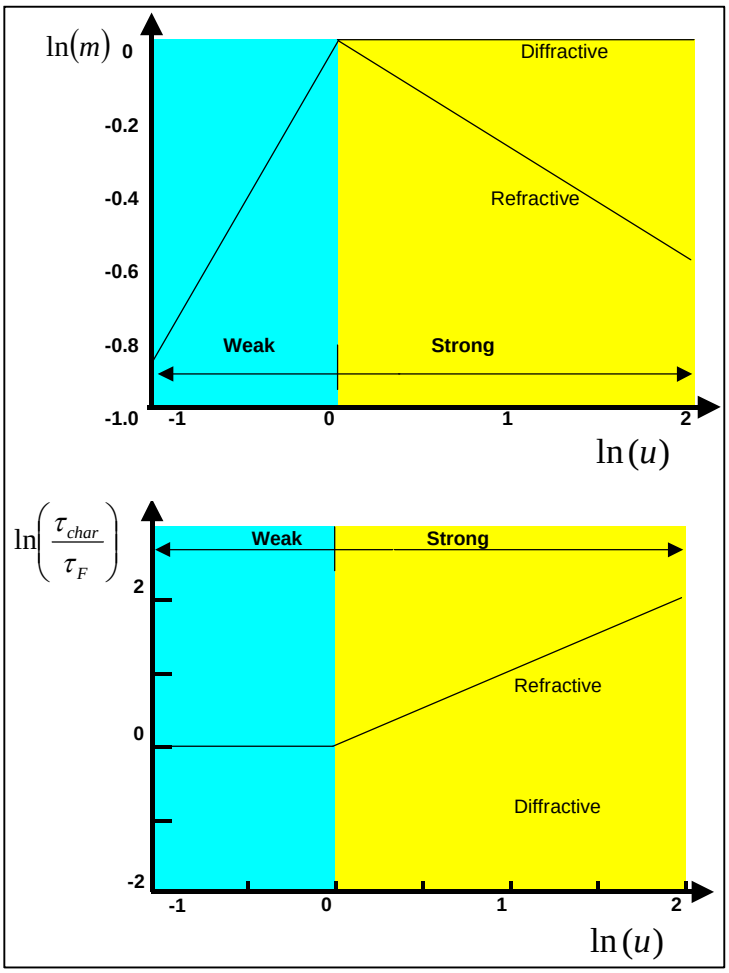

The modulation index, *m*, is defined as I_{rms}/I_{mean} , measured over a suitable averaging period. As discussed in Chapter 4, the intensity RMS, I_{rms}, includes a measurement error, while the mean source intensity, I_{mean}, may include a non-scintillating component.

Figure 2.13 shows how the variability time scale and modulation index vary with scattering strength, for a scintillating point source (Narayan, 1992).

Figure 2.13 Point radio source variability time scales and modulation index as a function of scattering strength (Narayan, 1992).

In Figure 2.13, a Kolmogorov ISM free electron density fluctuation spectrum is assumed, and the variability time scale, $T_{\rm char}$, is normalised by the Fresnel time scale, $\tau_F = L_F / V_{rel}$, where V_{rel} is the Earth's speed relative to the ISM scattering screen. The overall modulation index in the strong scattering régime is given by (e.g. Rickett, 1990):

$$m^2 \approx m_d^2 + m_r^2 + m_d^2\ m_r^2 .$$

where the cross-product term is typically small. Table 2.4 gives the point source modulation index and variability time scale relationships that underlie Figure 2.13, for the WISS and RISS régimes that usually underlie AGN variability observations, and the corresponding relationships for an extended source of angular size θ (Narayan, 1992; Walker, 1998).

	Point source	**Extended source**
WISS	$\tau_p = s_w / V_{rel} \approx \tau_F$	$\tau_\theta = \tau_F \left(\theta/\theta_F\right)$
	$m_p = u^{5/6}$	$m_\theta = m_p \left(\theta_F/\theta\right)^{7/6}$
RISS	$\tau_p = s_r / V_{rel}$	$\tau_\theta = \tau_F \left(\theta/\theta_{scatt}\right)$
	$m_p = u^{-1/3}$	$m_\theta = m_p \left(\theta_{Scatt}/\theta\right)^{7/6}$

Table 2.4 Variability time scales and modulation indices for WISS and RISS in point source and extended source radio emissions.

2.6 The Standard ISS Model for AGN Signals

2.6.1 Model Description

A glossary of Interstellar Scintillation (ISS) modelling symbols is provided in Section 2.9. The standard model of ISS in AGN radio signals is described by Codona & Frehlich (1987) and Coles et al. (1987). The model assumes DISS is completely quenched, which is a good assumption for AGN radio signals at the 6.7 GHz observing frequency of Ceduna, and the time scales of over a day that Ceduna is able to monitor at present. However, Macquart & de Bruyn (2006; 2007) report the observation of rapid (20 to 120 minute) intensity variations in the quasar J1819+3845 at 21 cm, which they attribute to DISS, superimposed on slower variations which they attribute to refractive ISS in the strong scattering régime.

Electron density fluctuation power spectrum

The ISS model describes ISM electron density fluctuations by a power spectrum of the form

$$P_{Ne}\left(\bar{q}\right) = C_N^2 \quad q^{-\beta}$$

in which a spectral coefficient, C_N^2, is scaled by a wavenumber power law, $q^{-\beta}$, where $\bar{q}$ is the wavenumber vector of the ISM electron density fluctuations. Figure 2.14 shows the power spectrum for the Kolmogorov case of $\beta \approx -11/3$, which is a straight line in log space.

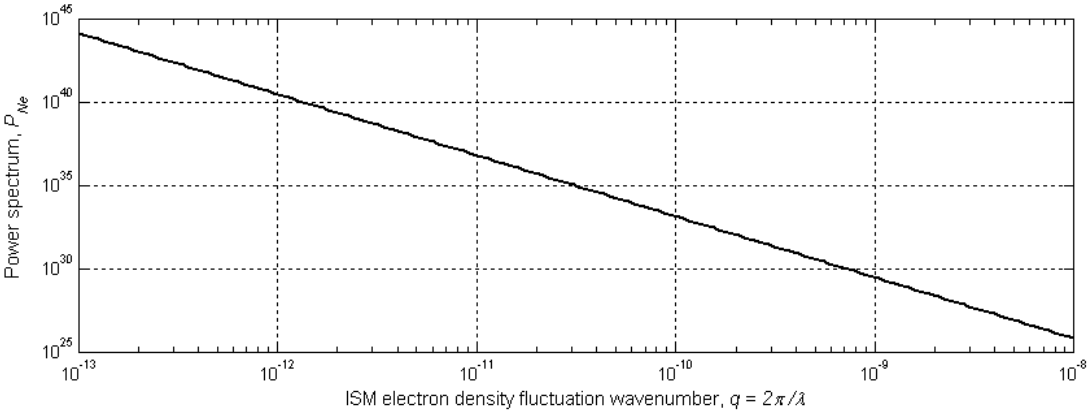

Figure 2.14 Kolmogorov ISM electron fluctuation power spectrum (m^{-3}) as a function of wavenumber (m^{-1}). Log scale to highlight $\beta \approx -11/3$.

As discussed in Section 2.5.3, the electron density fluctuations are a passive tracer for turbulence in the ISM, and the Kolmogorov spectrum describes an eddy energy cascade between an inner wavenumber scale (i.e. large distances) at which energy is input and an outer wavenumber scale at which energy is dissipated, such that $q_{outer} < q < q_{inner}$.

The spectral coefficient for the local ISM is usually modelled in one of two ways:

Thin scattering screen $\quad C_N^2(z) = C_{No}^2\ \delta(z - R)$

Extended scattering screen $\quad C_N^2(z) = C_{No}^2\ \exp\left(-z^2/R_o^2\right)$

where *z* is distance along the blazars' line of sight from Earth. In the thin scattering screen model, the screen is at distance R from Earth, while in the extended scattering screen model the spectral coefficient is assumed to have a Gaussian profile with a scale distance R_o. Cordes & Rickett (1998) suggest a spectral coefficient value of $C_{No}^2 \approx 10^{-3.5}\ \mathrm{m}^{-20/3}$, but the spectral coefficient is characterised by extreme variability, with very high values associated with HII regions (Spangler, 1999).

ISM turbulence is magnetohydrodynamic in nature, since it involves plasma moving in magnetic fields, and magnetic fields should produce anisotropic ISM plasma scattering structures, with their major axes aligned with the field. In the case of the ISM, the energy cascade from large to small scales across the inertial régime likely involves substantial magnetic energy. This line of reasoning led Goldreich & Sridhar (1995) to propose an anisotropic power spectrum of electron density fluctuations, with small-scale fluctuations

significantly elongated parallel to the magnetic field compared to the transverse direction. Radio wave propagation through ISM material described by a Goldreich-Sridhar power spectrum has been examined by Chandran & Backer (2002). The anisotropic form of the electron density fluctuation power spectrum is:

$$P_{Ne}(\bar{q}) = C_N^2 \; q^{-\beta} \quad \rightarrow \quad C_N^2(z)\left[\Omega\, q_x^2 + q_y^2/\Omega\right]^{-\beta/2}$$

where β = 11/3 corresponds to the Kolmogorov spectrum, and Ω is the axial ratio of the scattering structures [This is given the symbol R in Chapter 7, but R in this chapter is the scattering screen distance]. Values of Ω<1 correspond to sampling the spatial modulation pattern along the minor axis of the scattering structures (the *x*-direction of the wavenumber vector, $\bar{q}$). One effect of scattering by anisotropic turbulence is a large negative overshoot in the autocorrelation function, explained in Chapter 4, and by Rickett et al. (2002).

Signal intensity power spectrum

The electron density fluctuation power spectrum generates a signal intensity power spectrum given by (Codona & Frehlich, 1987):

$$P_{\Delta I}(\bar{q}) = 8\pi r_e^2 \lambda^2 \; P_{Ne}(\bar{q}) \times \sin^2\left(\frac{q^2 R}{2k}\right) \times \left|V\left(\frac{\bar{q}\,R}{k}\right)\right|^2 \times \exp\left[-D_\phi\left(\frac{\bar{q}\,R}{k}\right)\right]$$

where r_e = 2.82 x 10^{-15} m is the classical electron radius, *R* is the distance from the Earth to the ISM scattering screen, the sine-squared term is known as the Fresnel filter, and $V(\bar{r})$ is the source visibility, where $\bar{r} = \bar{q}\,R/k$.

D_ϕ is the phase structure function, introduced in Section 2.5.2. It can be expressed in terms of gamma functions (e.g. Coles et al., 1987), but if the phase fluctuations are due to isotropic Kolmogorov turbulence with a large outer scale and a small inner scale, as Armstrong et al. (1995) show is approximately valid for the ISM, then (Narayan, 1992):

$$D_\phi(s) = \left(s/s_o\right)^{5/3}$$

In the régime of weak scattering $s > s_o$, and $D_\phi \rightarrow 0$, so that $\exp(-D_\phi) \rightarrow 1$ and the signal intensity power spectrum simplifies to:

$$P_{\Delta I}(\bar{q}) = \left\{8\pi r_e^2 \lambda^2\right\} P_{Ne}(\bar{q}) \times \sin^2\left(\frac{q^2 R}{2k}\right) \times \left|V\left(\frac{\bar{q}\,R}{k}\right)\right|^2$$

$$= P_{\Delta I}^{\text{point}}(\bar{q}) \times \left|V\left(\frac{\bar{q}\,R}{k}\right)\right|^2$$

such that the observed intensity power spectrum is a result of $|V(\bar{r})|^2$ acting as a low pass filter applied to the point source intensity fluctuation spectrum. The power spectrum of temporal intensity variations is obtained by dividing through by the relative transverse speed of the ISM with respect to Earth, V_{rel}, which is taken to be directed along the *x*-component of the 2-dimensional wavenumber vector, $\bar{q}$, such that (e.g. Macquart & de Bruyn, 2006):

$$P_{\Delta I}(\omega) = \frac{1}{V_{rel}} \int_{-\infty}^{+\infty} dq_y \;\; P_{\Delta I}^{Po\,\mathrm{int}}\left(\frac{\omega}{V_{rel}}, q_y\right) \times \left| V\left(\frac{\omega\, z}{V_{rel}\, k}, \frac{q_y\, R}{k}\right)\right|^2$$

Intensity covariance and model predictions
The spatial signal intensity covariance, is defined as spatial correlation of the intensity signal with itself:

$$R_{\Delta I}(\bar{r}) = \left\langle \Delta I(\bar{r}_1)\, \Delta I(\bar{r}_1 + \bar{r}) \right\rangle$$

where $\Delta I = I - I_{mean}$ and $\bar{r} = \bar{V}_{ISS}\, \Delta t$ is the distance moved by the Earth through the spatial intensity pattern in time Δt, assuming a frozen pattern on time scales of Δt. In practice, $R_{\Delta I}$ is computed as the Fourier transform of the scintillation intensity power spectrum, $P_{\Delta I}(\bar{q})$:

$$R_{\Delta I}(\bar{r}) = \int_{-\infty}^{+\infty}\int_{-\infty}^{+\infty} P_{\Delta I}(\bar{q}) \exp(i\, \bar{q}.\bar{r})\, d^2\bar{q}$$

The intensity modulation index (*m*) and the scintillation time scale (τ_{char}) are computed from the intensity covariance as follows (Rickett et al., 1995):

$$m = \sqrt{R_{\Delta I}(0)} \text{ and } \tau_{char} = s / V_{rel} \text{ where } R_{\Delta I}(s) = 0.5\, R_{\Delta I}(0)$$

2.6.2 A Demonstration Model

Rickett et al. (1995) described scintillation of the radio source 0917+624 using an isotropic version of the ISS model, in which the intensity power spectrum is approximated as:

$$P_{\Delta I}(\bar{q}) \;\; = A\, P_{Ne}(\bar{q}) \exp\left[-(q\, L_F\, u)^{5/3}\right](1+B)^{-1/2} \left\{1 - \exp\left(\frac{-q^4 L_F^4}{4(1+B)}\right)\right\}$$

Where $A = 4\pi^{3/2}\, r_e^2\, \lambda^2\, R$, $B = 0.5\, q^2\, R^2\, \theta^2$, and the scattering strength is $u = L_F / s_o$.

In the electron density fluctuation power spectrum, $P_{Ne}(\bar{q}) = C_N^2 \;\; q^{-\beta}$, Rickett et al. (1995) assumed the spectral coefficient to fall off as a Gaussian function of distance from Earth, *z*, to 1/*e* at a scale height distance R_o = 1 kpc, under the thick scattering screen expression given in the previous section as $C_N^2(z) = C_{No}^2 \exp\left(-z^2 / R_o^2\right)$.

Rickett et al. (1995) assumed the source to have a Gaussian brightness distribution, and hence an effective angular size of $\theta \approx \theta_\lambda$ / 2.35 at wavelength λ. For a point source, $\theta \to 0$ and $B \to 0$, and a J_o Bessel function was used to compute the two dimensional Fourier transform of the intensity power spectrum, to obtain the intensity covariance.

$$R_{\Delta I}(\bar{r}) = \int_{-\infty}^{+\infty}\int_{-\infty}^{+\infty} P_{\Delta I}(\bar{q}) \exp(i\,\bar{q}.\bar{r})\, d^2\bar{q}$$

The author developed a variation of the Rickett et al. (1995) model, to develop a working knowledge of ISS modelling. In the variation model, a thin scattering screen is assumed, $C_N^2(z) = C_{No}^2\ \delta(z-R)$, with $C_{No}^2 \approx 10^{-3.5}$ m$^{-20/3}$. Radial symmetry is used to compute one integral in the above expression, introducing a $2\pi q$ factor. The second integral is computed using standard quadrature, with the lower limit now 0 instead of -∞, and including the real component of the term exp(i *q.r*). The approach was implemented using *Matlab's* recursive adaptive quadrature algorithm, *quadl*.

Figure 2.15 gives the model predictions, assuming a transition frequency of $\nu_o \approx 6$ GHz (wavelength $\lambda_o \approx 5$ cm), following Rickett et al. (1995). The modulation index, *m*, is the square root of the intensity covariance for $\bar{r} = 0$, computed for each source size across a range of wavelengths. The decorrelation spatial separation, *s*, at which $R_{\Delta I}(s) = 0.5\, R_{\Delta I}(0)$, is found by trial and error. The Earth's speed relative to the scattering screen is assumed to be V_{rel} = 50 km/s, and hence the variability time scale is τ_{char}= s / V_{rel}.

Figure 2.15 gives predictions of *m* and T_{char} for a thin scattering screen located at *R* = 1 kpc. The solid lines show the predictions for a point source, with $m \approx 0.9$ and $\tau_{char} \approx 0.1$ days near the transition wavelength. These predictions closely match the predictions presented in Figure 3 of Rickett et al. (1995) for a point source with an extended scattering screen with a scale height of R_o = 1 kpc. Such agreement is expected, as discussed in appendix B3 of Rickett et al. (1995).

Some AGNs exhibit scintillation which is associated with closer scattering material, and the transition frequency is expected to decrease for a given C_{No}^2 for closer scattering screens. However, the maximum RISS scintillation index remains about 1 at the transition frequency regardless of the distance to the scattering screen, since this is what defines the transition frequency.

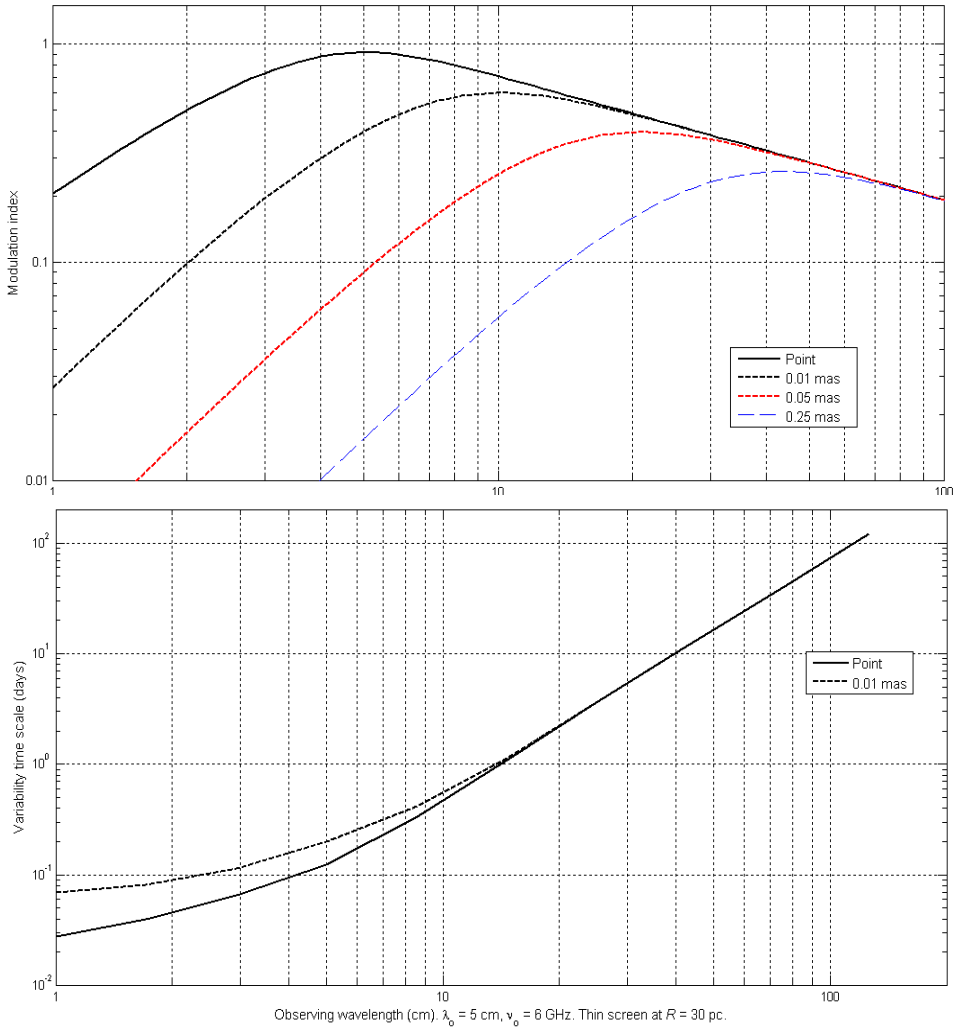

Figure 2.15 ISS model predictions of modulation index (top) and variability time scale (bottom). See text for discussion.

The model predicts that the modulation index increases with wavelength, to a maximum in the transition region in the case of a point source, and to a maximum at longer wavelengths in the case of extended sources. This accords with the theory outlined in previous sections. However, the model also predicts that the modulation index will decrease as the wavelength continues to increase into the strong scattering régime. This is a characteristic of RISS, and the model, as explained above, does not include the DISS strong scattering component.

2.7 Annual Cycle and Time Delay Tests

An intrinsic explanation of blazar radio variability requires a compact source, and it is expected that scintillation will also be apparent in such a source if a suitable ISM scattering screen exists along its line of sight (Narayan, 1992). However, either of two observational tests provide unequivocal support for ISS as the principal cause of variability in an AGN radio signal.

The tests rely on the fact that ISS occurs because the ISM produces a spatial pattern of intensity modulations in the plane of the Earth's orbit. This pattern moves at the speed of the scattering screen, changing only slowly compared to the scintillation time scale.

Figure 2.16 shows that:

1) An annual cycle in the scintillation time scale results when the Earth's orbital speed is similar to the relative speed of the Earth with respect to the ISM scattering screen, causing a seasonal variation in the rate at which the Earth encounters scintles.

2) The time offset between IDV intensity measurements by widely separated telescopes is caused by the finite speed at which the Earth moves through the scintillation pattern.

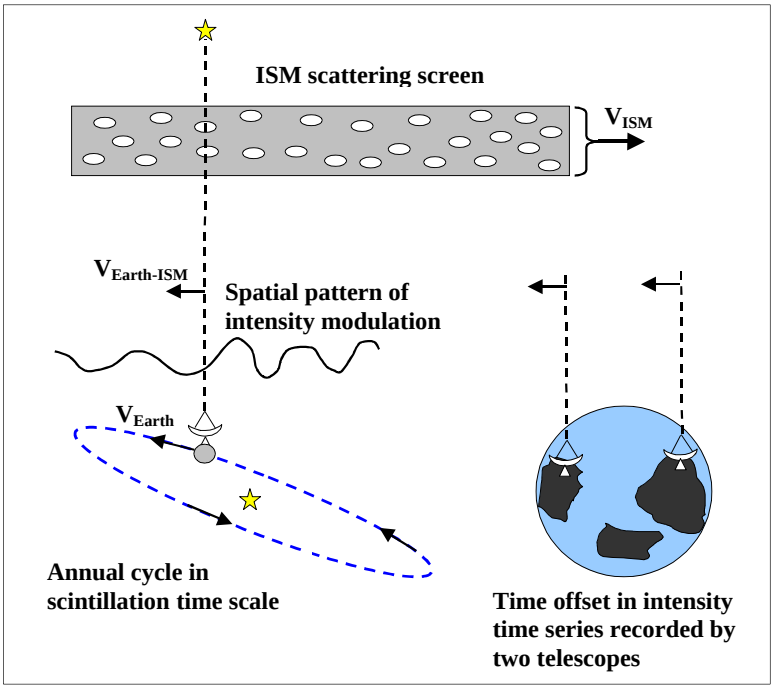

Figure 2.16 Annual cycle and time delay tests of whether or not variability is due to ISS.

Mechanisms intrinsic to the source are not able to explain either of these phenomena, but both can be explained by ISS, although both tests have limitations. An annual cycle in the scintillation time scale is not easily discerned if the Earth's orbital speed is much slower than its speed with respect to the ISM. The time delay test requires rapid scintillation, and a large modulation index, so the signals recorded by the two telescopes change significantly over the pattern delay time scale of a few minutes, enabling a delay to be identified.

The annual cycle test is of principal interest in analysing data from Ceduna. Professor Barney Rickett of the University of California at San Diego has developed a model that predicts the annual time scale cycle for a source, with declination δ and right ascension α.

The model is derived by considering the Earth-ISM motion in rectangular equatorial coordinates, in which the *x*-axis is towards the vernal equinox ($\delta = 0°$, $\alpha = 0$ h), the *y*-axis

points along α = 6 h (δ = 0°), and the *z* axis is oriented parallel to the North Celestial Pole (for which δ = 90°). In these coordinates, the unit position vector, $\hat{e}_{source}$,of the source is (e.g. Taff, 1981):

$$\hat{e}_{Source} = \begin{bmatrix} x \\ y \\ z \end{bmatrix} = \begin{bmatrix} \cos\delta \cos\alpha \\ \cos\delta \sin\alpha \\ \sin\delta \end{bmatrix}$$

Figure 2.17 shows that the scintillation pattern velocity, $V_{Earth\text{-}ISM}$, which is transverse to the line of sight from Earth to the source, can be decomposed into component velocity vectors that lie parallel and perpendicular to the equatorial plane, with the unit vectors in these directions denoted $\hat{e}_\alpha$ and $\hat{e}_\delta$ respectively.

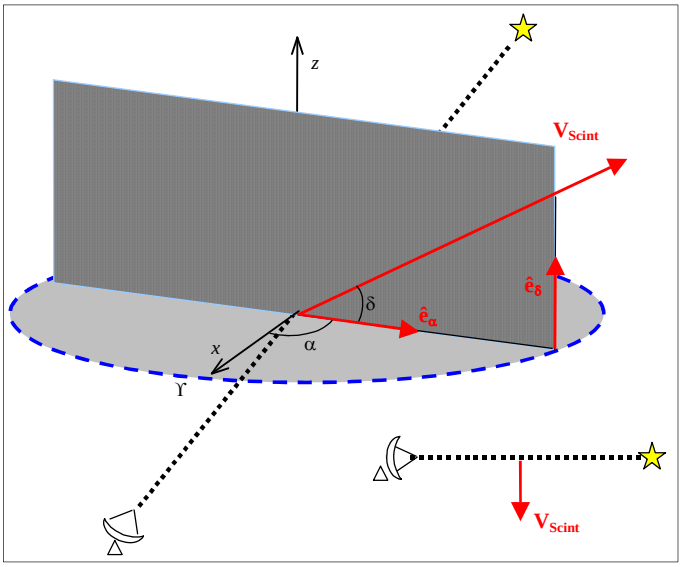

Figure 2.17. Decomposition of the scintillation velocity vector into components parallel ($\hat{e}_\alpha$) and perpendicular ($\hat{e}_\delta$) to the equatorial plane.

The unit vector $\hat{e}_\alpha$, which lies in the equatorial plane, depends only on right ascension, α, and has no *z*-component in rectangular coordinates. The $\hat{e}_\delta$ unit vector depends on both right ascension and declination, δ. In rectangular equatorial coordinates, these unit vectors are (Macquart & Jauncey, 2002):

$$\hat{e}_\alpha = \begin{bmatrix} -\sin\alpha \\ \cos\alpha \\ 0 \end{bmatrix} \qquad \hat{e}_\delta = \begin{bmatrix} -\cos\alpha \sin\delta \\ -\sin\alpha \sin\delta \\ \cos\delta \end{bmatrix}$$

Now the relative speed of the Earth with respect to the ISM scattering medium must be calculated. As a first approximation, the ISM is assumed to travel at the galactic orbital speed of the Local Standard of Rest (LSR). The relative speed of the Sun with respect to the LSR, $V_{Sun\text{-}LSR}$, is about 19.7 km/s towards $\{\delta_{Sun}, \alpha_{Sun}\} \approx \{30°, 18\text{ h}\}$ which, in rectangular equatorial coordinates is, with angles expressed in radians:

$$V_{Sun-LSR} = 19.7 \begin{bmatrix} \cos\delta_{Sun}\ \cos\alpha_{Sun} \\ \cos\delta_{Sun} \sin\alpha_{Sun} \\ \sin\delta_{Sun} \end{bmatrix} \quad \text{km/s}$$

In general, the ISM scattering material has a velocity different to the LSR, described by an offset velocity with components $\{V_\delta, V_\alpha\}$ in declination and right ascension. The offset velocity is a free parameter.

The Earth's velocity with respect to the Sun, $V_{Earth\text{-}Sun}$, is (e.g. Taff, 1981):

$$V_{Earth-Sun} = 29.86\ R_1(-\varepsilon) \begin{bmatrix} -\sin\Phi \\ \cos\Phi \\ 0 \end{bmatrix} = 29.86 \begin{bmatrix} -\sin\Phi \\ \cos\Phi\cos\varepsilon \\ \sin\varepsilon\cos\Phi \end{bmatrix} \quad \text{km/s}$$

where the obliquity of the ecliptic is $\varepsilon = 23.5°$, and $R_1(-\varepsilon)$ is a rotation of $-\varepsilon$ about the *z*-axis, to transform from ecliptic to equatorial coordinates. The vernal equinox occurs on day 80 of the year, and on day *d* the Earth's equatorial longitude, Φ, is:

$$\Phi = 2\pi \frac{(d-1)-80}{365} - \pi \qquad 1 \le d \le 365 \text{ and } -\pi \le \Phi \le +\pi$$

The overall velocity of the Earth with respect to the ISM is thus:

$$V_{Earth-ISM} = V_{Earth-Sun} + V_{Sun-LSR} - (V_\alpha\ \hat{e}_\alpha + V_\delta\ \hat{e}_\delta)$$

The scintillation pattern moves transversely across the line of sight with a velocity V_{rel}, which has components parallel and perpendicular to the equatorial plane of V_α and V_δ respectively (i.e. parallel to the RA axis). In rectangular equatorial coordinates:

$$V_{rel} = \hat{e}_{source} \times (V_{Earth-ISM} \times \hat{e}_{source}) \qquad V_{//} = V_{rel} \,.\, \hat{e}_\alpha \qquad V_\perp = V_{rel} \,.\, \hat{e}_\delta$$

Figure 2.18 shows the basic annual cycle for PKS B1622-253, one of the Ceduna blazar sources, assuming no velocity offset. For sources near the ecliptic plane, the plot of V_α against V_δ reduces to a straight line. For sources at high ecliptic latitudes, the plot approaches a circle. If the characteristic spatial scale is taken to be the coherence scale, s_o, then as discussed in Section 2.6, the characteristic scintillation time scale is $\tau_{\text{char}} = s_o / V_{rel}$.

Coles & Kaufman (1978) extended this model to consider an anisotropic spatial pattern of intensity modulations. The pattern is assumed to form elliptical contours with axial ratio Ω, and the major axes of the ellipses are inclined at angle β to the direction of the scintillation velocity. The direction of these lines is defined by $\hat{S} = \{\cos\beta, \sin\beta\}$.

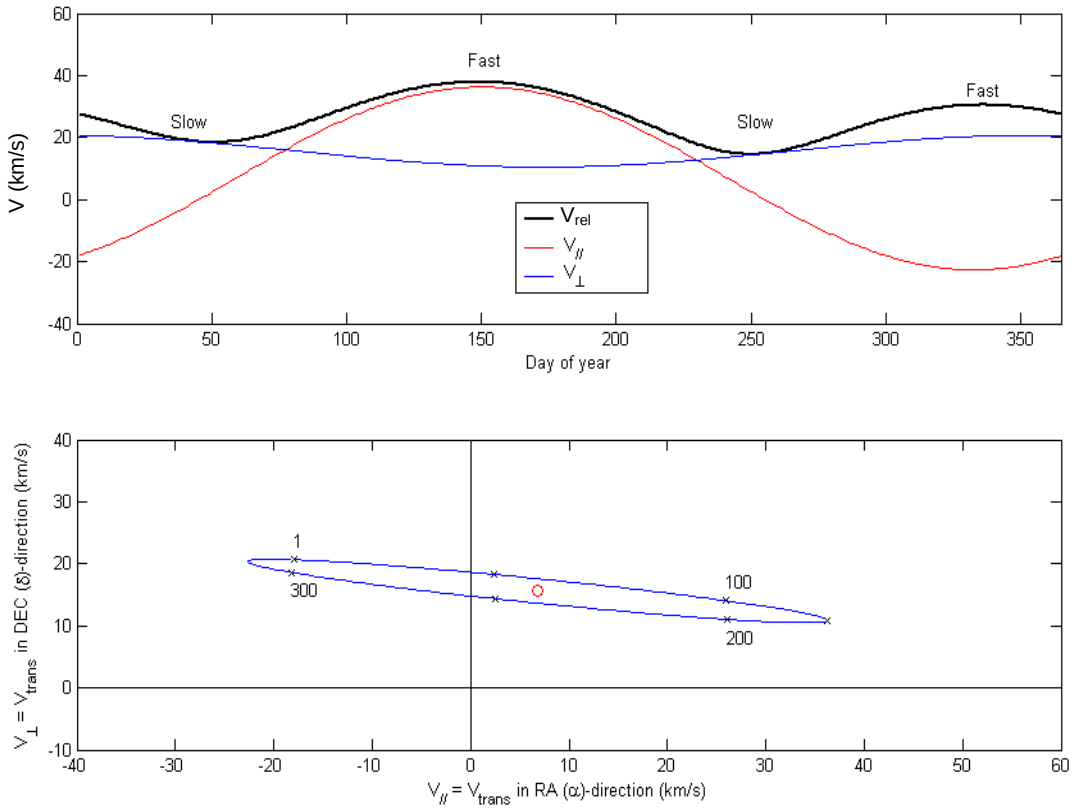

Figure 2.18 Annual cycle in V_{rel} for PKS B1622-253.

The scintillation velocity changes during the year, but this does not affect the definition, and simply requires that a different value of β is used for each epoch. The anisotropy, defined by the matrix C (below), is set up in a fixed co-ordinate frame, and the scintillation velocity is free to change as necessary.

The intensity covariance function (see Section 2.6) has the form:

$$R_{\Delta I}(\bar{r}) = f\left(\frac{\left|C\left(\bar{r}-\bar{V}\,t\right)\right|^2}{s_o^2}\right) \qquad C=\begin{bmatrix}\cos\beta/\sqrt{\Omega} & \sin\beta/\sqrt{\Omega}\\ -\sqrt{\Omega}\sin\beta & \sqrt{\Omega}\cos\beta\end{bmatrix}$$

where the scintillation pattern moves transversely across the line of sight with a velocity V. If the decorrelation time scale is defined as the time lag for which

$$\left|\left(C\,\bar{V}\right)\,\tau_{\text{char}}\,\right|^2 = s_o^2$$

then it can be shown that $\left|\,C\,\bar{V}\,\right|^2 = \frac{1}{\Omega}\left[\,V^2+\left(\Omega^2-1\right)\left(\bar{V}\times\,\hat{S}\right)^2\right]$, which gives:

$$\tau_{\text{char}} = \frac{\sqrt{\Omega}\;s_o}{\sqrt{V^2+\left(\Omega^2-1\right)\left(\bar{V}\times\,\hat{S}\right)^2}} \quad \xrightarrow{\Omega=1} \quad \tau_{\text{char}} = \frac{s_o}{V}$$

Figure 2.19 shows the effect on the annual cycle in $V_{Earth\text{-}ISM}$ for anisotropic scintles, with an aspect ratio of $\Omega = 2$. When $\beta = 90°$, the minor axis of the elliptical scintles is aligned with the scintillation velocity, and the annual cycle is accentuated compared to the $\Omega = 1$ cycle. The Earth encounters peaks and troughs even faster during speed-up times of the year, and slower during the slow-down times, as shown in Figure 2.19 by the red line. When $\beta = 0°$ the major axis of the scintles is aligned with the scintillation velocity, and the annual cycle is flattened compared to the $\Omega = 1$ cycle, as shown in Figure 2.19 by the blue line.

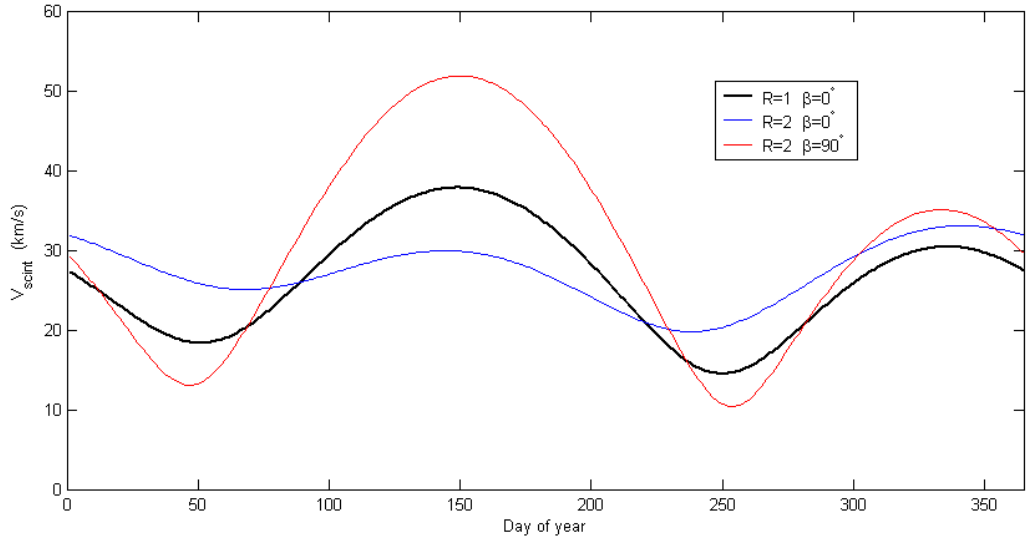

Figure 2.19 Effect of anisotropy on the annual cycle in V_{rel} for PKS B1622-253.

2.8 The Need for Annual Data: The Ceduna Project

Considering our present understanding of AGN structure, an apt quotation by Martin Rees of Cambridge is that "the central engine model is a mountain of theory built on a molehill of evidence". Malkan (2001) agrees that our understanding of AGNs is a seriously data-limited problem, but notes that AGN radio variability can alleviate the problem if extensive, nearly continuous time histories of the emissions from individual AGN can be obtained.

Variability due to scintillation can help to map the electron density structure of the local ISM. Assuming that density is a good passive tracer for turbulence, this in turn will aid our understanding of the turbulence processes that are operating in the local ISM. One way to further blazar radio variability research is to carry out a dedicated long-term observing campaign to gather detailed quasi-continuous data on several sources. The benefits of such time series are that they can:

a) test if signal variability is intrinsic or due to interstellar scintillation, by establishing whether an annual cycle is present in the variability time scale;

b) facilitate detection of signal variability with periods of weeks or longer;

c) enable the statistical nature of the variability to be examined; and

d) possibly enable the two-dimensional geometry of the scintillation pattern to be deduced using the Earth-orbit synthesis method (e.g. Macquart & Jauncey, 2002).

Unfortunately, a long term continuous monitoring program is not possible using a major radio telescope facility, such as the Australia Telescope Compact this research, which aims to determine whether the 30m single-dish at Ceduna can record blazar radio intensity time series that are quasi-continuous over a period of a year or more, and of sufficiently high quality that a variability analysis can be performed. Ceduna can observe only relatively strong radio sources, but there are enough of these to make the effort worthwhile.

2.9 Glossary of ISS Modelling Symbols

The ISS modelling literature is not consistent in its use of ISS modelling symbols. The symbols used in this thesis have the meanings set out below.

R	Distance from Earth to the ISM scattering screen
λ k, ν, ω	Signal wavelength, wavenumber, frequency and angular frequency
θ_F , L_F	Fresnel scales
D_ϕ	Phase structure function
s_o	Coherence (decorrelation) scale, $D_\phi(s_o) = 1$
θ_{scatt}	Scattering angle, $\theta_{scatt} = 1/(k\ s_o)$
u	Scattering strength parameter, $u = L_F / s_o$
C_N^2	Spectral coefficient of the electron density spectrum
ν_o	Transition frequency
τ_{char}	Characteristic variability time scale
V_{rel}	Scintillation pattern velocity transverse to line of sight
m	Modulation index, $m = I_{rms} / I_{mean}$
s_d, s_r, s_w	DISS, RISS and WISS spatial scales, $s_w \approx L_F = \sqrt{R/k}$
θ_d, θ_r, θ_w	DISS, RISS and WISS angular scales, $\theta_w \approx \theta_F = s_w / R = \sqrt{1/Rk}$
$\bar{q}$	Wavenumber vector, with q_x aligned to V_{rel}
$P_{Ne}(\bar{q})$	Electron density fluctuation power spectrum
$P_{\Delta I}(\bar{q})$	Signal intensity power spectrum
$R_{\Delta I}(s)$	Spatial signal intensity covariance
Ω	Axial ratio of the ISM scattering structures.
$V(\bar{r})$	Source visibility, $\bar{r} = \bar{q}\, R/k$

3.0 CEDUNA AND THE 2003/05 COSMIC PROGRAM

3.1 History of the Ceduna Radio Telescope

McCulloch et al. (2005) provide a summary of the Ceduna earth station's history, the 1990s conversion of one of its antennae to a radio telescope, the procedures developed to process Ceduna data, and the telescope's performance. This chapter provides a detailed discussion of this work, and introduces the initial (2003-2005) COSMIC observing program.

The Ceduna radio astronomy observatory is located 34 km inland from the South Australian coastal town of Ceduna about 850 km north-west of Adelaide, as shown in Figure 3.1, at longitude E133° 48' 36".57, latitude S31° 52' 05".04 and altitude 161m above sea level. The facility was built in 1969, as an 4-6 GHz up/downlink earth station for the Intelsat series of satellites. These satellites are in geostationary orbits over the Indian Ocean, where they are visible from both Europe and Australia simultaneously. The satellites are just 3° above the north west horizon at Ceduna.

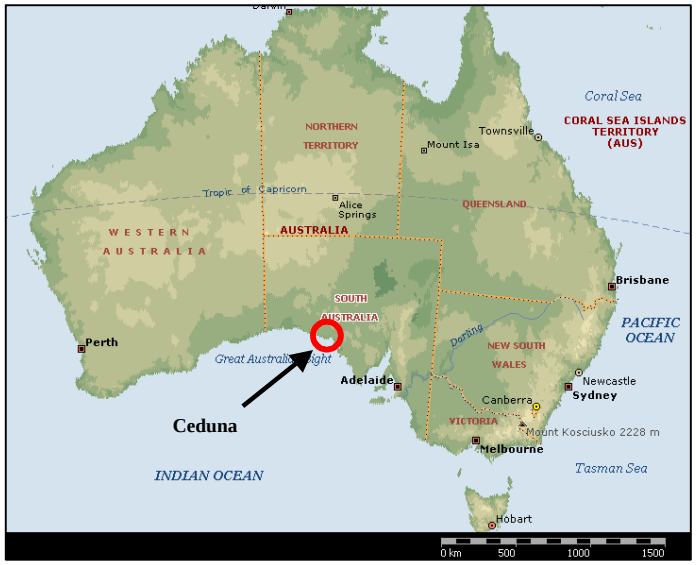

Figure 3.1 Location of the Ceduna station.

A microwave relay network carried telecommunication traffic between Ceduna and the east coast cities. In the 1990s, with the advent of fibre optics networks, Telstra consolidated its resources, moving the newer of the two 30 m station antennas to Perth, and in 1995 donated the other antenna to the University of Tasmania, to be converted for radio astronomy use.

Conversion work was carried out at a cost of $2.5 million, and radio astronomy observations were first made in March 1997. The antenna has an azimuth-elevation mount with Naysmyth optics. The terminating sections for the Naysmyth waveguide feed operate in the frequency bands of 2.2, 4.8, 6.7, 8.4, 12.2 and 22 GHz. The dual circular polarization receivers are uncooled and, except for the 22 GHz system, have a bandwidth of about 500 MHz.

Ceduna now participates regularly in Very Long Baseline Interferometry (VLBI) programs, notably as part of the Australian Long Baseline Array network. The other radio telescopes in the LBA network all lie at roughly the same longitude in eastern Australia, so Ceduna has significantly enhanced the nation's VLBI ability by extending the network's (u, v) coverage.

As discussed in Chapter 2, long term observations of variability in blazar radio signals have the potential to reveal information that cannot be deduced from short term observations, about both AGN source structure and the interstellar medium. The key question is how this could be achieved, given the international competition to use Australia's National Facility telescopes in New South Wales, the 64 m Parkes telescope, and the six-telescope compact array at Narrabri.

These premier facilities cannot be used to monitor a source for periods of weeks or longer, due to the intense demand for observing time. It was thought such a monitoring program using the Ceduna radio telescope might be possible, especially since it is a University facility, but it would require high-quality stand-alone continuous remote operation.

Figure 3.2 The Ceduna 30 m azimuth-elevation dish.

In early 2002, the author met Dr Simon Ellingsen, Dr David Jauncey, Dr Jim Lovell, and Professor Peter McCulloch. It was agreed that if Ceduna could achieve the performance needed for long-term monitoring of radio sources, this could provide the basis for a PhD research program carried out by the author. By early 2003, the telescope control software written by Dr Ellingsen and others, and the data processing software written by the author, were performing well enough to start a monitoring program that promised to be capable of producing the required high-quality intensity time series.

3.2 Telescope Operation

Telescope operation methodologies are similar for all radio telescopes, and much of the software used by the University of Tasmania's radio telescope at Mount Pleasant near Hobart was able to be applied to the Ceduna facility. Some additional hardware-specific interface software needed to be written, with credit primarily due to Dr Ellingsen. The Ceduna system was also developed with remote operation capability: an astronomer in Hobart (1,700 km from Ceduna) or elsewhere can control the telescope in real-time, program it with observing instructions, start it, monitor its operation, stop it, and stow it.

The back-end system. Figure 3.3 shows the signal processing hardware schematic. The Ceduna observations presented in this thesis were made using an uncooled receiver with two orthogonal circular polarisation channels (LCP & RCP) operating over the frequency range 6.4-6.9 GHz. The channels are separate, with independent signal paths, each as shown in Figure 3.3. A low phase-noise local oscillator (LO) set to 11.4 GHz mixes the radio frequency (RF) signal into the intermediate frequency (IF) range of the observatory down-conversion system.

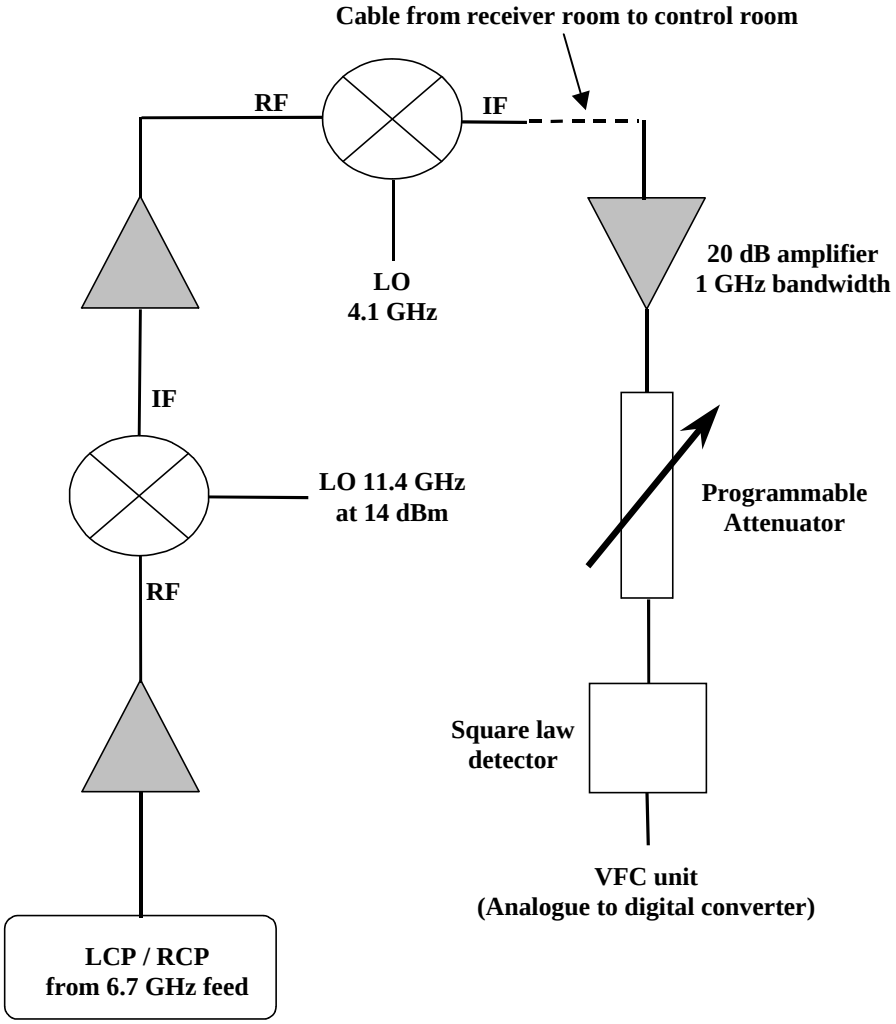

Figure 3.3 Signal processing back-end system schematic.

The down-conversion system contains a fixed-frequency local oscillator set to 4.1 GHz, and the effective front-end local oscillator is the difference between these two frequencies (i.e. 7.3 GHz). The IF signal from the down-conversion system is transferred from the upper-equipment room on the telescope to the control room using low-loss coaxial cables. It is then amplified, and attenuated to optimise the signal level for the square-law detectors, which convert the broadband signal into a DC-voltage that is proportional to the power in the broadband signal. This DC-voltage is then passed to the analogue-to-digital converters.

The Ceduna receiver system is able to switch between source observations and measurement of a calibration noise diode. The noise diode is injected by a probe which just in front of the receiver ports and placed at 45° to each of the receiver ports. It is measured prior to each scan across a source, to determine any change in the gain, and is not switched during the scanning across a source.

This approach is used because testing prior to the start of the COSMIC campaign found that the system gain varies only slowly. Subsequent investigations have shown that some "1/f" noise is present on timescales longer than ~1 second (see Section 5.2.3), and this might be mitigated by a noise-adding radiometer. But this would decrease the effective observing time, and it is not clear that the effort required to implement this (notably the modifications required to observing and processing software) would be justified by the improvements.

The noise diode is compared with a 1dB (~5K) step in the initial data processing, although it has been found that minor calibrator amplitudes changes occur over time. PhD student Cliff Senkbeil has investigated the gain stability of the receiver system in detail, and his work suggests that small changes in the output power of the noise diode are produced in response to changing air temperature. However, this process cannot be quantified easily, because the noise diode is housed within the telescope structure. This causes a time lag between a change in the ambient air temperature, which is measured, and the subsequent change in the temperature of the air around the noise diode, which is measured now, but was not measured during the period of data collection for this thesis.

The slow changes in system gain are removed by the polynomial filtering process, described in Chapter 4. Comparison of this technique with methods which use the changes in ambient temperature and a model of the noise diode output power show that the effective differences are minimal.

There is no temperature stabilization of the receiver system or backend. In hot weather, air conditioning is used to reduce the ambient air temperature around the receiver and backend systems. However, given Mr Cliff Senkbeil's findings, temperature stabilization of as much equipment as possible is recommended for future work.

The frequency bandpass of the receiver and backend system was investigated in June 2003 by Dr Simon Ellingsen and the author, a few months after the start of blazar observations. At that time, bandpass equalising filters were installed in the system, and these significantly flattened the bandpass. The difference in bandpass amplitude over the 500 MHz frequency range after installation of the filters was measured to be less than 3 dB. Prior to installation of the filters, it is estimated that the effective bandpass was of the order of 250 MHz.

There is no amplification of the post square-law detected signal, as experience has shown this tends to introduce additional noise. There is no measurable DC offset voltage from the square-law detectors: this was suspected in the early part of the COSMIC campaign, but investigation showed the effect was due to the changing output from the noise diode. The analogue to digital conversion system is achieved using 16-bit voltage to frequency (VFC) converters. The square-law detector and the VFC converters been shown to be linear in the range over which the system is operated. The VFC converters are linear for input voltages in the range 0-2 V, and the system is operated at ~1 V to give maximum allowance for voltage variation. The changes in system gain with changing air temperature and telescope elevation are such that the system always operates well within this linear range.

The effect of the atmosphere at 6.7 GHz is quite small. In the worst weather conditions the change in the observed SEFD at the zenith is no more than 7% of the typical value for good weather conditions (see Section 5.2.2). In poor weather, the atmosphere thus contributes no more than ~7K to the antenna temperature; and typically much less than this.

Source observation strategy. A software program called 'Bruce' controls the telescope and the sampling system which reads the analogue-to-digital converters. Bruce examines a user-specified list of both blazar and calibrator sources, determines which sources are currently above an elevation of 10 degrees, and selects the source for which the previous observation was longest ago. The relative frequency with which each source is observed is controlled by listing the same source more than once in the source selection catalogue. The general aim is to ensure that blazar sources are observed twice as often as calibrator sources.

A radio telescope can measure the flux density of a source by scanning across it according to an observing strategy. The strategy at Ceduna, implemented by 'Bruce', is to scan across the source back and forth in right ascension (RA), and back and forth in declination (DEC), as shown in Figure 3.4. Each scan takes about 15 seconds at the telescope drive rate of 3º/min. As noted above, the system equivalent flux density is determined prior to each scan by comparing the height of the noise diode to a 1 dB step (a well calibrated attenuator), and the flux density data are measured in units of the noise diode.

For the two DEC scans, the antenna traverses across the source at constant right ascension, with the declination varying across about 0.75 degrees (i.e. 45 arc minutes) of sky. As discussed in the next section, the on-source (FWHM) portion of the scan is about one-third of the total scan. The analogue-to-digital converters are sampled at 847 Hz, and it was determined through experimentation that angular binning of data in increments of 0.004 degrees was sufficient to define the signal's peak.

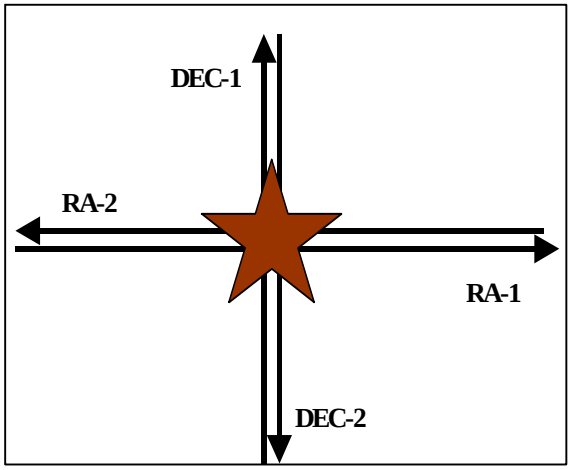

Figure 3.4 Orthogonal scans across a source.

For the two RA scans, the antenna traverses across the source at constant declination. The scans are of equal length on the sky at the celestial equator, where 1º of declination equals four minutes of right ascension. Elsewhere, the equality of the scan lengths is automatically maintained by Bruce, which increases the length of scans in right ascension by 1 / cos(dec).

Data re-sampling and archiving. Bruce removes any data points that differ significantly from their surrounding samples, such outliers being produced by interference or occasional converter misreads. The data are re-sampled as a function of telescope position, with each re-sampled scan consisting of two sets of 187 sample points across the 45 arc minutes of sky, with a resampling time of 0.085 s (see Section 5.2.2), one set for each circular polarisation component. The data are saved in FITS format using a local implementation of the single dish conventions (Garwood, 2000) developed by Dr Chris Phillips.

Pointing corrections. Small inaccuracies in antenna pointing result in a telescope rarely scanning through the center of a source, introducing pointing errors as shown in Figure 3.5.

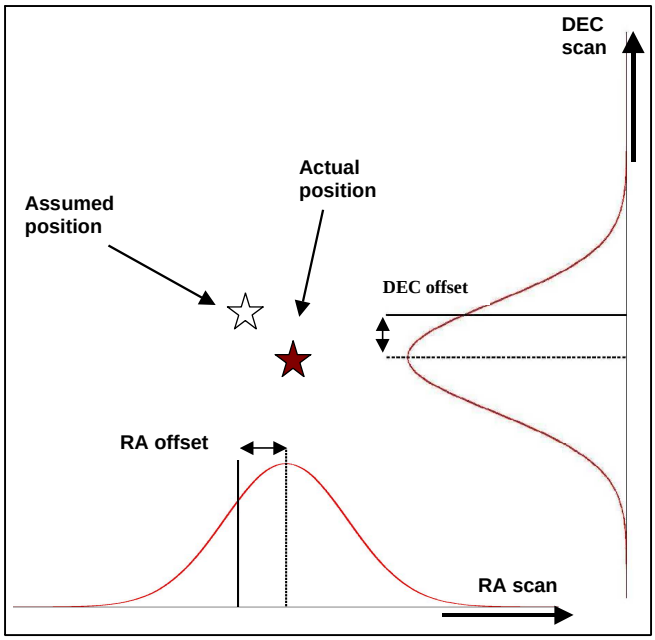

Figure 3.5 A pointing offset in right ascension reduces the peak flux density of the scan in declination, and vice-versa.

In Figure 3.5, consider the scan across a source in right ascension, at a constant declination that is offset with respect to the actual source declination. The flux density profile measured by this scan will be reduced compared to a scan with no offset. Similarly, the orthogonal scan in declination, holding the right ascension constant, expects a flux density peak in the middle of the scan. However, the peak will instead occur at a location which is offset from the middle of the scan.

A default (global) pointing model is applied by Bruce to correct the direction of the antenna for deviations due to the telescope's weight. Additional residual pointing corrections are made by Bruce to the antenna itself during an observing session, enabling the telescope to track a source across the sky as accurately as possible during operation. Ceduna is a parabolic reflector telescope, and the recorded flux density profile for each scan (the beam pattern) rises to a peak and then falls in a manner that is well described by a Gaussian curve.

Bruce therefore fits Gaussian profiles to each scan and updates the telescope pointing for that source if:

a) the fitted peak is positive;

b) the measured offsets for the scan pairs in RA agree within 0.5 arcminutes (an empirically determined tolerance), and similarly for the scan pairs in DEC; and

c) the reduced chi-squared of the fit is sufficiently good (see also Chapter 7).

The algorithm that decides if the source pointing should be updated is conservative and has never yet been known to make an incorrect pointing update due to poor data in more than a 1,000 days of COSMIC observations. An incorrect pointing update could happen, but it is clearly a very rare occurrence. The next time the source is observed Bruce compares the location (in azimuth and elevation) to the previous observation: if either has changed by more than 4 degrees, then the pointing corrections computed for application to the previous scan are deemed to be out of date, and Bruce reverts to the catalogue position for the source.

The Ceduna observing strategy enables further pointing corrections to be computed and applied to the recorded data, as described in Section 3.5.

3.3 Data Processing Software

Ceduna's data are stored in the Flexible Image Transport System (FITS) format developed by Wells et al. (1981). The author downloaded basic FITS reading routines made available by NASA, and wrote a suite of data processing and analysis programs using the *Matlab* technical computing software package.

The programs are menu-driven and highly automated, which minimises the chance of data processing errors due to users entering incorrect information.

The principal programs are:

- *Headers.m* and *FitsSources.m*. Support programs which respectively show the file header information and the radio sources associated with a given FITS file.

- *ScanData.m*. Extracts data for a specified source, using a two-pass strategy described below. The program is typically applied to a maximum of 5 FITS files, to keep data arrays to manageable sizes.

- *ScanFit.m*. Processes the data extracted by *ScanData.m*, to produce quality-controlled flux density data, with ancillary information such as source elevation.

- *ScanPlot.m*. Displays plots of the flux density data produced by *ScanFit.m*, converted from VFC units to Janskys, and corrected for pointing errors and gain-elevation effects. The user can examine the data, and produce a data file ready for analysis.

- *ScanAnalysis.m*. A package of data processing, display, and analysis tools.

Typical data processing sequence

The software programs outlined above operate together to provide a semi-automated data processing sequence to support the observing program. As explained in Section 3.6, the program divides blazar and calibrator sources into northern and southern groups with respect to the zenith at Ceduna, and each group is observed in turn for some 10-15 days.

Consider northern group observing period 16, which spanned U.T. days 132 to 148 of 2004. The 17 FITS files for this observing period are *bruce_04132.fit* to *bruce_04148.fit*. Each FITS file contains several hundred scans of each northern group source, with a total of about 1400 scans per file. For each source, *ScanData.m* extracted scan data from sequential groups of FITS files for days 132-136, 137-140, 141-144, and 145-148, and each data set was then processed by *ScanFit.m*. For example, for PKS B1519-273, *ScanFit.m* produced output file *D_1519-273_04132* from the data within the FITS files for days 132-136. The other output files were: *D_1519-273_04137*, *D_1519-273_04141*, and *D_1519-273_04145*.

ScanPlot.m was then applied to the set of four *ScanFit.m* output files, and a single file *RM_1519-273_04132* was produced for the entire observing period. *ScanAnalysis.m* takes as its input the data within all the *RM* files for a given source, and its suite of display and analysis routines are applied to the concatenated time series.

Scan groups

Each application of the Ceduna observing strategy produces a set of flux density scans known as a scan group. A "scan" refers to a set of flux density measurements recorded as the antenna traverses across a source. As shown in Figure 3.4, a scan group consists of orthogonal pairs of scans across the source, each with two channels corresponding to the left-hand (*L*) and right-hand (*R*) circularly polarised components of the radio signal.

The Gaussian flux density profile of the source roughly corresponds to the middle one-third of each set of data points, and the adjacent data points correspond to black sky. There are thus eight data sets in a scan group, each consisting of 187 binned data points of the *L* / *R* circular polarisation components, recorded as the antenna traverses back / forth across the source in right ascension / declination.

The *ScanData.m* data extraction algorithm

ScanData.m is an automated routine that applies a two-pass strategy to data extraction. The first pass examines the data in the FITS files, and identifies any incomplete scan groups for the specified source, usually a consequence of the telescope stopping and automatically restarting after a power failure or other interruption. The second pass extracts the data from the FITS files, excluding incomplete scan groups, and normalises the data for each scan by dividing them by the noise diode amplitude (CAL height), in VFC units, for the scan. The resulting data set is stored in a temporary file for subsequent processing by *ScanFit.m*.

As noted, the antenna records two channels of data as it traverses a source, corresponding to the two circular polarisation components of the radio wave. The CAL heights for the two channels of a scan can be sufficiently different that accuracy would be lost if they were averaged, so each channel of each scan is associated with a distinct CAL height.

The *ScanFit.m* data processing algorithm

ScanFit.m is an automated routine, although prior to its use a user can adjust data quality control parameters if need be, and can also specify that only one data channel be processed if necessary. Figure 3.6 shows the data processing strategy used to calculate two source flux density data points from a scan group.

It is now recognised that the algorithm, which is described below, can be improved by treating data from the two polarisation channels separately instead of combining them, such that the individual polarisation scan amplitudes are equated to the calibrator flux densities. The consistency tests described in Section 3.4 ensure the algorithm is effective, but the overall number of accepted data points is less than achieved with the improved algorithm. This is discussed further in Section 5.6.

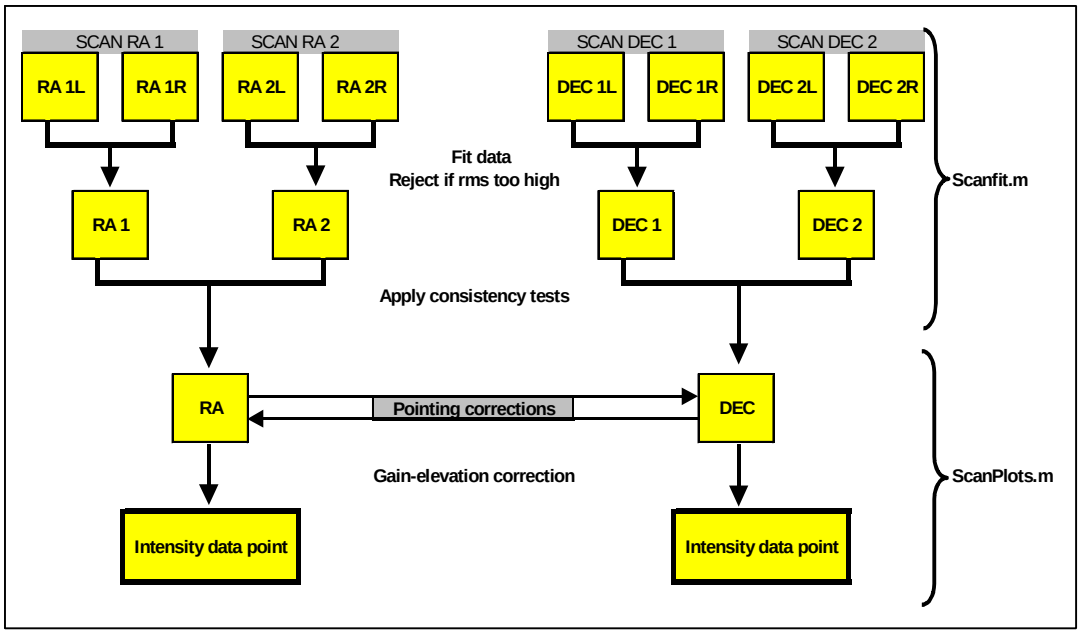

Figure 3.6 Computing two flux density (intensity) data points from a scan group.

Step 1: Data fitting

The flux density data for each polarisation channel of each scan consist of a Gaussian source profile superimposed on a black-sky noise component. This latter is not constant because of the atmosphere's contribution to the system noise, and is fitted by a quadratic polynomial (although a linear approximation would be sufficient for most cases). The combined flux density profile is thus defined by six parameters, λ_{1-6}:

$$I_i = \lambda_1 \exp\left[\frac{-(x_i - \lambda_2)^2}{\lambda_3}\right] + \left[\lambda_4 {x_i}^2 + \lambda_5 x_i + \lambda_6\right]$$

where:

- x_i are the coordinates of the flux density data points, corresponding to the centers of the 187 x 0.004 degree bins. The coordinates are expressed as offsets between ± 0.372 degrees from the middle (94th) bin, such that $x_{94} = 0$.
- λ_1 is the amplitude of the Gaussian source profile;
- λ_2 is the offset of the Gaussian's peak from the center of the scan (i.e. the assumed position of the source) in right ascension or declination as appropriate;
- λ_3 is a measure of the Gaussian's spread, $\lambda_3 = 2\sigma_x^2$, in units of (degrees)^2;
- λ_{4-6} define the quadratic black-sky profile.

The combined source / black sky profile is fitted to the flux density data for each scan using the Gauss-Newton non-linear least squares method in the *Matlab* optimisation toolbox (Mathworks, 2000). Figure 3.7 shows the result of a typical scan fitting exercise.

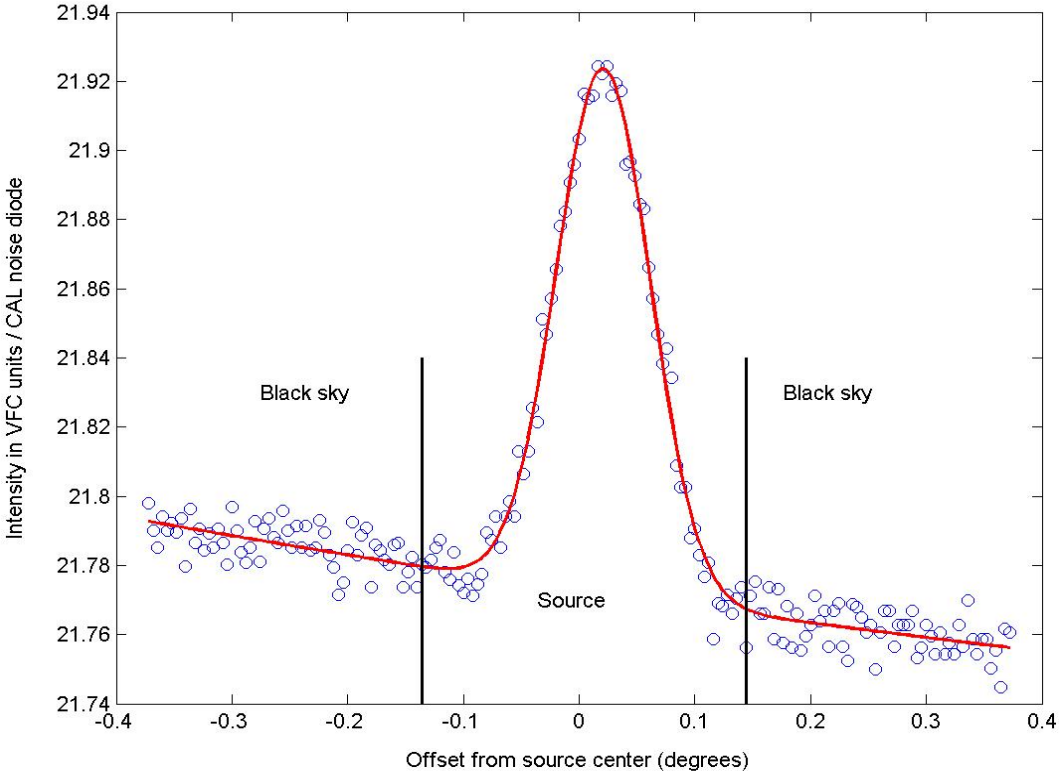

Figure 3.7 Best-fit of typical scan data by a Gaussian source plus black sky profile. The data are the *L* circular polarisation channel, scanning in declination.

The beam pattern of the Ceduna antenna at 6.65 GHz is well approximated by a circularly symmetric Gaussian profile with a Full Width Half Maximum (FWHM) of 5.8'. The spread parameter, λ_3, is constant to a good approximation, although it is a free parameter in the scan fitting exercises, and it is related to the FWHM by:

$$\text{FWHM (arcmin)} = 120\sqrt{\ln(4)}\sqrt{\frac{\lambda_3}{2}} \qquad (\lambda_3 \text{ in degrees})$$

Step 2: Combining fitted data sets

The next data processing step is to combine the *L* and *R* circular polarisation channel data sets for each scan, which produces the second row of boxes in Figure 3.6. Consider an *L* channel data set. The combination strategy starts by using the λ_{1-3} parameters for this data set to generate a new flux density data set:

$$I_i = \lambda_1 \exp\left[\frac{-(x_i - \lambda_2)^2}{\lambda_3}\right]$$

which defines the on-source Gaussian component of the curve fit through the original data, in the absence of the black-sky background component. The new data set is computed for the same 187 offset coordinates (the x_i values) which define the centers of the data bins, although the source profile is essentially confined to the middle one-third of these data bins.

The same procedure is applied to the *R* channel data set. The two fitted data sets are added, and the combined data set is fitted with a new Gaussian curve, giving new λ_{1-3} parameters for the total flux density profile of the source. Figure 3.8 shows a typical data combination exercise, in which the continuous lines are the fitted curves.

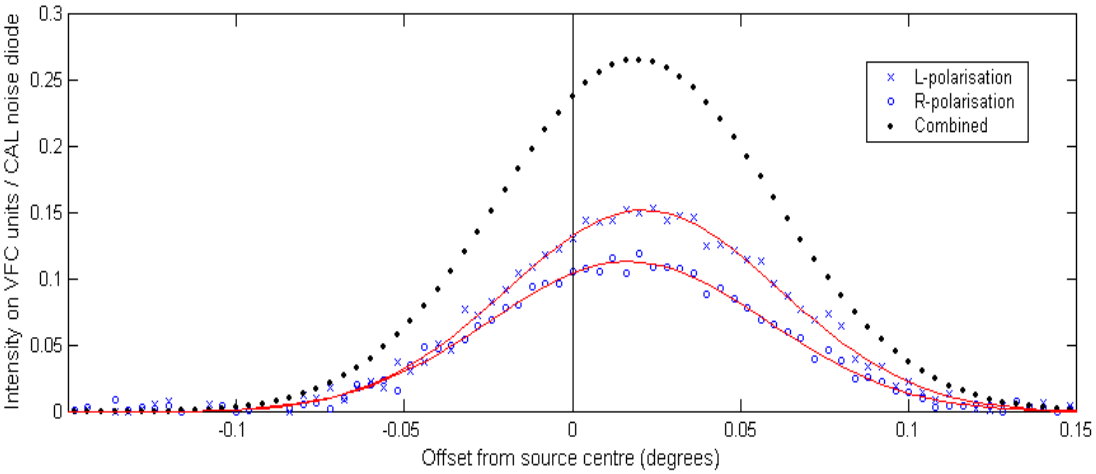

Figure 3.8 Combining data sets generated from on-source components of curves fitted to L and R polarisation channel data for a typical scan.

In Figure 3.8, the solid dots are generated from the curve fit to the combined data set, and are not the actual combined data. The stronger of the two polarisation scans (the *L* data set in Figure 3.8) contributes most to the combined data set, a bias that is avoided if the two polarisation data sets are treated separately. Fortunately, the data quality control tests described in Section 3.4 reject scan groups whose component λ_1 parameters (the amplitudes) differ appreciably.

The λ_2 parameters (the offsets) for the *L* and *R* scans should be the same, because they are gathered during the same scan. However, as shown in Figure 3.8, the fitting procedure can lead to minor differences (< 0.01 degrees) in these parameters.

For the scan in right ascension, denoted RA-1 in Figure 3.4, the equation for combining the on-source components of the curves fitted to *L* and *R* polarisation channel data is:

$$I_i^{RA1} = \lambda_1^{RA1-L} \exp\left[\frac{-(x_i - \lambda_2^{RA1-L})^2}{\lambda_3^{RA1-L}}\right] + \lambda_1^{RA1-R} \exp\left[\frac{-(x_i - \lambda_2^{RA1-R})^2}{\lambda_3^{RA1-R}}\right]$$

where x_i are the right ascension coordinates, expressed as offsets from the scan center. The combined data set of 187 total flux density data points, I_i^{RA1}, is then fitted with a new Gaussian profile (black dots in Figure 3.8), defined by:

$$I_i^{RA1} = \lambda_1^{RA1} \exp\left[\frac{-(x_i - \lambda_2^{RA1})^2}{\lambda_3^{RA1}}\right]$$

Step 3: Averaging the total intensity scans

The third data processing step is to average the offset and amplitude parameters for the total on-source flux density Gaussian profiles for the two right ascension scans, and separately for the two declination scans. This results in two orthogonal intensity curve fits for the scan group, denoted by the two boxes labelled RA and DEC in the third row of Figure 3.6.

To be specific, consider the averaging process for the two right ascension scans across the source, holding the declination constant. The flux density data points that define the average scan, denoted RA in Figure 3.6, are given by:

$$I_i^{RA} = \lambda_1^{RA} \exp\left[\frac{-(x_i - \lambda_2^{RA})^2}{\lambda_3^{RA}}\right]$$

where as before the x_i are the right ascension offset coordinates. The scan's amplitude, λ_1^{RA}, and its offset in right ascension from the source, λ_2^{RA}, are given respectively by:

$$\lambda_1^{RA} = 0.5\left(\lambda_1^{RA1} + \lambda_1^{RA2}\right) \text{ and } \lambda_2^{RA} = 0.5\left(\lambda_2^{RA1} + \lambda_2^{RA2}\right).$$

The observation time (Julian days) and the source elevation (degrees) associated with this scan are also defined to be the mean values for the two component scans, denoted RA-1 and RA-2 in Figure 3.6. The averaging process for the scan in declination across the source, holding the right ascension constant, is similar.

Summary

In summary, the Ceduna telescope produces a FITS file for each day of operation. The FITS file contains flux density scans of all the blazar and calibrator radio sources being observed, plus ancillary information such as system temperature. The telescope takes ~15 seconds to carry out a scan, but the additional operations of antenna slewing, calibration measurements, data outlier excision, data resampling, and pointing corrections result in a mean scan rate of about one per minute. Each FITS file thus contains $N \sim 1{,}400$ individual scans.

Each scan contains two data sets, which correspond to the simultaneous measurements of the left (*L*) and right (*R*) circular polarisation components of the radio signal. The individual scans are grouped into $N/4$ scan groups, with a single scan group corresponding to the top line in Figure 3.6 (i.e. SCAN RA 1 to SCAN DEC 2). The first step in processing a scan group is to compute best fits of the on-source plus black sky combined profile for both the *L* and *R* data sets of each scan, denoted RA-1L to RA-1R in Figure 3.6.

The second step is to sum the Gaussian on-source components of each pair of fits, denoted RA 1 to DEC 2 in Figure 3.6, although it is now appreciated that a better approach is to treat the *L* and *R* circular polarisation measurements separately. The third step is to average the flux density fits of the two scans in right ascension, and of the two scans in declination, denoted RA and DEC respectively in Figure 3.6.

The amplitudes of the Gaussian on-source component of these intensity profiles across the source (λ_1^{RA} and λ_1^{DEC}) are then corrected (by *ScanPlots.m*) for pointing errors using their associated offsets with respect to the scan center (λ_2^{RA} and λ_2^{DEC}). Each *N*/4 scan group thus produces two flux density values, and the final time series has *N*/2 data points.

3.4 Data Quality Control

ScanFit.m subjects the scan data to a suite of quality control tests devised by the author. As noted in the previous section, and discussed at the conclusion of Chapter 5, it is now known that the need for these data quality control tests can largely be avoided by treating the polarisation data separately. However, the data processing method described above works satisfactorily when supported by these quality control tests.

Rejection of poorly fitted data.
In Step 2 of the data processing procedure, described above, the parameters defining a best-fit curve through an *L* or *R* channel flux density data set are used to generate a data set of fitted points spanning the 187 offset values. Figure 3.8 shows the on-source component of these data sets, with the original data shown as circles and crosses, and the best fit curves shown as continuous red lines (passing through the data set of fitted points).
The residuals are the differences between the original and the fitted data values, and a fitting exercise is deemed to have failed if the standard deviation of the sum-squared residuals is greater than an empirical tolerance set to 0.1, with units of intensity-squared, with intensity expressed in VFC units / CAL noise diode. In the case of the data shown in Figure 3.8 the sum- squared residuals of the *L* or *R* fitted data set were 0.0057 and 0.0030 respectively.

Rejection of inconsistent scans.
Several tests are applied to ensure that the *L* and *R* data sets are consistent and sensible. Consider the four polarisation data sets for the two scans in right ascension of a given scan group, denoted RA-1L to RA-2R in Figure 3.6. The four λ_2 curve fit parameters define the offsets of the flux density peaks with respect to the scan centers. These offsets must agree within a specified tolerance, typically 1 arcminute (4 of the 187 data points). The offsets are also required to be reasonably small, typically less than 3 arcminutes: larger values indicate the antenna traverse was only barely on source, which leads to large pointing corrections.

Similar consistency tests are applied to the λ_1 curve fit parameters that define the amplitudes of the four scans. A scan is rejected if λ_1 is greater than ± 70% of the median λ_1 value of all the scans in the FITS files being processed by *Scanfit.m*, typically 2-3 days of data.

The same tests are applied to the offsets and amplitudes of the four polarisation scans in declination, denoted DEC-1L to DEC-2R in Figure 3.6. Table 3.1 summarises the results of quality control tests applied to typical calibrator data over a three week period in 2003.

	3C227		**PKS B1934-638**	
Observed days (2003)	147-160		160-169	
Total scan groups	421		773	
Failed fitting exercise	21	5.0%	17	2.2%
Failed offset tests	38	9.0%	50	6.5%
Failed amplitude tests	112	26.6%	151	19.5%
Passed data	250	59.4%	555	71.8%

Table 3.1 Summary of quality control tests applied to 2003 calibrator source data.

Table 3.1 shows that the tests pass roughly 60% of the scan groups. The pass rate tends to be higher for strong sources and good observing conditions, presumably because the pointing corrections applied during telescope operation are more effective for stronger sources, and in good weather conditions. Some people feel that more data points should be accepted. The author, in consultation with others, believes it is better to reject some good data points than risk problems in the analysis caused by failing to exclude bad data points.

The *L* and *R* channel data sets of a given scan are similar, but can be sufficiently different that if the curve fit of either data set is rejected, it is best not to attempt to compensate for its loss. In this case, the entire scan group is rejected rather than compute pointing offsets with an incomplete scan group. It is necessary to make an exception to this rule when one polarisation channel is not working, which happened for about two weeks in early 2004. However, calculating flux density values and pointing offset corrections from a single *L* or *R* polarisation channel data set reduces the sensitivity of the exercise by a factor of $\sqrt{2}$.

3.5 Data Scaling, Pointing and Gain-Elevation Corrections

A *ScanFit.m* output file contains a quality controlled flux density time series for a given source, calculated from the data contained in several FITS files. *ScanPlot.m* concatenates the *ScanFit.m* output files that together span an entire observing period, applies corrections to the overall time series, and produces a file for subsequent input to *ScanAnalysis.m*.

Flux density units. The Ceduna blazar observing program, described in Section 3.6, uses PKS B1934-638 as its primary calibrator. Reynolds (1994) reviews PKS B1934-638 flux density observations, and shows that it has a strength of 3.92 Jy at 6.65 GHz, subject to an error of ~2%. The conversion of VFC units to Janskys is directly achieved by equating the mean value in VFC units/CAL of a month of PKS B1934-638 flux density observations to 3.92 Jy. Changes in the noise diode power are corrected using calibrator data, as described in Chapter 4. The strength of the secondary Ceduna calibrator, 3C227, is not relied upon, but instead found by the conversion factor to be 1.90 Jy at 6.65 GHz, which agrees with the observations reported by Baars et al. (1977).

Pointing corrections. As noted, the beam pattern of the Ceduna antenna at 6.7 GHz is well approximated by a circular Gaussian with a FWHM of 5.8'. The beam side-lobes are ~1% of the main peak and for observations of radio sources of a few Jy are well below the baseline noise level (Simon Ellingsen, pers. comm.). The reduction in measured flux density caused by a pointing error can easily be corrected since the declination pointing offset is measured by a scan in right ascension, and vice-versa, as follows:

$$\left(\lambda_1^{\,RA}\right)_{True} = \lambda_1^{\,RA} \;/\exp\left(\frac{-\lambda_2^{\,2}}{\lambda_3}\right)^{DEC} \quad \text{and} \quad \left(\lambda_1^{\,DEC}\right)_{True} = \lambda_1^{\,DEC} \;/\exp\left(\frac{-\lambda_2^{\,2}}{\lambda_3}\right)^{RA}$$

Gain-elevation effects. Correcting flux densities for gain-elevation effects is achieved by monitoring one or more calibrator sources, and fitting curves to the calibrator data plotted as a function of source elevation and normalised to unity at an elevation of 50°, close to the peak in the curve. The curve is assumed to have a quadratic form.

Figure 3.9 shows the gain-elevation curve fitted to data recorded for PKS B1934-638. The elevation cut-off of 58° marks the maximum elevation of PKS B1934-638 at Ceduna. A refined gain-elevation curve was obtained by extending the data set to include PKS B1921-293 and PKS 0208-512, both of which rise higher at Ceduna than the primary calibrator.

Figure 3.10 shows the individual gain-elevation curves for the three sources, and the equations for each gain-elevation correction, *S*, are:

$$S_{\mathrm{B1934}} = 3.825 \,\mathrm{x}\, 10^{-5}\ \mathrm{el}^2 - 0.0035719\,\mathrm{el} + 1.083$$

$$S_{\mathrm{B0208}} = 3.971 \,\mathrm{x}\, 10^{-5}\ \mathrm{el}^2 - 0.0037870\,\mathrm{el} + 1.090$$

$$S_{\mathrm{B1921}} = 3.369 \,\mathrm{x}\, 10^{-5}\ \mathrm{el}^2 - 0.0030844\,\mathrm{el} + 1.070$$

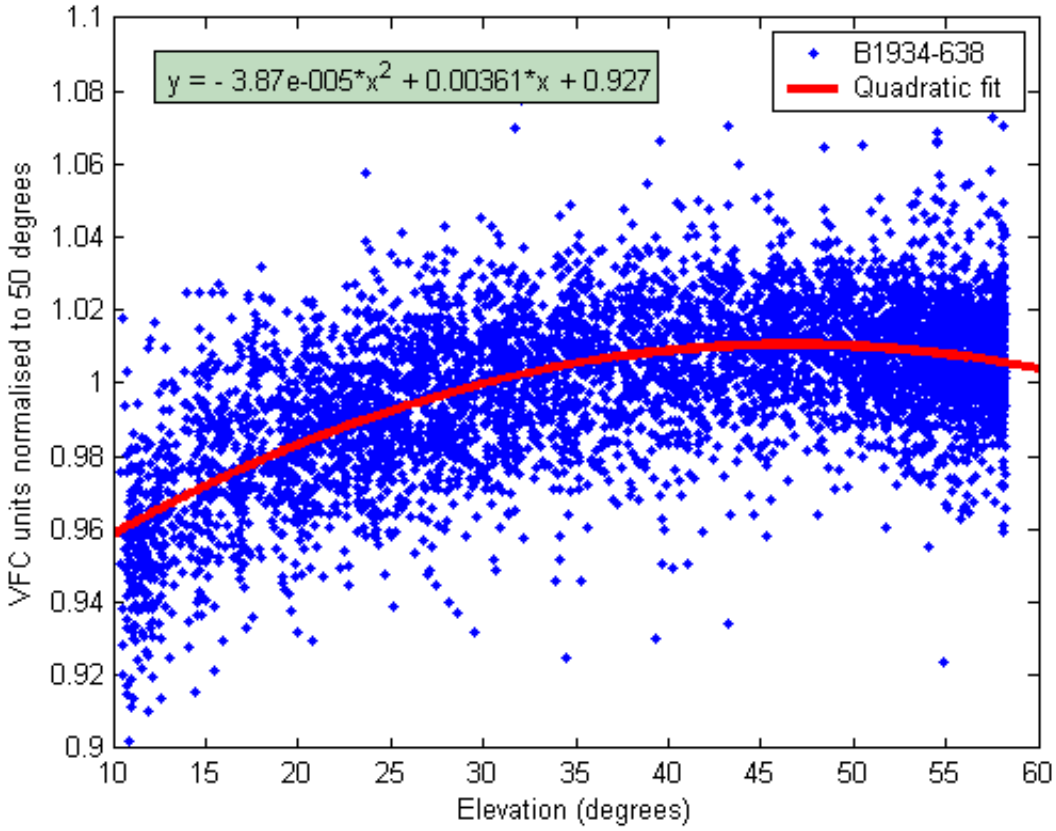

Figure 3.9 The gain-elevation curve for PKS B1934-638.

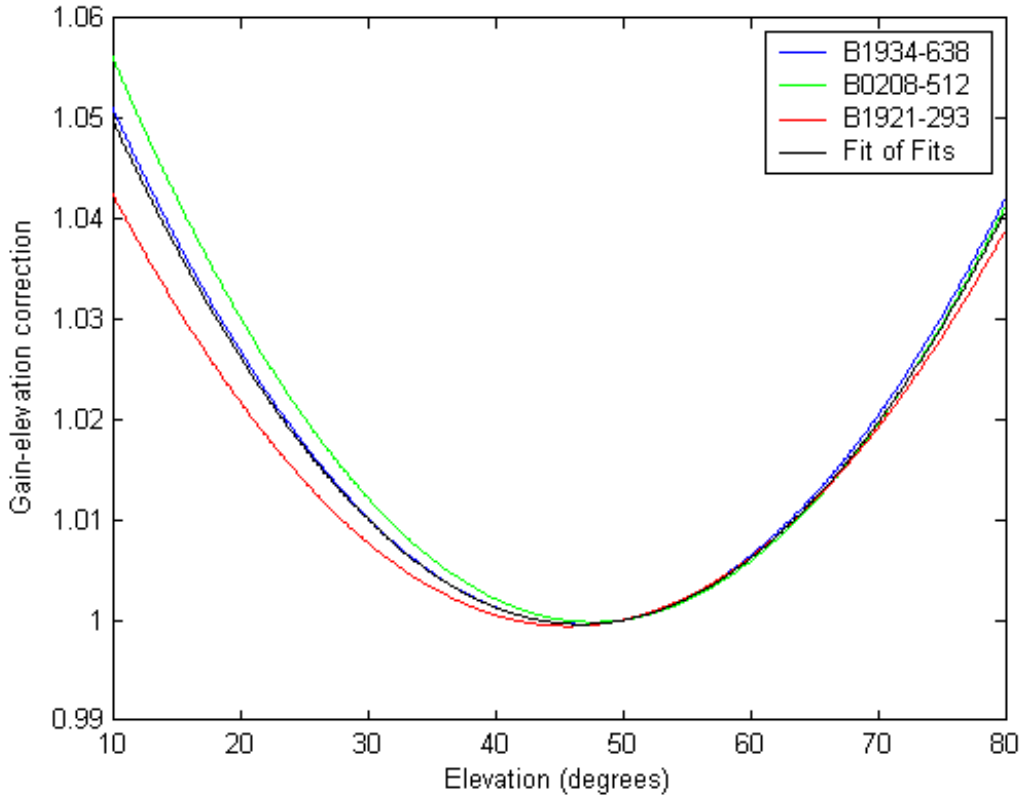

Figure 3.10 Individual and overall gain-elevation curves for three calibrator sources.

An overall gain-elevation curve is obtained by fitting the three fits, the result being the black line shown in Figure 3.10. The alternative approach of fitting the overall data risks bias if unequal numbers of data points are associated with the three sources, although this could be largely avoided by binning the data. However, the equations are very similar, and the gain variations are less than 5%.

Preferred correction $S_{\text{Fit of fits}} = 3.722 \text{ x } 10^{-5} \text{ el}^2 - 0.003481 \text{el} + 1.081$

Alternative correction $S_{\text{Fit of data}} = 3.803 \text{ x } 10^{-5} \text{ el}^2 - 0.003575 \text{el} + 1.084$

Towards the end of the initial observing campaign, it was realised that the flux density data contain systematic flux density fluctuations, primarily on diurnal time scales. This problem is discussed in detail in Chapters 4 and 5, and is now attributed to small changes in the noise diode output power with ambient air temperature. Subsequent investigations by PhD student Cliff Senkbeil has found that the systematic variations are entangled with the gain-elevation curve, but this is unavoidable as they are both determined by assuming that the calibrator is constant amplitude. The entanglement of these two effects made the systematic variations less apparent in the early investigations of the system performance. To date no completely satisfactory solution has been found to this problem.

3.6 The 2003/05 COSMIC Program

The Ceduna blazar observing program quickly acquired the acronym COSMIC, short for COntinuous Single dish Monitoring of Intraday variables at Ceduna. Table 3.2 lists the five blazars and two calibrator sources for the initial COSMIC campaign, which ran from March 2003 to early 2005. The sources were recommended by Drs Dave Jauncey, Simon Ellingsen, Jim Lovell, and Hayley Bignall, on the basis that the blazars were all known to exhibit pronounced radio variability, and their flux densities of ~1 Jy or more could be monitored by the 30 m Ceduna antenna. Another consideration was that the set of sources should have rise and set times such that the telescope can always observe at least one source.

Table 3.2 also gives the flux density ranges of all the sources over the campaign period, measured at the Ceduna central observing frequency of 6.7 GHz.

Source	**Flux density**	**Source**	**Flux density**
PKS B1622-253	~ 2.0 – 5.0 Jy	AO B0235+164	~ 1.5 – 2.0 Jy
PKS B1519-273	~ 1.0 – 3.0 Jy	PKS B1934-638 (Calib)	3.9 Jy
PKS B1144-379	~ 0.5 – 2.5 Jy	3C 227 (Calib)	1.9 Jy
PMN J1326-5256	~ 1.0 – 2.5 Jy		

Table 3.2 Radio sources in the COSMIC program, with observations at 6.7 GHz.

Véron-Cetty & Véron (2006) present the 12th edition of their catalogue of quasars and active galactic nuclei. The catalogue tables report that:

- PKS B1622-253 is a (B filter) magnitude 20.6 blazar, with z = 0.786.
- PKS B1519-273 is a (B filter) magnitude 17.7 BL Lac object with z = 1.294.
- PKS B1144-379 is a (V filter) magnitude 16.2 BL Lac object with z = 1.048.
- AO 0235+164 is a (V filter) magnitude 15.5 BL Lac object with z = 0.940.

PMN J1326-5206 has not yet been classified, and its magnitude and redshift are not known. However, the NASA/IPAC Extragalactic Database provides additional reference material on this source and the other blazars. PKS B1144-379 and PKS B1519-273 were included (and IDV discovered) in the ATCA IDV survey of 1994 (Kedziora-Chudzer et al., 2001). All five sources were observed in the 1997-2001 southern sky blazar monitoring campaigns reported in Bignall (2003).

The observation histories and nature of PKS B1622-253 and PKS B1519-273 are discussed in detail in Chapter 7. In brief, both blazars display radio variability on time scales of days. PKS B1622-253 has extended structure at radio wavelengths, whereas PKS B1519-273 is essentially a point source. An annual variability cycle has been detected in PKS B1519-273 data gathered by the Australia Telescope Compact Array (Jauncey et al., 2003), but the observations were too short to enable the detailed analysis that is possible with Ceduna data.

Figure 3.11 shows Very Long Baseline Array radio images of four of the blazars. The PKS B1144-379 image was made at 2.3 GHz (13 cm) by the U.S. Naval Observatory (RRFID, 2002). The PKS B1519-273, PKS B1622-253 and AO 0235+164 images were all made at 15 GHz (2 cm) (Lister & Homan, 2005; Kellermann et al., 1998). Additional images are provided by Kellermann et al. (2004). The images all display evidence of sub-milliarcsecond structure consistent with the core-jet morphology associated with the central engine model.

Table 3.3 gives the astronomical coordinates of the COSMIC 2003/05 radio sources. The positions of PKS B1934-638, PKS B1144-379, and AO B0235+164 are given by Ma et al. (1998), and the positions of PMN J1326-5206 and 3C 227 are given by Wright et al. (1994) and Clements (1981) respectively.

Figure 3.12 shows that AO B0235+164 is a galactic mid-latitude source, but the other four blazars lie at Galactic Latitudes between 10° and 25°. Figure 3.13 shows that PKS B1144-379 and PMN J1326-5206 lie at ecliptic mid-latitudes, while PKS B1622-253, PKS B1519-273, and AO B0235+164 lie close to the ecliptic plane.

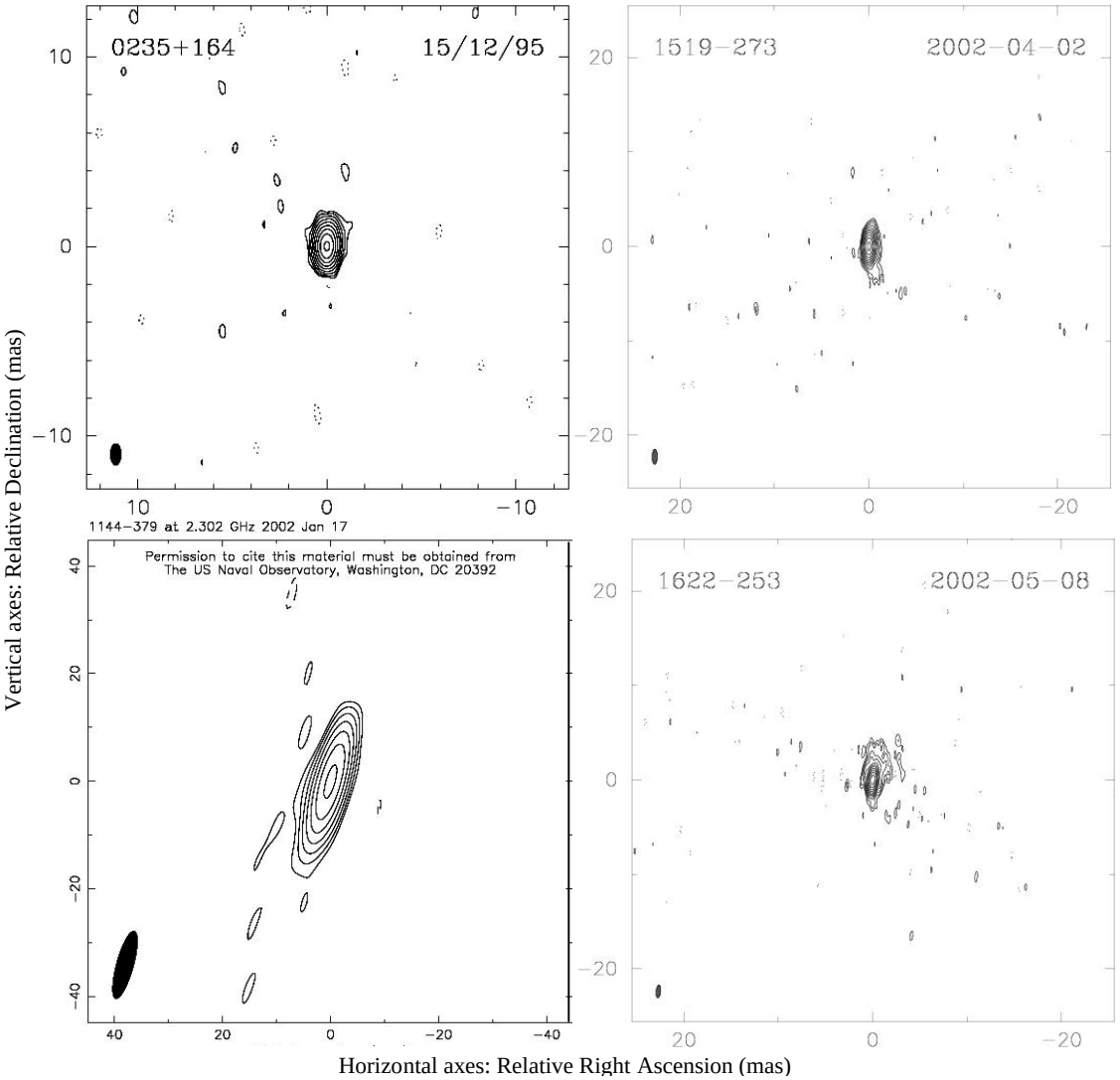

Figure 3.11 15 GHz images of PKS B1622-253, PKS B1519-273 and AO B0235+164, and a 2.3 GHz image of PKS B1144-379. Beam sizes shown in lower left hand of each image. See text for references.

Sources South of zenith	**Right Ascension J2000**	**Declination J2000**	**Ecliptic Long. (°)**	**Ecliptic Lat. (°)**	**Galactic Long. (°)**	**Galactic Lat. (°)**
PKS B1934-638	19h 39m 25.0s	-63d 42m 46s	284.39	-41.51	332.75	-29.39
PMN J1326-5206	13h 26m 49.2s	-52d 06m 24s	222.38	-39.36	308.36	10.40
PKS B1144-379	11h 47m 01.4s	-38d 12m 11s	194.66	-35.81	289.24	22.95
North of zenith AO B0235+164	02h 38m 38.9s	+16d 36m 59s	42.46	1.09	156.77	-39.11
PKS B1519-273	15h 22m 37.7s	-27d 30m 11s	235.33	-8.67	339.58	24.41
PKS B1622-253	16h 25m 46.9s	-25d 27m 39s	248.80	-3.74	352.14	16.32
3C 227	09h 47m 46.4s	+07d 25m 21s	146.61	-5.55	228.58	42.29

Table 3.3 COSMIC radio source coordinates. Equatorial coordinates are referred to J2000, and Galactic coordinates are $\{l_{II}\ b_{II}\}$.

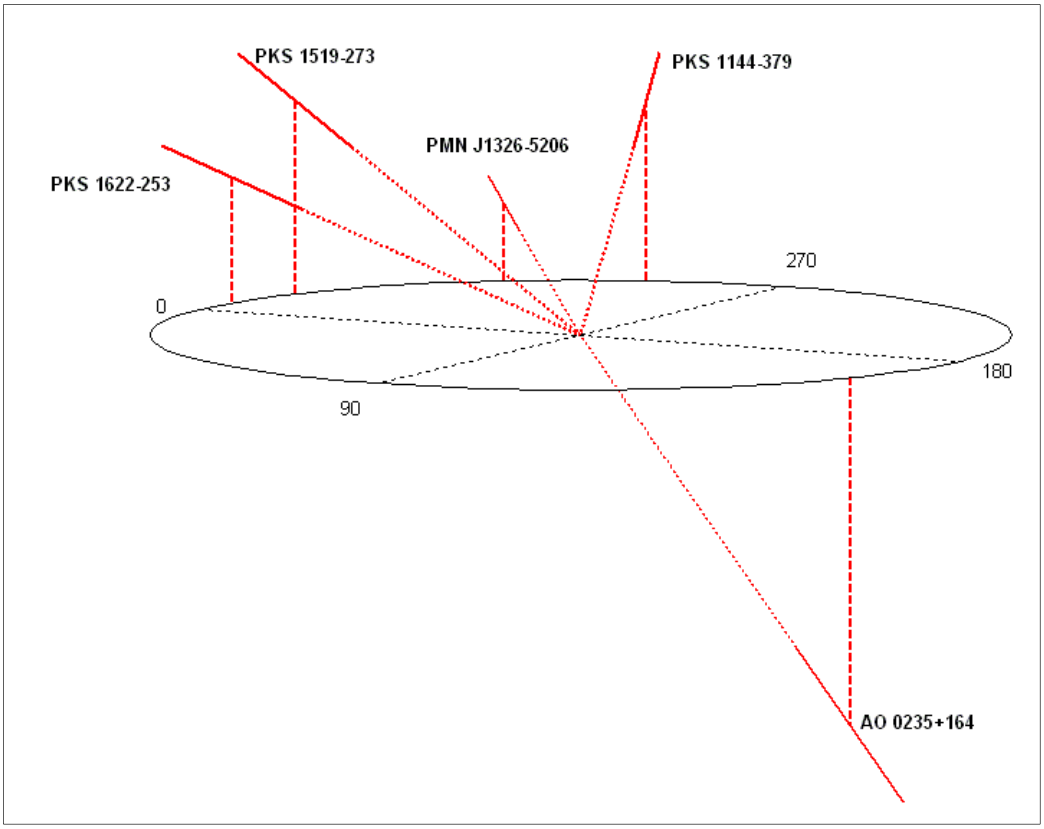

Figure 3.12 COSMIC source locations with respect to the galactic plane.

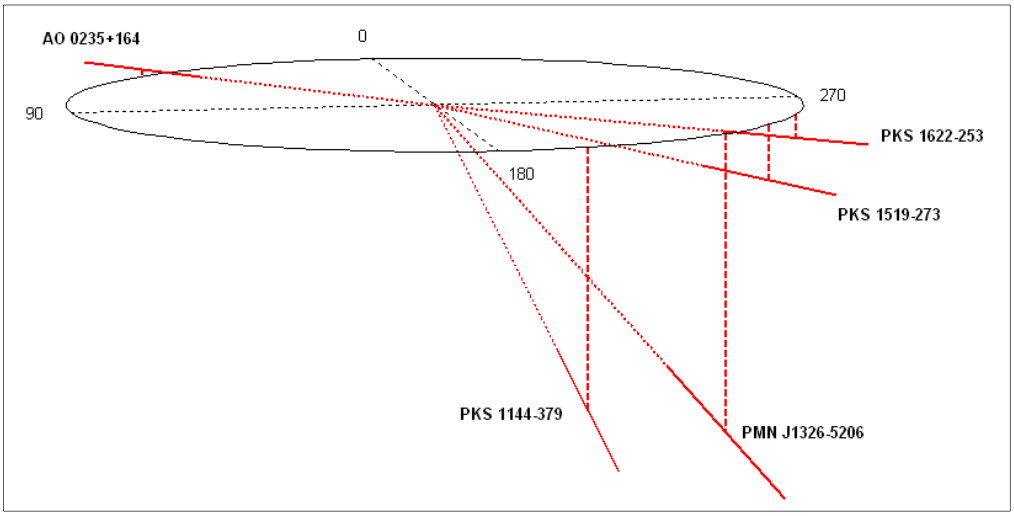

Figure 3.13 COSMIC source locations with respect to the ecliptic plane.

Figure 3.14 shows the source declinations with respect to the zenith at Ceduna, at ~32° S. To avoid excessive telescope slewing, the radio sources were divided into two groups, as shown in Table 3.3 on the previous page, consisting of those sources passing north and south of the zenith at Ceduna, with each group including a calibrator.

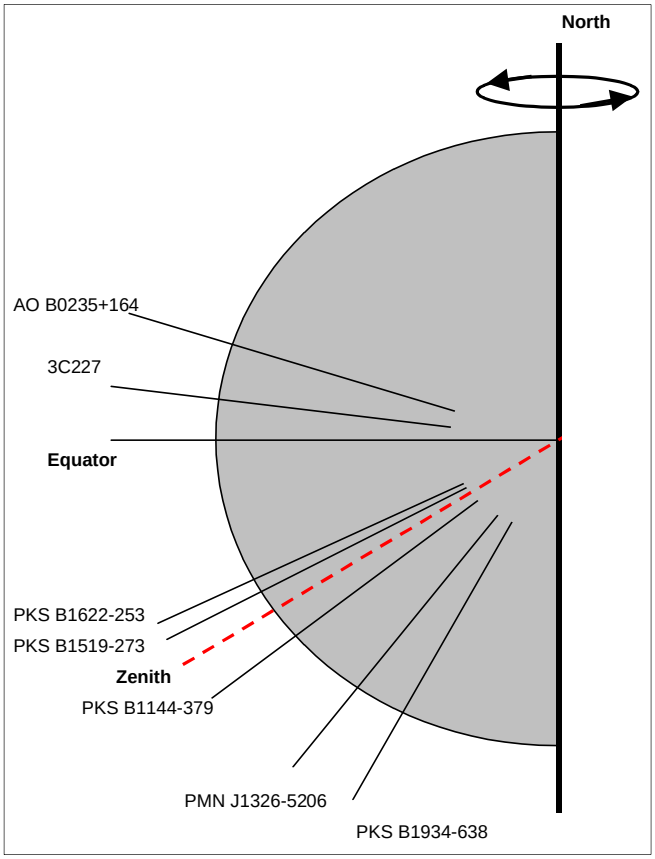

Figure 3.14 COSMIC source declinations compared to the Ceduna zenith.

The COSMIC program observed each group in turn for 10-15 days. The blazars observed in the program have variability timescales of typically a few days, measured as peak-to-peak scintle times, so a 10-15 day observing period is long enough to ensure that multiple scintles are usually recorded. In addition, if these time scales display an annual cycle in the event that the variability is due to interstellar scintillation, then the variability timescales are not expected to change greatly over a 10-15 day period.

Chapters 6 and 7 present the variability analysis of PKS B1519-273 and PKS B1622-253. Section 7.5 presents baseline predictions by the standard ISS model for these two blazars: the variability time scales are 1 to 5 days and 3 to 8 days respectively, while the mean and maximum changes in scintle period over a two week period are about 11% and 30% of the mean period in both cases. The actual annual cycles detected in the variability time scales of these two blazars are a little more pronounced than the baseline scenario, as discussed in Section 7.5, but for most of the year the scintle periods and the fractional changes in the scintle periods during a 10-15 day observing session are small, only increasing significantly during the slow-down times of year, particularly near day 250 of the year.

The COSMIC program started in March 2003, and Table 3.4 lists the observing periods to the end of the initial program in early 2005.

Southern sources		Observing	Northern sources	
Start day	**End day**	**period**	**Start day**	**End day**
83	103	1	105	112
114	135	2	135	140
141	147	3	147	159
160	169	4	174	194
194	203	5	204	215
216	222	6	223	233
238	245	7	246	254
255	263	8	264	272
275	286	9	287	296
297	307	10	308	320
332	341	11	352	361
364	19	12	20	35
36	48	13	49	56
68	86	14	58	67
114	131	15	88	105
149	161	16	132	148
176	209	17	162	175
190	209	18	190	209
229	245	19	215	225
273	288	20	246	272
303	315	21	289	302
341	354	22	326	338
1	10	23	355	366
31	45	24	15	30

Table 3.4 COSMIC 2003/05 observing periods.

The strategy of alternating observations between the two groups of sources has continued. However, northern group observing periods 13 and 14 ran sequentially, and are counted for the purpose of data analysis as a single observing period. Also, observing period 18 trialled a scheme to monitor all the sources, but the resulting data collection was insufficient for some sources, prompting a return to the alternate group observation strategy.

Minor modifications to the observing program were made in the first few observing periods. PKS B1144-379 was added to the southern source group during the first observing period; and PKS B1622-253 replaced PKS J2346+0930 in the northern source group, starting in observing period 3.

The set of target sources has occasionally been extended to accommodate requests from other researchers. The compact steep-spectrum source PKS B2004-447 was included for about six months in the southern source group, starting in early February 2004. These observations assisted in determining the spectral energy distribution of this source, which is believed to be a radio-loud narrow-line Seyfert 1 galaxy (Gallo et al., 2006).

The Ceduna observing program now includes the rapid scintillator PKS B0405-385, which was found to be a strong scintillator in the 1994 ATCA survey of IDV sources (Kedziora-Chudzer et al., 1997), but was quiescent during the subsequent ATCA southern sky blazar monitoring program (Bignall, 2003). PKS B0405-385 was found to be still quiescent during the first COSMIC southern source observing period, and was removed from the COSMIC program. However, the source became active again in mid-2004 and, at the request of Dr Kedziora-Chudzer, was reinserted in COSMIC program from observing period 19 onwards.

Figure 3.15 shows the variation of a source's elevation during an observing period, and highlights Ceduna's ability to observe sources fairly well at low elevations. This particular source, PKS B1622-253, has a maximum elevation of 83.5 °, and has an observable period of about 12.5 hours during which it is higher than the 10º elevation observation cut-off.

[The maximum elevation of a source above the southern horizon ($0^o \leq \theta \leq 180^o$) is related to the observatory latitude (ϕ) and the source declination (δ) by $\theta = \delta - \phi + 90^o$. For the source PKS B1622-253 ($\delta \approx -25½$ °) observed at Ceduna ($\phi \approx 32^o$ S), we have $\theta = -25½ - (-32) + 90^o = 96.5°$ above the southern horizon, or 83½ ° above the northern horizon.]

Atmospheric effects mean that flux density data gathered while a radio source is at a low elevation are often significantly noisier than data gathered when the source is at a high elevation. However, Figure 3.15 shows that data gathered by Ceduna at elevations as low as 10° are usually quite good, meaning the data RMS values are similar to the RMS values of data gathered at higher elevations.

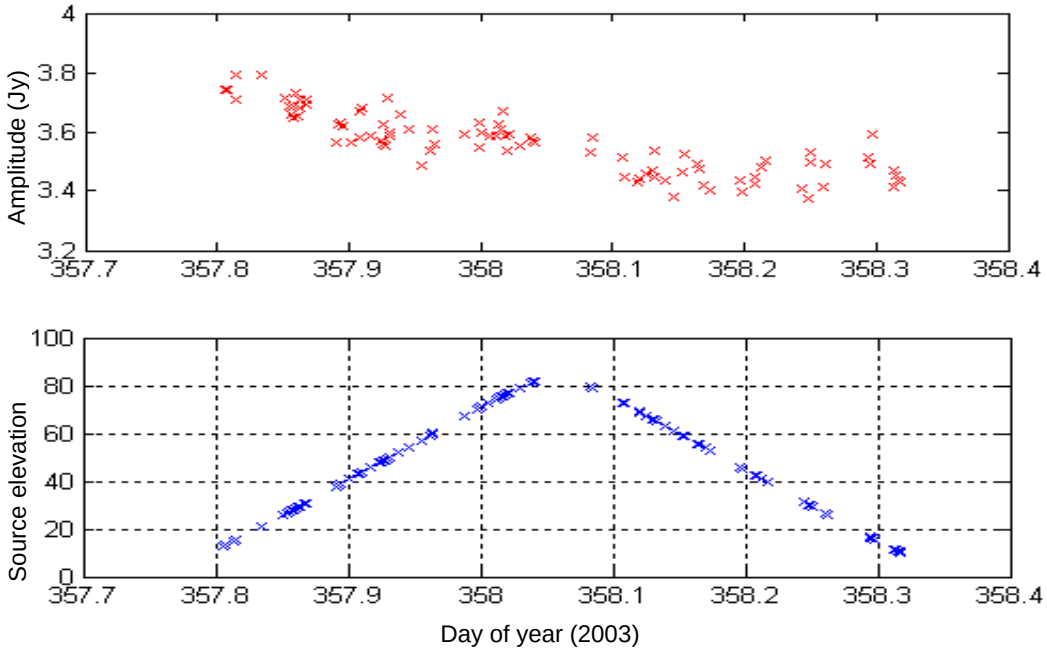

Figure 3.15 Time – elevation plot for PKS B1622-253, showing Ceduna's ability to gather quality data when the source is as low as 10° above the horizon.

Table 3.5 summarises the maximum elevations and observing durations for each source in the COSMIC program.

Source	Declination	Maximum elevation	Time above horizon (0°)	Observing time above 10°	Unobserved time
AO B0235+164	+16½ °	42 °	10½ h	9 h	15 h = 0.63 day
PKS B1622-253	-25½ °	83½ °	14 h	12½ h	11½ h = 0.48 day
PKS B1519-273	-27½ °	85½ °	14½ h	13 h	11 h = 0.46 day
PKS B1144-379	-38 °	84 °	15 h	13½ h	10½ h = 0.44 day
PMN J1326-5206	-52 °	70 °	17 ½ h	15 ½ h	8½ h = 0.35 day

Table 3.5 Daily observing durations for COSMIC sources.

4.0 DATA ANALYSIS METHODOLOGY

4.1 Methods of Estimating Variability Time Scales

A key analysis goal is to estimate the characteristic variability time scale, T_{char}, of a flux density time series. The Ceduna data are extensive enough to allow T_{char} to be defined in this research as T_{period}, denoted $T_{char} \sim T_{period}$, which is the mean scintle period, measured for each scintle as its peak-to-peak (or trough-to-trough) time. [A scintle is a characteristic element – a fluctuation – in the spatial modulation field]. The characteristic variability frequency is thus $f_{period} = 1/T_{period}$. Alternative definitions of T_{char} are discussed in Section 4.4.

Two major analysis problems are non-uniform data sampling, and gaps in the time series record. Non-uniform sampling occurs because the telescope observes multiple sources, and it regularly reviews which sources above the horizon are due for new observations. *Regular* data gaps occur because a source can be observed only when it is above the elevation cut-off. A 10° cut-off is applied at Ceduna: the antenna can observe sources at lower elevations, but not without experiencing significant gain loss due to atmospheric effects and antenna deformation. *Irregular* data gaps occur due to observing program interruptions, such as VLBI sessions, maintenance, equipment failures, and power failures.

In response to this, three analysis methods are used to estimate T_{period}.

- ***Scintle counting (Section 4.2).*** Scintle counting is one of several empirical methods used to determine flux density variability based on a direct examination of the data.

- ***Data folding (Section 4.3).*** Data folding assumes quasi- periodicity of the data, and this approach is the time domain equivalent of the periodogram used in spectral analysis.

- ***Spectral analysis (Section 4.4).*** $T_{char} \sim T_{period}$ values are evaluated in the frequency domain as the primary peak of the Power Spectral Density function (PSD), which is computed from the Autocorrelation Function (ACF). The ACF also enables alternative definitions of T_{char} to be used, and these are reviewed in Section 4.4. In addition, spectral purity is indicated in the time domain by the extent of the first negative ACF overshoot, while in the frequency domain it is indicated by the absence of secondary PSD peaks.

T_{period} is determined from the PSD, with scintle counting and the data folding plot providing cross-checks. This is because a scintle counting exercise does not usually consider the entire time series, while in a data folding exercise there is often some minor uncertainty between the frequencies defined by the plot of amplitude versus folding frequency and the plot of residuals versus folding frequency (see Section 4.3).

One disadvantage of defining $T_{char} \sim T_{period}$ is that the quasi-random nature of scintillation means the variability in a time series is also only quasi-periodic. Scintles observed over an observing period of, say, 10-15 days are not expected to occur at precisely regular intervals or with the same morphology. However, the scintle intervals, amplitudes and widths are consistent enough that $T_{char} \sim T_{period}$ is a meaningful definition, while the negative overshoot of the ACF, and the strength of any secondary PSD peaks, provide measures of the spectral purity of the signal.

Defining $T_{char} \sim T_{period}$ also leans towards a determination that interstellar scintillation is the principal cause of the flux density variability. Flux density variations intrinsic to the source might be quasi-periodic in nature, but the variability time scales of the sources studied by this research, PKS B1622-253 and PKS B1519-273, display annual cycles, which proves interstellar scintillation to be the cause of the variability in these sources (see Chapter 2). Also, interpreting flux density variability on time scales of days as interstellar scintillation, rather than due to variability of the source, reduces the implied minimum brightness temperature, which in the source-intrinsic interpretation can be many orders of magnitude above the inverse Compton limit.

Ceduna data contain systematic fast (diurnal) small amplitude flux density variations. These fluctuations are removed by the data processing procedure discussed in Section 4.5, but the variability in unprocessed PKS B1144-379 data from (southern source) observing period 4 is clear enough to illustrate the various approaches to determining T_{period}, described below.

4.2 Scintle Counting

Scintle counting relies on being able to visually identify peaks and troughs in a flux density time series. This is possible in the case of Ceduna data, and hence this method is used by this research to provide an empirical estimate of T_{period}. Figure 4.1 shows a scintle counting exercise applied to PKS B1144-379 data for observing period 4, giving an estimate of T_{period} ≈ 6 days / 2.5 scintles = 2.4 days.

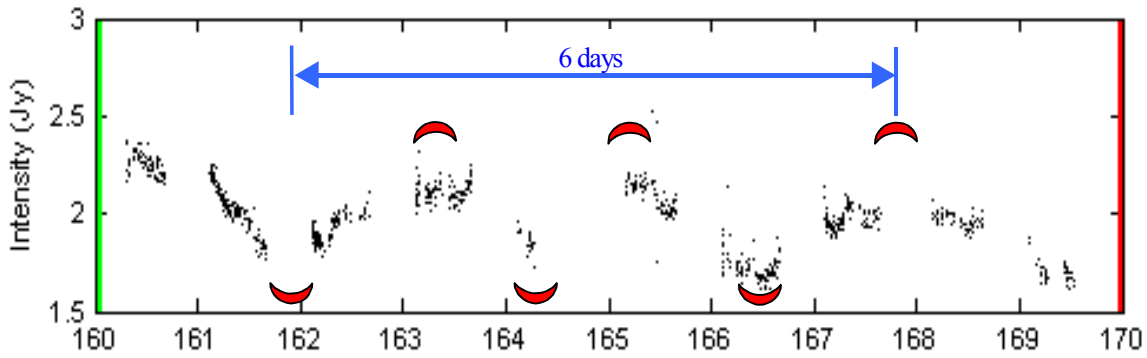

Figure 4.1 Scintle counting for PKS B1144-379 data for days 160-170 in 2003.

Scintle counting provides a cross-check on T_{period} values determined by spectral analysis, and the fact that the flux density variability can be recognised by eye using scintle counting provides confidence in these T_{period} values.

Scintle peaks and troughs may not be obvious in time series with noisy, low amplitude variability. The data processing methodology presented later in this chapter converts the data to a zero-mean time series, and counting the number of zero-crossing events can help to separate true peaks and troughs from spurious rises and dips.

Daily mean flux density plots are routinely produced for all Ceduna data (see Chapter 6), primarily for comparison to calibrator sources. However, these plots sometimes assist T_{period} estimates when the T_{period} values are on the order of days. Figure 4.2 shows the daily mean flux densities (intensities) of the raw PKS B1144-379 data in Figure 4.1. The plot clearly supports the conclusion that T_{period} is just over 2 days.

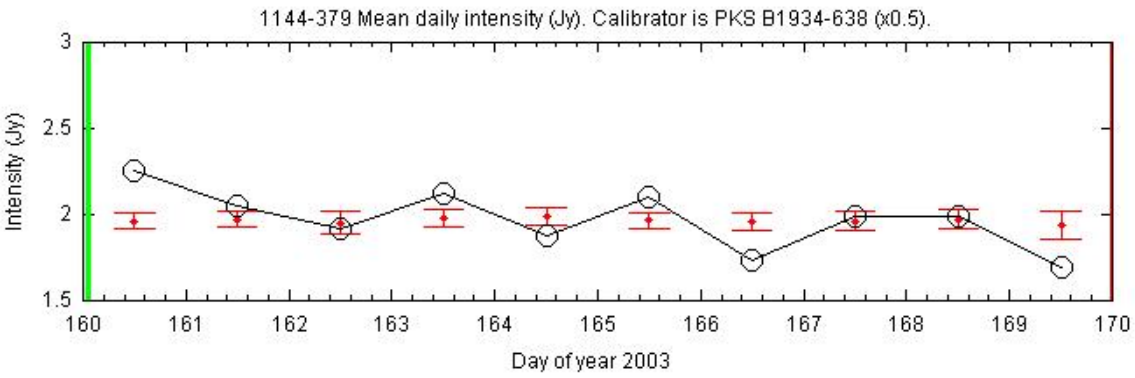

Figure 4.2 Scintle counting using daily mean intensities of PKS B1144-379 (circles) and PKS B1934-638 (dots) from observing period 4.

Flux density change rate. Alternative empirical approaches to examining flux density time series variability are based on estimating the rate of change of flux density, *I*. Variations on this theme include:

$$T_{char} \approx \left| \frac{dt}{d(\ln I)} \right| \qquad \text{Burbidge et al. (1974)}$$

$$T_{char} \approx I_{\max} \left(\frac{dI}{dt} \right)^{-1}_{\max} \qquad \text{McAdam (1978)}$$

where *dI* is the rise or fall in flux density over time *dt*. Definitions of the variability time scale in terms of flux density change rates are useful when the data are limited and do not fully capture a scintle. This is the case, for example, with observations of blazar variability using facilities such as the Australia Telescope Compact Array, which are often limited by competing demands for telescope time to sessions of 12 hours or so.

Bignall (2003) notes that the flux density change method places a limit on the size of the emitting region, assuming intrinsic variability, but can also overestimate $T_{\rm char}$ if a significant fraction of the source's emission is non-variable. Blazar emissions are highly variable, and at least some of their radio variability is certainly intrinsic to the source, but that portion of a blazar's emissions associated with a large emission region are non-variable. Fortunately, the Ceduna monitoring program gathered data on a daily basis over many months, avoiding the need to use flux density change methods because scintle periods can be observed directly.

4.3 Data Folding

The assumption of quasi- periodicity in Ceduna blazar data is a fairly good one, although inspection of the flux density time series shows that scintles do not occur at strictly regular intervals, nor with regular morphologies. Fortunately, quasi-periodicity is sufficient for a periodicity search method to yield a credible estimate of the characteristic variability time scale, $T_{\rm char} \sim T_{\rm period}$.

Periodicity searches obviously work best for time series that are at least several times $T_{\rm period}$ in length. They can be made either in the frequency domain by computing a periodogram to estimate the power spectral density; or in the time domain, through data folding. The two approaches are equivalent if the periodogram is appropriately defined (Scargle, 1982). The *Matlab* signal processing toolbox provides several periodograms, which were found to produce nearly identical results to a data folding procedure written by the author.

It was decided to use the data folding method to estimate $T_{\rm period}$ in the flux density time series, although a periodogram could have done the job as well. The data folding method is to fold the data at a trial period, $T_{\rm trial}$ (for example, folding a time series at a trial period of 2 days means the time series is divided into 2 day long sections which are then superimposed), subtracting the average value of each data fold so the final data set has a zero mean. A sine wave of the form

$$x(t) = A \sin\left(\frac{2\pi}{T_{\rm trial}} t + \phi\right)$$

is fitted to the folded data, with the wave amplitude, A, and the phase, ϕ, as free parameters. This was done by applying a non-linear least squares optimisation technique, using the *Matlab* function *lsqnonlin*. The residuals are the differences between the folded data and the best-fit sine wave. This exercise is repeated across a range of trial frequencies, and $T_{\rm period}$ corresponds to the frequency at which the minimum sum-squared residual occurs. The data folding method usually produces a $T_{\rm period}$ cross-check value that agrees with the $T_{\rm period}$ value estimated by spectral analysis, although the plots are sometimes hard to interpret.

Occasionally more than one minimum appears in the plot of residuals as a function of data folding frequency. The two possible reasons for this are that either a second variability time scale is present, or the multiple minima are due to harmonics. If the frequency spacing suggests the minima are due to harmonics, two additional data folding plots can assist in identifying the correct characteristic variability frequency, $f_{\text{period}} = 1/ T_{\text{period}}$. First, a plot of the variation with frequency of the best-fit wave amplitude, A. Second, a plot of residuals verses data folding frequency, with the data binned into hourly phase bins.

Figure 4.3 shows this method applied to the PKS B1144-379 data from observing period 4 (i.e. the data shown in Figure 4.1). T_{period} corresponds to the frequency at which there are minima in the two residual plots, and a maximum in the amplitude plot. Inspection of these plots in Figure 4.4 makes it clear that 0.42 days^{-1} is the actual variability frequency, and that the feature at 0.21 days^{-1} is only a sub-harmonic of this frequency.

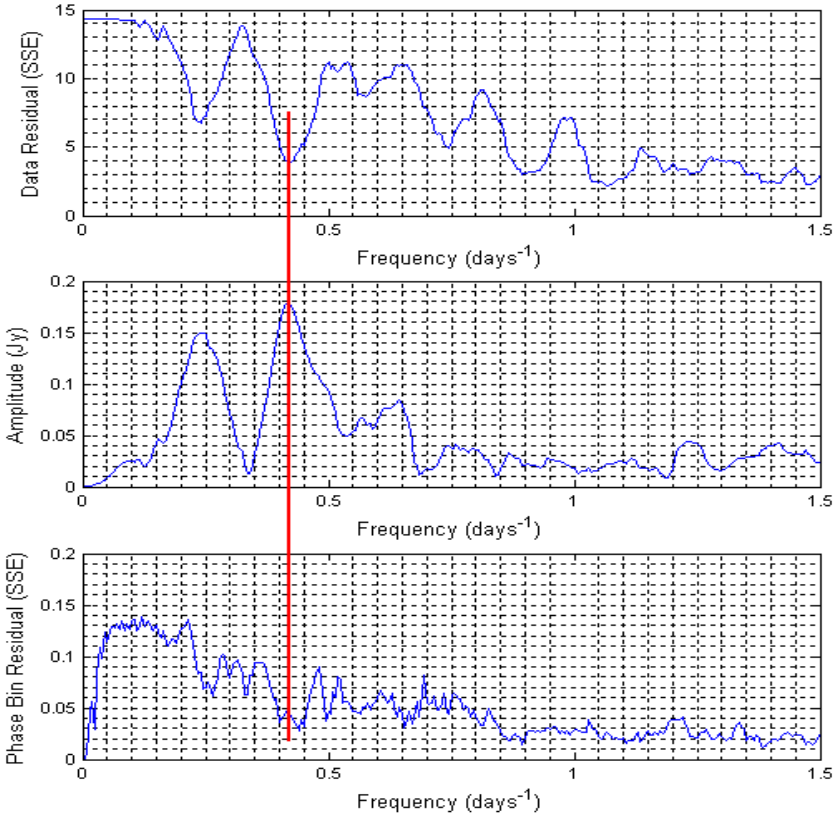

Figure 4.3 Data folding analysis of the PKS B1144-379 data for observing period 4. The solid vertical line indicates the variability frequency of 0.42 days^{-1}, corresponding to a peak in the amplitude of the fitted sinusoid, and troughs in both the residual and the 1 h phase bin residual plots.

Figure 4.4 shows the data folding and phase bin plots at the frequency of ~0.42 days^{-1}. This corresponds to a variability period value of $T_{\text{period}} \approx 2.38$ days, an estimate that agrees well with the value of $T_{\text{period}} \approx 2.4$ days estimated by the scintle counting method (Section 4.2).

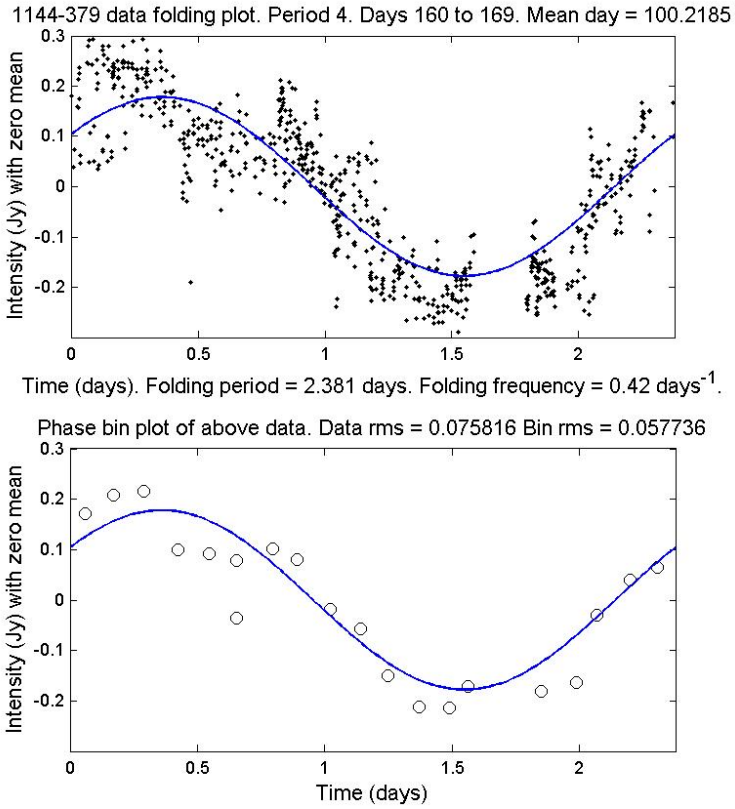

Figure 4.4 Data folding and phase bin plots at the variability frequency of 0.42 days^{-1}.

In Figure 4.3, the low residual (sum square error) values that characterise the data folding plot at high frequencies are also associated with near-zero amplitude values. This is simply a consequence of folding a time series on time scales much shorter than its actual variability.

A data folding exercise should not be applied to a time series which is so long that the value of $T_{\rm period}$ changes significantly. Figure 4.5 presents the results of a data folding exercise carried out on a PKS B1519-273 time series that is 87 days long. Chapters 6 and 7 show that the variability time scale, $T_{\rm period}$, of this source follows an annual cycle, and the value of $T_{\rm period}$ changes significantly over 87 days, which smears out the data folding features.

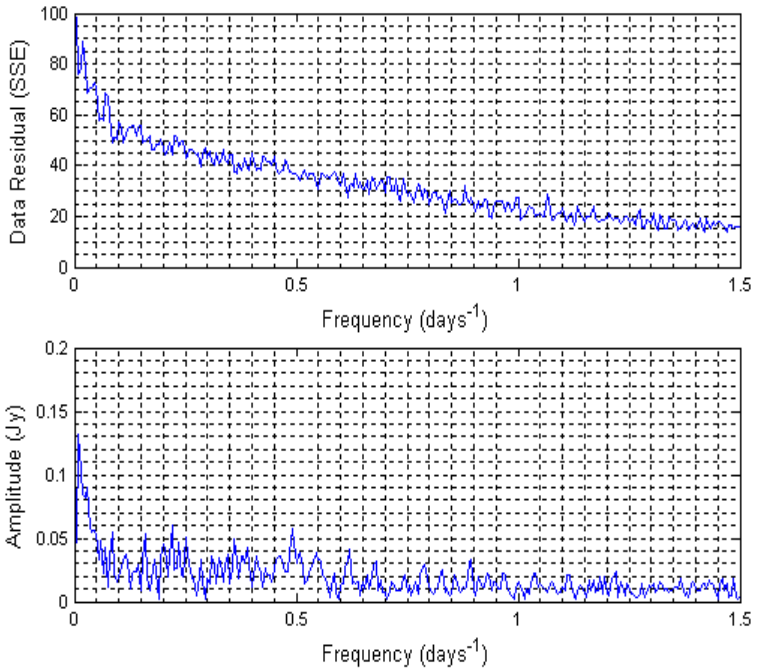

Figure 4.5 Data folding of an overly long time series, here 87 days of 2003 PKS B1519-273 data.

Finally, a folding plot is clumpy if T_{period} is close to an integral number of days. Figure 4.6 shows this in the case of PKS B1519-273 data from northern source group observing period 14, which has a period of ~3 days, producing four clumps of data in a data folding plot given that the observing period is ~10 days long.

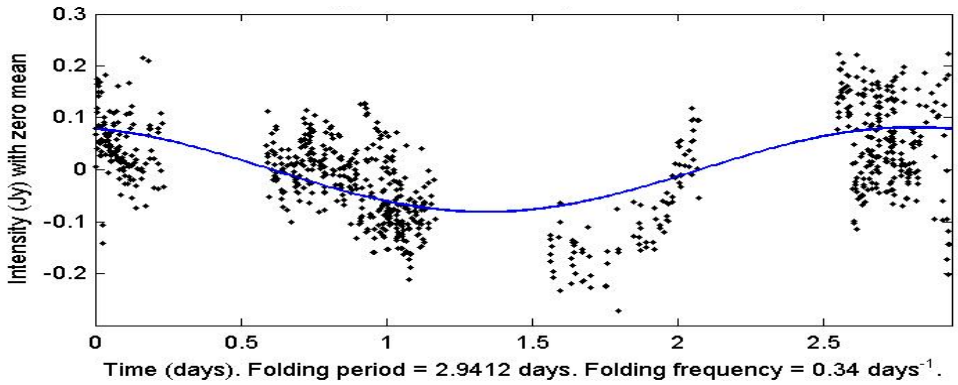

Figure 4.6 A clumpy data folding plot, from examination of PKS B1519-273 data for days 58 to 67 in 2004, with $T_{period} \approx 3$ days.

4.4 Spectral Analysis

4.4.1 Introduction

Modern software packages provide arsenals of spectral analysis routines, and *Matlab* has been used for this research (Mathworks, 2002).

Consider a flux density time series, $X(t)$, consisting of N_0 data points, x_j, recorded at times t_j where $j = 1$ to N_0. The goal of spectral analysis applied to $X(t)$ is to estimate its characteristic variability time scale, T_{char}. Studies based on limited observational data usually compute the autocorrelation function (ACF) and define T_{char} as the lag time at which the ACF falls to some value, the definitions $T_{char} \sim T_{0.5}$ and $T_{char} \sim T_{1/e}$ being common choices. $T_{0.5}$ is the lag time at which the ACF, normalised to unity at zero lag, falls to a value of 0.5. Similarly, $T_{1/e}$ is the lag time at which the normalised ACF falls to a value of $1/e$. This is the decorrelation time of the ACF, consistent with the definition of the coherence scale (Section 2.5.2).

As discussed, Ceduna data are sufficiently comprehensive to enable T_{char} to be defined as T_{period} (i.e. $T_{char} \sim T_{period}$). This definition is both intuitively appealing, and also avoids the problem that ACFs computed from data that span many days of observations occasionally fail to correctly evaluate $T_{0.5}$ and $T_{1/e}$. The reasons for this, discussed in Sections 4.4.6 and 4.4.7, are that computation of an ACF can be affected by regular (i.e. daily) data gaps longer than about 12 hours, and by peak-to-peak variability time scales on the order of an integral number of days.

Ceduna ACFs are better behaved in their evaluation of T_{period}, which is the lag time at which the ACF rises to its first peak. In practice, the spectral characteristics of a time series are easier to determine in the frequency domain from the Power Spectral Density function (PSD), although the PSD and the ACF are a Fourier transform pair and thus contain the same spectral information. Hence the strategy, which is presented in detail in the following sections, is to compute the PSD from the ACF and use it to identify the value of T_{period}.

First order structure functions are also used to quantify variability time scales. For example, Beckert et al. (2002) define T_{char} as the time lag, τ, at which the structure function, $SF(\tau)$, saturates to form a plateau. Dennett-Thorpe & de Bruyn (2003) define T_{char} to be 1/e of this value, and this is its standard definition in the pulsar scintillation literature. However, the structure function is related to the ACF, with $SF(\tau) = 2\,[R_x(0) - R_x(\tau)]$, and it is not used to determine variability scales for Ceduna data for the same reasons the ACF is not used.

4.4.2 Autocorrelation Function

The autocorrelation function (ACF) between a time series and itself, but separated by a lag time τ, is $E\,[x(t)\,x\,(t+\tau)]$, where E is the expectation operator. For a uniform and complete time series, the ACF is evaluated as:

$$R_x = \frac{1}{N}\sum_{i=1}^{N} x_i(t)\,x_i(t+\tau)$$

This calculation is not suitable for application to a flux density time series, which is neither uniform nor complete. Interpolating data to even spacing is not an attractive way forward, given the size of the daily data gaps, but a modified version of the discrete autocorrelation function method of Edelson & Krolik (1988) performs well.

Edelson & Krolik (1988) suggested a data binning approach to computing the ACF of a time series. They assumed the time series to be *wide-sense stationary*, whereby two conditions are met (Madisetti & Williams, 1998): the ACF depends only on the lag time τ; and the time series mean is constant over time:

$$R_x = R_x(\tau) \quad \text{and} \quad E\,[x(t)] = x_{mean} \neq f\,(t).$$

Both conditions are approximately met by a Ceduna flux density time series that spans an observing period of 10-15 days. A modified Edelson & Krolik (1988) approach is used:

$$R_I(\tau) = \frac{1}{M}\,.\mathrm{Bin}\left\{\frac{(I_i - I_{mean})(I_j - I_{mean})}{I_{mean}^2}\right\}$$

where the flux density data points I_i and I_j are separated by time lag $\Delta t_{ij} = t_j - t_i$. The discrete correlations are accumulated into bins at lag increments of $\Delta\tau$. The bin at lag τ accepts data pairs for which $(\tau - \Delta\tau/2) \leq \Delta t_{ij} < (\tau + \Delta\tau/2)$, and the ACF value at this lag, $R_I(\tau)$, is obtained by averaging the bin total by the number of data pairs it contains, M.

This autocorrelation function definition is appropriate for the standard model of interstellar scintillation in AGN signals, presented in Chapter 2:

$$R_I(\tau) = \frac{E\left[\{I(t) - I_{mean}\}\{I(t+\tau) - I_{mean}\}\right]}{I_{mean}^2}$$

which is normalised at zero lag to the square of the scintillation modulation index, which as explained in Section 4.6 is defined as:

$$m = \sqrt{R_I(0)} = I_{RMS} / I_{mean} \ .$$

Edelson & Krolik (1988) normalised the ACF at zero lag to unity, using the variance, σ^2, instead of I_{mean}^2.

$$\frac{E\left[\{I(t) - I_{mean}\}\{I(t+\tau) - I_{mean}\}\right]}{\sigma^2} \xrightarrow{\tau = 0} \frac{E\left[\{I(t)\, I(t)\}\right] - I_{mean}^2}{\sigma^2} = 1$$

Figure 4.7 shows the ACF for PKS B1144-379 data of observing period 4 (the data analysed in previous sections using scintle counting and data folding), computed out to a maximum lag time of four days. The ACF points are evaluated using 0.5 h bins, and a polynomial fit to these points indicates that the first peak occurs at $T_{\text{period}} \approx 2.4$ days, which agrees with the values estimated in previous sections by the scintle counting and data folding exercises.

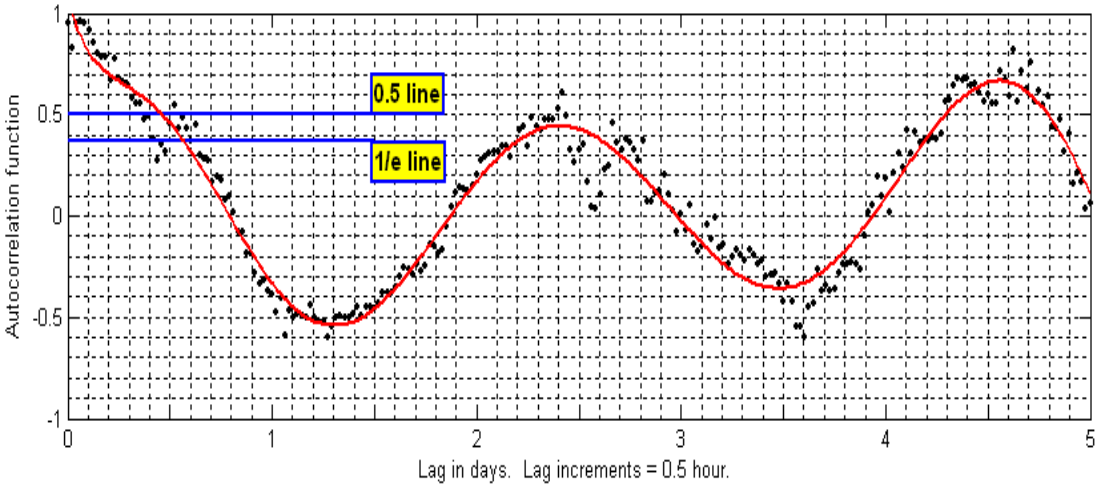

Figure 4.7 Autocorrelation function of PKS B1144-379 data from observing period 4.

Figure 4.7 shows the ACF normalised using the variance, σ^2. The noise spike at zero lag, due to uncorrelated receiver noise, has been suppressed by setting the ACF's value at zero lag to unity. For an ACF which is not normalised, the effect of the spike can be removed by extrapolating to the zero lag ($\lim \Delta t \to 0$). The ACF is a little unclear in the vicinity of $T_{0.5}$ and $T_{1/e}$, but the polynomial fit indicates that $T_{0.5} \approx 0.45$ days, in good agreement with the expected value for sinusoidal scintles, $T_{0.5} \approx T_{\text{period}} / 6 = 2.4/6 = 0.4$ days.

[Consider a random process, $x(t) = A_0 \sin(\omega t + \phi)$, where $\omega = 2\pi / T$, and the phase angle, ϕ, is random. The ACF is given by $R(\tau) = 0.5 A_0^2 \cos(\omega \tau)$, which falls from unity to ½ $R(0)$ at $\tau = T / 6$ (Newland, 1975)].

Normalising the ACF using I_{mean}^2 instead of σ^2, to correspond to the standard ISS model, would result in a plot of exactly the same form, but with a different vertical scale. The zero lag ACF for this plot gives the modulation index as $m \approx \sqrt{0.0065} = 0.08$. This is actually a naïvely high value of *m*, and calculation of the correct value is discussed in Section 4.6.

Edelson & Krolik (1988) recommended modifying the normalisation factor for dealing with noisy data, by subtracting the mean square of the estimated uncertainties inherent in the observations: $\sigma^2 \rightarrow \sigma^2 - \left(I_{rms}^{obs}\right)^2$. White & Peterson (1994) argue that this modification is not necessary, and this is the case for the Ceduna data once the data have been processed in the manner described later in this chapter, but the suggestion may well have merit for a time series with significantly noisy data.

ACF negative overshoot

In Figure 4.7, the first ACF minimum has a value of ~-0.5. Coincidentally, this is almost the same value as that found by an autocorrelation analysis of PKS 0405-385 data from 1996. The analysis of the PKS 0405-385 data is presented by Rickett et al. (2002), who note that the depth of the first ACF minimum (its *negative overshoot*) is related to the spectral purity of the spatial modulation pattern through which the Earth moves, which in turn reflects the extent to which the ISM scattering material is anisotropic.

This effect can be examined using the anisotropic form of the standard model for interstellar scintillation of AGN signals, discussed in Chapter 2. Rickett et al. (2002) found that scattering structures with an aspect ratio of $\Omega \approx 0.25$ could explain the negative overshoot of about -0.5 in the PKS 0405-385 ACF (see their Figures 9 and 11). They also investigated the effect of different scattering material profiles on the ISS model predictions, and found that deeper ACF overshoots are associated with thin scattering screens rather than extended scattering screens.

4.4.3 Power Spectral Density Function

Studies based on limited data usually compute the autocorrelation function (ACF) and define T_{char} in terms of the ACF, for example $T_{char} \sim T_{0.5}$ or $T_{char} \sim T_{1/e}$, while Ceduna data typically capture several scintles in each observing period, and thus enable $T_{char} \sim T_{period}$ to be estimated with confidence. In addition, as shown later in this chapter, the ACF fails to properly compute $T_{0.5}$ and $T_{1/e}$ in certain situations. The ACF does a better job of identifying T_{period} in these situations, but its value is sometimes clearer in the frequency domain.

This motivates estimation of the *Power Spectral Density* function (PSD), $P_I(\omega = 2\pi f)$. This could be estimated directly from a flux density time series, $I(t)$, using a discrete Fourier transform, not a fast Fourier transform, since $I(t)$ has non-uniform data (Deeming, 1974; Madisetti & Williams, 1998). This approach is not fully appropriate for a random process time series, which cannot be truly represented by a discrete Fourier series (Newland, 1975), but is expected to be acceptable for a flux density time series whose variability is due to the quasi-periodic scintillation phenomenon: the power spectra of several snapshots of the scintillation pattern should be similar within limits set by sampling errors.

However, any problems of using a discrete Fourier transform can be avoided by computing the PSD from the ACF of the time series. For a random process, the ACF meets the Fourier transform condition, and it contains information about the frequency content of $I(t)$, since it is a maximum when $I(t)$ and $I(t+\tau)$ are in phase, and a minimum when they are in antiphase (Newland, 1975).

By Wold's theorem, the PSD, $P_I(\omega)$, is the Fourier transform of the ACF, $R_I(\tau)$:

$$P_I(\omega) = \frac{1}{\sqrt{2\pi}} \int_{-\infty}^{+\infty} R_x I(\tau) e^{-i\omega\tau} d\tau \qquad R_I(\tau) = \frac{1}{\sqrt{2\pi}} \int_{-\infty}^{+\infty} P_I(\omega) e^{i\omega\tau} d\omega$$

The PSD estimation approach used herein is to compute a periodogram, and this time a Fast Fourier Transform does work:

$$P_I(\omega) \approx \frac{1}{N_0} \left| \sum_{j=1}^{N_0} R_I(t_j) \exp(-i\omega t_j) \right|^2$$

The terms PSD and periodogram are often used interchangeably in the literature, although strictly the periodogram is only an estimate of the PSD, since $I(t)$ only samples the random process (Scargle, 1982). The periodogram is a *non-parametric* approach to estimating the PSD. Both the basic method and variations thereon are described by Madisetti & Williams (1998), and are available in the *Matlab* signal processing toolbox (Mathworks, 2002).

Considering the main options, the Bartlett Method subdivides $I(t)$ into segments, and the estimated PSD is the average of each segment's PSD. The Welch Method is similar, but with overlapping segments. Neither method is appropriate for a Ceduna time series, which has only a limited number of scintles in a 10-15 day time series, thereby leading to a set of very different segment PSDs, while using a longer time series sample would risk violating the stationarity condition. The Blackman-Tukey Method weights the ACF in favour of shorter lag times, which have greater contribution to the calculation, and this method could be applied. However, the binning strategy of the Edelson & Krolik (1988) method has a similar effect, and this method is preferred given its prior usage by other researchers.

Alternative PSD estimation approaches that do not rely on manipulation of the ACF are discussed by Mathworks (2002). *Subspace methods* are effective in detecting sinusoids in signals with low signal-to-noise ratios, but Ceduna data have reasonably good signal-to-noise ratios, as shown in the next section, even before application of the data filtering procedures described later in this chapter. *Parametric methods* model the process and then estimate the PSD in terms of the model parameters. In this case the process is scintillation, and the standard ISS model described in Chapter 2 might be developed to describe the scintillation characteristics of a given source. In this case, a parametric approach might be of value in estimating the PSD from data recorded by unusually short observing periods, which occur from time to time for various reasons.

Table 4.1 gives *Matlab* code for determining the PSD from the ACF, written by the author based on Mathworks (2002). It is convenient to measure lag times in days, so the frequency scale has units of days^{-1}, and the PSD has units of power per unit frequency. This exercise is of key importance to the spectral analysis, and thus is explained in detail below.

```
1. ACF = ACF – mean(ACF);                              % Compute zero mean ACF
2. NFFT=2048;                                          % Require NFFT-point FFT
3. NFFTnext=2^( nextpow2(length(ACF)) );               % Find next highest power of 2
4. If NNFTnext>NFFT; disp('NFFT Warning'); end;        % We want to pad ACF, not truncate it
5. PSDtwo = fft( ACF, NFFT );                          % FFT of ACF, zero padded to NFFT
6. PSDtwo_real = PSDtwo.* conj(PSDtwo) / NFFT;         % Compute real part of PSD
7. PSDsingle = 2*PSDtwo(1:1+NFFT/2);                   % Single sided PSD
8. Freq = (1/Laginc) * (0:NFFT/2) / NFFT;              % Frequencies out to NFFT/2
9. plot( Freq, (NFFT / NFFTnext)*PSDsingle);           % PSD plot (NFFT equivalent)
```

Table 4.1 *Matlab* code for computing the Power Spectral Density function (PSD) from an Autocorrelation Function (ACF).

In Table 4.1, the *Matlab* Fast Fourier Transform (FFT) routine *fft* computes the complex two-sided ($-\infty$ to ∞) PSD, *PSDtwo,* from the ACF. Code lines 6 and 7 then produce a real single-sided (0 to ∞) PSD, *PSDsingle,* in terms of frequency instead of angular frequency. *PSDsingle* contains the zero frequency component as its first element, *PSsingle*(1), which is zero since line 1 recalculates the ACF to have zero mean.

The routine *fft* either pads or truncates the ACF to *NFFT* points before computing its Fourier transform, where *NFFT* is a power of two to facilitate the computation. The ACF of a Ceduna time series is not very long, so padding is preferable to truncation, and larger values of *NFFT* enable the PSD peaks to be more accurately identified. The computing strategy in Table 4.1 (lines 2, 3 and 4) is to specify an $NFFT = 2^{11} = 2048$ point FFT, and check that this is larger than *NFFTnext*, the next highest power of 2 greater than the ACF's length.

The Nyquist frequency component is *PSDsingle*(1+NFFT/2). If the ACF is computed at lag intervals of $\Delta\tau = 1/6$ days (4 hours), the Nyquist frequency is $(2\Delta\tau)^{-1}$ days^{-1} = 3 days^{-1}, which corresponds to a minimum resolvable period of 8 hours. Higher frequencies can be studied by recomputing $R_I(\tau)$ at smaller lags: if future telescope operation manages to avoid the problem of systematic intensity fluctuations, discussed later in this Chapter and in Chapters 3 and 5, Ceduna should be able to resolve flux density variations on the order of an hour.

Line 7 of the Table 4.1 code applies a factor of two multiplier in extracting the single-sided PSD from the two-sided PSD. In addition, line 9 of the code converts PSD plots to their NFFT-point FFT equivalent, since a PSD function computed using an N point FFT should be divided by two in order to compare it to a PSD function computed using a $2N$ point FFT.

Figure 4.8 shows the PSD for the PKS B1144-379 data of observing period 4, computed from the ACF shown in Figure 4.7. The spectral peak has a central frequency of 0.46 days^{-1} which corresponds to $T_{\text{period}} \approx 2.2$ days, and agrees with previous estimates. Secondary spectral features are discussed in the next section.

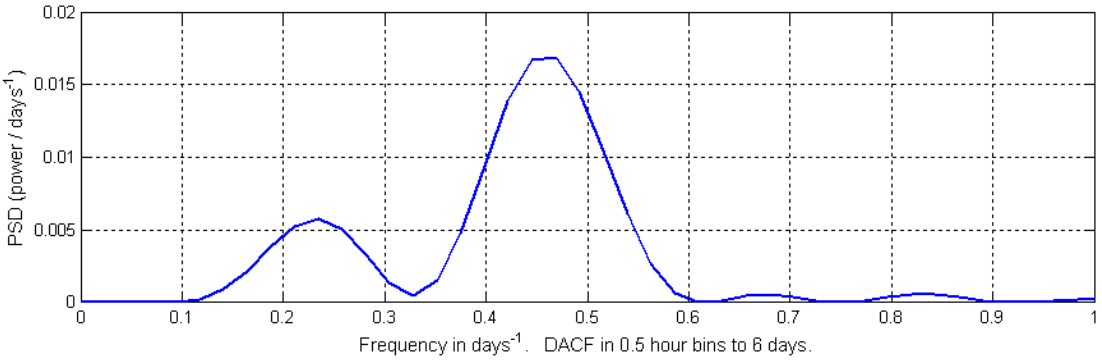

Figure 4.8 Power spectral density function computed from the ACF of Figure 4.7.

As a Ceduna time series analysis tool, the main purpose of the PSD function is to identify the variability period, $T_{period} = 1 / f_o$. Actual spectral power values are not overly important. The practice followed herein is to remove the ACF's normalisation ahead of computing the PSD, such that the total spectral power depends on the ACF lag increments, and on the maximum lag of the ACF, including its zero padded part.

Conclusion of the PKS B1144-379 case study analysis
The variability time scale, T_{period}, for PKS B1144-379 during observing period 4 has been unambiguously estimated to be just over 2 days by all three analysis tools: spectral analysis, supported by scintle counting and data folding cross-checks.

4.4.4 Effects of Noise and Spectral Leakage

Noisy data results in a PSD function with secondary spectral peaks that can be quite large. Scargle (1982) notes that the signal-to-noise (S:N) ratio is proportional to the number of data samples, and his calculation of PSD functions from 107 data samples with S:N ratios of 65, 2.6, and 0.65 shows that the signal is only just detected for the S:N ratio of 2.6, and is not detected for the S:N ratio of 0.65.

The PKS B1144-379 data for observing period 4 has 670 samples, perhaps a little lower than average, and a mean strength of 1.981 Jy. Figure 4.4 shows a sinusoidal fit to the folded data, with an RMS value of 0.076 Jy, giving an S:N ratio of 26 for these data. The Edelson & Krolik (1988) data binning method used to compute a discrete ACF from Ceduna data improves the S:N ratio further, and it is thus expected that the PSD function estimated from this ACF, shown in Figure 4.8, should not suffer from noise effects. Further improvement in the signal-to-noise ratio results from smoothing through the data to remove the high frequency component that is due to systematic effects, as described later in this chapter.

Spectral leakage produces secondary peaks in the PSD function due to the finite nature of the ACF from which the PSD is computed. The phenomenon takes several forms.

- Aliasing is power leakage from high to low frequencies. It arises if the sampling interval is too large to detect the highest frequency component in the signal (Newland, 1975), and is a particular problem for uniformly sampled data (Scargle, 1982). For a sampling interval Δt, the highest detectable frequency is $(2\ \Delta t)^{-1}$, the Nyquist frequency.

  The Ceduna sources considered by this research vary on time scales (T_{period}) of typically several days, so aliasing is not a problem. The ACF is usually computed at bin intervals of $\Delta t = 4$ hours, giving a Nyquist frequency of 3 days^{-1} (see previous section), well above the highest frequency (about 1 day^{-1}) of interest.

- The finite length of the ACF causes power to leak to frequencies near the principal frequency, producing side lobes and secondary PSD peaks. This "spectral window" phenomenon is a particular problem for short observing periods, discussed below.

The leakage due to the finite length of the ACF is best understood by considering an infinite sinusoidal plane wave, $\exp(i\omega_o t)$, and its Fourier transform, the delta function $\delta(\omega - \omega_o)$. Chopping in the time domain produces additional frequencies close to the wave frequency, $\omega_o = 2\pi f_o$, with the Fourier transform for a chop length $2T$ given by (e.g. Anderson 1971):

$$g(\omega) = \frac{1}{\sqrt{2\pi}} \int_{-T}^{+T} e^{i(\omega_o - \omega)t}\, dt \quad = \sqrt{\frac{2}{\pi}}\, T\, \frac{\sin(\omega_o - \omega)}{(\omega_o - \omega)}$$

Figure 4.9 shows this (Sinc) function for a sinusoidal plane wave of frequency $f_o = 1.25$ days^{-1} that is chopped to a length of $T = 10$ days.

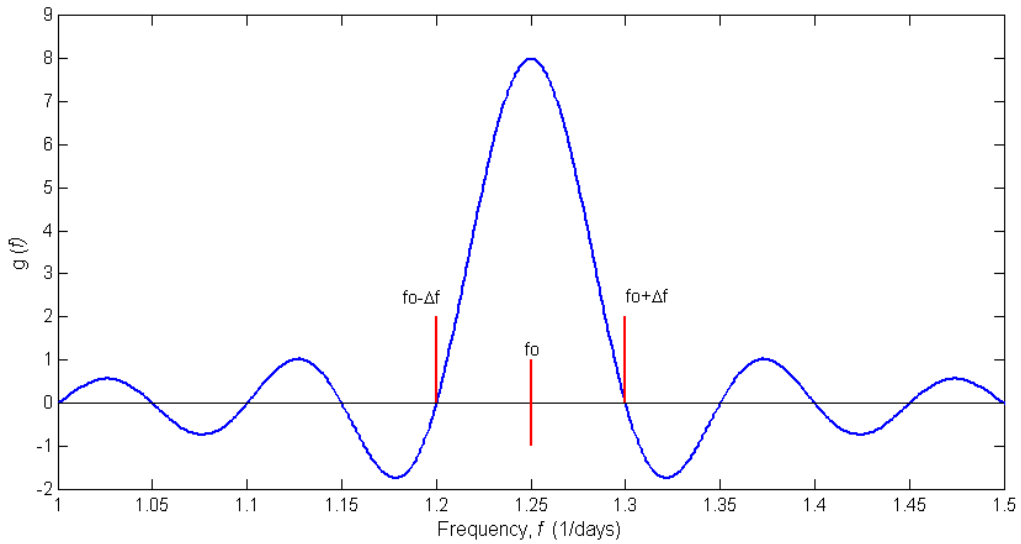

Figure 4.9 The spectral distribution resulting from chopping an infinite sinusoidal plane wave of period 0.8 days to a length of 10 days.

The function is dominated by the contribution at frequency f_o, with minor contributions from adjacent frequencies. The function falls to zero at 1.20 days^{-1} and 1.30 days^{-1}, and adjacent peaks are found at 1.125 days^{-1} and 1.375 days^{-1}, given by:

$$\text{Zeros:} \quad (\omega - \omega_o)T = \pm\pi \quad \text{or} \quad f_o \pm \Delta f = f_o \pm \left(\frac{1}{2T}\right)$$

$$\text{Adjacent peaks:} \quad (\omega - \omega_o)T = \pm\frac{5\pi}{2} \quad \text{or} \quad f_o \pm \Delta f = f_o \pm \left(\frac{5}{4T}\right)$$

The width of the f_o peak thus depends solely on the length of the chopped time series, with greater lengths resulting in narrower, sharper, f_o peaks.

The chopping phenomenon also affects a PSD function, for which the appropriate value of T is the length of the ACF (i.e. its maximum lag time). The ACF lag increment also influences the PSD computation. Figure 4.10 shows three PSD functions computed from ACFs of different lengths and lag increments. The underlying time series is again a sinusoidal plane wave of frequency f_o = 1.25 days^{-1}.

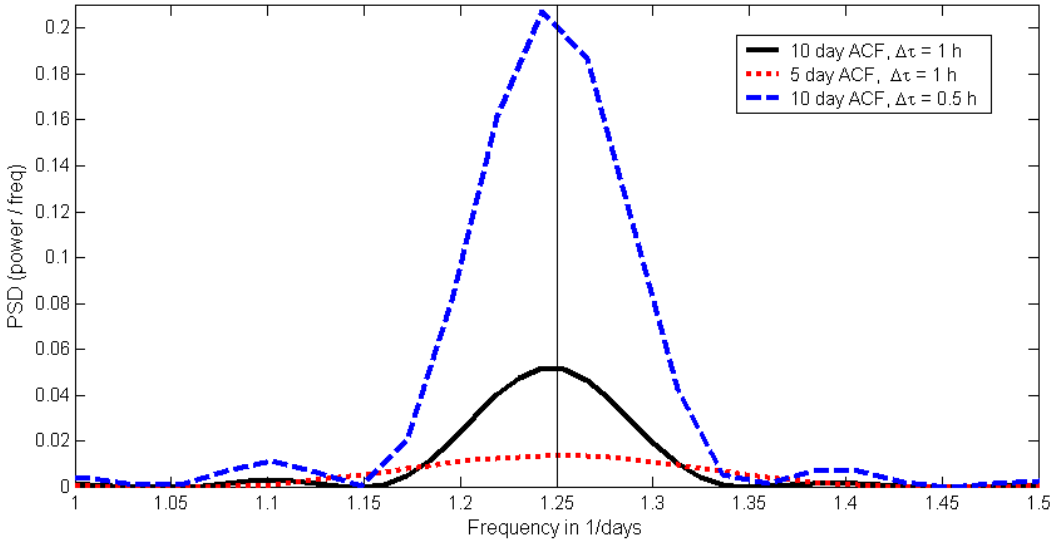

Figure 4.10 PSDs calculated from ACFs with a different maximum lag times and lag increments, Δτ. The underlying time series is a continuous sinusoidal plane wave of frequency 1.25 days^{-1}.

The ACF calculation effectively multiplies two wave functions together, so the location of zeros and secondary peaks adjacent to the principal PSD peak must be adjusted.

$$\text{Zeros: } f_o \pm \Delta f = f_o \pm \left(\frac{1}{T}\right) \qquad \text{Adjacent peaks: } f_o \pm \Delta f = f_o \pm \left(\frac{3}{2T}\right)$$

For example, consider the two PSDs in Figure 4.10 which are computed from ACFs with maximum lag times of 10 days. Since f_o = 1.25 days^{-1}, and T = 10 days, these PSDs have zeros at 1.15 days^{-1} and 1.35 days^{-1}, with adjacent peaks at 1.10 days^{-1} and 1.40 days^{-1}.

Alternative measures of the spectral characteristics of the PSD can be introduced by noting that the f_o peak has a Gaussian form and is thus defined by its amplitude, A, and standard deviation (measuring its spread), σ.

$$\text{PSD}(f) = A \exp\left\{\frac{-(f - f_o)^2}{2\sigma^2}\right\}$$

Table 4.2 summarises the characteristics of the three PSD f_o peaks shown in Figure 4.10. Increasing the ACF length increases the height of the f_o peak, and decreases its width, while increasing the lag increment reduces the height of the f_o peak, but increases the PSD resolution (i.e. number of points) so the middle of the f_o peak is better defined.

ACF Length (days)	$\Delta\tau$ (hours)	Resolution (No points)	Amplitude, A (power/freq)	Spread, σ (days^{-1})
10	1.0	17	0.05	0.037
10	0.5	8	0.21	0.037
5	1.0	34	0.01	0.071

Table 4.2 Effect of ACF length and lag increment on f_o peak characteristics.

The specification of an ACF length (i.e. maximum lag time) must enable the ACF to capture the variability time scale, T_{period} , and specification of the ACF lag increment should enable the ACF to adequately resolve the first peak at a lag time of T_{period} , which is typically on the order of several days. For PKS B1519-273 and PKS B1622-253 flux density data, the usual specification is a 10 day ACF length and a lag increment of 4 hours. The observing period length is usually a few days longer than 10 days, but the ACF calculation is not reliable at lag times close to the length of the time series.

4.4.5 Effect of Daily Observing Gaps

The discrete ACF computation method of Edelson & Krolik (1988) averages the values of correlations collected in a set of bins. This approach allows the ACF of a flux density time series with regular data gaps (when the source is below the horizon) to be estimated, but the discrete ACF is only an approximation of the ACF of the underlying continuous flux density time series. The exact nature of the discrete ACF depends on which portion of the scintle pattern through which the Earth is moving is sampled by the daily observations, a point which is illustrated by Figure 4.11.

In the top plot of Figure 4.11, the red line is a synthetic Ceduna time series whose scintles have a 1.8 day period, and an amplitude of 0.25 Jy, values typical of the blazars monitored by Ceduna. The synthetic time series has 13 hours of data recorded daily over a period of 10 days, with observations starting at 16.8 h (0.7 days) each day (the source rise time), and daily observing gaps of 11 hours. In reality, a source rises ~ 4 minutes earlier each day, but this is unimportant over an observing period of only 10 days. The solid blue line shows the continuous underlying time series.

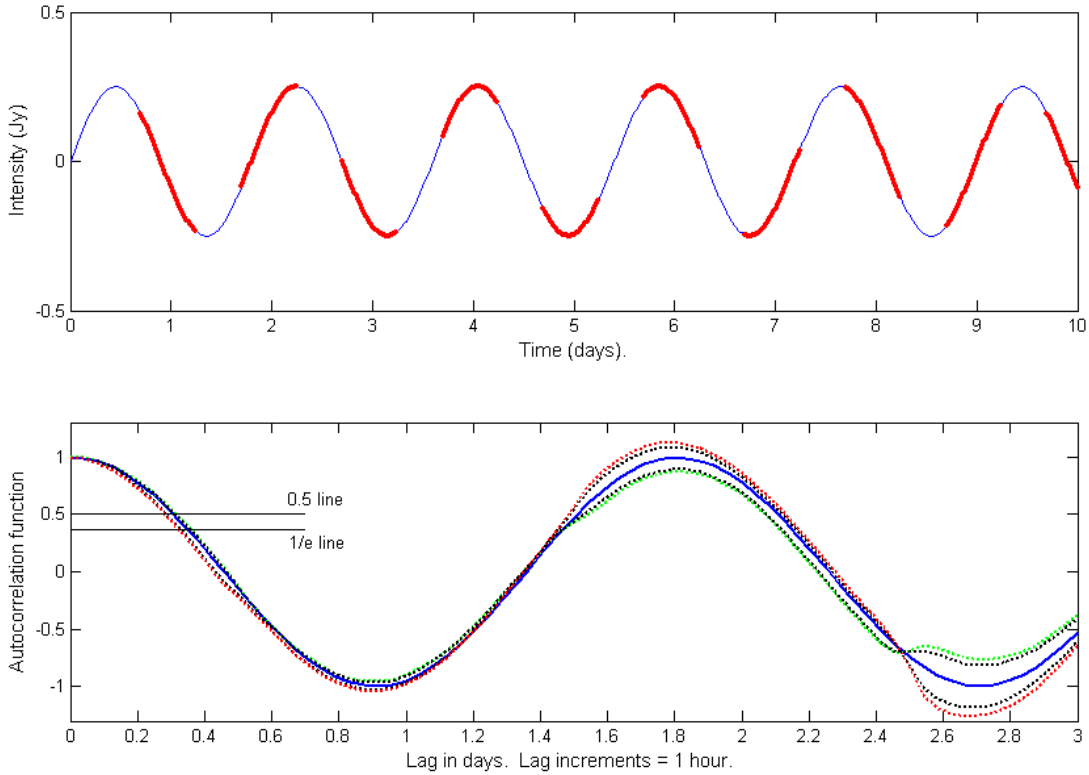

Figure 4.11 **ACFs of a synthetic IDV time series with 1.8 day period, and different daily observation start times. See text for explanation.**

In the bottom plot of Figure 4.11, the solid blue line shows the ACF computed from the continuous underlying time series, normalised to unity at zero lag. Since there are no data gaps in the underlying time series, the discrete ACF calculated by the Edelson & Krolik (1988) method is the same as the standard ACF.

The dotted red line shows the discrete ACF computed from the synthetic Ceduna time series shown in the top plot, and discussed above. The other dotted lines show the discrete ACFs computed from synthetic time series which are identical except for having different daily observation start times of 0.1 days (green line), 0.3 and 0.5 days (the two black lines). The discrete ACFs of the synthetic Ceduna time series with their regular data gaps do not exactly track the ACF of the underlying continuous time series, and the difference depends on the daily observation start times.

This phenomenon carries over to PSDs computed from discrete ACFs. Figure 4.12 shows the corresponding variations in T_{char} estimates. The left hand plot is an expanded portion of the discrete ACFs shown in Figure 4.11, while the right hand plot shows the primary peaks of the PSDs computed from these discrete ACFs. The solid and dashed lines have the same meaning as those in Figure 4.11.

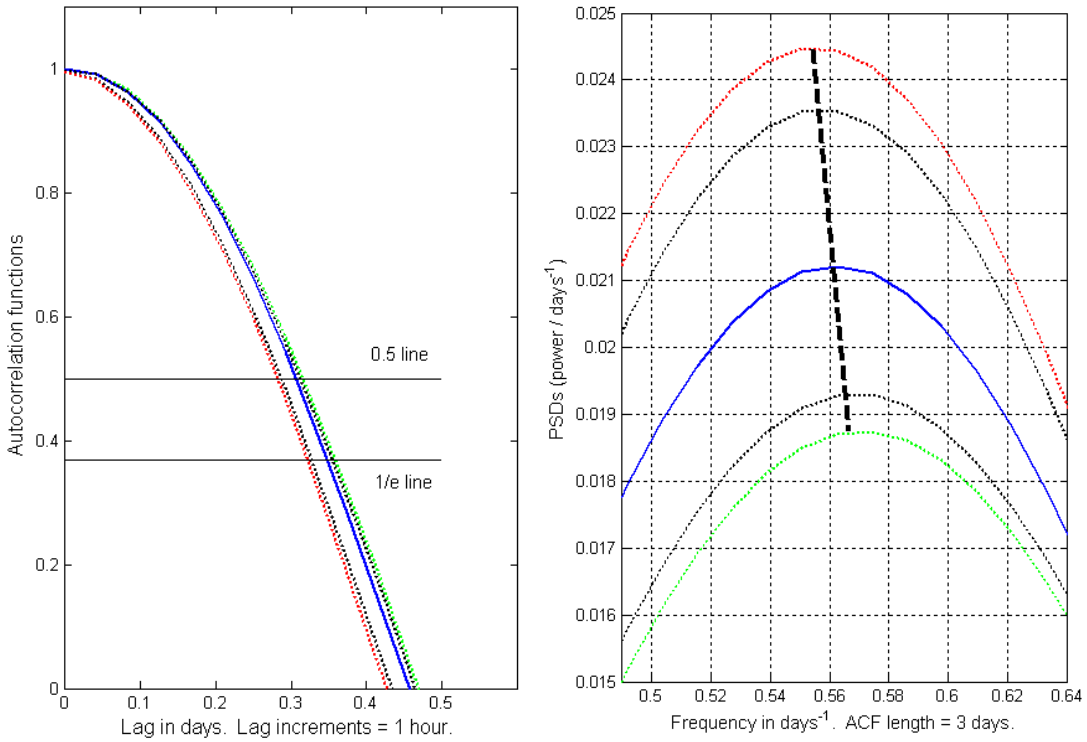

Figure 4.12 Effect of daily observing gaps on estimation of characteristic variability time scales. Left: expanded portion of the ACF plots in Figure 4.11. Right: the corresponding PSDs, showing the f_o peak.

The left hand plot in Figure 4.12 shows that $T_{char} \sim T_{0.5}$, and $T_{char} \sim T_{1/e}$ estimates derived by examination of the discrete ACFs calculated from the synthetic Ceduna flux density time series used for this demonstration differ by up to about an hour from the estimates computed from the ACF of the underlying time series, depending on the observation daily start times.

The right hand plot in Figure 4.12 shows that the PSDs produced from the discrete ACFs also differ slightly in their estimates of $T_{char} \sim T_{period}$, again depending on the observation daily start times. In the right hand plot, the heavy black dash line tracks the f_o (= 1/ T_{period}) peaks for the various Ceduna time series.

4.4.6 Effect of Short Observing Periods

The previous section assumed the source is observed each day for a period longer than the period during which it is not observed ($T_{obs} > T_{unobs}$). If the converse is true, $T_{unobs} > T_{obs}$, then the ACF computation will find no data pairs at lag times between T_{obs} and T_{unobs}, nor during this period every 24 hours thereafter. Table 3.7 in Chapter 3 shows that, for the sources observed by Ceduna, this applies to AO 0235+164, which only rises above the 10° elevation cut-off for 9 hours a day.

AO 0235+164 is not a source whose analysis is pursued by the present research, but it is nevertheless worth examining the effect on a spectral analysis exercise of a flux density time series of a source with a short observing period, $T_{unobs} > T_{obs}$.

Figure 4.13 illustrates the problem. In the top plot, the broken black line is a synthetic flux density time series with 9 h of data each day, simulating AO 0235+164, with a rise time of 0.3 days. The solid blue line shows the underlying time series, with a period of 2.6 days and an amplitude of 0.25 Jy. In the bottom plot, the black dotted line shows the discrete ACF of the Ceduna time series, and the solid blue line shows the ACF of the underlying time series. The problem portions of the discrete ACF of the Ceduna time series occur at lag times between hours 9 and 15 each day, when it is undefined due to lack of data pairs.

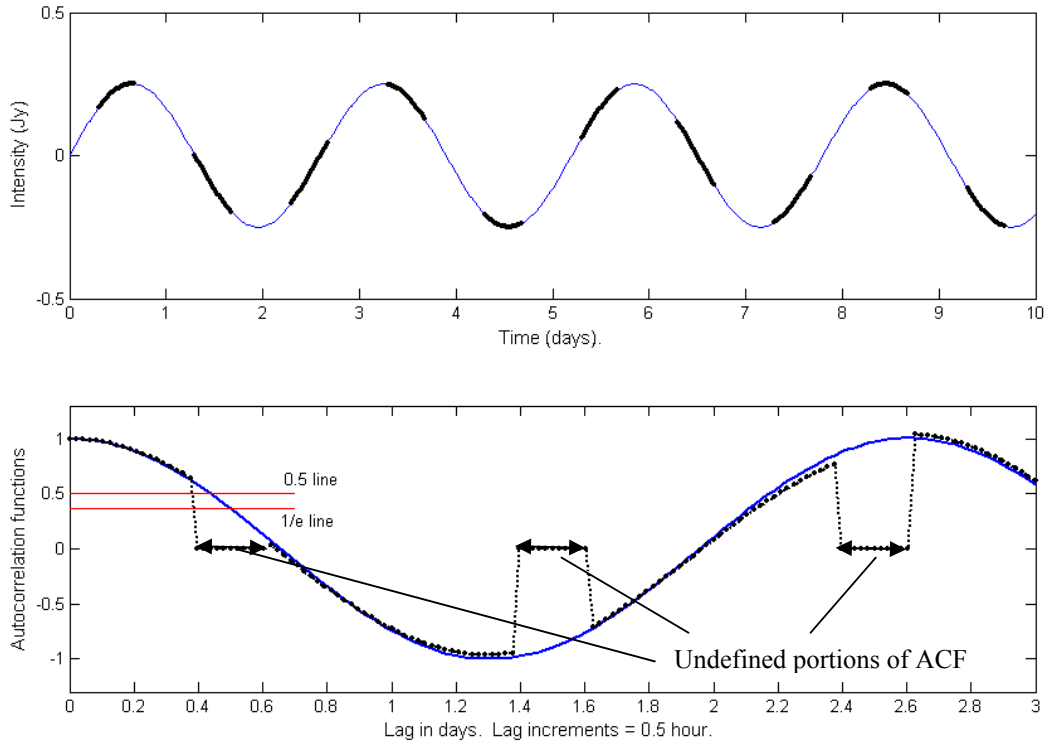

Figure 4.13 Synthetic Ceduna time series for a source with a daily observing period which is shorter short (9 h) than the non-observed period.

Figure 4.13 shows that if a source can only be observed for a short period each day, such that $T_{unobs} > T_{obs}$, and the scintles peak-to-peak times are 2-3 days long, then definitions of the characteristic variability time scale as $T_{char} \sim T_{0.5}$ or $T_{char} \sim T_{1/e}$ cannot be used directly since they fall within the discrete ACF's undefined portion, although interpolation might provide reasonable estimates of these values and, for quasi-sinusoidal scintles, the peak-to-peak time is ~6 times the value of $T_{0.5}$ or $T_{1/e}$. The problem does not entirely disappear when T_{unobs} becomes shorter than T_{obs}: the daily weak portion of the discrete ACF of the observed time series steadily degrades the extent to which it follows the ACF of the underlying continuous time series, especially at long lag times.

Definitions such as $T_{char} \sim T_{0.25}$ might be introduced to avoid the problem, but this is not necessary because the definition of $T_{char} \sim T_{period}$ remains valid: the lag time at which the ACF rises to its first peak can still be identified when $T_{unobs} > T_{obs}$.

Because of this, a Ceduna time series with $T_{unobs} > T_{obs}$ has a fairly well behaved PSD whose primary peak corresponds to $f_{period} = 1/ T_{period}$. The ACF's undefined values for daily lags between T_{obs} and T_{unobs} must be included as zero values in the PSD calculation, and the smallest ACF length (i.e. maximum lag time) able to capture the variability time scale should be specified.

4.4.7 Effect of Periods Close to Integral Days

A Ceduna flux density time series whose characteristic scintle peak-to-peak time (i.e. T_{period}) is near an integral number of days also causes discrete ACF calculation difficulties. Figure 4.14 illustrates the problem, using synthetic data which simulate the observing times of PMN J1326-5206 at Ceduna, with 15 hours of data each day. The flux density amplitude is 0.25 Jy, with a 0.3 day source rise time.

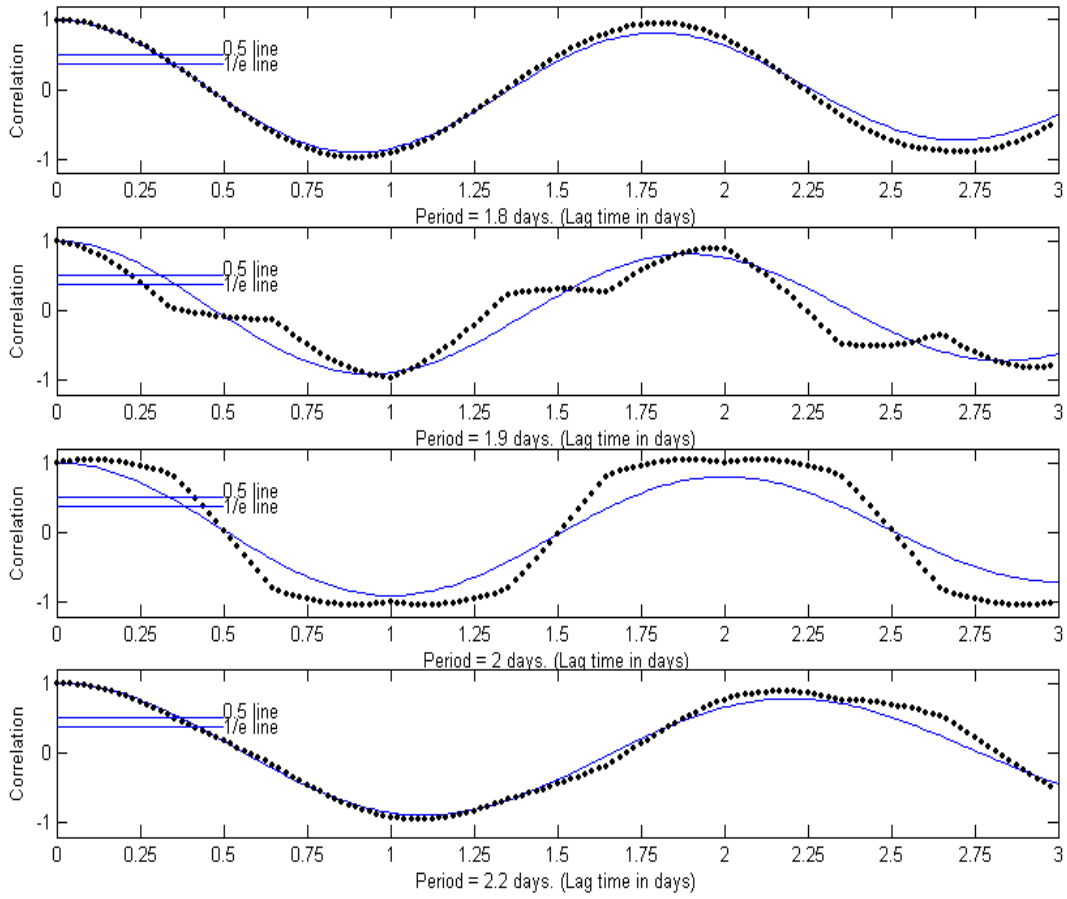

Figure 4.14 ACFs of a set of synthetic Ceduna time series whose periods are near an integral number of days. The periods increase from 1.8 days to 1.9 days, 2.0 days, and 2.2 days (top to bottom). In each plot, the dash line shows the ACF of the Ceduna time series, and the solid blue line shows the ACF of the underlying continuous time series.

In Figure 4.14, the solid blue lines in each plot show the ACFs of the underlying continuous flux density time series, whose scintle periods range from 1.8 to 2.2 days (top to bottom). The dotted lines show the discrete ACFs computed from the same flux density time series, but subject to the daily data gaps.

Figure 4.14 shows that the discrete ACF plot of a Ceduna flux density time series is poorly behaved when T_{period} lies near an integral number of days (here T_{period} = 2 days), deviating significantly from the ACF of the underlying continuous time series. This problem is mainly caused by the daily gaps in the observations, but also depends in part on the source rise time. Figure 4.15 illustrates this, showing discrete ACFs calculated from a synthetic Ceduna time series with a 1.9 day period, for source rise times of 0.1, 0.3, 0.5, 0.7, and 0.9 days.

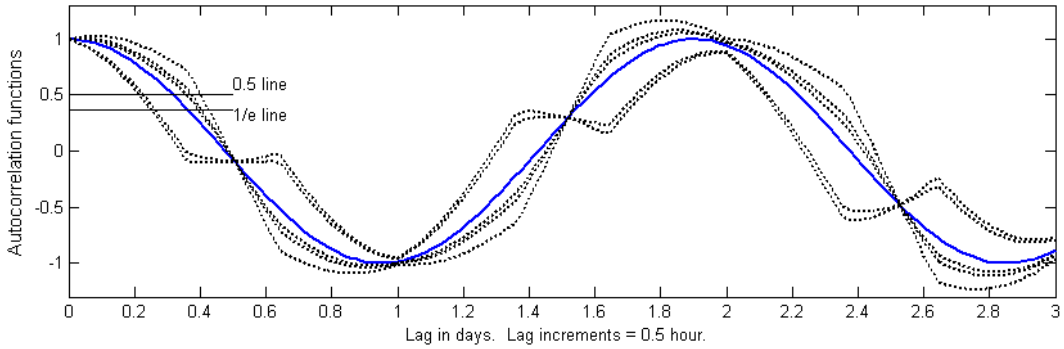

Figure 4.15 ACFs of a set of synthetic time series with a 1.9 day period but different source rise times. Solid blue line: ACF of the underlying continuous time series. Black dash lines: Discrete ACFs of the Ceduna time series.

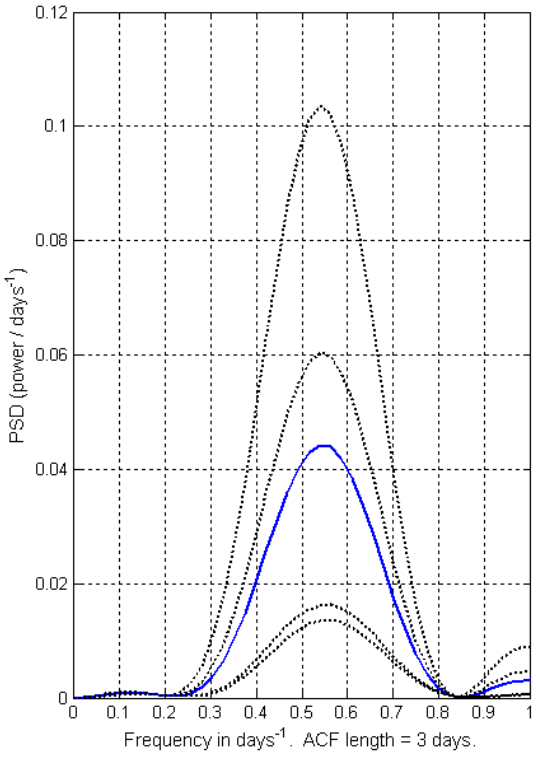

In conclusion, the $T_{0.5}$ and $T_{1/e}$ values of the discrete ACFs computed from Ceduna flux density data with peak-to-peak scintle times lying near an integral number of days can be quite different from the correct values that would be obtained from an ACF computed from the underlying continuous time series.

Discrete ACFs do better in identifying the location of a first peak at a lag of T_{period}, although they are poorly behaved in the vicinity of the peak. Figure 4.16 shows the corresponding PSDs.

Figure 4.16 PSDs computed from the ACFs in Figure 4.15 correctly identify the value of $f_{\text{period}} = 1 / T_{\text{period}} = 0.53$ days^{-1}. The line codes are as for Figure 4.15.

4.4.8 Effect of Stochasticity

The quasi-stochastic scattering of radio waves by the interstellar medium produces a spatial modulation pattern that is also quasi-stochastic. As the Earth moves through the modulation pattern, recording spatial flux density variations as a time series, adjacent scintles are found to have slightly different properties. The scintle amplitudes, periods (peak-to-peak times), and the spacing between scintles are only quasi-regular. This section examines the effect of stochasticity in the scintle pattern on the ability of a spectral analysis exercise to determine a characteristic variability time scale, $T_{char} \sim T_{period}$.

Figure 4.17 shows the effect of minor stochasticity in a synthetic flux density time series. The blue line shows a continuous time series spanning a 10 day period, with a period of 1.6 days and amplitude of 0.25 Jy, and a daily source observing time of 15 hours. Stochasticity is introduced into a recorded time series by allowing the scintle amplitudes (A), periods (T), and phase shifts (ϕ) to depart from their reference values as follows:

$$\text{Flux density} = I = A \sin\left(\frac{2\pi}{T} t + \phi\right).$$

$$A = 0.25\ (1 \pm 0.03r)\ \text{Jy} \qquad T = 1.6\ (1 \pm 0.03r)\ \text{days} \qquad \phi = \pi\ (1 \pm 0.03r)\ \text{radians}$$

where a random number generator produces normally distributed values of r that have a zero mean and unit standard deviation. Figure 4.17 shows the observed portion of 50 time series, each denoted by a broken black lines, each characterised by a $0.03r$ level of stochasticity in A, T, and ϕ. For each time series, new values of A, T and ϕ are computed for each day of observations, independently of each other, and the specified stochasticity means that ~68% of scintle periods lie between 1.3 and 1.9 days and so forth.

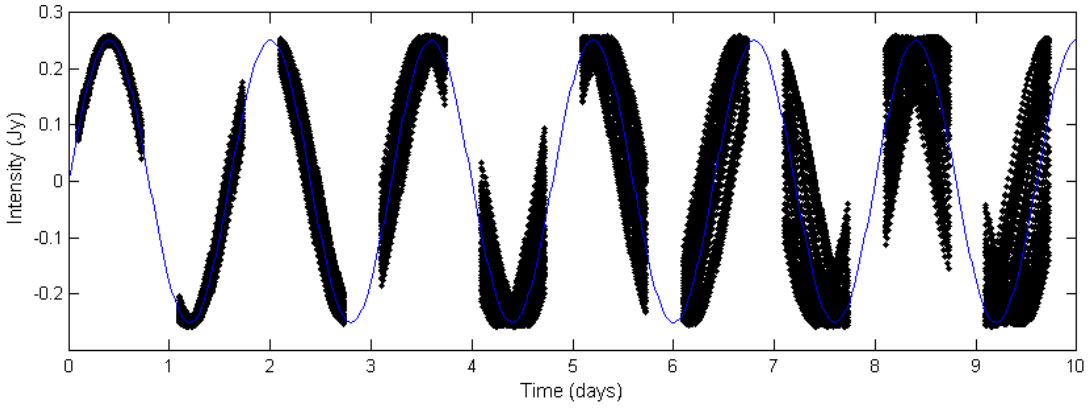

Figure 4.17 Composite plot of 50 synthetic Ceduna time series with stochastic scintle amplitudes, periods, and phases. The random variations have a 3% standard deviation from reference values of 0.25 Jy, 1.6 days, and π radians respectively.

Figure 4.18 shows the effect on the discrete ACFs and PSDs of allowing scintle amplitudes, periods, and phase shifts all to vary randomly with standard deviations up to 5% (left hand plots) and 10% (right hand plots). The time series reference values are the same as those used above . Five examples are shown, each of a time series computed with the specified degree of stochasticity. The plots show that discrete ACFs and PSDs appear generally acceptable and poorly behaved at the 5% and 10% levels of stochasticity respectively.

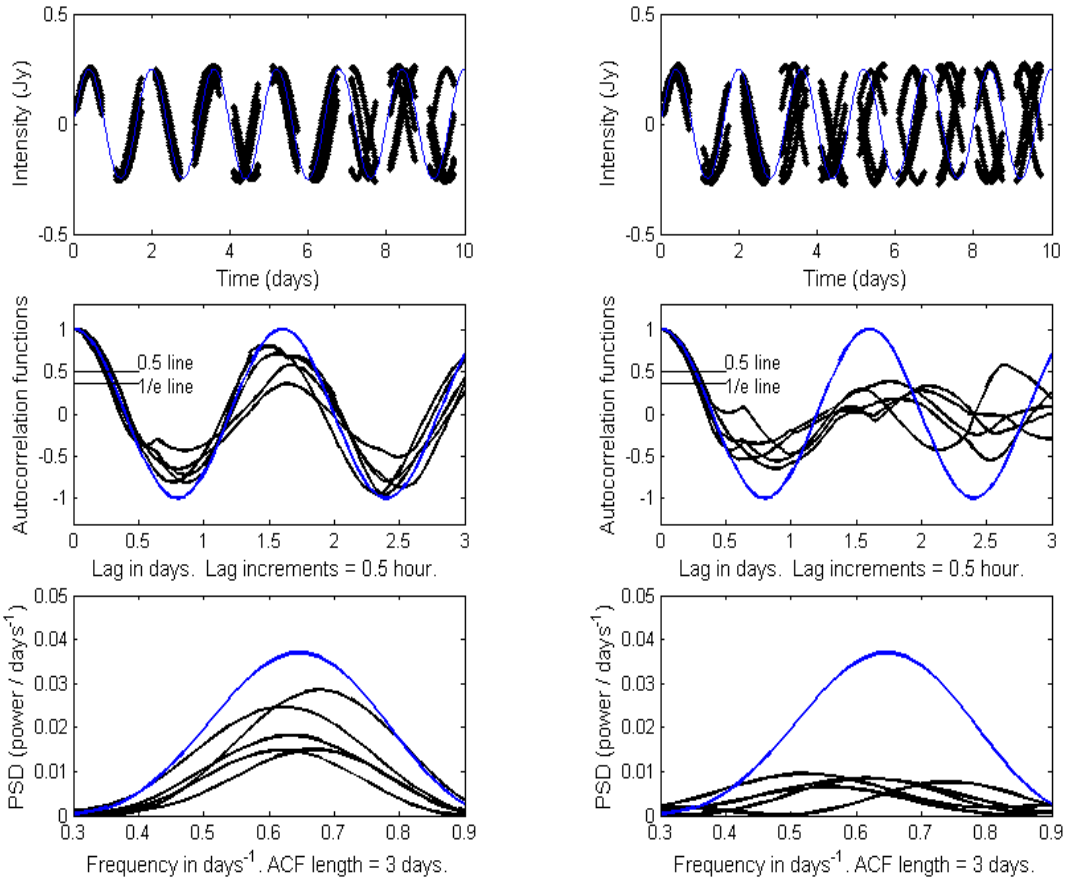

Figure 4.18 ACFs and PSDs influenced by stochasticity in the scintle amplitudes, periods, and phases, all randomly varying by up to 5% and 10% (left and right hand plot respectively) from their reference values (blue lines)

Table 4.3 presents the results of Monte Carlo simulations to quantify the extent to which stochasticity affects determination of the f_o peak by PSDs computed from synthetic Ceduna flux density data.

	5%	10%	50%
Amplitude	—	—	0.002
Period	0.086	0.242	—
Phase	0.007	0.015	—
Period & phase	0.103	0.254	—

Table 4.3 Effect of stochasticity on determination of the f_o = 0.625 days^{-1} peak. See text for explanation.

In Table 4.3, the 5%, 10%, and 50% variations measure the stochasticity in a synthetic flux density time series. As explained above, they are the standard deviations of the random scintle amplitudes, periods, and phases with respect to their reference values of 0.25 Jy, 1.6 days, and π radians.

Each result in Table 4.3 is the standard deviation of the f_o values determined from analysis of 100 flux density time series with the stated percent variation in one of these parameters, the mean of the 100 f_o values being very close to 1 / 1.6 days = 0.625 days^{-1} in all cases.

Amplitude stochasticity. Table 4.3 shows, unsurprisingly, that stochasticity in the scintle amplitudes has almost no effect on the ability of spectral analysis to accurately determine the f_o peak. The standard deviation of the 100 f_o values is low even at a 50% variation limit.

Period stochasticity. Table 4.3 also shows, again unsurprisingly, that a small degree of stochasticity in the scintle periods is sufficient to significantly influence the PSD's ability to accurately determine the f_o peak. Figure 4.19 is a composite plot of 100 PSDs with a 5% degree of stochasticity in the scintle periods, resulting in $f_o = 0.625 \pm 0.086$ days^{-1}. The blue line represents the PSD of the underlying non-random time series.

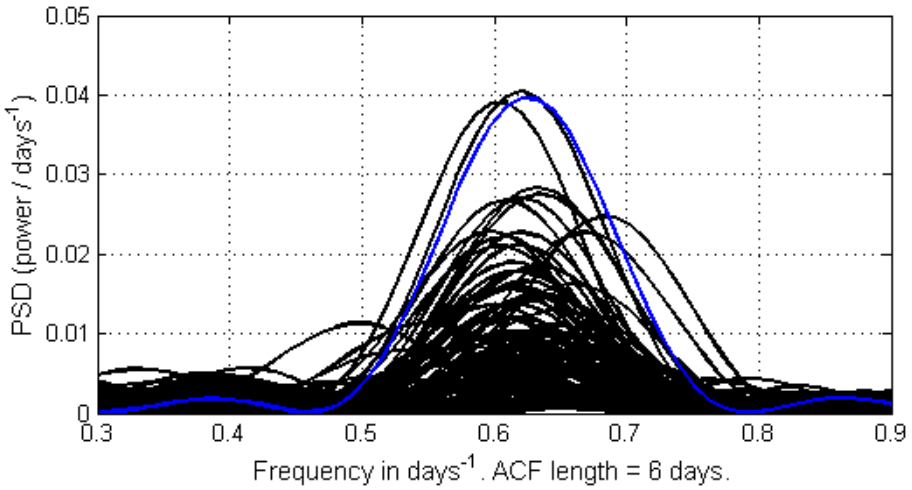

Figure 4.19 Composite plot of PSDs computed from 100 flux density time series with 5% stochasticity in the scintle periods.

Phase stochasticity. Table 4.3 shows that determination of the f_o peak is slightly sensitive to stochasticity in the phase of the scintles. However, the PSD remains a useful tool for determining the f_o peak at the 10% random variation limit.

Period and phase stochasticity. The above comments apply to stochastic effects in *individual* parameters. Table 4.3 also shows the result of allowing both the scintle period and phase to vary randomly, using a different random number for each quantity. The *combined* effect is approximately the arithmetic sum of the individual effects.

It is worth examining whether stochasticity in a flux density time series has a similar effect on the computation of $T_{char} \sim T_{0.5}$ from a discrete ACF. For a time series recorded for a source observed for only a short time each day, or for which the peak-to-peak scintle times lie close to an integral number of days, a discrete ACF may fail to properly compute $T_{0.5}$ and yet correctly identify the lag time corresponding to T_{period}, as discussed in Sections 4.4.6 and 4.4.7. Could the reverse somehow be true for a discrete ACF computed from a stochastic flux density time series?

Table 4.4 revisits the results of the 100 Monte Carlo simulations in the last line of Table 4.3, with stochasticity in both the scintle periods and phases. The results of 100 simulations at the 20% degree of dual stochasticity are also presented. In Table 4.3, each discrete ACF computed from one of the 100 stochastic time series was used to produce a PSD, and hence identify an f_o value, and the standard deviation of these 100 f_o values was reported as the result of the Monte Carlo exercise. In Table 4.4, the $T_{0.5}$ value for each discrete ACF is computed, and the standard deviation of these 100 $T_{0.5}$ values is reported as the result of the Monte Carlo exercise.

	5%	**10%**	**20%**
Period & phase	0.84 h	0.96 h	1.08 h

Table 4.4 Effect of stochasticity on determination of $T_{0.5} \approx 6.5$ hours by an ACF. See text for explanation.

The correct value of $T_{0.5}$ is ~6.40 hours, $1/6^{th}$ of the value of $T_{period} = 1.6$ days given that the synthetic scintles are sinusoidal. Considering the result of analysing the 100 time series with 5% degree of stochasticity, the value of $T_{0.5} = 6.40 \pm 0.84$ hours (Table 4.4) can be compared to $f_o = 0.625 \pm 0.103$ days^{-1} (Table 4.3). These are similar levels of uncertainty, but at higher levels of stochasticity in the time series the uncertainty (standard deviation) in a $T_{0.5}$ value does not increase as fast as the uncertainty in an f_o value.

These Monte Carlo exercises provide insight into the statistical characteristics of scintles in a real Ceduna flux density time series. The fact that Ceduna data are amenable to spectral analysis suggests that stochastic variation in scintle periods and phases observed over a 10-15 day observing period must be fairly small, although there is no such constraint on the variation in scintle amplitudes. This is found to indeed be the case. Looking ahead, scintle statistics for PKS B1622-253 and PKS B1519-273 are presented in Chapter 6, and Section 6.4.4 finds that these statistics compare favourably with the limitations on stochasticity set by the above Monte Carlo predictions.

The ACF negative overshoot

As noted in Section 4.4.2, the depth of the first negative overshoot in an ACF measures the spectral purity of the scintillation process, with smaller overshoots resulting from additional wave directions and wavelengths (Rickett et al., 2002). A large negative overshoot also corresponds to a pattern dominated by a highly anisotropic spatial scintle pattern, sampled along the short axis.

Figure 4.20 shows the effect on the first negative overshoot of discrete ACFs calculated from flux density time series with concurrent stochasticity effects in the scintle period and phase. Each data point is based on 100 Monte Carlo simulations.

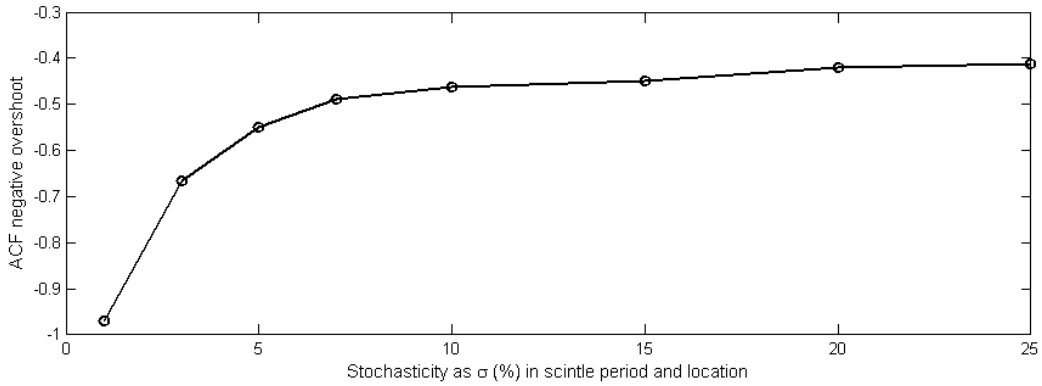

Figure 4.20 Effect of stochasticity on the mean negative overshoot.

Figure 4.20 shows that the discrete ACF negative overshoot quickly reduces from –1 to about –0.5 as the stochasticity increases to the level of ~5%, then reduces more slowly in response to further increases in stochasticity. Combining this observation with consideration of Tables 4.3 and 4.4 suggests a rule-of-thumb that if a discrete ACF negative overshoot is shallower than ~ -0.55, then the flux density time series from which the discrete ACF has been calculated may be influenced by significant stochasticity in the scintle parameters.

4.4.9 Section Summary

Ceduna flux density data are sufficiently comprehensive to enable T_{char} to be defined as T_{period} (i.e. $T_{char} \sim T_{period}$). Spectral analysis is the principal method used to determine T_{period} values, with cross-checks by scintle counting and data folding exercises.

T_{period} corresponds to the lag time of the first peak of the discrete Autocorrelation Function (ACF), and hence to the primary peak ($f_o = 1 / T_{period}$) of a Power Spectral Density function (PSD) computed from the discrete ACF by a fast Fourier transform. Sections 4.4.2 and 4.4.3 describe the calculation of the discrete ACF and the PSD respectively, illustrated by application to case study data (PKS B1144-379 observing period 4).

Section 4.4.4 examines the effects of noise and spectral leakage on the PSD. The signal-to-noise ratio typical of Ceduna data is well above the level at which a PSD is expected to clearly detect the signal. Spectral leakage due to aliasing is not a problem, since a typical discrete ACF calculation uses a bin size of 4 hours, giving a Nyquist frequency of 3 $days^{-1}$, well above the highest flux density variability frequency of interest (about 1 day^{-1}). Leakage due to the finite length of the discrete ACF determines the width of the central PSD peak, and produces secondary peaks adjacent to the central peak.

Sections 4.4.5 and 4.4.6 examine the effect of daily gaps in the recorded flux density time series on calculation of the discrete ACF, and the PSD obtained from the discrete ACF. Section 4.4.5 shows that the effect of daily data gaps is usually minor, but Section 4.4.6 shows that a problem arises if the period T_{obs} over which a source can be observed is shorter than the period T_{unobs} during which it is unobserved, which will happen if a source is sufficiently far north of the zenith at Ceduna (see Section 3.6). In this case, the discrete ACF computation will find no data pairs at lag times between T_{obs} and T_{unobs}, nor during this period every 24 hours thereafter. This situation fortunately does not arise for the sources of interest to the present research.

Section 4.4.7 shows that a Ceduna time series whose characteristic scintle peak-to-peak time (i.e. T_{period}) lies near an integral number of days also causes difficulties in the computation of a discrete ACF. In particular, the discrete ACF displays erratic behaviour as it falls away from its zero lag value, such that characteristic variability time scale definitions which rely on this portion of the discrete ACF, notably $T_{\mathrm{char}} \sim T_{0.5}$ and $T_{\mathrm{char}} \sim T_{1/e}$ (see Section 4.4.1) should be avoided. However, the discrete ACF performs better in determining T_{period}, which is thus a strong reason for an analysis of Ceduna data to define the characteristic variability as $T_{\mathrm{char}} \sim T_{\mathrm{period}}$.

Section 4.4.8 examines the effect of stochasticity in a flux density time series, using Monte Carlo simulations based on synthetic Ceduna data. The principal conclusion is that a small degree of stochasticity in the scintle periods is sufficient to significantly influence the PSD's ability to accurately determine the f_o peak, and to a lesser extent the spectral analysis is also affected by stochasticity in the scintle phases. Stochasticity is measured as the standard deviation of the scintle periods recorded over the course of an observing period with respect to the mean period (T_{period}). The Monte Carlo simulations conclude that the PSD will have difficulty in determining a $T_{\mathrm{char}} \sim T_{\mathrm{period}} = 1 / f_o$ if the stochasticity in the scintle periods recorded in an observing period is greater than about 5% of T_{period}. This conclusion is confirmed in Chapter 6.

4.5 Data Filtering to Remove Fast and Slow Variations

4.5.1 Nature of the Problems

a) *Short time scale systematic fluctuations.* As discussed in more detail in Chapter 5, the data recorded in the Ceduna monitoring campaign through to early 2005 contain systematic fluctuations which are most pronounced on time scales on the order of a few hours. For a discrete ACF computed at typical lag intervals of 4 hours, the highest variability frequency that can be identified is 3 days^{-1}, some three times higher than the ~1 days^{-1} frequency limit imposed by the presence of systematic fluctuations on diurnal time scales.

It seems clear that the systematic fluctuations have a thermal origin, and result from changes in the ambient temperature, but at the time of finalising this thesis, the problem has not been resolved at a telescope operational level and efforts to develop a data processing procedure to remove the fluctuations have not been successful (see Section 5.6).

The systematic fluctuations are present in the PKS B1144-379 observing period 4 data used in this chapter to illustrate scintle counting, data folding and spectral analysis methods of estimating $T_{\rm char} \sim T_{\rm period}$. However, the true variability signal in this data set is quite strong, (see Figure 4.1), and a $T_{\rm period}$ value of just over 2 days is sufficiently long that the systematic diurnal fluctuations can be ignored without significantly influencing the analysis results.

Nevertheless, the systematic fluctuations are a nuisance that can hinder a variability analysis by obscuring a scintle counting exercise, introducing spurious high-frequency PSD peaks, and producing minor irregularities in data folding plots.

b) *Weekly time scale systematic fluctuations.* The calibrator flux densities vary slightly, usually by less than 4%, over the course of an observing period. These variations are largely systematic in nature, and are believed to be a manifestation of the thermally induced systematic fluctuations discussed above, due to the passage of weather systems. Synoptic time scales are similar to the variability time scales of the blazars monitored by Ceduna, and it is thus necessary to use the calibrator flux density data to correct the blazar flux density data in a refined manner: a bulk correction factor for each observing period is not sufficient.

c) *Long time scale flux density trends.* All the blazar flux density time series recorded by Ceduna exhibit significant changes over periods of months to years, presumably due to processes intrinsic to the source. The flux density thus typically changes over an observing period in a fairly steady fashion, and introduces a low frequency PSD peak which roughly corresponds to the length of the observing period. This peak can be quite strong, making it difficult for spectral analysis to identify variations on the order of several days.

4.5.2 Data Filtering

After consultation, the author decided to address the problems described in the previous section by filtering the data in the time domain. High and low pass filtering in the frequency domain could remove the fast systematic fluctuations and the flux density trends over the observing period respectively. However, time domain filtering facilitates removal of the small systematic flux density variations on time scales of days, using concurrent calibrator data. Emeritus Professor Peter McCulluch (University of Tasmania) favoured the time domain filtering option because it enabled visual inspection of the process, which is always reassuring when dealing with the processing of data from an initial observing campaign.

Step 1. Smooth the diurnal data fluctuations with polynomial

A polynomial fitted to the data for a given observing period enables the systematic diurnal fluctuations to be smoothed out, leaving slower fluctuations on the order of several days. Polynomial fits are notoriously bad near the start and end of the data to which they are applied, so a strategy was developed by the author whereby the smoothing polynomial is fitted to an *extended* data set in which the first and last days of data are repeated:

Extended data for an M-day observing period = {day 1 + days 1 to M + day M}

A polynomial of too low an order will over-smooth the data, failing to capture the longer term variations that are of interest, while a polynomial of too high an order will follow the unwanted faster variations. For data from an observing period of M = 10-15 days duration, a polynomial of order M+5 produces an acceptable fit to the M+2 days of data.

In practice, the success of the polynomial filter is not too sensitive to its order, so long as it is close to order M+5. The reason is shown in Figure 4.21, which plots the sum-square error between PKS B1622-253 data from observing period 10, and the fitting polynomial as a function of the polynomial order.

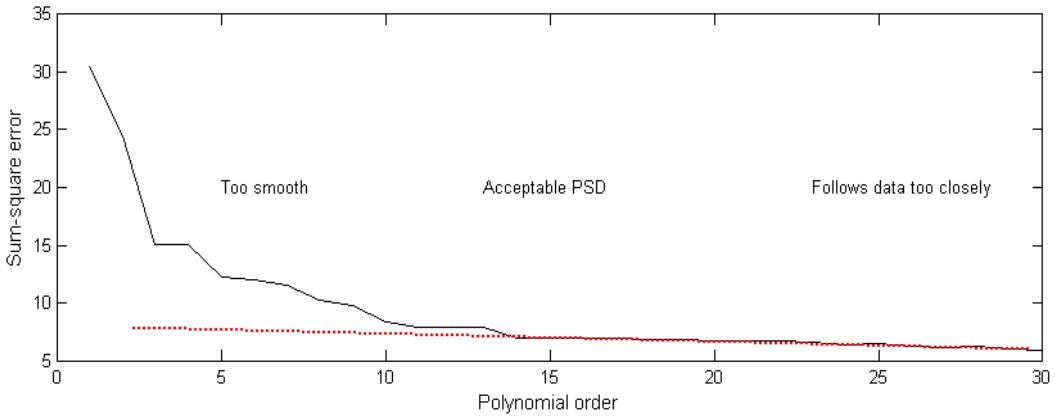

Figure 4.21 Sum-square error for various polynomial fits to PKS B1622-253 data. The red dashed line highlights the gradual error reduction as high order polynomials start to follow diurnal flux density variations.

Figure 4.21 shows a rapid decrease in the sum-square error with increasing polynomial order, signifying progressively better fits smoothing through the daily means of the data. The dashed red line shows that additional reductions in the sum-square error are gradually achieved by progressively higher order polynomials starting to follow the diurnal variations. Observing period 10 has 12 days of data, so a 17th order filtering polynomial is specified by the M+5 prescription. Figure 4.21 shows that a polynomial of order much greater than 17 would be needed for a polynomial fit to start to follow the diurnal variations.

Importantly, overfitting is not a problem because the only polynomial values used are those computed at times corresponding to actual data. Overfitting occurs when a polynomial used to fit a set of data points produces the required values at those points, but varies wildly and incorrectly between the data points, which can happen when the polynomial order is higher than necessary, for example if a 10th order polynomial is used to model cubic variations.

A smoothed data set, $x_{\text{smooth}}^{\text{Data}}$, is obtained by evaluating the polynomial fitted through the data, x^{Data}, at the times associated with each data point (ignoring the repeated first and last days of data that were added to ensure the polynomial was well behaved).

$$x^{Data} \xrightarrow{M+5 \text{ polynomial}} x_{\text{smooth}}^{\text{Data}}$$

Step 2. Apply calibrator correction to the smoothed data set

The calibrator data are fitted with a (different) polynomial of the same order, M+5, which describes the minor fluctuations on time scales of days. This enables correction of the smoothed blazar data set, $x_{\text{smooth}}^{\text{Data}}$:

$$x_{\text{smooth}}^{\text{Data}} = \left(\frac{\text{Calibrator flux density}}{x_{\text{smooth}}^{\text{Calibrator}}} \right) x_{\text{smooth}}^{\text{Data}}$$

where the $x_{\text{smooth}}^{\text{Calibrator}}$ values are obtained by evaluating the calibrator polynomial at the same times as the $x_{\text{smooth}}^{\text{Data}}$ values.

Step 3. Remove long term flux density trends and convert to a zero-mean data set

Next, the smoothed data set, $x_{\text{smooth}}^{\text{Data}}$, is fitted by a low order polynomial to remove any flux density trend over the observing period. Any such trend is associated with intrinsic changes in the blazar's emissions over time scales of weeks to months and, as noted in the previous section, needs to be removed to avoid a low frequency PSD peak. The polynomial must be low order to avoid following the genuine scintles in $x_{\text{smooth}}^{\text{Data}}$.

Figure 4.22 shows the different PSDs for PKS B1622-253 observing periods 10 and 12, that result from specifying 1st to 4th order polynomials. the different order polynomials produce principal PSD peaks that range from 0.20 to 0.23 days^{-1} and 0.13 to 0.15 days^{-1} in observing periods 10 and 12 respectively.

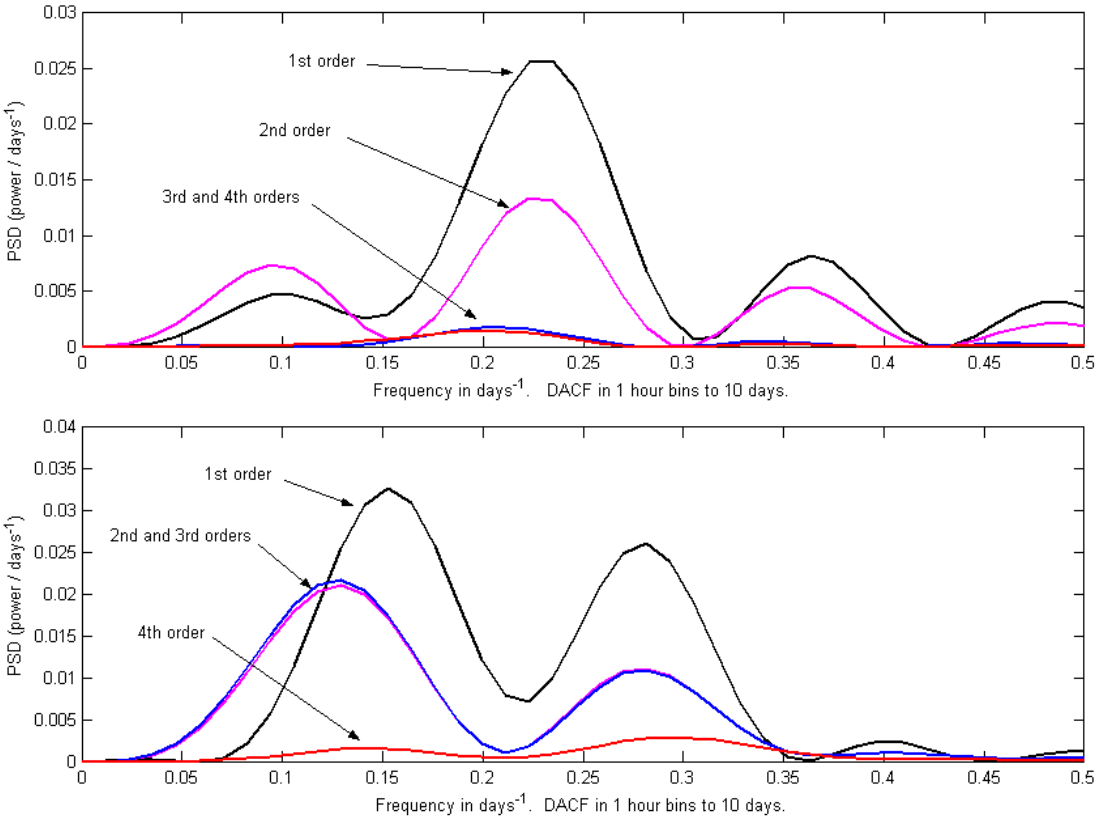

Figure 4.22 PSDs for PKS B1622-253 zero-mean data for observing periods 10 (top) and 12 (bottom), using various low-order polynomials.

Removing a flux density trend over an observing period of 10-15 days rarely requires more that a linear polynomial, and this has been adopted as a general rule for the present research. The few exceptions are identified in the data processing plots (see Chapter 6).

Evaluating the low order polynomial at the times associated with each data point gives values $x_{\text{trend}}^{\text{Data}}$ which enable a zero-trend smoothed data set to be produced:

$$x_{\text{zero}}^{\text{Data}} = x_{\text{smooth}}^{\text{Data}} - x_{\text{trend}}^{\text{Data}}$$

The $x_{\text{zero}}^{\text{Data}}$ data set contains the genuine flux density fluctuations with respect to a zero mean that vary on time scales greater than a day. It is the basis for analysis of the Ceduna data considered by this research.

The diurnal fluctuations

Subtraction of the smoothed data set, $x_{\text{smooth}}^{\text{Data}}$, (after the Step 2 correction) from the original data from which it was derived, x^{Data}, produces a data set, $x_{\text{zero}}^{\text{Fast}}$, that contains fluctuations that vary on diurnal time scales.

$$x_{\text{zero}}^{\text{Fast}} = x^{\text{Data}} - x_{\text{smooth}}^{\text{Data}}$$

In Chapter 5, the $x_{\text{zero}}^{\text{Fast}}$ data sets of the two calibrator sources are compared to the $x_{\text{zero}}^{\text{Fast}}$ data sets of PKS B1622-253 and PKS B1519-273, the blazars considered by the present research. It is found that the $x_{\text{zero}}^{\text{Fast}}$ data sets of both blazars are dominated by systematic fluctuations, with little or no sign of real variability. The analysis of variability in the flux densities of these two sources can thus be based on $x_{\text{smooth}}^{\text{Data}}$, and the $x_{\text{zero}}^{\text{Fast}}$ data sets can be discarded. However, when a procedure is developed to avoid or correct for these systematic variations, the Ceduna program should be able to monitor variability on time scales of less than a day.

Example: PKS B1144-379 data

Figure 4.23 shows the above data processing procedure applied to PKS B1144-379 data from observing period 4. For this source, the short term fluctuations (bottom plot) appear to show quite different time scales, and may include some genuine variability in addition to systematic fluctuations.

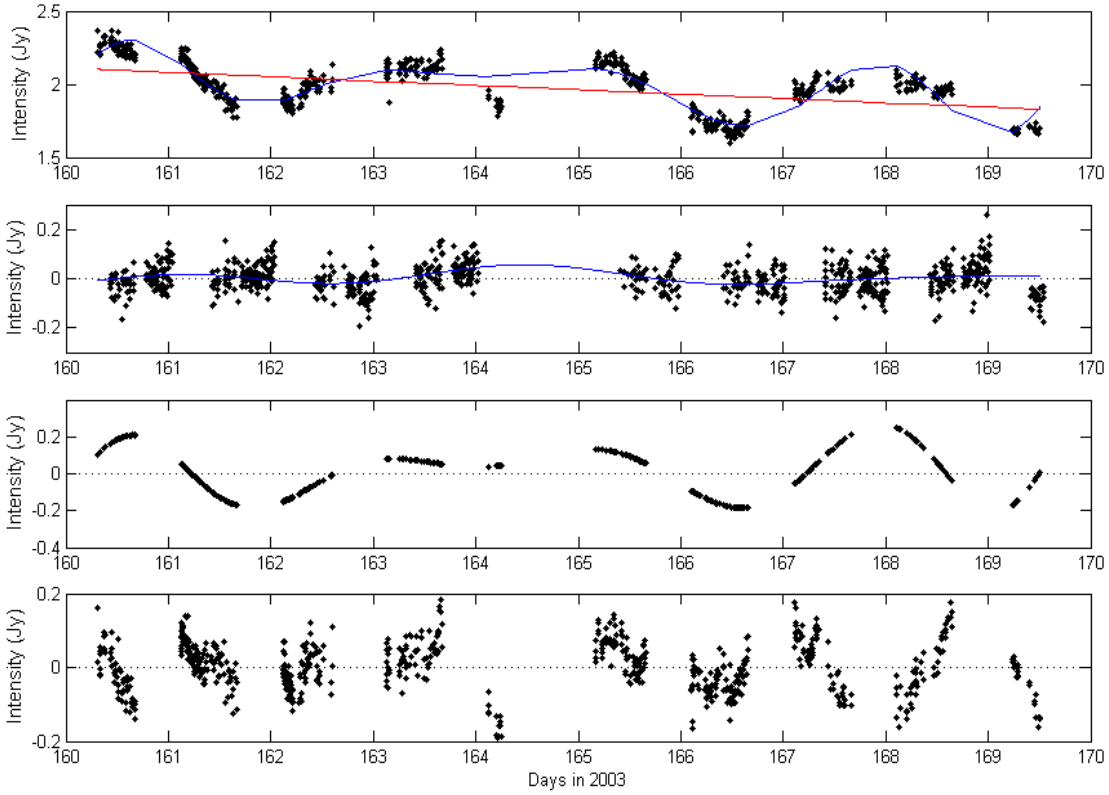

Figure 4.23 Processing of PKS B1144-379 data for observing period 4. Details are discussed in the text.

- The top plot shows the flux density data, x^{Data}, and the M+5 = 14$^{\text{th}}$ order smoothing polynomial (blue line) that produces the $x^{\text{Data}}_{\text{smooth}}$ data set (Step 1). The plot also shows the linear polynomial (red line) that produces the $x^{\text{Data}}_{\text{trend}}$ data trend set.
- The next plot shows the zero-mean PKS B1934-638 calibrator data, and a (different) 14$^{\text{th}}$ order polynomial through these data, which produces the $x^{\text{Calibrator}}_{\text{smooth}}$ data set.
- The third plot shows the $x^{\text{Data}}_{\text{zero}}$ data set evaluated at the times associated with the x^{Data} data points. The $x^{\text{Data}}_{\text{zero}}$ data set is the basis for variability analysis. It is produced by using the $x^{\text{Calibrator}}_{\text{smooth}}$ data set to correct for fluctuations in the calibrator data (Step 2), and using the $x^{\text{Data}}_{\text{trend}}$ data set to remove the flux density trend in the x^{Data} data set (Step 3).
- The bottom plot shows the $x^{\text{Fast}}_{\text{zero}}$ data set containing the fast (diurnal) signal component that is dominated by systematic fluctuations.

It is worth emphasising that fluctuations in the PKS B1934-638 calibrator data *are* minor. On time scales long than a day, the $x^{\text{Data}}_{\text{smooth}}$ data set fluctuations are ± 0.2 Jy, while the $x^{\text{Calibrator}}_{\text{smooth}}$ data set fluctuations are about 1/10$^{\text{th}}$ the size.

4.6 ISS Process Simulations

This section responds to concerns raised by peer reviews of the data filtering and analysis methods set out in this chapter.

Polynomial filters and spectral analysis

One concern that has been raised is that the polynomials are used to represent the Interstellar Scintillation (ISS) process, such that data analysis is performed on pseudo-data constructed from a polynomial fit to the data. This concern is invalid: the two polynomials are simply low-pass and high-pass filters. The low-pass polynomial smooths through the diurnal flux density fluctuations, and the existing data points are adjusted to accord with the smoothing process. This removes fluctuations on time scales of less than a day, and no additional data points are created from the polynomial. Chapter 5 shows that all the genuine variability of the two blazars studied by this research occurs on time scales longer than a day.

The high-pass polynomial, usually just a straight line, removes flux density trends across the observing period that would otherwise produce a low frequency peak in the PSD.

Neither filtering polynomial is used to represent the ISS process. The filtered time series presented to the spectral analysis is silent on the nature of the ISS process during times when the source is unobserved. The spectral analysis methods to identify the characteristic variability timescale (computing the discrete ACF and PSD) are standard practice.

A time domain approach to filtering was used instead of a frequency domain approach, because Emeritus Professor Peter McCulloch recommended that the filtering process be subject to visual scrutiny given that the characteristics of the Ceduna flux density time series were not well understood in the early days of the blazar monitoring campaign.

Data folding and scintle counting

A second concern is that data folding is only formally appropriate for a periodic process, while the idea of a scintle is poorly defined, so neither the data folding nor the scintle counting methods are reliable ways of assessing variability. This concern is valid to an extent, but data folding and scintle counting are only used as cross-checks on the spectral analysis. Both techniques are widely used because they usually work quite well, since the ISS process is indeed quasi-periodic to a first approximation, as shown below.

ISS time series simulation

As discussed in Chapter 2, turbulence causes electron density fluctuations in the interstellar medium, which scatter blazar radio emissions and produce random phase fluctuations in the radio wave front at distance D from the scattering material. If an isotropic Kolmogorov turbulence spectrum is assumed, then in the weak scattering régime the random phase fluctuations are small on spatial scales comparable to the Fresnel scale, $(\lambda D)^{0.5}$, where λ is the radio wavelength.

Chapter 2 discusses the theoretical power spectrum with ISS viewed as a stationary random process. The weak scattering ISS time series is expected to be a random process with a power law spectrum above a cut-off frequency, high passed by the Fresnel filter. Software to simulate the weak scattering ISS process was kindly provided by PhD candidate Jamie McCallum. It produces the power spectrum of isotropic spatial fluctuations in the weak scattering régime from equation 3.2 of Narayan (1992), convolves this spectrum with a random phase sequence, and then Fourier transforms the result to the time domain. Figure 4.24 shows a typical ISS time series produced by this software. It is only an approximation to the true two-dimensional ISS process, but shows that the band-limited time series is a much closer representation of the ISS process than a sinusoid. The time scale is arbitrary, since it depends on the relative speed of the Earth with respect to the scattering material. The flux density scale has been set to be typical of the blazars observed by Ceduna.

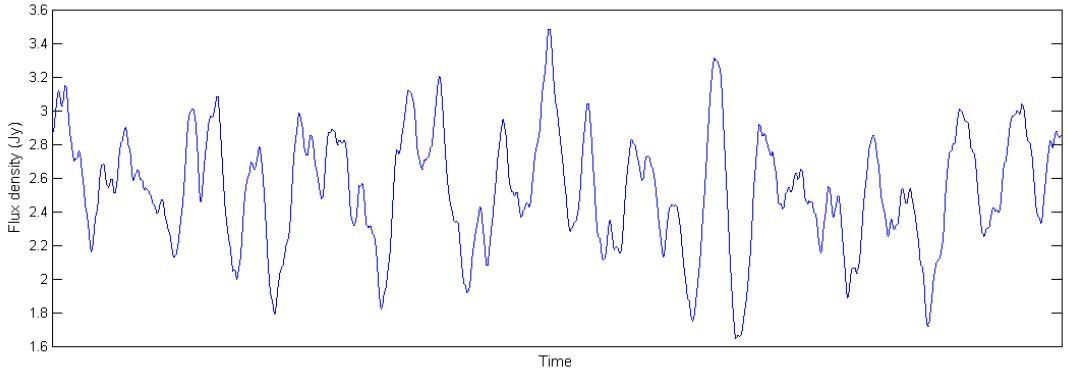

Figure 4.24 Simulated ISS time series due to weak scattering.

Data processing methods

Simulated ISS data corresponding to the Ceduna time series are obtained by windowing out data during the daily source observing times, at 20 minute intervals, and adjusting the time scale to produce fluctuations similar to those recorded by Ceduna. Figure 4.25 shows the results of this exercise for a 9 h daily observing period, and the good agreement between the ~0.37 day^{-1} PSDs for a) the complete simulated ISS time series; b) the time series portion observed at Ceduna; and c) the slow component of the time series, obtained by data filtering.

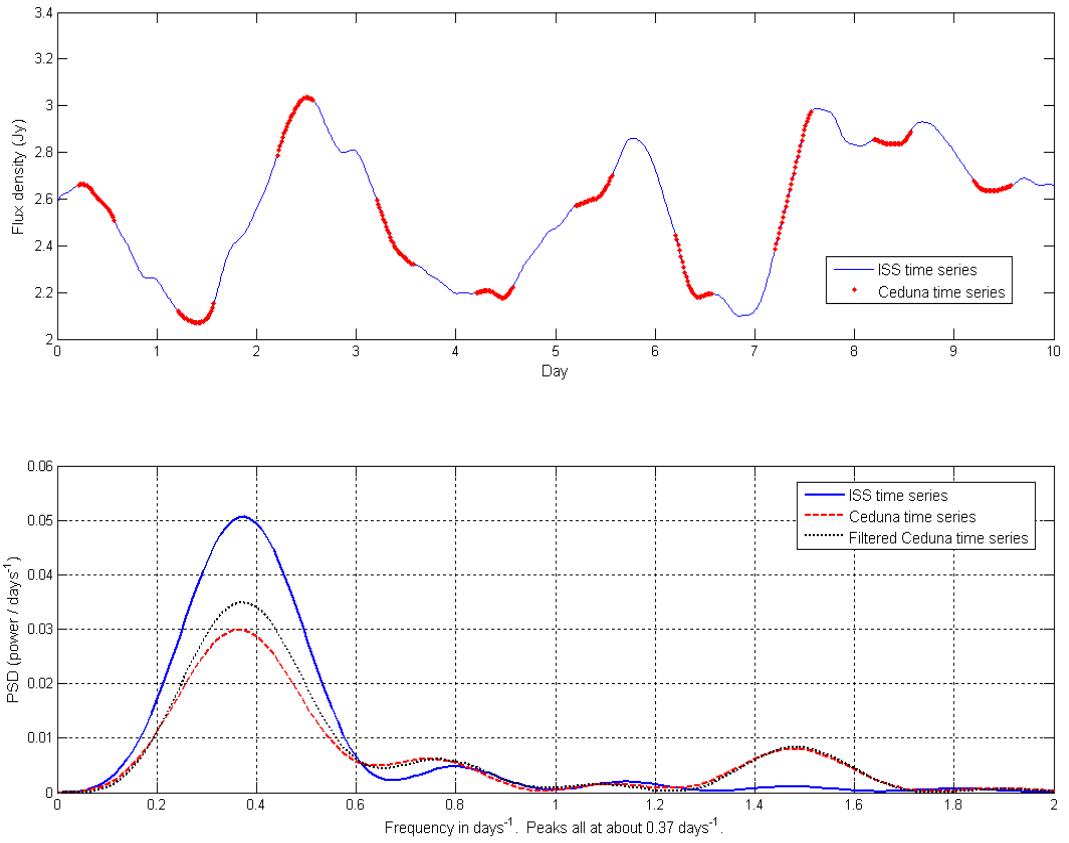

Figure 4.25 Top: Simulated ISS data for a typical 10 day observing period. Bottom: PSDs computed from the simulated data (see text)

In Figure 4.25, the complete ISS time series has a mean strength of ~2.5 Jy, and an RMS of ~0.14 Jy, typical of PKS B1519-273 and PKS B1622-253 (see Section 7.7). The PSDs of the Ceduna time series and the filtered Ceduna time series both have secondary (and almost identical) peaks at ~1.5 days^{-1}, due to the sampling window. This secondary peak is absent from the PSD of the complete ISS time series.

Figure 4.26 shows the separation of the time series into slow and fast components by the two filtering polynomials. For these simulated ISS data, there is no need to apply corrections based on calibrator observations.

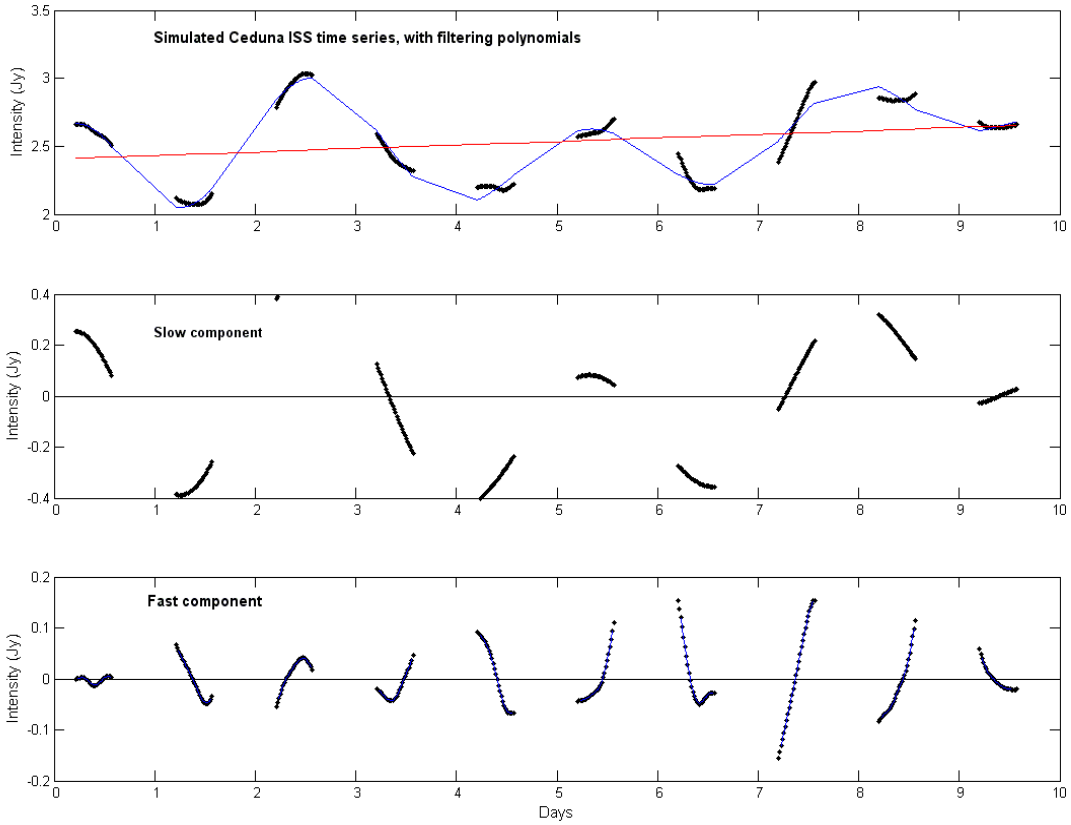

Figure 4.26 Data filtering of the simulated Ceduna ISS time series.

In Figure 4.26, the slow time series component is used to produce the "Filtered Ceduna time series" PSD in Figure 4.25. This component is used for the spectral analysis in the present research because PKS B1519-273 and PKS B1622-253 have little or no genuine variability on diurnal timescales, and the PSD is messy unless the data are low-pass filtered. However, the ISS simulation leads to the expectation that at least some genuine variability should be present on diurnal time scales. If so, then in the case of these two blazars it is presumably dominated by the systematic fluctuations. However, comparison of the PSDs in Figure 4.25 shows that the smoothing process has not significantly affected the conclusions of the spectral analysis, which firmly indicates that the characteristic variability peak-to-peak time scale is on the order of 2-3 days, irrespective of the presence of some faster fluctuations.

The next question is the extent to which the quasi-sinusoidal time series assumption that underpins data folding and scintle counting is valid. Figure 4.27 shows the results of a data folding exercise applied to the filtered Ceduna time series (i.e. the slow component), which agrees with, and hence cross-checks, the ~0.37 day^{-1} variability frequency estimated by the PSD. Similarly, the slow component of the filtered time series has 2.5 scintles between the flux density troughs near day 1, and the peak near day 8, which gives a scintle counting cross-check of ~0.36 day^{-1}.

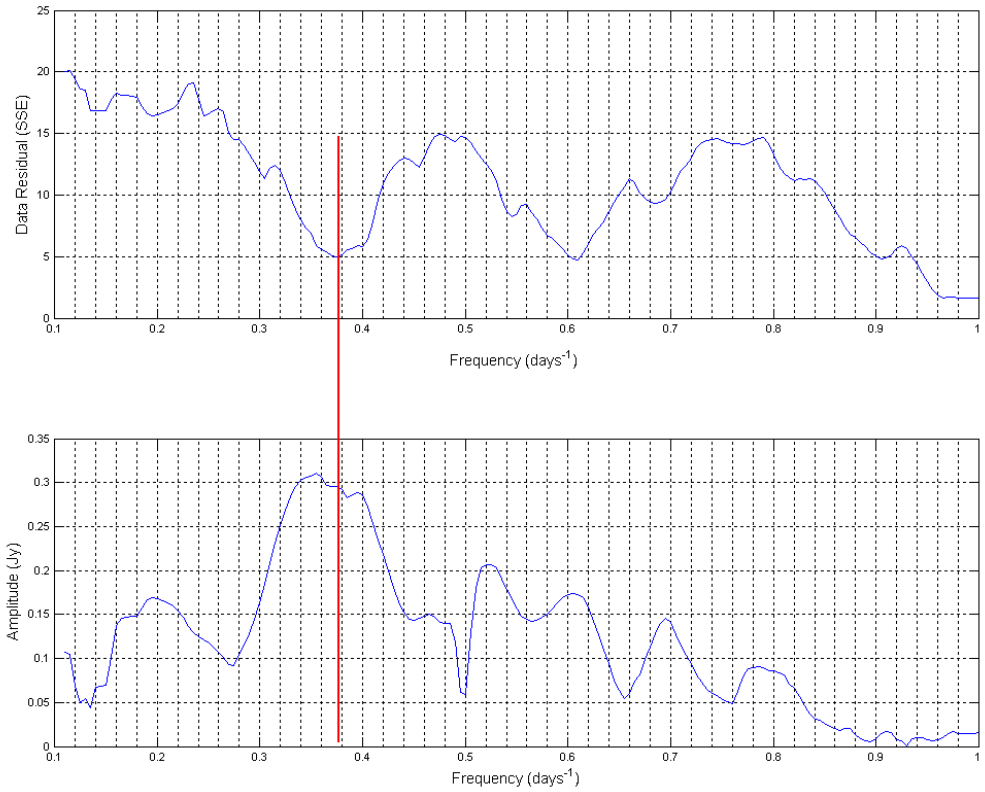

Figure 4.27 Data folding of the filtered simulated Ceduna time series. The variability frequency of ~0.38 days^{-1} cross-checks the spectral analysis estimate.

Variability of simulations

The sampling window applied to the complete ISS time series is only 9 hours long in the simulation exercise presented above, whereas the observing times for PKS B1519-273 and PKS B1622-253 are significantly longer: about 13 h and 12.5 h respectively (see Table 3.5). Even better agreement between the PSDs of the complete ISS time series and the sampled time series is expected for these longer sampling windows.

A number of ISS simulated time series were examined and, unsurprisingly, not all enjoyed such good agreement as the above example between spectral analysis of the complete ISS simulated data, and spectral analyses of both the portion of the time series corresponding to Ceduna observations, and the filtered times series. Figure 4.28 shows an example of a such a simulated time series.

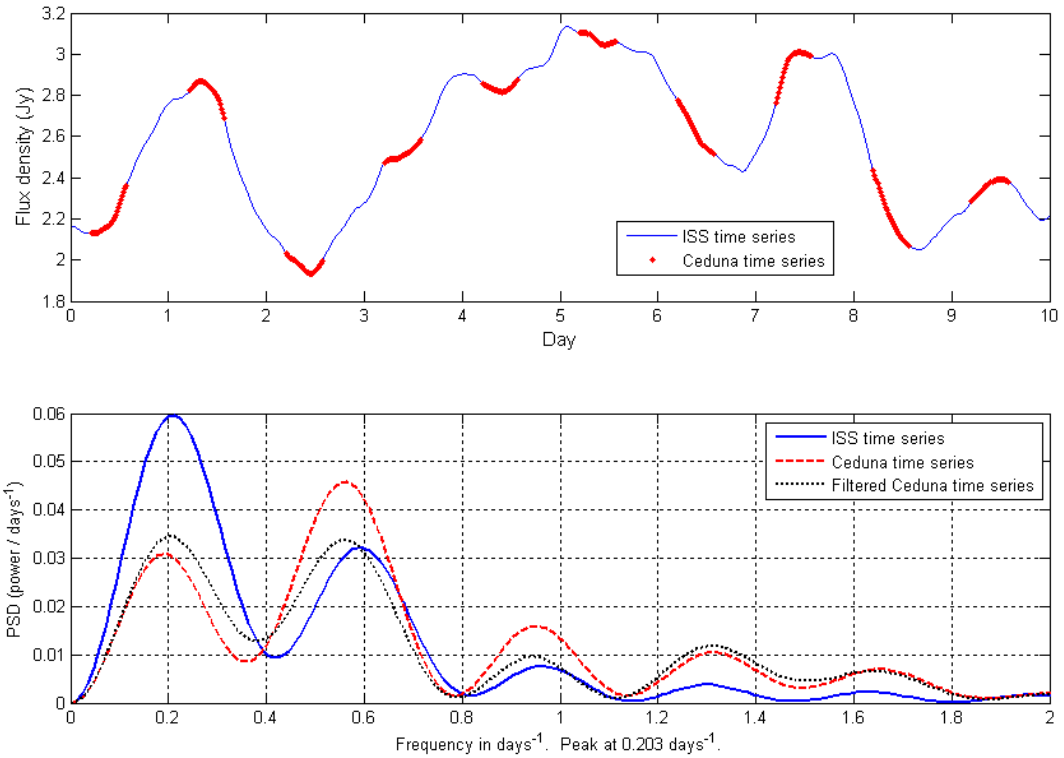

Figure 4.28 Example of a simulated ISS data time series with noticeable differences between the PSDs of the complete time series, the Ceduna time series for a 9h daily observing period, and the filtered Ceduna time series.

The simulated data and PSDs shown in Figure 4.28 are similar to, for example, the actual data and PSDs for observing period 12 of PKS B1622-253, the plots of which are presented in the appendices.

Nevertheless, it is firmly concluded that the data processing and analysis methods applied in this research are usually able to correctly and unambiguously estimate the characteristic variability time scale of simulated ISS time series similar to the time series associated with Ceduna observations of PKS B1622-253 and PKS B1519-273.

Minor fluctuations

One interesting characteristic of the simulated ISS data is the presence of minor fluctuations in the simulated flux density time series. Section 6.3.4 discusses these small fluctuations and their interpretation when analysing PKS B1519-273 and PKS B1622-253 data.

The simulated ISS time series presented above clearly and unambiguously supported both the data filtering approach, and the data analysis tools applied to the filtered time series. The quasi-sinusoidality assumption that underpins the present version of the data folding method is strictly only valid in the case of extreme anisotropy sampled perpendicular to the long axis (and assuming an isotropic source structure), but data folding has proven that it can usually provide a cross-check on the spectral analysis results.

4.7 Intensity Modulation Index

The modulation index, *m,* is defined as $m = I_{\text{rms}}^{\text{Var}} / I_{\text{mean}}^{\text{Var}}$, where $I_{\text{rms}}^{\text{Var}}$ and $I_{\text{mean}}^{\text{Var}}$ are the RMS and mean values respectively of the variable component of the flux density time series.

RMS estimation

A flux density time series recorded over an observing period has a total RMS, I_{rms}, which has one component due to genuine flux density variability, $I_{\text{rms}}^{\text{Var}}$, and a second component due to measurement errors, $I_{\text{rms}}^{\text{Obs}}$.

The RMS component due to measurement errors, $I_{\text{rms}}^{\text{Obs}}$, in turn has two components. One is assumed to be the same value as the RMS of a calibrator with the same mean flux density, I_{mean}, as the blazar over the observing period. The other component is associated with any flux density trend across the observing period.

Consider data for PKS B1144-379 observing period 4, our example throughout this chapter. Its x^{Data} data set has I_{mean} = 1.991 Jy and I_{rms} ≈162 mJy.

From Section 5.3, a calibrator of strength 1.991 Jy would have an RMS value of:

$$I_{\text{rms}}^{\text{Cal}}\,(\text{mJy}) \approx \sqrt{\left[12.28\, I_{\text{mean}}\,(\text{Jy})\right]^2 + (29)^2} \;= 38 \text{ mJy}.$$

Independent RMS components add in quadrature, so:

$$(I_{rms})^2 = (162)^2 = (I_{rms}^{Var})^2 + (I_{rms}^{Obs})^2$$

If the approximation $I_{\text{rms}}^{\text{Obs}} \approx I_{\text{rms}}^{\text{Cal}} = 38$ mJy is made, then $I_{\text{rms}}^{\text{Var}}$ for the PKS B1144-379 data set is expected to be 158 mJy. This agrees well with the measured RMS of 148 mJy for the $x_{\text{smooth}}^{\text{Data}}$ data set. The true value of $I_{\text{rms}}^{\text{Var}} \approx 127$ mJy is that of the $x_{\text{zero}}^{\text{Data}}$ zero-mean flux density data set, which has no flux density trend across the observing period.

An RMS value can be computed directly from a flux density data set, since it is simply the standard deviation of the data. Alternatively, if the noise is uncorrelated between adjacent time steps, Δ t, then the correlation function will give a good estimate of the RMS value.

$$(RMS)^2 = \langle \Delta I(t)\, \Delta I(t + \Delta t) \rangle$$

Mean strength estimation

The total mean blazar flux density, I_{mean} (1.991 Jy for PKS B1144-379 observing period 4) in general has two components: $I_{\text{mean}} = I_{\text{mean}}^{\text{Constant}} + I_{\text{mean}}^{\text{Var}}$.

$I_{\text{mean}}^{\text{Constant}}$ is the component of the mean flux density which is associated with source emissions that are steady over the observing period, and from a source region which is too large for the interstellar medium to cause its emissions to scintillate. $I_{\text{mean}}^{\text{Var}}$ is the component of the mean flux density associated with emissions from a smaller source region whose emissions are intrinsically variable, or are caused to scintillate by the interstellar medium, or both.

Rickett et al. (1995) applied a two-component scintillation model to B0917+624. Their motivation was to explain an observed anti-correlation of total and polarised flux densities, but although sources such as PKS B1519-273 are known to be strongly polarised (Macquart et al., 2000), examination of polarised flux densities is beyond the Ceduna telescope, at least at present.

Estimating $I_{\text{mean}}^{\text{Var}}$ is difficult. However, if it can be established that the variability is due to interstellar scintillation, then the theory presented in Chapter 2 enables $I_{\text{mean}}^{\text{Var}}$ to be estimated from $I_{\text{rms}}^{\text{Var}}$ if the scattering régime is known.

Modulation index estimation

There are two methods of estimating the modulation index, *m,* which from above is defined as $m = I_{\text{rms}}^{\text{Var}} / I_{\text{mean}}^{\text{Var}}$. The first method is to use the $I_{\text{rms}}^{\text{Var}}$ and $I_{\text{mean}}^{\text{Var}}$ estimates described above.

The second method, discussed in Section 4.4.2, is to estimate *m* from the autocorrelation function (ACF), normalised by I_{mean}^2, as $m = \sqrt{R_I(0)}$. Since the ACF at zero lag, $R_I(0)$, is contaminated by noise, a better expression might be $m = \sqrt{\lim R_I(\Delta t \to 0)}$, where the limit operation is designed to remove the noise spike.

In the case of the PKS B1144-379 data, if it assumed that $I_{\text{mean}}^{\text{Constant}}$=0, then the two estimates of the modulation index are $m \approx 0.127 / 1.991 = 0.06$ and $m \approx \sqrt{0.00423} = 0.07$ (the value of $m = 0.08$ given in Section 4.4.2 was from the ACF of all the data, not the smoothed zero-trend data). The two methods yield slightly different results, since the discrete ACF method of Edelson & Krolik (1988) used for Ceduna data involves a binning operation, and for this reason the direct calculation approach is favoured in the case of Ceduna data.

5.0 TELESCOPE PERFORMANCE

5.1 Operational Experience

The Ceduna telescope's operation is checked daily by a radio astronomer in Hobart, and the FITS file for each day's observing is transferred to Hobart for data processing and analysis. A perl script monitors the telescope's operation, enabling automatic recovery from common problems such as power cuts, and issuing an alert if a problem persists. Human intervention is seldom required more often than twice a month.

The most common problem early in the COSMIC program was the sampler computer requiring a re-boot and the follow-on need to restart the telescope operating software, Bruce. A supervising program, SmartBruce, was subsequently written by Dr Simon Ellingsen to detect this problem and respond to it.

Maintenance — The telescope required only occasional maintenance through to early 2005, although a visit was made in late 2003 to address several minor mechanical problems. The worst problem was failure of a back-end amplifier in January 2004, which resulted in data only being gathered on one channel during southern source observing period 12. The data processing software was adjusted to take this into account, but the RMS of data recorded during this period was increased by a factor of $\sqrt{2}$.

Weather — Extreme weather occasionally affected telescope operation, notably during the summer months when the region suffers dust storms and bushfires. The Ceduna weather station near the coast recorded wind gusts of 80 km/h in December 2003, and a record temperature of 47°C in February 2004, with high humidity. The telescope is located about 35 km inland from the coast, away from the ocean's moderating influence, and during hot weather the operating environment of some equipment can exceed 50°C. In particular, a period of poor quality data recorded in mid-2004 is associated with extreme weather.

Power cuts — Power cuts affect almost all observing periods. These interruptions usually last only minutes or hours, but in the early part of the monitoring campaign could require a remote operator to assist the telescope's recovery. In early 2004, the telescope operating software and perl script noted above were refined by Dr Ellingsen to enable better recovery from such interruptions.

Ceduna performed well overall during 2003. Data quality was generally lower in 2004 than in 2003, although there were several periods of successful remote operation. In March 2005, the telescope experienced significant operational problems, and the monitoring program was suspended while major maintenance was carried out. The telescope was then needed for VLBI work, and thus the data presented in this thesis extend only to early 2005.

5.2 Noise Levels and Measurement Uncertainty

5.2.1 Introduction

The Ceduna antenna observes with *dual* polarisation. An antenna with a *single* polarisation receiver measures a total power (P_T) which consists of a contribution from the source (P_S) and noise (P_N) (Crane & Napier, 1989; Wrobel & Walker, 1999):

$$\begin{aligned} P_T &= P_S + P_N \\ &= 0.5\, G\, \eta_a\, A\, S\, \Delta\nu + G\, k_B\, T_{sys}\, S\, \Delta\nu \\ &= G\, k_B\, K\, S\, \Delta\nu + G\, k_B\, T_{sys}\, S\, \Delta\nu \end{aligned}$$

where the factor of half in the source power term accounts for the single polarisation, since only half the total flux density is measured. G is the power gain of the system, η_a is the antenna efficiency, A is the collecting area of the antenna, S is the source total flux density, T_{sys} is the system temperature, $\Delta\nu$ is the observing frequency bandwidth, $k_B = 1.380 \times 10^{-23}$ J/K is the Boltzmann constant, and:

$$K = \frac{\eta_a A}{2 k_B} \quad \text{K Jy}^{-1}$$

is the antenna gain in units of antenna temperature in Kelvin per Jansky of flux density (Wrobel & Walker, 1999). The efficiency (and therefore K) is elevation dependent, and is actually the antenna's gain curve. The Ceduna antenna diameter of 29.6 m gives a collecting area A = 688.1 m^2, and its efficiency is $\eta_a \approx 0.6$. This gives $K \approx 0.071$ K Jy^{-1}.

The system temperature (T_{sys}) contains contributions from the receiver noise, feed losses, spillover, the atmosphere, the galactic background and the cosmic microwave background (Crane & Napier, 1989). The dominant component in C-band for the Ceduna antenna is the receiver temperature. The changes in telescope gain with elevation were carefully measured and are described in Section 3.5. For a tertiary reflector system like Ceduna, the changes in received power due to spillover radiation from the ground are much less severe than for a prime focus system.

The changes in gain with elevation are likely to be due to a combination of changes in the reflector geometry with elevation, and changes in the spillover contribution. The relative contribution of these and any other terms is of minimal significance to the science, which requires that the effects be accurately removed regardless of their source.

The above expression for the total antenna power can be simplified to:

$$P_T = g\,T_s + g\,T_{sys} \qquad \text{where} \quad g = G\,k_B\,\Delta\nu \quad \text{and} \quad T_s = K\,S$$

The System Equivalent Flux Density (SEFD) is the flux density of a source that would double the power output. It is expressed as SEFD = T_{sys} / K, and is used to compare antenna sensitivities since it takes into account antenna efficiency, collecting area, system noise and gain (Wrobel & Walker, 1999). The blazars monitored by Ceduna have strengths of only a few Janskys, ~1% of the total signal received by the antenna. For the Ceduna antenna, an SEFD of about 545 Jy is typical when observing ~1 to 4 Jy sources, which corresponds to a system temperature of $T_{sys} \approx 87$ K.

The signal detection ability of an antenna depends on the observing frequency bandwidth $\Delta\nu$ (Hz), and the measurement integration time, τ (seconds). The RMS value of measurements of a calibrator with mean flux density S , RMS_S , is expected to consist of a constant term, δ, due to thermal plus "1/f" noise; and a term $\alpha\,S$ which is known as the "fractional" noise (with α being the fraction), or "percentage" noise if α is defined accordingly. The two terms are independent and thus add in quadrature:

$$\mathrm{RMS}_S = \sqrt{\delta^2 + (\alpha\,S)^2}$$

Thermal noise is discussed in the next section, while the "1/f" and "fractional" noise components are discussed further in Sections 5.2.3 and 5.2.4 respectively. The 1/f noise is about 2½ times greater than thermal noise at the integration times relevant to flux density measurements; "fractional" noise for Ceduna data is ~1% of the total flux density, and is believed to be due to electronic gain fluctuations.

5.2.2 Thermal noise

When the flux density is subject to noise that is purely thermal in origin, Dicke's radiometer equation gives the minimum uncertainty (RMS) in the flux density measurements, expressed in terms of either flux density (ΔS in Jy) or temperature (ΔT in K), of a *single* polarisation by an antenna as (e.g. Burke & Graham-Smith, 2002):

$$\frac{\Delta S}{\mathrm{SEFD}} = \frac{\Delta T}{T_{sys}} = \frac{1}{\sqrt{\Delta\nu\,\tau}}$$

As discussed in Section 3.2, the author and Dr Simon Ellingsen visited Ceduna in June 2003 and measured the observing bandwidth to be $\Delta\nu \approx 250$ MHz; a scan across a source takes ~15.9 s; and the converters are sampled at 847 Hz. The data are re-sampled to produce a set of 187 data points for each polarisation channel, giving an integration time of $\tau \approx 0.085$ s for each data point. Substituting into the radiometer equation gives a minimum uncertainty level for the Ceduna antenna of:

$$\frac{1}{\sqrt{\Delta\nu\,\tau}} \approx \frac{1}{\sqrt{2.5 \times 10^{8} \times 0.085}} = 0.217 \times 10^{-3}$$

This minimum uncertainty applied to an SEFD of 545 Jy equates to $\Delta S \approx 118$ mJy, which is interpreted as the RMS value of a set of measurements each made over a period of 0.085 s. In June 2003, the observing bandwidth was increased to $\Delta\nu \approx 500$ MHz, reducing the minimum uncertainty level to $\sim 0.153 \times 10^{-3}$, or $\Delta S \approx 83$ mJy for an SEFD of 545 Jy.

The basic data recorded in a FITS file are the *L* and *R* circular polarisation data sets for each scan. A typical sample of PKS B1934-638 data, from days 98 to 101 of 2003, was analysed for measurement error. The data consisted of 327 scan groups *prior* to removal of 32% of the scan groups by the quality control tests applied by *ScanFit.m*, described in Section 3.4.

These 327 scan groups contained 654 scans in declination and 654 scans in right ascension, with a total of 1,308 *L* and 1,308 *R* data sets. The mean amplitudes of the curves fitted to the *L* and *R* data sets were 0.152 and 0.113 respectively, and the mean system temperatures measured for the two data channels were 21.4 and 15.9 respectively, expressed in units of the noise diode (CAL), the amplitude of which depends on the polarisation channel.

PKS B1934-638 has a circular polarisation << 1% of its total flux density of 3.92 Jy at the observation frequency of 6.65 GHz (see Chapter 3). Scaling factors to convert normalised *L* and *R* flux density data to Janskys are obtained by equating the mean *L* and *R* fitted curve amplitudes each to 3.92 Jy, giving scaling factors of about 25.71 and 34.64 respectively.

A program was written by the author to examine the residuals of the curve fits to the *L* and *R* polarisation data sets (i.e. the differences between the data and the quadratic black sky and Gaussian source curve fit to the data). For each scan data set, the program calculated the RMS values of the residuals of the two black sky components of the scan; and the on-source component of the scan, which is approximately the middle one-third of the 187 data points. The program also gives the mean of the RMS values for the *L* and *R* data sets. Table 5.1 sets out the results of this exercise.

	Sky (left)	Source	Sky (right)	All data set
L-data sets	143	149	141	145
R-data sets	135	140	133	138

Table 5.1 Mean RMS values (mJy) of the curve-fit residuals for 1,308 *L* and 1,308 *R* data sets.

Applying the conversion factors, the mean SEFDs for the *L* and *R* polarisation channels were calculated to be 549.5 Jy and 550.7 Jy respectively, which are typical values when observing ~1 to 4 Jy sources. Dividing the mean on-source RMS values by the measured system temperatures gives:

$$\left(\frac{\Delta S}{\text{SEFD}}\right)_L = \frac{148.9\ \text{mJy}}{549.5\ \text{Jy}} = 0.271\,\text{x}10^{-3} \quad \text{and} \quad \left(\frac{\Delta S}{\text{SEFD}}\right)_R = \frac{140.2\ \text{mJy}}{550.7\ \text{Jy}} = 0.255\,\text{x}10^{-3}$$

These uncertainty values are slightly larger than the black sky values, due to the Gaussian source profile not being quite perfect, but compare favourably to the theoretical minimum uncertainty of 0.217 x 10^{-3} for an integration time of $\tau \approx 0.085$ s per data point, as estimated above for an observing bandwidth of $\Delta\nu \approx 250$ MHz, which applies to these data.

5.2.3 1/*f* noise

"1/*f*" noise is caused by fluctuations in the antenna gain, *G*, over time scales of a second or longer. Yerbury (1975) found that such noise follows an $f^{-\beta}$ power density spectrum in the frequency domain, and since β is close to unity it is commonly referred to as "1/*f*" noise.

It was initially suspected that the "fractional" noise component of the RMS in Ceduna data corresponds to 1/*f* noise, since the data contain significant antenna gain fluctuations, which affect both the system temperature and the source flux density, the greatest effects being due to changes in the component of power due to noise (P_N). However, it can be shown that the 1/*f* phenomenon is <u>not</u> responsible for the "fractional" noise component of the RMS in Ceduna data.

Figure 5.1 is an Allen Variance plot that shows the variation of black-sky flux density data RMS with measurement integration time for the two polarisation channels. The figure was kindly provided by PhD candidate Mr Cliff Senkbeil, based on data obtained by sampling the converters at 847 Hz. Each plot is produced by computing the RMS of the data as they are binned into progressively longer bins, the bin size being the integration time. The dashed lines show the thermal noise component of the total RMS for each polarisation channel, in sampler units. Thermal noise follows the radiometer equation, and thus falls off as the square root of the integration time.

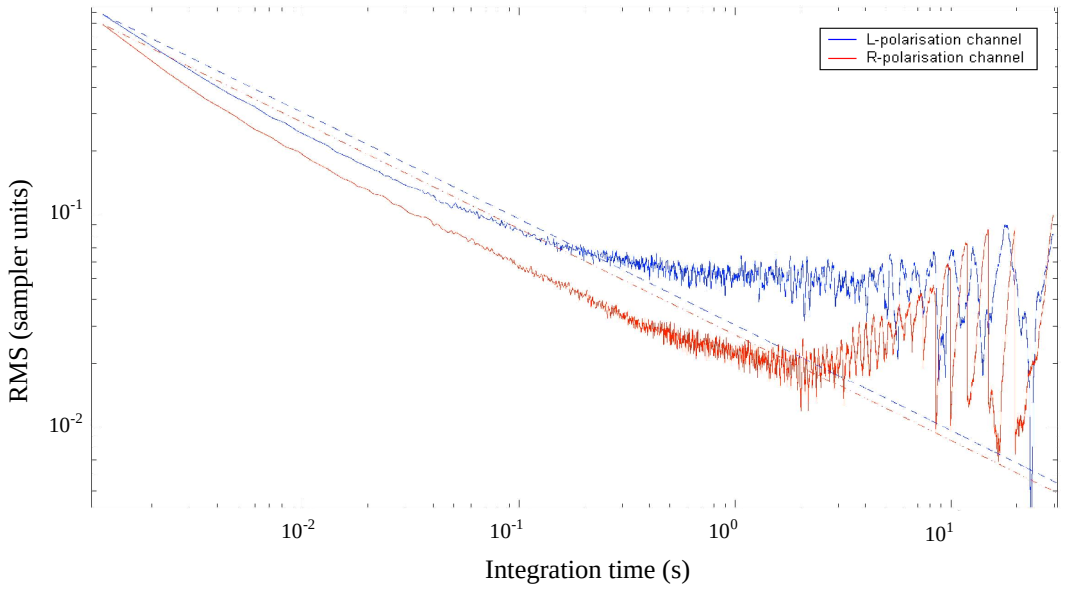

Figure 5.1 Allen Variance plot of Ceduna sampler data, courtesy of Mr Cliff Senkbeil.

For short integration times, up to about one second, Figure 5.1 shows that thermal noise is the dominant component of the total RMS, while 1/*f* noise becomes a significant effect for longer flux density measurement integration times.

The author repeated this exercise using PKS B1934-638 data from early 2003, with the source and the mean black sky signals removed from the 187 data points for each scan by subtracting the curve fitted to the scan data from the actual data (see Chapter 3). Figure 5.2 shows the mean Allen Variance plots for 150 separate scans in each polarisation channel.

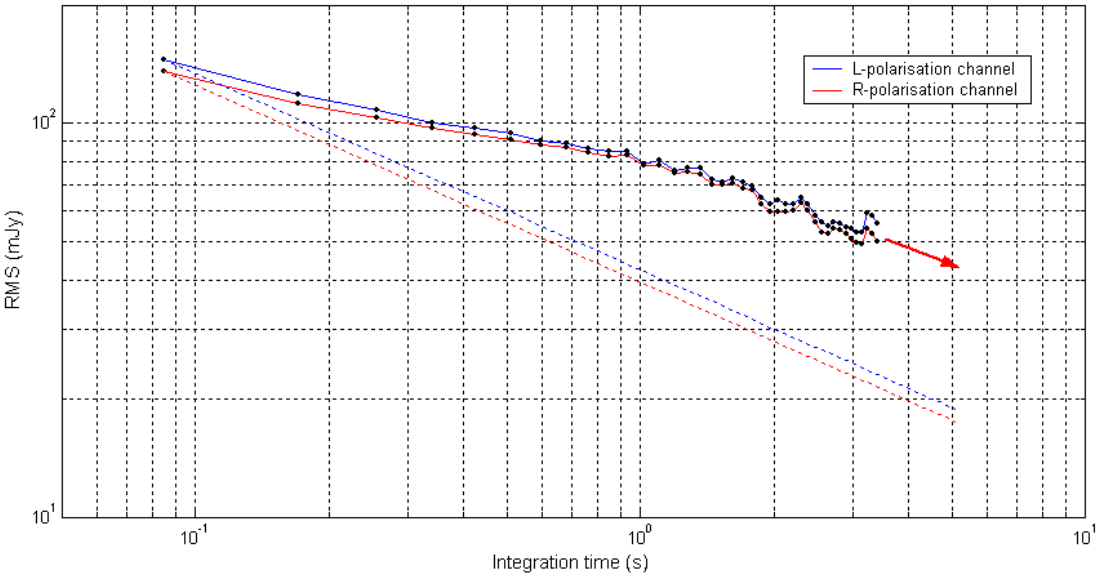

Figure 5.2 Mean Allen Variance plot of data from 150 scans of PKS B1934-638. The source and mean black sky signals have been removed from the data.

Figures 5.1 and 5.2 are not quite comparable, since in Figure 5.2 RMS values are converted to mJy using the scaling factors explained in the previous section, and some receiver system components were replaced between the two data gathering periods. The RMS values of the 187 data points binned into the 0.085 s initial integration time are 145 mJy and 135 mJy for the *L* and *R* polarisation channels respectively. These values agree well with the values of 149 mJy and 140 mJy estimated from the radiometer equation, in the previous section, confirming that thermal noise is the dominant cause of measurement error at this small integration time.

The dashed lines show the change in RMS expected if the noise at longer integration times is also purely thermal, extending out to an integration time of 5 seconds. However, at longer integration time the actual RMS values deviate from those predicted by the radiometer equation. In Figure 5.2, the data bin sizes were increased as multiples of the shortest bin size (0.085 s), and the largest bin size was 40 x 0.085 = 3.4 s, corresponding to four full bins in a ~15.9 s scan. Figure 5.3 replots the data shown in Figure 5.2, but subtracting the thermal noise from the total RMS as the integration time increases.

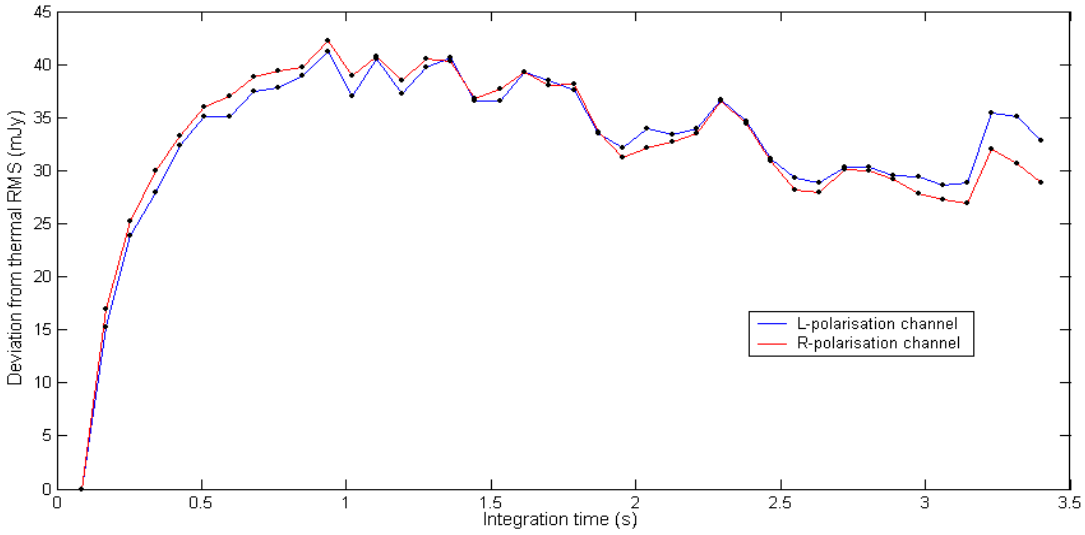

Figure 5.3 Re-plot of Figure 5.2, showing the 1/*f* noise RMS component obtained by subtracting the thermal noise RMS component from the total RMS.

Although thermal noise is the principal cause of measurement error at short integration times, 1/*f* noise *does* significantly contribute to the overall flux density measurement errors in Ceduna data. The on-source signal is recorded in the middle one-third of the scan, with the adjacent portions of the scan being black sky signal (see Chapter 3). A scan takes about 15.9 s, so the difference between the total power while on-source, and the total power while on black sky, is the difference between two measurements effectively made about 5 s apart.

Figure 5.2 shows that 1/*f* noise is ~2½ times larger than the thermal noise at an integration time of 5 s (the slight extrapolation is shown in the figure). The total RMS measurement errors in the left and right polarisation channel data are estimated to each be ~45 mJy, with 1/*f* components of about 19 mJy.

Combining the two polarisation data sets reduces the RMS by factor of $\sqrt{2}$, so the RMS expected following this combination is $\delta = 45/\sqrt{2} \approx 32$ mJy. As discussed in the previous section, the RMS value of measurements of a calibrator source of mean flux density *S* consists of a constant term due to thermal plus 1/*f* noise, and $\delta \approx 32$ mJy is this term for a bandwidth of $\Delta\nu \approx 250$ MHz.

But 1/*f* noise is *additive* in nature, since it has a significant impact only on the black sky component of the system temperature. It does *not* cause the observed fractional error component of the RMS in Ceduna data.

An alternative argument that arrives at the same conclusion is that, if 1/*f* noise were the principal cause of the approximately 1% fractional noise contribution to radio source flux density measurements, then the system gain, *G*, would also be exhibiting 1% fluctuations. The system gain fluctuations would thus be about 5 Jy given that the SEFD is about 545 Jy, and if the black sky flux densities were fluctuating with amplitudes of about 5 Jy, there would be no hope of detecting any source signal.

5.2.4 Fractional noise

As discussed in Section 5.2.1, the RMS value of calibrator flux density measurements varies with mean flux density, *S*, in a relationship of the form $\mathrm{RMS}_S^2 = (\alpha S)^2 + \delta^2$, where the constant component is estimated above to be $\delta \approx 32$ mJy; and αS is the "fractional" noise.

To determine the value of α and confirm the value of δ, the light curves of three calibrators were measured over the course of several days. The calibrators PKS B1934-638 (~ 3.92 Jy) and 3C227 (~1.90 Jy) are used throughout the Ceduna program, so their flux density RMS values are well known. A strong source B1921-293 (~9.1 Jy) was also monitored for a short time, to aid the examination of how RMS values vary with source strength, and to aid calculation of the gain-elevation curve.

Table 5.2 and Figure 5.4 show the flux density RMS values for these three sources. The data have been quality controlled. A curve-fitting exercise determination of the required relationship, shown as the solid line in Figure 5.4, gives:

$$RMS_S \text{ (mJy)} = \sqrt{(13S \text{ (Jy)})^2 + (29)^2}$$

The constant term, 29 mJy, agrees well with the previously estimated value of $\delta \approx 32$ mJy. This term in the RMS prediction equation is associated with an integration time of only a few seconds. However, the RMS prediction relates to flux density data gathered in an observing period that spans days, and through the fractional term the RMS value is sensitive to fluctuations on time scales of hours to days. On these time scales, the mean flux density of a calibrator is expected to be constant, with actual flux density measurements varying in an essentially random fashion due to measurement errors. Unfortunately it is now known that small systematic fluctuations are present in the data, and this is discussed in Section 5.5.

	Flux density (S)	**RMS**
3C227	~1.91 Jy	34 mJy (2.4 %)
PKS B1934-638	~3.92 Jy	69 mJy (1.8 %)
PKS B1921-293	~9.10 Jy	123 mJy (1.4 %)

Table 5.2 Mean and RMS flux densities for three calibrator sources, based on 3-4 days of observations in early 2003.

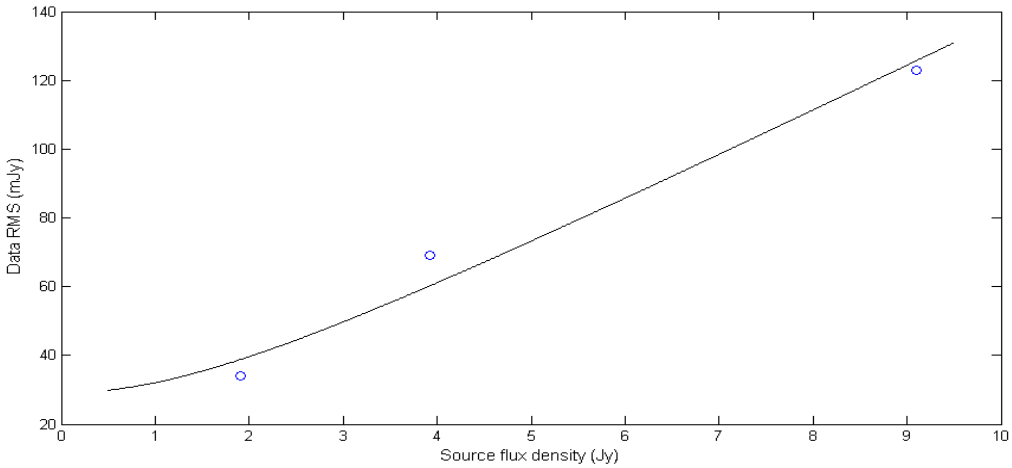

Figure 5.4 RMS noise levels for the calibrator flux densities data in Table 5.2.

The "fractional" noise term is roughly 1% of the source flux density, *S*. The initial Ceduna blazar monitoring campaign can thus observe sources of flux density ~1 Jy with an accuracy of RMS ~40 mJy or 4% of the source strength, which is quite acceptable.

5.2.5 Confusion limit

Confusion is the random occurrence of multiple sources in a telescope's beamwidth. The confusion limit for a 30 m radio telescope operating at 6.65 GHz is ~20 mJy, and confusion is thus expected to make only a small contribution to the noise of data measured by Ceduna, and is not a limiting factor in the present system (McCulloch et al., 2005). The confusion associated with a given source can be determined by premier facilities such as the Australia Telescope Compact Array in New South Wales, which can map the field around a source.

5.3 Long Term Calibrator Performance: Seasonal Corrections

Figure 5.5 shows the flux density time series for the southern and northern group calibrators, PKS B1934-638 and 3C227 respectively, from the start of the COSMIC blazar monitoring program in March 2003, through to early 2005. The data alternate between northern and southern observing periods, except for days 190-210 in 2004, when an attempt was made to combine the observing groups (see Section 3.6).

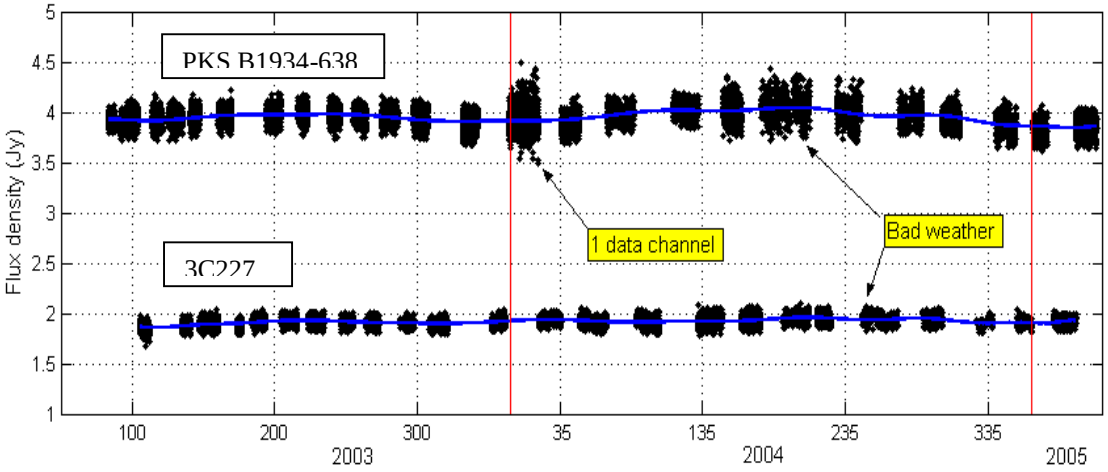

Figure 5.5 Calibrator flux density time series for the 2003/05 campaign.

Chapter 3 describes the data processing method used to obtain these data, including pointing and gain-elevation corrections. Overall, Ceduna performed well over the initial 694 day blazar monitoring campaign, a remarkable achievement. The mean flux densities of PKS B1934-638 and 3C227 were 3.952 ± 0.093 Jy and 1.925 ± 0.048 Jy respectively, agreeing with the known calibrator flux densities at 6.7 GHz of 3.92 Jy and 1.90 Jy.

Figure 5.5 shows minor long term variations in the calibrator flux density time series, which are attributed to seasonal thermal effects such as air temperature changes. The top plots of Figures 5.6 and 5.7 show the PKS B1934-638 and 3C227 daily mean flux densities, with a low order polynomial highlighting the seasonal variations. The polynomial fits for 3C227 and PKS B1934-638 do not strongly match each other, but are similar. Both show maxima in winter, and minima in summer.

The bottom plots of Figures 5.6 and 5.7 replot the mean daily flux density data, following application of bulk correction factors for each observing period to remove seasonal effects. The corrected PKS B1934-638 and 3C227 mean flux densities are 3.92 Jy and 1.90 Jy respectively, as required, with RMS values of 80 mJy and 42 mJy respectively. The seasonal correction factors are computed by *ScanAnalysis.m*, and for the southern and northern group observing periods range from 0.966 to 1.011 and from 0.964 to 1.022 respectively, with means of 0.989 and 0.987 respectively.

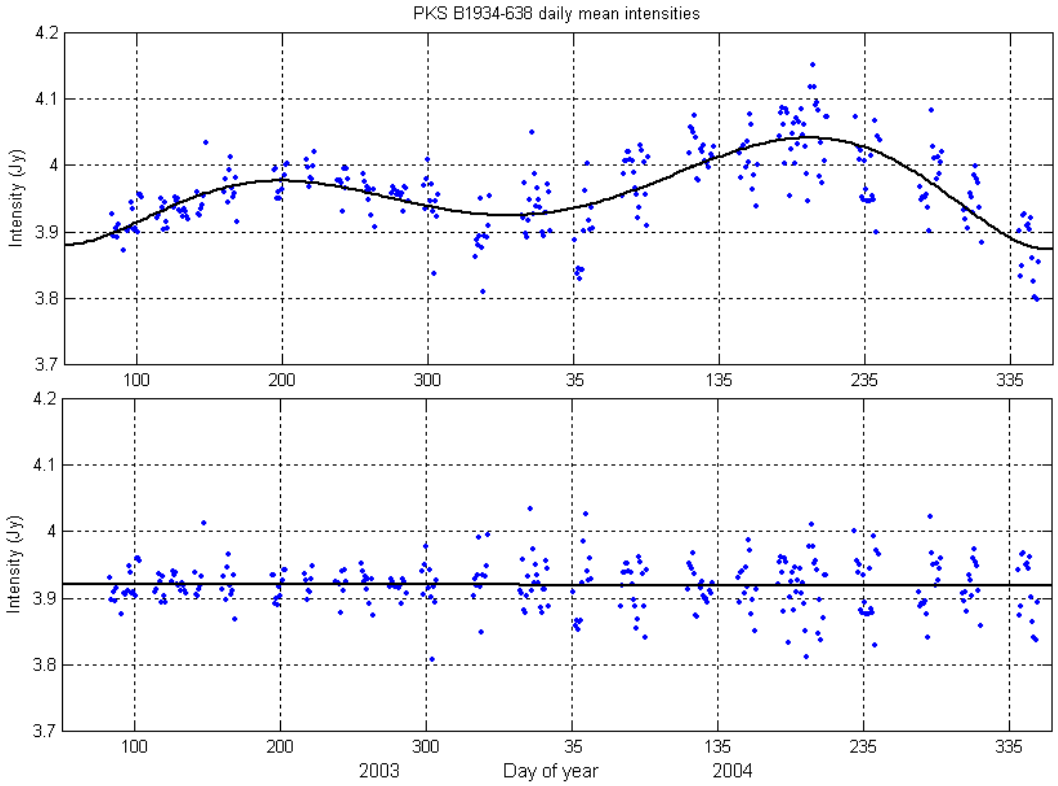

Figure 5.6 **PKS B1934-638 mean daily intensity plots, showing seasonal effects (top), and following corrections for each observing period (bottom).**

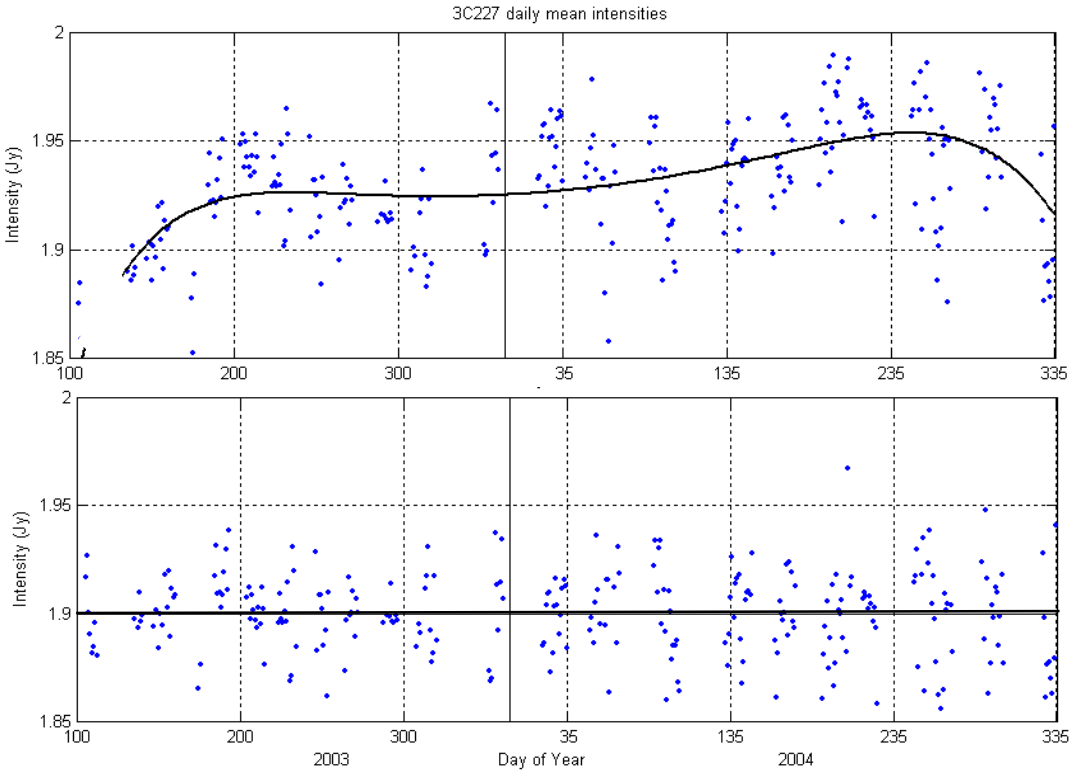

Figure 5.7 **3C227 mean daily intensity plots, showing seasonal effects (top), and following corrections for each observing period (bottom).**

Table 5.3 gives the RMS values of the calibrator data before correction for seasonal effects, separated into 2003 and 2004/05 data sets. The 2004/05 RMS values are elevated compared to the 2003 values, attributed to the period of only single polarisation channel operation in early 2004, extreme weather in mid-2004, observing period 18 which trialled a scheme to monitor all the sources (insufficient data per source resulted, and the data were noisier than usual due to excessive telescope slewing), and increasing problems with the telescope ahead of its 2005 maintenance overhaul.

PKS B1934-638	**2003**	**2004/05**
Uncorrected	65 mJy	93 mJy
Zero mean	61 mJy	86 mJy
3C227		
Uncorrected	40 mJy	44 mJy
Zero mean	36 mJy	39 mJy

Table 5.3 Calibrator performance 2003-2005

The slightly revised RMS prediction equation based on the 2003 RMS values is:

$$RMS_S \text{ (mJy)} = \sqrt{(13\,S\text{ (Jy)})^2 + (34)^2}$$

Table 5.3 also gives "zero mean" calibrator data RMS values. These are the RMS values after correction of the flux density data for seasonal effects; and after reduction to a zero-mean data set following the procedure described in Chapter 4. The resulting time series are shown in Figure 5.8. The RMS values of the zero-mean calibrator data are ~5 mJy smaller than the RMS values of the raw data, because some variability is removed by the corrections for seasonal effects and for minor fluctuations on time scales of days (these latter attributed to synoptic weather effects, as discussed in Chapter 4).

The RMS values relate partly to systematic flux density fluctuations, which primarily occur on time scales of hours: they do not reflect observation errors of a purely random nature. Figure 5.8 shows the systematic fluctuations are about ± 0.15 Jy for PKS B1934-638 and about ± 0.1 Jy for 3C227. with 6.7 GHz strengths of 3.92 Jy and 1.90 Jy respectively.

The systematic fluctuations are discussed in the next section. Their presence prevents an analysis of genuine variability in the Ceduna data from the initial campaign at time scales of less than a day, whereas such an analysis would be possible for data whose RMS is random.

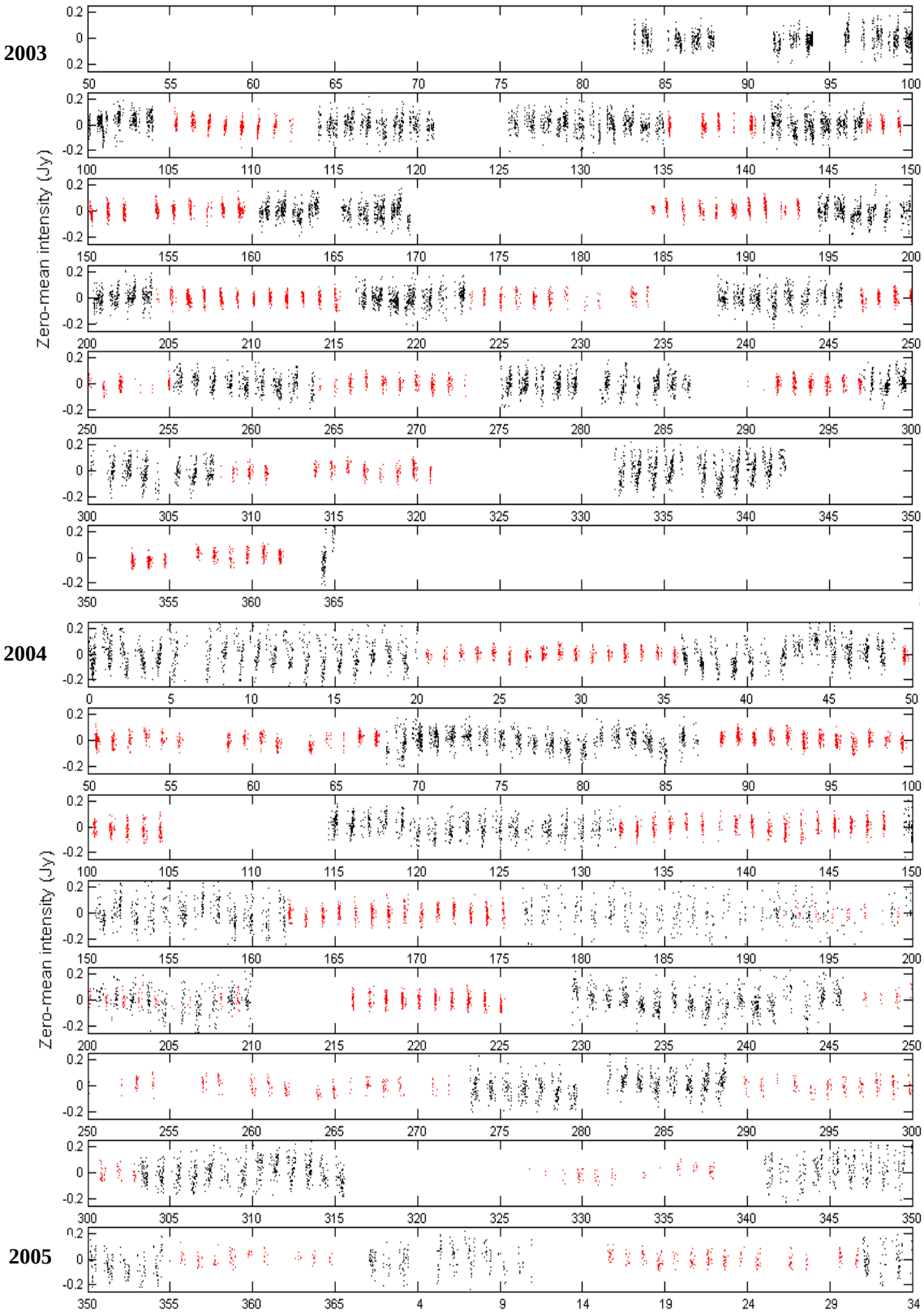

Figure 5.8 **Zero-mean calibrator flux density time series for PKS B1934-638 (black), and 3C227 (red). The observations alternate, except for concurrent date gathered during days 190-210 in 2004. Mean flux densities at 6.7 GHz are: PKS B1934-638 = 3.92 Jy and 3C227 = 1.90 Jy.**

5.5 Systematic Fast Variability

5.4.1 Calibrator data

The problem of systematic fluctuations in the data recorded by the Ceduna antenna is now considered in detail. Figure 5.9 shows the roughly ± 0.15 Jy systematic fluctuations in 2003 PKS B1934-638 calibrator flux density data, highlighted by running means through the data. Figure 5.10 shows cumulative Power Spectral Densities (PSDs) for both calibrators.

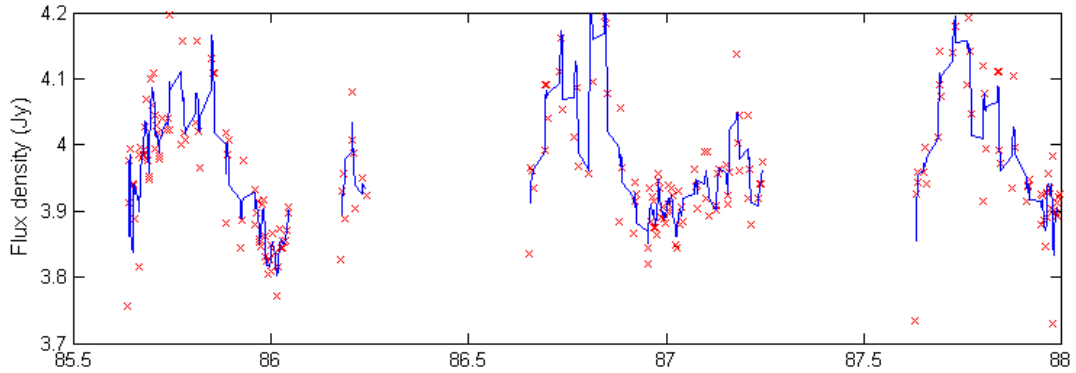

Figure 5.9 Typical systematic fluctuations in PKS B1934-638 data. The solid blue lines are 5-point running means.

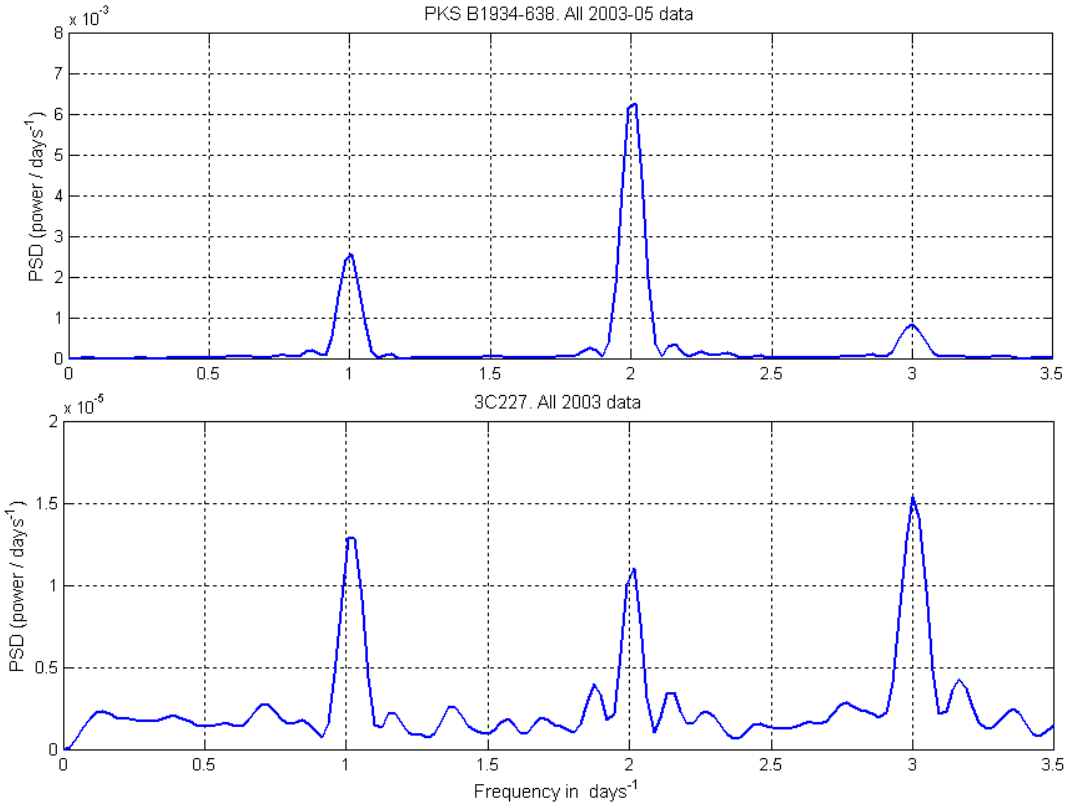

Figure 5.10 Cumulative calibrator Power Spectral Density functions, with peaks corresponding to the systematic fluctuations. Top: PKS B1934-638 for 2003-05. Bottom: 3C227 for 2003.

In Figure 5.10, the summation is of the individual PSDs calculated from the data for each 2003/05 observing period considered separately in the case of PKS B1934-638; and for each 2003 observing period considered separately in the case of 3C227 which, as a fairly weak source, suffered more from the effects of occasionally poor data quality in 2004/05.

Both cumulative PSDs have peaks at 1, 2 and 3 days^{-1}, presumably harmonics, highlighting the presence of systematic fluctuations on diurnal time scales. The PSDs are tolerant of the fact that the two calibrators have quite different observing times, with 3C227 spending less than half a day above the 10° elevation cut-off, and PKS B1934-638 spending over half a day above the cut-off.

Figure 5.11 shows the essentially featureless calibrator PSDs expected if the variability in the calibrator data was purely random in nature, with no systematic effects. The PSDs have been computed by substituting random flux density data for the actual data. The random data have a zero-mean Gaussian distribution and standard deviations set to the values in Table 5.3: 61 mJy and 86 mJy for PKS B1934-638 in 2003 and 2004/05 respectively; and 36 mJy for 3C227 in 2003. The cumulative 3C227 PSD is multiplied by 30 for clarity.

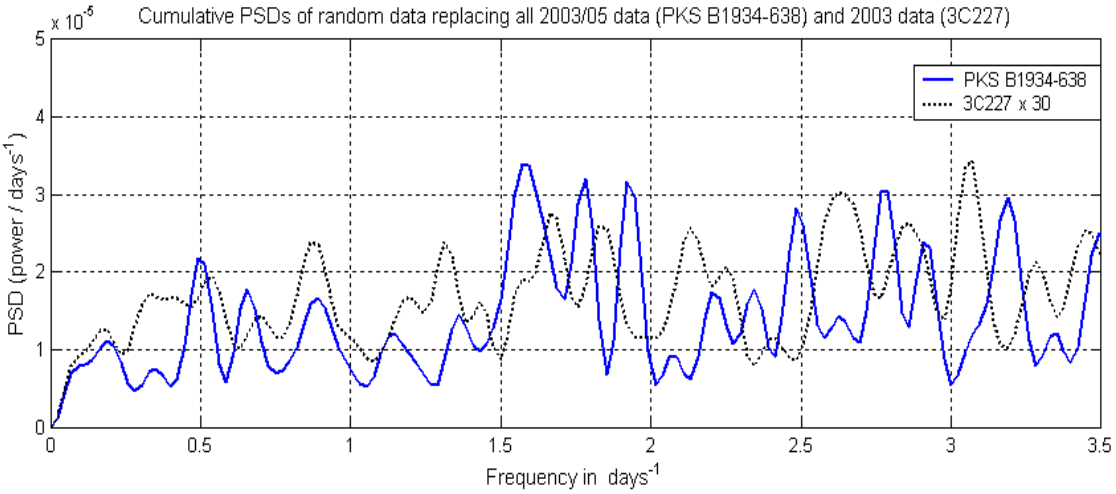

Figure 5.11 Cumulative PSDs of synthetic calibrator flux density data, with random data of the same RMS values replacing the actual data.

5.4.2 Blazar data

Chapter 4 described the procedure for separating a Ceduna flux density time series into two complementary zero-mean components. The $x_{\text{zero}}^{\text{Data}}$ data set contains flux density fluctuations on time scales longer than about a day, after correction for the minor fluctuations observed in calibrator data on these time scales, which are interpreted as synoptic weather effects; and is the basis for the analysis of the PKS B1622-253 and PKS B1519-273 data considered by this thesis.

The $x_{\text{zero}}^{\text{Fast}}$ data contain flux density fluctuations on time scales of less than a day. The key assertion is that, for PKS B1622-253 and PKS B1519-273, this variability is a combination of systematic fluctuations and random observation errors, and can be ignored in a variability analysis of these two blazars. Three lines of evidence support this assertion.

1) Fluctuation correlations

Figure 5.12 shows three days of $x_{\text{zero}}^{\text{Fast}}$ flux density data, and running means through the data, for PKS B1622-253 and PKS B1519-273, both northern observing group sources. Figure 5.13 presents all the $x_{\text{zero}}^{\text{Fast}}$ data for these two blazars, for the second half of 2003.

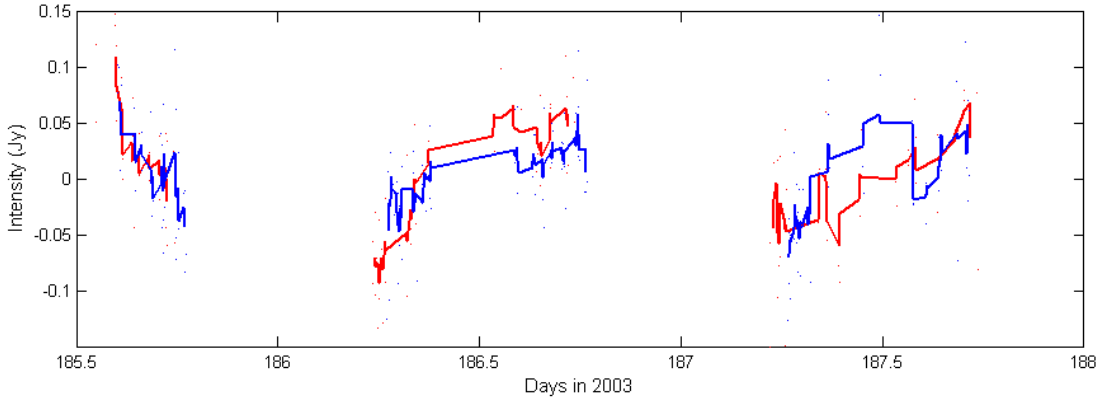

Figure 5.12 Three days of PKS B1622-253 (blue) and PKS B1519-273 (red) data, with 3-point running means highlighting correlation of the variations.

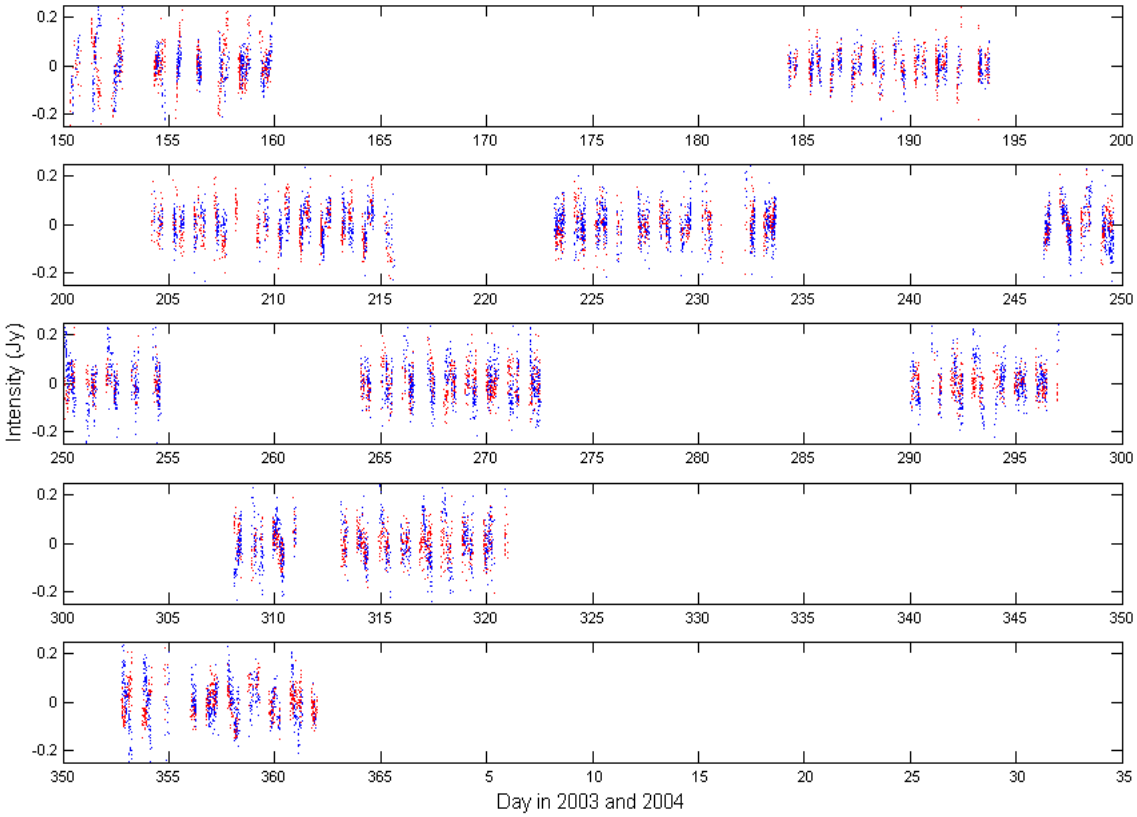

Figure 5.13 Fast components of PKS B1622-253 (blue) and PKS B1519-273 (red) data.

The 3C227 calibrator data are not shown in Figures 5.12 and 5.13, since there is almost no overlap between its daily observation times and the observation times of the two blazars.

The flux density fluctuations of the two $x_{\text{zero}}^{\text{Fast}}$ data sets are clearly well correlated, which is strong evidence that the fluctuations are systematic in nature and do not represent genuine variability. However, Dr Jim Lovell pointed out that there are rare occasions in Figure 5.13 when the fluctuations are *not* well correlated, such as the data for day 151. This is believed to be due to interstellar scintillation in PKS B1519-273 occurring on time scales of just over a day during the speed-up time of year. For observing periods near the speed-up time of year, PKS B1519-273 variability must thus be analysed using *all* the flux density data, not just the $x_{\text{zero}}^{\text{Data}}$ data set.

2) Blazar RMS values vs calibrator RMS values

Figure 5.14 shows the data processing procedure, as described in Chapter 4, applied to flux density data for PKS B1622-253 observing period 9.

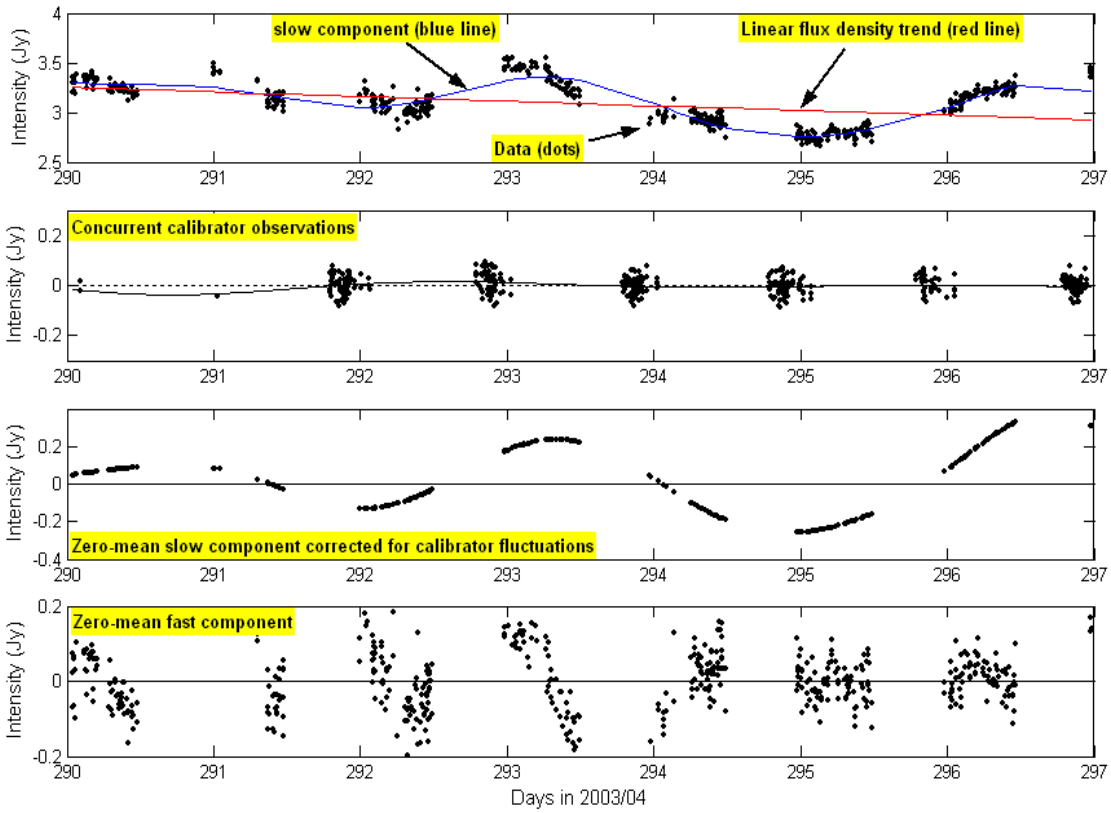

Figure 5.14 Data processing applied to PKS B1622-253 observing period 9.

The RMS values of the slow and fast flux density components, $x_{\text{smooth}}^{\text{Data}}$ and $x_{\text{zero}}^{\text{Fast}}$ are related in quadrature to the RMS value of the data, x^{Data}, as follows:

$$(\text{RMS } x_{\text{smooth}}^{\text{Data}})^2 + (\text{RMS } x_{\text{zero}}^{\text{Fast}})^2 \approx (\text{RMS } x^{\text{Data}})^2$$

Table 5.4 gives the RMS values associated with the data shown in Figure 5.14.

Component	**Plot**	**RMS**
Data, x^{Data}	Top plot	213 mJy
Slow component, $x^{\text{Data}}_{\text{smooth}}$	Top plot	195 mJy
Zero-mean slow component, $x^{\text{Data}}_{\text{zero}}$	Third plot	170 mJy
Zero-mean fast component, $x^{\text{Fast}}_{\text{zero}}$	Bottom plot	83 mJy

Table 5.4 RMS values (mJy) for the data components shown in Figure 5.14

The relationship between the RMS values is thus confirmed:

$$(195)^2 + (83)^2 \approx (213)^2 \qquad \text{All values in mJy}$$

The RMS value of $x^{\text{Data}}_{\text{smooth}}$ is lower that of $x^{\text{Data}}_{\text{zero}}$ because $x^{\text{Data}}_{\text{smooth}}$ includes corrections for the linear flux density trend across the observing period, and corrections (based on the calibrator data) for minor weather-related fluctuations on time scales of days. If genuine variability in PKS B1622-253 and PKS B1519-273 is all contained in the $x^{\text{Data}}_{\text{zero}}$ flux density components, then the $x^{\text{Fast}}_{\text{zero}}$ components should be comparable to the calibrator data. Figure 5.15 shows this comparison.

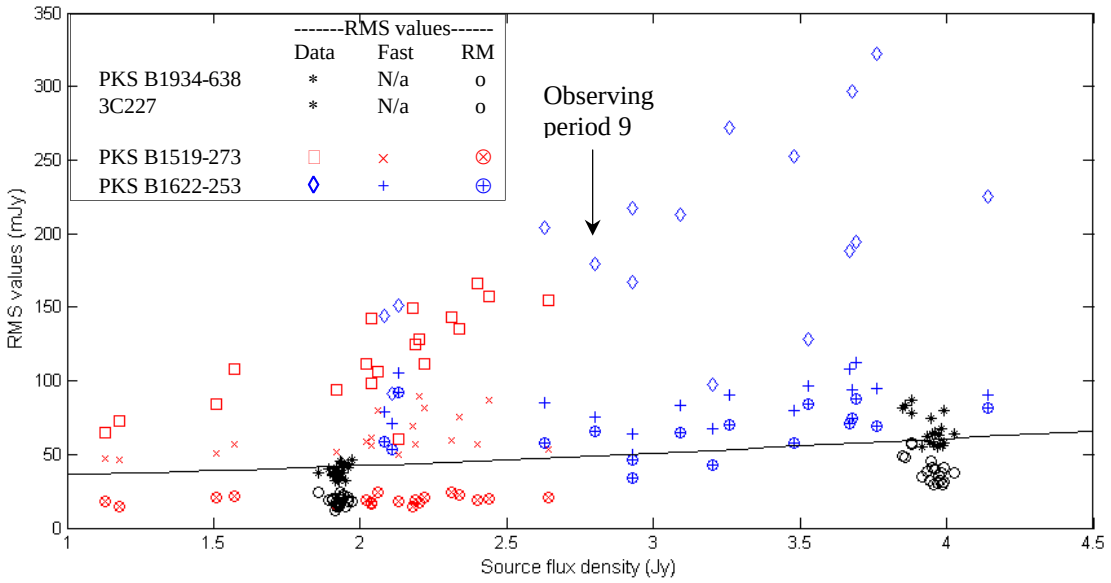

Figure 5.15 Comparison of the $x^{\text{Fast}}_{\text{zero}}$ data components of PKS B1622-253 and PKS B1519-273 with calibrator data. RM = running mean.

Figure 5.15 omits PKS B1934-638 data points for southern source observing periods 12, because Ceduna was then recording with only one polarisation channel, and for observing periods 15, 16, & 17 which were characterised by bad weather and poor data. It also omits data points for northern source (3C227 and the blazars) observing periods 13 &14, and observing periods 19 & 20, for the same reasons. These data are given in Chapter 6.

In Figure 5.15, the calibrator data RMS values are separated into the RMS of the data (*), and the RMS of a 5-point running mean (RM) through the data (o), which is a measure of the systematic fluctuations. The flux densities of 3C227 and PKS B1934-638 at 6.7 GHz are 1.9 Jy and 3.92 Jy respectively, and have not been corrected for seasonal effects (which would affect the RMS values by less than 1 mJy). The solid black line shows the RMS prediction curve (see Section 5.3), which of course fits the calibrator total RMS data from which it was derived.

For PKS B1519-273 and PKS B1622-253, Figure 5.15 shows the RMS values of:

a) the overall data, x^{Data} (□ and ◊);

b) the $x_{\text{zero}}^{\text{Fast}}$ data (x and +); and

c) a 5-point running mean through the $x_{\text{zero}}^{\text{Fast}}$ data (⊗ and ⊕).

PKS B1519-273. The RMS values of the running means through the PKS B1519-273 $x_{\text{zero}}^{\text{Fast}}$ data (⊗) and the 3C227 data (o) are clearly in excellent agreement, strong evidence that the PKS B1519-273 $x_{\text{zero}}^{\text{Fast}}$ data component contains only variability associated with the systematic fluctuations and random observation errors.

PKS B1622-253. The RMS values of the running means through the PKS B1622-253 $x_{\text{zero}}^{\text{Fast}}$ data (⊕) are slightly elevated compared to the RMS values of the running means through the calibrator data (o). This is believed *not* to be due to the presence of genuine variability, but rather is attributed to quite pronounced variability in the overall data (◊), such that the data filtering procedure is harder pressed to properly smooth through the data and isolate the $x_{\text{zero}}^{\text{Fast}}$ data component.

Consider, for example, the PKS B1622-253 $x_{\text{zero}}^{\text{Fast}}$ data from observing period 9 shown in the last sub-plot of Figure 5.14. These data are flagged in Figure 5.15, which shows that the total $x_{\text{zero}}^{\text{Fast}}$ RMS is 83 mJy (+), and the RMS value of the running means is 65 mJy (⊕).

However, Figure 5.16 shows the running means through the data. The running means have means of {-13 +34 -15 +22 +21 -5 +6} mJy, and the genuine variability signal is not entirely contained in the $x_{\text{zero}}^{\text{Data}}$ component of the data. However, the genuine variability is pronounced, so this does not pose a problem for its analysis.

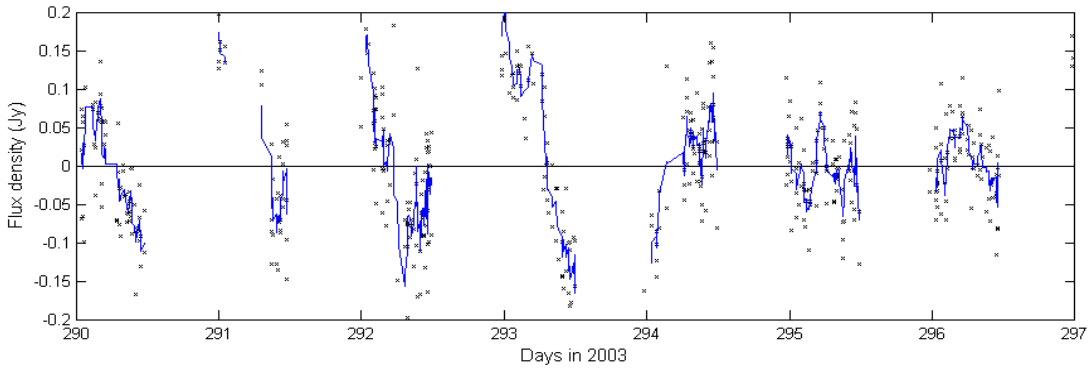

Figure 5.16 Running means through PKS B1622-253 $x_{\text{zero}}^{\text{Fast}}$ data. Observing period 9.

3) Blazar Power Spectral Densities (PSDs) vs calibrator PSDs

Figure 5.17 shows cumulative PSDs for the fast signal components of PKS B1622-253 and PKS B1519-273. As before, each cumulative PSD is calculated by summing the individual PSDs of the $x_{\text{zero}}^{\text{Fast}}$ data sets, considered separately, for each observing period in 2003.

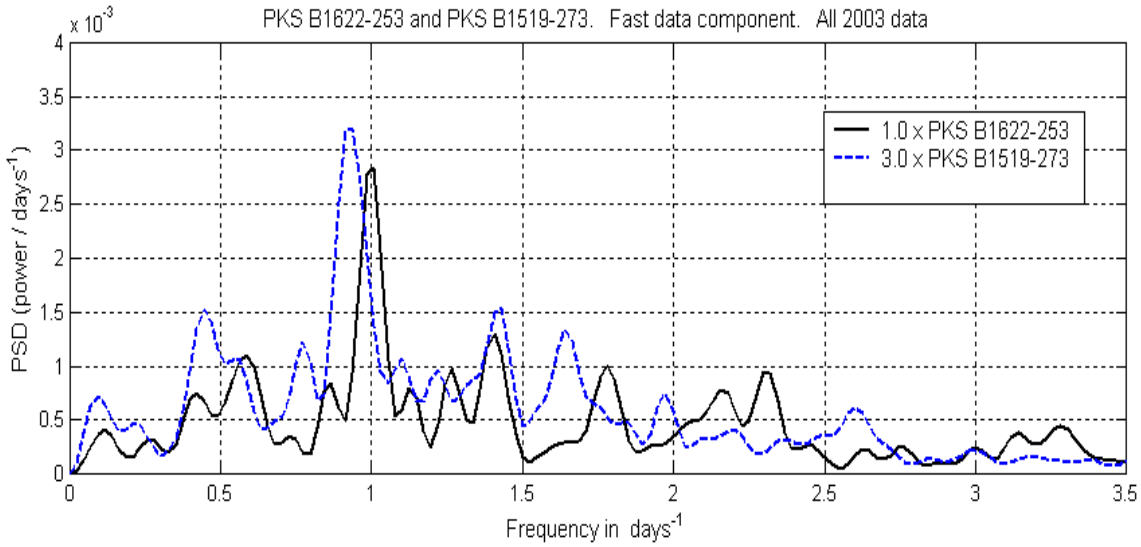

Figure 5.17 Cumulative PSDs for the fast components of PKS B1622-253 and PKS B1519-273 2003 data.

The PSDs in Figure 5.17 are similar to the cumulative PSDs of the two calibrators, shown in Figure 5.10. The dominant peaks in the vicinity of 1 day^{-1} are further evidence that the $x_{\text{zero}}^{\text{Fast}}$ data components of PKS B1622-253 and PKS B1519-273 contain diurnal fluctuations which are of a systematic nature, and contain little, if any, genuine variability. The dominant peak for PKS B1519-273 is at slightly less than 1 day^{-1} because this source exhibits some genuine variability on timescales of just over a day during the speed-up time of year, as noted above.

5.5 Evaluation of New Data Processing Method

The data processing method developed by the author for the present research is described in Chapter 3. In summary, it divides raw measurements for a polarisation channel by the noise diode amplitude (CAL height) measurement for that channel; the polarisation channel data are combined, and the scans back and forth across the source in declination are combined, as are the scans back and forth in right ascension.

This gives two flux density values, which are then corrected for pointing and gain-elevation effects, and scaled by equating measurements of the primary calibrator, PKS B1934-638, to its known flux density of 3.92 Jy at 6.7 GHz. Weather-related variations of the calibrator on time scales of days are used to further correct the blazar data using the procedure described in Chapter 4; and minor seasonal variations of the calibrator are also corrected for, as described in Section 5.3.

In mid 2005, the author recognised that the diurnal fluctuations in the Ceduna data were systematic in nature. Fortunately, variability analysis of the two blazars presented in this research is not compromised by the presence of these fluctuations. PhD candidate Mr Cliff Senkbeil, then began a study of the systematic fluctuations in the Ceduna data. One possible cause of the systematic fluctuations was the side lobes associated with the Ceduna beam, which are fixed in Az/El, while the antenna scans in RA/Dec. However, no evidence was found that this affects the scan fitting procedures.

In late 2006, Mr Senkbeil completed the development of an alternative data processing method, which treats flux density measurements made by the two polarisation channels separately, and uses a more sophisticated calibration procedure. In the new method the calibrator flux amplitude measurements for each polarisation channel are corrected for pointing and gain-elevation effects, and a linear fit is made of these corrected calibrator flux amplitudes with respect to the noise diode amplitudes. The blazar data are corrected on a day-to-day basis using this linear model.

Unfortunately, this method can only be applied if sufficient calibrator data are available. The calibrator 3C227 is not observed for long enough every day to enable the new method to be applied to sources in the northern observing group, which includes PKS B1622-253 and PKS B1519-273.

For the southern sources, the new method is superior to the present approach, in that fewer data points are rejected by the quality control tests. The need for such tests is reduced by treating the polarisation channels separately, although not altogether avoided. However, the new method does <u>not</u> remove the systematic fluctuations, although it reduces them.

Figure 5.18 compares the application of the two data processing methods to southern source PKS B1144-379 observing period 4, used to illustrate the data analysis methods described in Chapter 4. The additional data points produced by the new method mark it as the superior method, but the old method produced sufficient data points to enable a credible analysis.

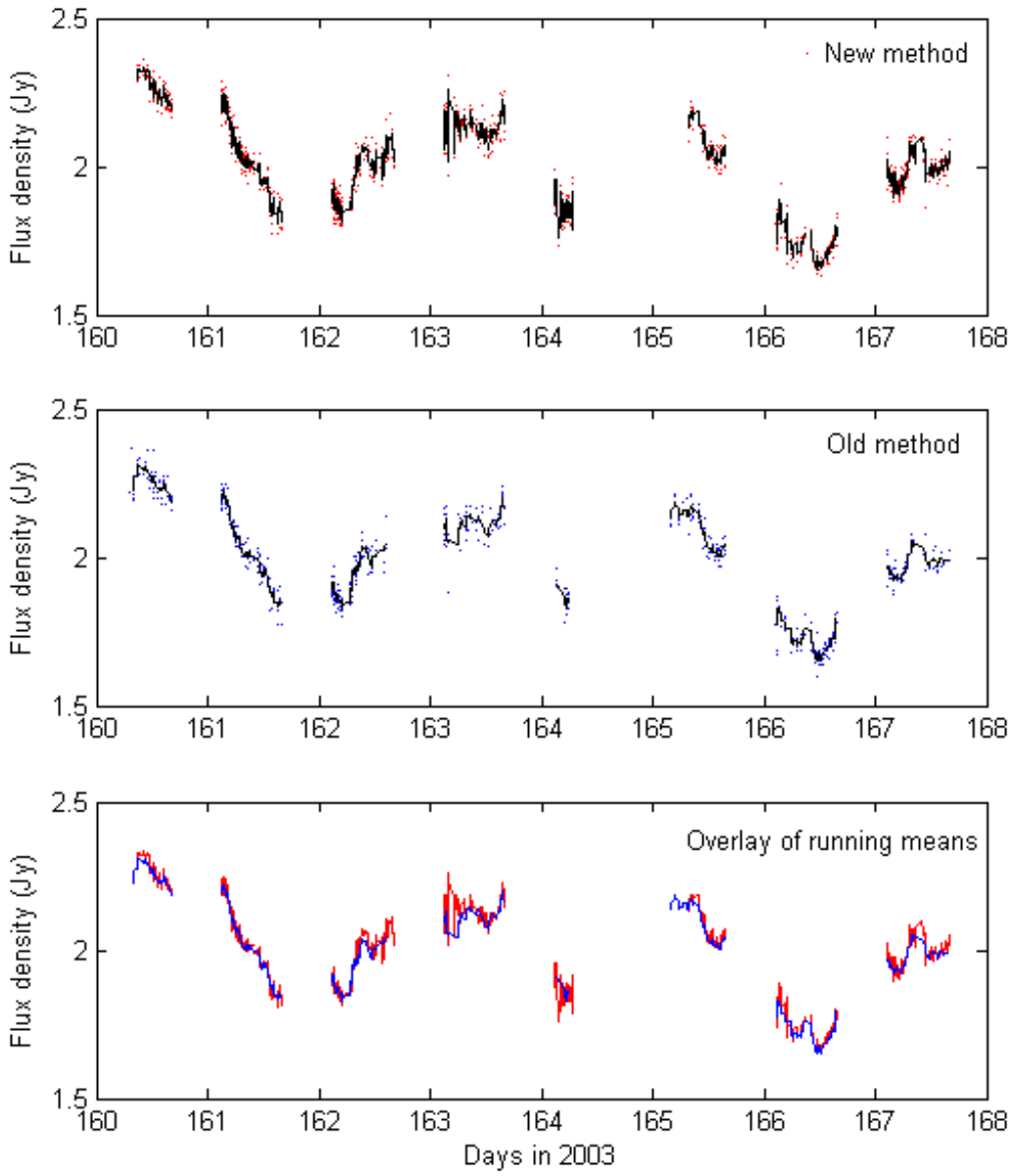

Figure 5.18 Comparison of PKS B1144-379 observing period 4 data processed by the old and new methods.

Figure 5.19 shows PKS B1934-638 calibrator data (red dots) and running mean (solid blue line), processed by the new method. Compared to Figure 5.9, which shows the same data processed by the old method, the new method is better than the old method, but it does not remove the systematic fluctuations, although it reduced them by a factor of about half.

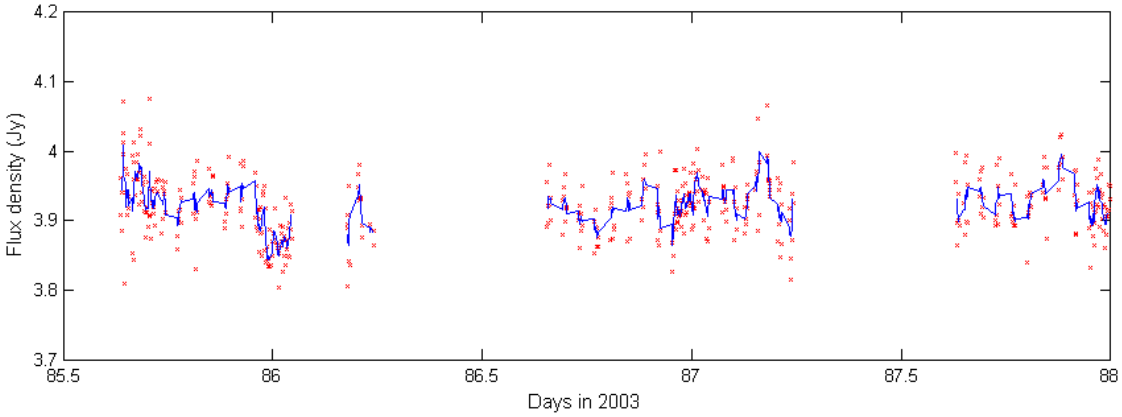

Figure 5.19 PKS B1934-638 time series produced by the new method. Compare to Figure 5.9, which shows data for the same period processed by the method described in Chapter 4.

5.6 Chapter Summary

This chapter has found a pleasing long term consistency in calibrator observations, which underpins the credibility of the COSMIC project. It proves that the Ceduna telescope can carry out long term monitoring of sources with strengths greater than ~1 Jy to the accuracy necessary for the analysis of variability on time scales of days.

Better performance was anticipated in the early months of the project, but was not achieved during the initial COSMIC program, for two reasons. First, the maintenance needs of the new radio telescope, operating continuously in remote mode, were not fully appreciated, and a program of regular servicing has now been developed. Second, the presence of systematic flux density fluctuations on diurnal time scales was not recognised. Fortunately, this chapter has shown that the blazars of interest to the present research exhibit radio variability time scales on longer time scales, on the order of days. The data processing procedure described in Chapter 4 isolates this variability in the $x_{\text{zero}}^{\text{Data}}$ data sets, and the complementary $x_{\text{zero}}^{\text{Fast}}$ data sets can be discarded. The exceptions are two PKS B1519-273 observing periods that span the speed-up time of year, when the variability analysis must be based on all the data.

Work by PhD candidate Mr Cliff Senkbeil has now confirmed that the systematic diurnal fluctuations have a thermal (i.e. weather related) origin. It is hoped that a method can be devised either to avoid recording these fluctuations during the telescope operation, or to subsequently remove the fluctuations from the data. In the meantime, the data filtering procedure presented in Chapter 4 smooths through the diurnal fluctuations and corrects for the small weather-related fluctuations on longer time scales. This procedure enables a credible analysis of blazar data whose variability time scale is longer than a day, which is true of the two blazars considered by this thesis.

6.0 DATA REDUCTION for PKS B1622-253 and PKS B1519-273

6.1 Structure of Chapter and Appendices

PKS B1519-273 and PKS B1622-253 are both northern group sources, for which 3C227 is the calibrator. The PKS B1519-273 data span observing periods 1 to 24, a total of 657 days from day 105 of 2003 to day 31 of 2005. PKS B1622-253 monitoring started in observing period 3, so data for this source span observing periods 3 to 24, a total of 615 days from day 147 of 2003 to day 31 of 2005. The various PKS B1622-253 and PKS B1519-273 plots and supporting discussion are presented as follows:

Appendices A (PKS B1622-253) and B (PKS B1519-273)	Section
1. Flux density plots.	6.2
2. Data processing plots (data filtering and calibrator correction).	4.5.2
3. Autocorrelation & Power Spectral Density functions.	6.3.1
4. Data folding plots.	6.3.2

Section 6.3.7 summarises the characteristic variability time scales of the two sources for all observing periods; and Section 6.4 examines the scintle statistics and estimates error bars.

6.2 Flux Density Time Series

6.2.1 Observing Period Flux Densities

Figure 6.1 shows flux density data for PKS B1622-253 observing period 15, extracted from the flux density plots in Appendix A. The systematic diurnal fluctuations are evident, but the true variability on time scales longer than a day is also quite clear.

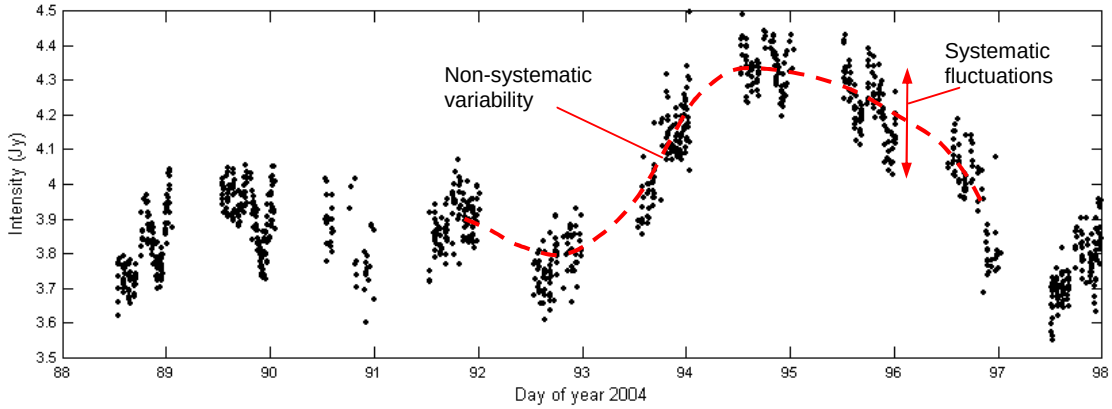

Figure 6.1 PKS B1622-253 flux density (Jy) data from observing period 15 in 2004.

Ceduna data in 2004/05 are generally of lower quality than 2003 data, as discussed in Chapter 5. Figure 6.2 shows PKS B1519-273 data for observing period 18, a period of extreme weather, extracted from the flux density plots in Appendix B. Less than 40% of the data passed the quality control tests, which usually pass at least 60% of the data.

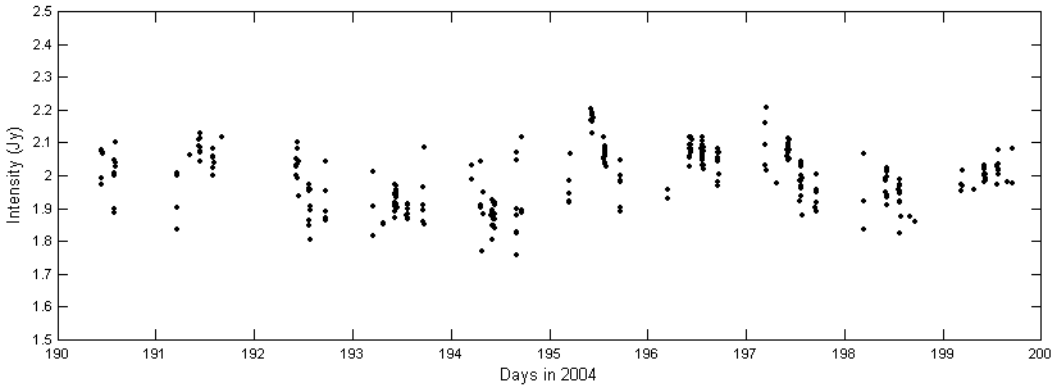

Figure 6.2 An example of bad data, in this case largely due to weather conditions. PKS B1519-273 flux density (Jy) data for days 190 - 200 in 2004.

6.2.2 Daily Mean Flux Densities

The daily mean flux density (Jy) plots show both the blazar data and the concurrent 3C227 calibrator data. Figure 6.3 shows the daily mean flux density plots of the PKS B1622-253 data shown in Figure 6.1, but spanning the entire observing period. PKS B1519-273 data are also shown. The RMS values of each day's data are shown as vertical error bars.

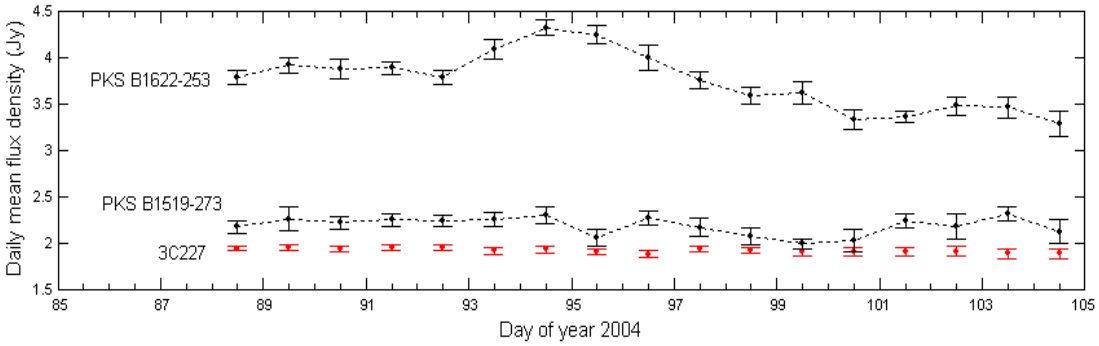

Figure 6.3 Daily mean flux density (Jy) plots for observing period 15 in 2004.

Daily mean flux density plots provide at-a-glance confirmation of the validity of the blazar data. The plots are also useful for examination of variability time scales on the order of several days, and they include periods of no data when the telescope was monitoring the southern source group, thereby giving an appreciation of the monitoring schedule.

6.2.3 Long Term Flux Densities

Ceduna's monitoring program is in a unique position to examine the presence of flux density variations on time scales of months to years. There have been other long term monitoring programs, such as those outlined in Section 2.4, but none with such complete intraday and interday sampling. Figure 6.4 shows the entire PKS B1519-273 and PKS B1622-253 data sets recorded over the 20-plus month period to early 2005.

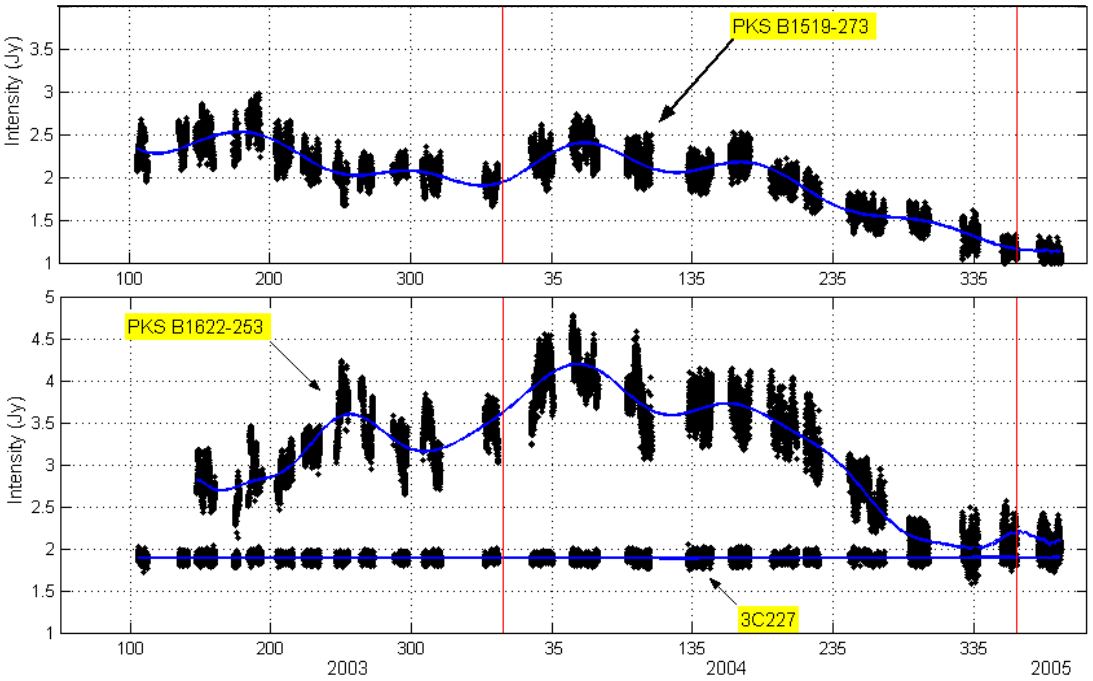

Figure 6.4 **2003/05 flux density (Jy) plots for PKS B1519-273 and PKS B1622-253. Data for the calibrator, 3C227, are also shown.**

In Figure 6.4, polynomial fits (the solid blue lines) track the variations in total flux density. The variations are superficially similar, particularly in 2004 when the flux densities of both sources at first increased, and then steadily decreased. However, this appears to be mere coincidence, given the flux densities of both the northern and southern group calibrators remained steady. In addition, the southern source PKS B1144-379 displayed a different flux density variation over the same 20 month period. An analysis of PKS B1144-379 data is planned as follow-on research.

Figures 6.5 and 6.6 show the flux density data for PKS B1622-253 and PKS B1519-273, for all the observing periods through to early 2005. The data have been converted to zero means with the flux density trend removed across each observing period, and corrections applied based on calibrator data (see Section 4.5). The low-frequency data component, $x_{\text{zero}}^{\text{Data}}$, is superimposed on the actual data as a solid black line. Each 50-day sub-plot has a vertical scale of ± 0.25 Jy, with tick marks at ± 0.20 Jy. Tables 6.1 and 6.2 set out observing period details and data statistics, with "Slow", "Slow zero", and "Fast" RMS values referring to the $x_{\text{smooth}}^{\text{Data}}$, $x_{\text{zero}}^{\text{Data}}$, and $x_{\text{zero}}^{\text{Fast}}$ data sets defined in Section 4.5. The "slow zero" RMS values are associated with flux density variability due to scintillation. Accurate monitoring of PKS B1519-273 became progressively more difficult in 2004, as its flux density decreased from over 2 Jy to ~1 Jy. However, this may not be the variability switching off: as discussed in Section 7.7, the modulation index does not show such a pronounced decrease, suggesting it is the flux density of the scintillating component of the source which has decreased.

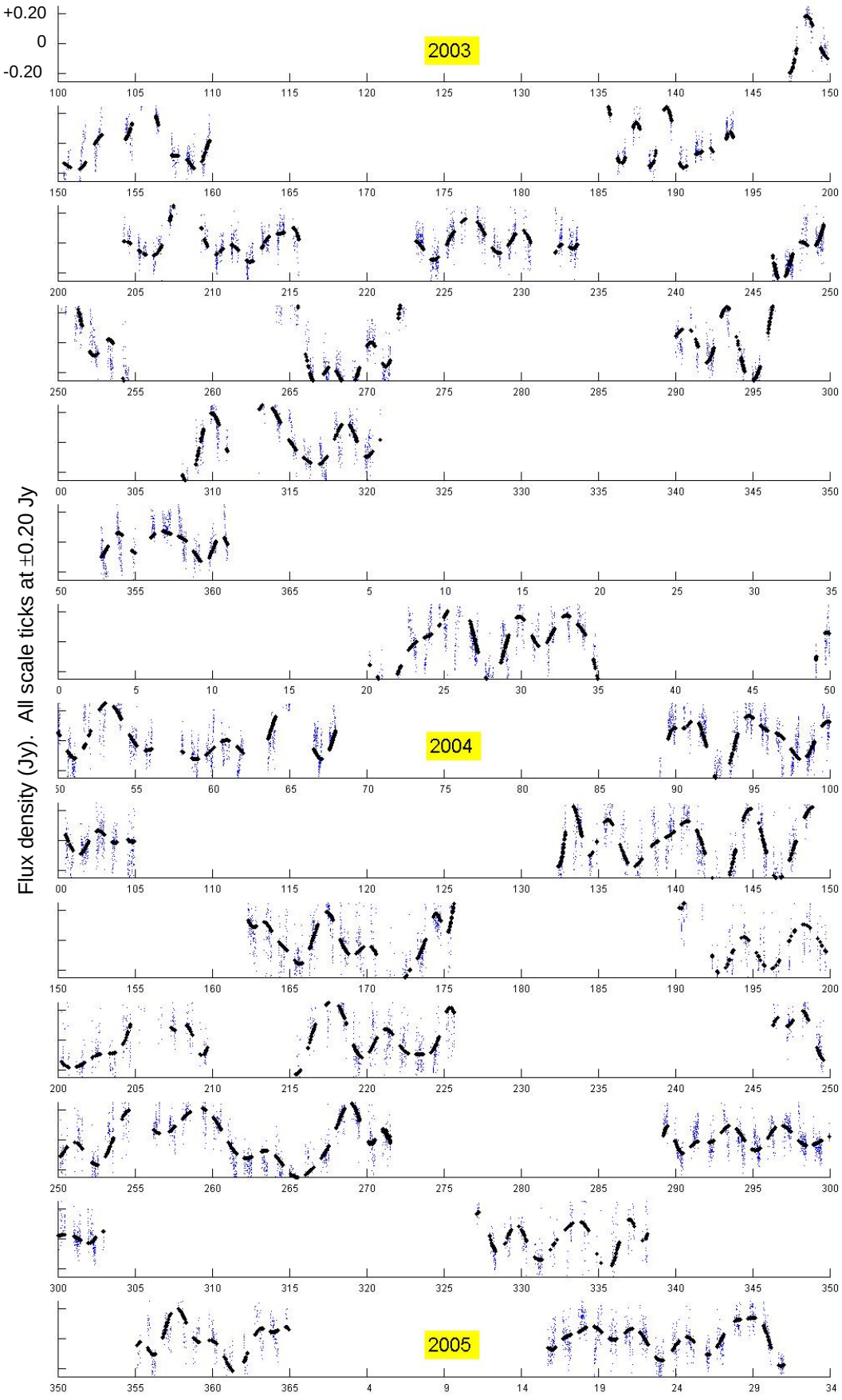

Figure 6.5 PKS B1622-253 flux density time series (Jy) in 2003/05. Compression of each time axis into 50 days of data tends to highlight the systematic fluctuations.

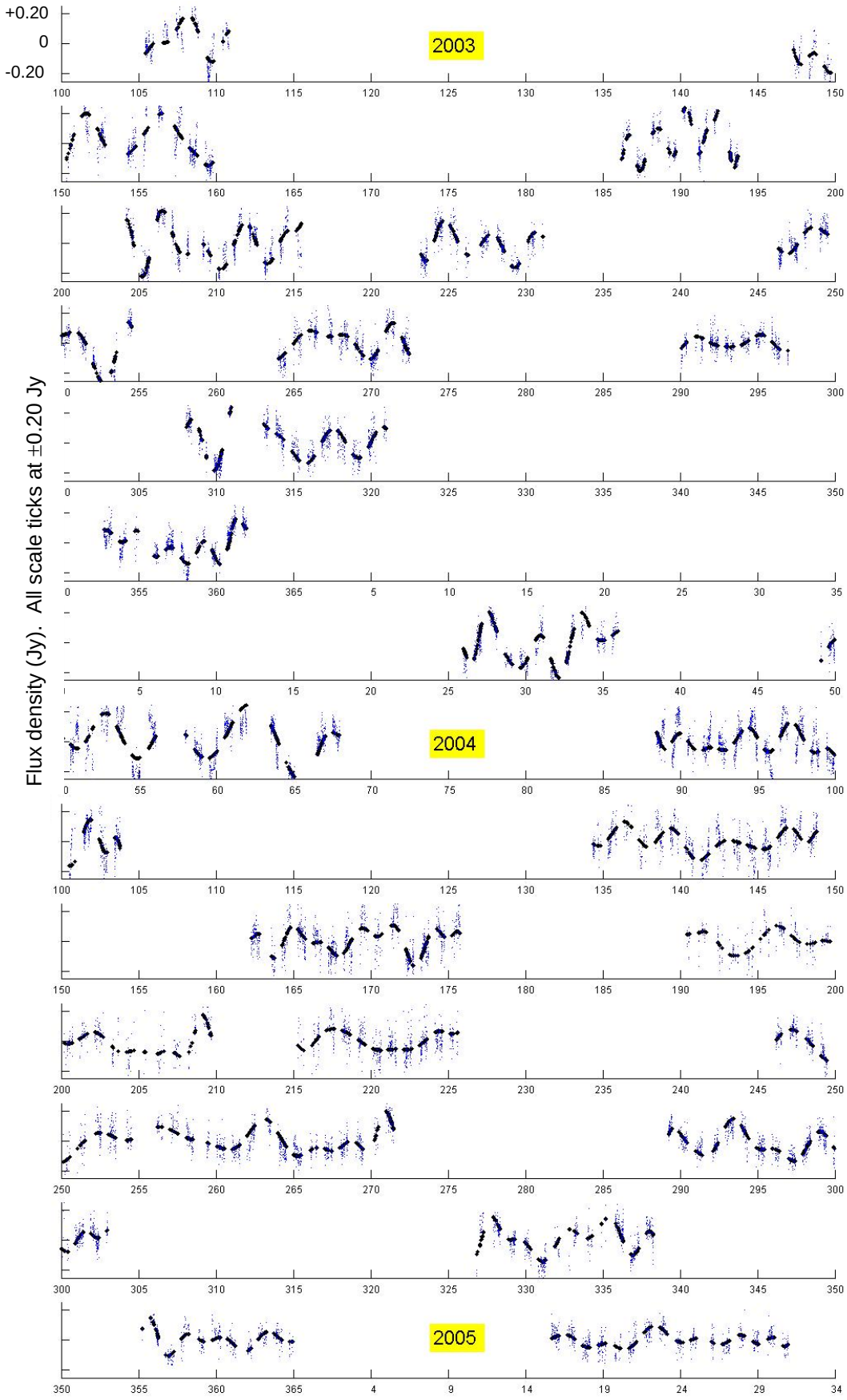

Figure 6.6 PKS B1519-273 flux density time series (Jy) in 2003/05. Compression of each time axis into 50 days of data tends to highlight the systematic fluctuations.

Table 6.1 PKS B1622-253

Period	Length (Days)	Middle day	Mean (Jy)	RMS values (mJy) Data	Slow	Slow zero	Fast	Fast RMS / Mean (%)
3	12.5	153.6	2.80	179	163	140	76	2.7
4	9.5	189.0	2.93	218	212	191	50	1.7
5	11.3	209.9	2.93	167	157	95	64	2.2
6	10.4	228.4	3.20	98	68	66	68	2.1
7	8.3	250.5	3.68	297	280	206	94	2.5
8	8.5	268.3	3.48	253	239	236	80	2.3
9	6.9	293.5	3.09	213	195	170	83	2.7
10	12.8	314.5	3.26	272	259	148	90	2.8
11	8.2	356.9	3.53	128	85	61	97	2.7
12	15.8	28.3	4.02	253	224	182	117	2.9
13&14	18.9	58.5	4.14	225	207	120	90	2.2
15	16.0	97.2	3.76	322	308	105	95	2.5
16	16.5	140.6	3.69	194	158	142	112	3.0
17	13.5	169.0	3.67	188	152	139	108	2.9
18	19.4	200.1	3.50	205	161	159	125	3.6
19	10.3	220.5	3.24	255	223	120	126	3.9
20	25.2	258.9	2.63	204	184	131	85	3.2
21	13.7	296.1	2.11	90.8	53	48	71	3.4
22	11.1	332.6	2.01	174	112	100	132	6.6
23	9.8	360.1	2.13	152	107	100	106	5.0
24	15.2	23.3	2.08	144	121	81	79	3.8

Table 6.2 PKS B1519-273

Period	Length (Days)	Middle (Day)	Mean (Jy)	RMS values (mJy) Data	Slow	Slow zero	Fast	Fast RMS / Mean (%)
1	5.3	109.2	2.31	143	131	107	59	2.6
2	5.5	138.1	2.40	166	155	158	57	2.4
3	12.5	153.6	2.44	158	131	115	86	3.5
4	7.5	189.0	2.64	155	145	116	53	2.0
5	11.3	209.9	2.34	135	115	113	75	3.2
6	7.9	228.4	2.19	125	112	88	57	2.6
7	8.3	250.5	2.04	143	132	98	56	2.8
8	8.5	268.3	2.04	98	76	71	62	3.0
9	6.9	293.5	2.13	60	33	29	50	2.3
10	12.8	314.5	2.02	112	95	95	58	2.9
11	9.2	357.4	1.92	94	78	83	52	2.7
12	10.0	393.3	2.18	149	133	118	69	3.2
13&14	18.9	423.5	2.40	158	121	101	96	4.0
15	15.3	462.2	2.20	128	92	68	90	4.1
16	14.5	505.6	2.06	106	70	60	80	3.9
17	13.5	534.0	2.22	112	76	69	81	3.7
18	19.4	565.1	1.98	96	65	63	70	3.5
19	10.3	585.5	1.81	105	74	52	74	4.1
20	25.2	623.9	1.57	108	92	71	57	3.6
21	13.7	661.1	1.51	84	66	68	50	3.3
22	11.1	697.6	1.33	104	81	76	63	4.7
23	9.8	725.1	1.18	73	56	50	46	3.9
24	15.2	754.3	1.13	65	43	38	47	4.2

Tables 6.1 & 6.2 Observing period details and data statistics for PKS B1622-253 and PKS B1519-273. The "slow zero" RMS values are associated with flux density variability due to scintillation.

6.3 Variability Characteristics

6.3.1 Autocorrelation and Power Spectral Density Functions

Autocorrelation functions (ACFs) and the associated power spectral density (PSD) functions are computed from the zero-mean low-frequency ("slow") data set, $x_{\text{zero}}^{\text{Data}}$, for each observing period. The lag increment is usually specified to be 4 hours, since the dominant variability time scale is on the order of days. The maximum lag time is usually specified as 10 days or the length of the observing period, whichever is greater, but is increased to 15 days for observing periods at the time of year in which scintillation-induced variability is expected to slow down (see Chapter 2). Figure 6.7 shows the ACF and PSD function computed from PKS B1622-253 observing period 9 data.

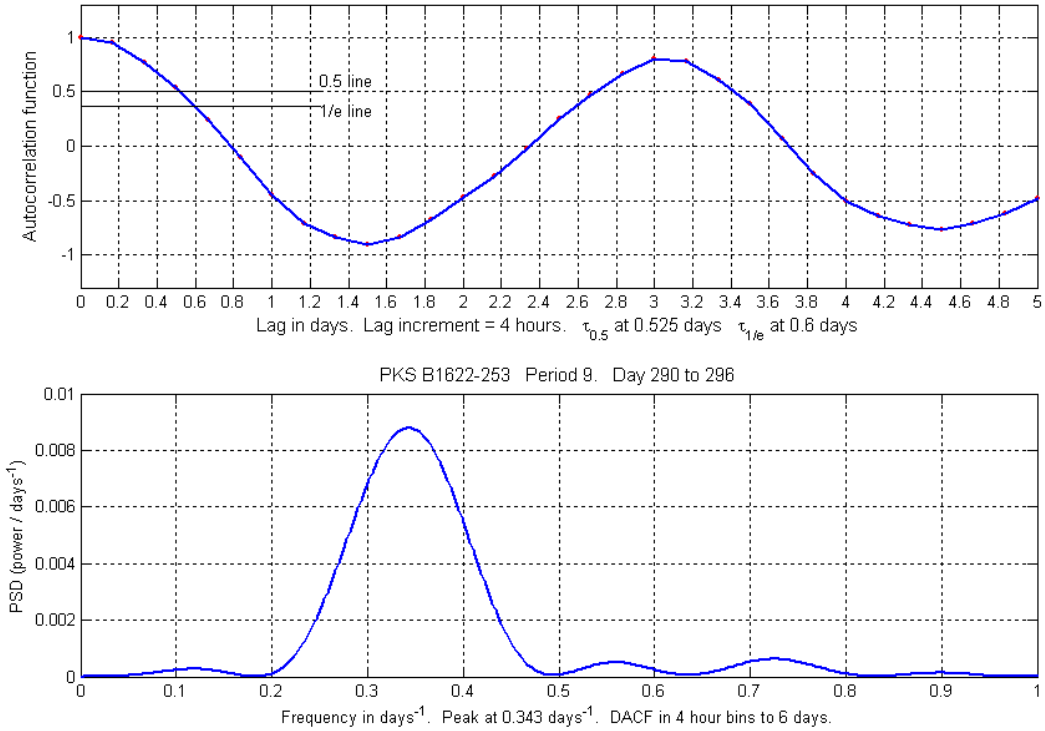

Figure 6.7 Autocorrelation function (top) and Power Spectral Density function (bottom) computed from PKS B1622-253 data for observing period 9.

The first ACF peak and the PSD peak correspond to the $T_{\text{char}} \sim T_{\text{period}} = 1 / f_{\text{period}}$ value, which is well defined at ~0.34 days^{-1}. The $T_{\text{char}} \sim T_{0.5}$ and $T_{\text{char}} \sim T_{1/e}$ lines are shown on the ACF plot, although these alternative definitions of the characteristic variability time scale are not used in this research for the reasons discussed in Section 4.4. As discussed in Section 4.4.2, the zero-lag noise spike is removed from each ACF, and the ACF is normalised to unity at zero lag time. For the example in Figure 6.7, the first negative overshoot is -0.92, which suggests the generating data set has a high degree of spectral purity, although a strong negative overshoot is also a feature of data sets that contain very few scintles, which may influence to some extent some of the values in Tables 6.4 and 6.5.

6.3.2 Data Folding Plots

Data folding plots provide a cross-check on the variability frequency determined by spectral analysis. Each data folding plot in the appendices is marked with a solid arrow denoting the folding frequency, and also with a dashed arrow denoting an alternative candidate variability frequency if one is apparent. The phase bin residual plot, in which the data are placed into hourly bins prior to folding, is useful in choosing between candidate frequencies.

Figure 6.8 shows a typical data folding plot, for PKS B1622-253 observing period 9 data. The arrow marks the frequency of ~0.32 days^{-1}, based on a clear match between a minimum in the data residual (sum-squared-error) plot, and a maximum of the expected size (~0.2 Jy) in the amplitude plot. As discussed in Section 4.3, the data folding exercise assumes a sinusoidal scintle morphology, an assumption which works well, and is justified by the high spectral purity evident in the ACFs from the high negative overshoots. However, it may be possible to refine the data folding exercise by fitting the folded data by a non-sinusoidal scintle, the nature of which would need to be determined by a study of scintle morphology.

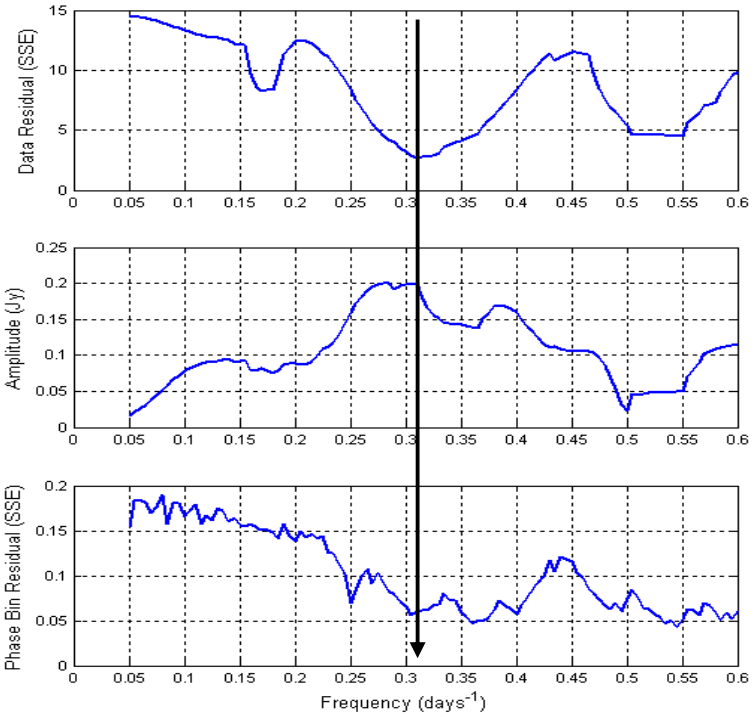

Figure 6.8 Data folding plot for PKS B1622-253 period 9 data.

6.3.3 Scintle Counting

Scintle counting provides an empirical cross-check on the variability frequency determined by spectral analysis. Scintle counting was facilitated by software developed by the author to locate peaks and troughs in an $x_{\text{zero}}^{\text{Data}}$ data set. The user identifies peaks and troughs of interest, with a cursor point-and-click direction, and the software pinpoints their locations. Figure 6.9 shows the procedure applied to PKS B1622-253 observing period 4 data.

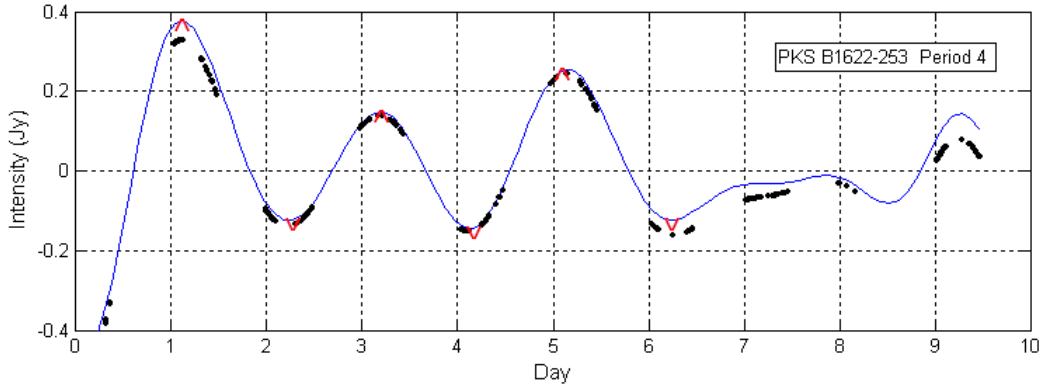

Figure 6.9 Semi-automated determination of scintle peak and troughs. The time differences between peaks and troughs are displayed as screen output.

The PSD for PKS B1622-253 observing period 4 has a clear peak that indicates a variability frequency of 0.5 days^{-1} and the data folding plot agees with this. In Figure 6.9, three peaks and three troughs are clear in the timeseries, defining 2½ scintles over a period of five days, which provides a second cross-check on the frequency determined by spectral analysis.

6.3.4 Small Flux Density Fluctuations

An interesting aspect of the blazar flux density data sets for some observing periods is the presence of small flux density fluctuations, in addition to more distinct fluctuations. Figure 6.10 gives examples of the phenomenon, all of which are discussed in the below sections.

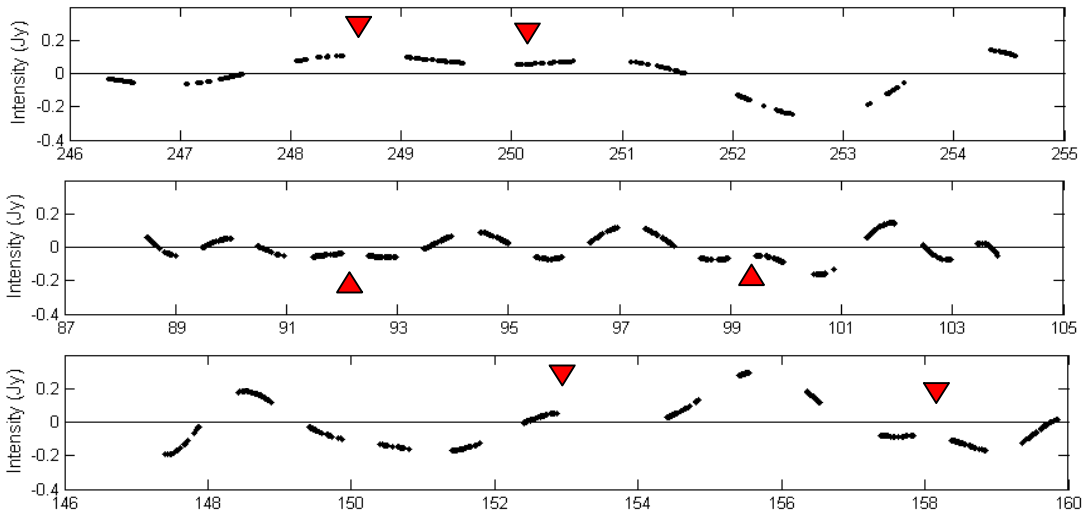

Figure 6.10 Examples of small flux density fluctuations. PKS B1519-273 observing periods 7 and 15; and PKS B1622-253 observing period 3.

Similar small flux density fluctuations are found in observations of scintillation in other blazars, an example being the PKS 1257-326 data shown in Figure 2 of the analysis reported by Bignall et al. (2003). The small flux density fluctuations are thus real: some may doubt the quality of the Ceduna data set, given the observations are made by a 30 m antenna, but there is no disputing the quality of the PKS 1257-326 data recorded by the ATCA.

These minor flux density fluctuations are expected. Section 4.6 examines flux density time series generated by simulations of power spectra associated with Interstellar Scintillation (ISS) in the weak scattering régime, and the random nature of the simulated ISS process indeed generates small fluctuations in addition to better defined scintles. In other words, a broad distribution of scintle heights is an expected characteristic of an ISS time series, and this is observed in the two blazars of interest to this research, as discussed in Section 6.4.4.

The presence of small flux density fluctuations often results in two candidate variability frequencies appearing in the PSDs, and in the data folding plots for those observing periods. The strongest PSD peak is not necessarily the one associated with the characteristic variability time scale, since it reflects the larger amplitude flux density fluctuations. Section 6.3.5 considers how best to take minor fluctuations into account in these situations, on a case-by-case basis.

The evidence suggests that PKS B1622-253 and PKS B1519-273 each scintillate with a single variability time scale, characterised by an annual cycle (see Chapter 7); and that the small flux density fluctuations seen in some observing periods are part of this variability. PKS B1622-253 and PKS B1519-273 data are adjusted in Chapter 7 to remove the annual cycle effects found in their variability time scales, and the cumulative PSDs of the adjusted data suggest the presence of only one scintillation time scale in each of these blazars.

Neverthless, alternative explanations for small flux density fluctuations are possible, notably either that the source has dual emission regions, or that a second ISM scattering screen present. In both cases, the small minor fluctuations would represent a genuine additional variability time scale. Scintillation on multiple time scales is often observed in pulsars, for example in PSR J0437-4715 (Gwinn et al., 2006). Dual variability has also been observed in quasar J1819+3845, but only the variability at 6 cm in this source is attributed to weak scattering (Macquart & de Bruyn 2007). Observations at 21 cm show additional, faster, variability which is attributed to DISS, and is probably unrelated to the physical mechanism that causes dual timescales in the weak scattering régime (Macquart & de Bruyn, 2006).

There are two aspects of the Ceduna observations in which possible additional variability characteristics may be present. First, when the source is observed during a “slow-down” time of year, which is the case for observing periods 7, 8, and 20, each scintle is observed over a period of many days instead of only a few days. Such observations have the potential to identify fine structure in the scintles, which Ceduna observations at other times of the year are unable to do.

In both sources, small flux density fluctuations are seen in these observing periods, and they are not accepted as defining scintles associated with the characteristic variability frequency, for the reasons given in the analysis notes set out in the two following sections.

Second, PKS B1519-273 observing periods 3 and 16, which span the "speed-up" time of year, show evidence of long period variability. The detection of variability in flux density data on time scales that are long compared to the length of an observing period may only be possible during the speed-up time of year.

The 2003/05 Ceduna data set is not of sufficient quality to examine the nature of small flux density fluctuations at the speed-up or slow down times of year. This is a goal of follow-on research, which hopefully will be based on data that are free of the systematic fluctuations contained in the 2003/05 data.

6.3.5 Variability Analysis Notes

Variability analysis notes for each PKS B1622-253 and PKS B1519-273 observing period are set out below, and refer to the plots attached in appendices A and B respectively. The variability frequencies are grouped into those which are well defined, fairly well defined, and poorly defined. Table 6.3 summarises the results of this classification scheme.

	PKS B1622-253	**PKS B1519-273**
Well defined	6 (0 of 6)	4 (0 of 4)
Fairly well defined	11 (6 of 11)	6 (3 of 6)
Poorly defined	4 (3 of 4)	5 (4 of 5)

Table 6.3 Number of observing periods associated with well, fairly well, and poorly defined variability frequencies. The brackets ( ) indicate the number of observing periods with two candidate variability frequencies.

- *Well defined variability frequencies* are those in which the PSD for the observing period has a strong single peak whose central frequency is unambiguously agreed both by the data folding plot and by a scintle counting exercise; the scintles have about the same amplitude; and the ACF negative overshoot is smooth and less than –0.55.
- *Fairly well defined variability frequencies* are those in which the variability analysis of the scintles recorded for the observing period is less clear. In several observing periods this is due to the presence of small flux density fluctuations, which in most cases are accepted as defining "genuine" scintles. Exceptions are discussed below.
- *Poorly defined variability frequencies* are those in which the variability analysis of the scintles recorded for the observing period is unclear. Also, several PKS B1519-273 observing periods are excluded from the analysis.

PKS B1622-253 Variability Analysis Notes

Well defined values (Periods 4, 6, 9, 10, 16 and 21)

Minor caveats on the classifying these six variability frequencies as well defined are:

- Period 6 has a small secondary peak associated with the 10 day length of the observing period, and the ACF has a kink as it falls to the first negative overshoot.
- Period 16 has a dominant PSD peak at 0.22 $days^{-1}$ that is not crisply defined due to non-uniformity in the scintle pattern. The data folding plot shows a single well defined feature at 0.20 $days^{-1}$.
- Period 21 has scintle amplitudes that are similar within the observing period, but a little smaller than those of the other five observing periods.

Fairly well defined values (Periods 3, 5, 7, 8, 12,15, 17, 18, 19, 20 and 22)

- In period 3, the flux density fluctuations at days 153 and 154 are accepted as defining a scintle. The resulting variability frequency of 0.29 $days^{-1}$ is agreed by the data folding plot, but corresponds to the secondary PSD peak.
- In period 5, the flux density fluctuations at days 210 and 211 are accepted as defining a scintle, giving a variability frequency of 0.29 $days^{-1}$ (as for period 3). This corresponds to the secondary PSD peak, with the dominant PSD peak reflecting the fact that the amplitude of one scintle is greater than the others, although the scintle is not completely observed due to a missing day of data. The data folding plot supports both possibilities.
- Periods 7, 8 and 20 span a slow-down time of year. Scintle counting shows the dominant PSD peaks result from ignoring the small flux density fluctuations at days 248 & 249, and days 252 & 253 in period 7; at days 267 & 268, and days 270 & 271 in period 8; and at days 250, 256 and 263 in period 20.

  Periods 7 and 8 thus each have a single scintle representing the characteristic variability frequency, and period 20 has only two scintles. The data folding plots also support ignoring the small fluctuations in favour of a variability frequency associated with the dominant PSD peaks, and the ACF negative overshoots are all strong.
- In period 15, a 5^{th} order polynomial is used to produce a zero-mean slow signal component. Usually a linear fit is sufficient for this purpose, but a linear fit applied to period 15 data produces a highly dominant scintle between days 93 and 97.
- Period 19 is similar to period 16: its dominant PSD peak is the only significant feature, and is strongly supported by the data folding plot. However, the scintles in the observing period are a little asymmetric, and the ACF's first negative overshoot is only -0.45.

- Periods 12 and 17 each have two dominant PSD peaks of roughly equal strength. The data folding plot for each period supports both possible variability frequencies, and the confusion results in ACF negative overshoots of only -0.41 and -0.46 respectively. The small flux density fluctuations in period 12 at days 23 & 25, and at day 31; and in period 17 at days 169 & 170, are accepted as defining scintles, and the higher frequency is thus chosen as the characteristic variability frequency.

- Period 18 is a long observing period with generally poor quality data, although the scintles are quite well defined. The PSD has two strong peaks, whose frequencies are both supported by the data folding plot. However, a small flux density fluctuation at day 203 appears to correspond to a poor polynomial fit through a genuine scintle. Taking this into account, scintle counting identifies the higher frequency PSD peak as characterising the variability.

- Period 22 has quite well defined scintles despite poor data quality in the second half of the period. The scintles are non-uniform, resulting in two PSD peaks of similar strength, and a data folding plot that supports both frequencies. The characteristic variability frequency is calculated from scintle counting as 0.29 $days^{-1}$.

<u>Poorly defined values (Periods 11, 13&14, 23 and 24)</u>

- In period 11, the scintles are non-uniform, resulting in two PSD peaks of similar strength, and data folding supports both frequencies. The ACF's negative overshoot is only -0.27. The variability frequency calculated from scintle counting is 0.31 $days^{-1}$.

- In the combined observing period 13&14, a 3rd order polynomial is used to produce a zero-mean slow signal component, since the 19 day period is too long for a linear fit to be appropriate. The scintle pattern has small flux density fluctuations, and analysis gives two PSD peaks of similar strength, and a data folding plot that supports both candidate frequencies. The lower candidate frequency is deemed to be characteristic, because the fluctuations are not accepted as defining scintles. They are believed to partly be due to the polynomial fit across missing data at days 57 and 63, and if accepted would define scintles with very different amplitudes.

- Period 23 appears to have a clear variability frequency of 0.175 $days^{-1}$, corresponding to a single strong PSD peak, and the data folding plot supports this finding. However, this peak corresponds to a single asymmetric scintle, and scintle counting shows the likely presence of an additional scintle defined by small fluctuations at days 359 & 360. This additional scintle is accepted as genuine, resulting in a more uniform scintle pattern that is fairly well supported by the data folding plot.

- In period 24, a 3rd order polynomial is used to produce a zero-mean slow signal component, since the period is quite long (16 days). This has the effect of clarifying the scintle pattern, and the dominant PSD peak is accepted as defining the characteristic variability frequency, supported by the data folding plot and by scintle counting.

PKS B1519-273 Variability Analysis Notes

Well defined values (Periods 4, 5, 6 and 12)

- The period 4, 5 and 6 scintle patterns are clear and fairly uniform. Each PSD function has a single dominant peak with a central frequency that agrees with the (unambiguous) values obtained from data folding and from scintle counting.
- Period 12 consists of a well defined, uniform set of scintles. A small fluctuation at day 26 represents a scintle that was not properly tracked by the polynomial fitting procedure to produce the zero-mean data set. The dominant PSD peak has a central frequency of 0.356 $days^{-1}$, which is supported by both scintle counting and the data folding plot.

Fairly well defined values (Periods 3, 7, 8, 14, 15 and 16)

- Period 7 spans the slow-down time of year. Small fluctuations are ignored in favour of recognising a single scintle with a trough-to-trough time of just over 5 days, a significant portion of the 9 day observing period. This scintle is clearly identified by the dominant PSD peak, and the data folding plot. The small fluctuations are associated with a weak secondary PSD peak and poorly defined secondary data folding plot feature.
- Period 8 is emerging from the slow-down time of year, and a long scintle similar to that of period 7 is followed by a distinctly shorter scintle. The PSD function and data folding plots reflect this dichotomy. A frequency of 0.259 $days^{-1}$, corresponding to the average of the two periods, is taken to be the characteristic frequency.
- Periods 13 & 14 and 15 are 18 and 17 days long respectively and a cubic polynomial was used to produce a zero mean slow variability data signal, rather than a linear fit. In period 13&14, the data was fitted with a polynomial of only order 16, to compensate for data missing at day 57, and poor data early in the observing period. The resulting scintle pattern is clear and uniform. The variability frequency is identified by the single dominant PSD peak, and supported by the data folding plot, and by scintle counting.
- In period 15, the scintle pattern is fairly uniform, but the variability analysis depends on whether or not minor flux density fluctuations at days 92 and 100 are interpreted as defining scintles. The PSD has a single peak that corresponds to the three scintles that remain in the absence of the additional scintles, but with an ACF negative overshoot of

only –0.45. Data folding supports both possibilities, but favours including all five scintles. The deciding factor in accepting the additional scintles is that this results in a more uniform scintle pattern, with a characteristic variability frequency of 0.41 $days^{-1}$.

- Periods 3 and 16 span the speed-up time of year, and some genuine variability occurs on time scales of just over a day, as discussed in Chapter 5. The PSD plots are thus based on analysis of <u>all</u> the data. The PSD peaks of 0.79 $days^{-1}$ and 0.96 $days^{-1}$ for periods 3 and 16 respectively are assumed to correspond to the variability frequencies. The data folding plots are messy and unhelpful. As discussed in Section 6.3.4, a puzzling feature of these two observing periods is that the PSDs and scintle counting exercises both show evidence of additional low frequency variability at about 0.2 to 0.3 $days^{-1}$.

<u>Poorly defined values (Periods 1, 9, 10, 11 and 17)</u>

- Period 1 spans only 7 days, and the data quality is generally poor, with substantial missing data. The data define two complete scintles, one of which is quite clear, with a variability frequency of 0.552 $days^{-1}$, and both the PSD and data folding plots support this value. A secondary PSD peak at 0.29 $days^{-1}$ is based on ignoring the poorly defined scintle, but neither the data folding plot nor scintle counting agree very well with this.

- Period 9 has one scintle that is well defined, but of very small amplitude. It is tempting to conclude that the source "switched off" for this observing period, but the scintle is real and is accepted. The frequency of the single PSD peak is at 0.288 $days^{-1}$. Scintle counting and the data folding plot suggest that the variability frequency lies closer to 0.26 $days^{-1}$.

- Period 10 finds the source back in action. However, the scintle pattern is quite non uniform, and is poorly defined near day 312 due to missing day and a half of data. The PSD function has two peaks of similar strength, and the data folding plot supports both candidate frequencies. The dominant PSD peak and the stronger data folding feature favour identifying two scintles between days 310 and 316, and this is accepted since the alternative is a single very asymmetric scintle.

- Period 11 has a PSD whose strongest peak is associated with the length of the observing period. The secondary peak at 0.48 $days^{-1}$ is believed to represent the true characteristic variability frequency. Similar comments apply to the data folding plot. Two reasonably clear scintles occur after day 357 of the observing period, and these have periods of just over 2 days, agreeing with the secondary PSD peak. Most of the data near day 355 is missing, but what remains defines the peak of a third scintle with a similar period.

- Period 17 has small flux density fluctuations that are accepted as defining scintles, giving four scintles between days 164 and 173. The strongest PSD peak favours ignoring the small fluctuations, but the scintle with a trough at day 173 is well defined, and its period favours the inclusion of the additional scintles. The data folding plot supports both possibilities.

Rejected values (Period 2, and periods 18-24)

Period 2 spans only 5 days, and two days have substantial missing data. This precludes detection of a variability frequency. The flux density of PKS B1519-253 decreases throughout 2004, and its variability becomes sporadic, possibly switching off. The poor data quality after period 17, the increasingly weak source strength, and the sporadic nature of the IDV behaviour, precludes variability analysis of periods 18-24.

6.3.6 Summary of Characteristic Variability Frequencies and Periods

Figures 6.5 and 6.6 show that PKS B1622-253 and PKS B1519-273 both have flux density fluctuations with characteristic variability times $T_{\rm char} \sim T_{\rm period}$ of typically several days, which change between observing periods.

Tables 6.4 and 6.5 summarise the estimated $T_{\rm period}$ values for the two sources in 2003/05. $T_{\rm char} \sim T_{0.5}$ estimates from the ACF are also given, although they are not used in the present research. The alternative candidate variability frequencies are shown for those observing periods in which the problem arises.

The variability periods shown in the tables, in the columns labelled $T_{\rm period}$, are calculated as the reciprocal of the variability frequencies determined by spectral analysis, shown in the columns labelled *PSD*. The cross-check frequencies provided by data folding are shown in the columns labelled *folding*. The cross-check variability frequencies determined by scintle counting are not shown, but are noted where appropriate in the analysis notes set out in the previous section.

In Tables 6.4 and 6.5, the first ACF negative overshoot values are given in the columns labelled *ACF overshoot*. These values are consistently large for both blazars, suggesting that in both cases the ISM scattering screen structures causing the scintillation have quite pronounced anisotropy. The ACF negative overshoots for PKS B1622-253 are consistently less than for PKS B1519-273, which suggests that the degree of anisotropy of the ISM scattering structures is greater for PKS B1622-253 than for PKS B1519-273.

Both these predictions are confirmed by the annual cycle analyses presented in Chapter 7.

Table 6.4 PKS B1622-253

Period	Middle day	ACF overshoot	---- Frequencies (1/days) ---- Folding	PSD		Times (days) T_{period}	$T_{0.5}$
3	153.6	-0.52	0.29	0.290	(0.145)	3.45	0.74
4	189.0	-0.87	0.47	0.503		1.99	0.34
5	209.9	-0.50	0.28	0.290	(0.151)	3.45	0.53
6	228.4	-0.81	0.25	0.231		4.33	0.51
7	250.5	-1.00	0.12	0.133		7.53	0.80
8	268.3	-0.47	0.10	0.129		7.77	0.60
9	293.5	-0.92	0.31	0.341		2.93	0.53
10	314.5	-0.85	0.24	0.237		4.22	0.60
11	357.4	-0.27	0.31	0.313	(0.140)	3.19	0.50
12	28.3	-0.41	0.28	0.280	(0.153)	3.57	0.76
13&14	58.5	-0.56	0.10	0.110	(0.273)	9.09	0.54
15	97.2	-0.53	0.22	0.220		4.55	0.48
16	140.6	-0.57	0.20	0.215		4.66	0.46
17	169.0	-0.46	0.27	0.283	(0.156)	3.53	0.53
18	200.1	-0.38	0.28	0.280	(0.151)	3.57	0.96
19	220.5	-0.48	0.25	0.256		3.90	0.47
20	258.9	-0.72	0.08	0.077		12.92	1.06
21	296.1	-0.67	0.26	0.255		3.92	0.42
22	332.6	-0.58	0.28	0.290	(0.416)	3.45	0.50
23	360.1	-0.65	0.17	0.176		2.63	0.67
24	23.3	-0.36	0.27	0.276	(0.130)	3.70	0.63

Table 6.5 PKS B1519-273

Period	Middle day	ACF overshoot	---- Frequencies (1/days) ---- Folding	PSD		Times (days) T_{period}	$T_{0.5}$
1	109.2	-0.52	0.60	0.552	(0.290)	1.81	0.35
3	153.6	0.13	Unclear	0.790	(0.206)	1.27	0.28
4	189.0	-0.52	0.58	0.500		2.00	0.30
5	209.9	-0.66	0.38	0.376		2.66	0.43
6	228.4	-0.71	0.32	0.348		2.87	0.45
7	250.5	-0.64	0.14	0.183		5.47	0.53
8	268.3	-0.61	0.21	0.259	(0.37, 0.20)	3.86	0.57
9	293.5	-0.71	0.26	0.288		3.47	0.53
10	314.5	-0.77	0.33	0.330	(0.200)	3.03	0.44
11	357.4	-0.01	0.48	0.480	(0.118)	2.08	0.70
12	28.3	-0.59	0.32	0.356		2.81	0.58
13&14	58.5	-0.64	0.20	0.219		4.57	0.45
15	97.2	-0.45	0.27	0.410	(0.271)	2.44	0.47
16	140.6	-0.10	Unclear	0.958	(0.100)	1.04	0.20
17	169.0	-0.50	0.44	0.460	(0.208)	2.17	0.55

Tables 6.4 & 6.5. Characteristic variability frequencies and periods for PKS B1622-253 and PKS B1519-273. Alternative candidate frequencies are shown in brackets. For PKS B1519-273, the Period 8 PSD is a mean value, while data for Periods 2 and 18-24 are not included in the variability analysis. See analysis notes for discussion.

6.4 Scintle Statistics and Error Bar Estimation

6.4.1 COSMIC Data vs ATCA Data

Data gathered by national facility telescopes are usually limited by telescope usage demands to fairly short observing periods, and error estimation methods for limited sampling of a stochastic process are required.

Data reduction and error estimation software packages are readily available, but the 2003/05 data gathered by the initial COSMIC blazar monitoring project enable a direct approach to estimating error bars for characteristic variability timescales, since sufficient scintles have been observed to examine the distribution of scintle periods and amplitudes. In the case of rapid scintillators, such as PKS 1257-326, the number of scintles recorded in an ATCA observing period is comparable to the number of scintles recorded by Ceduna for a slower scintillator in a 10-15 day observing period. However, the Ceduna data sets consist of many such observing periods, so the overall number of scintles is large even for a slow scintillator.

6.4.2 Estimation of Error Bars for T_{char} Values

The primary goal of error estimation is to place error bars on the characteristic variability time scales, $T_{char} \sim T_{period}$. In Chapter 7 the reduced chi-square values for the annual cycle model fits to the T_{char} values for PKS B1519-273 and PKS B1622-253 are shown to lie near unity, which indicates that the T_{char} error bars values estimated in the next section are appropriate, and have not been over-estimated or under-estimated.

There are two basic approaches to estimating error bars for T_{char}. The two approaches agree quite well, such that there is no need to pursue both. The approach used in this research is to use the distribution of scintle periods, normalised by T_{char} for each observing period (to remove the annual cycle effect), to assess the error bars associated with the T_{char} values. The empirical nature of this approach is an advantage, but it is subject to the assumption that the statistics of the normalised scintle distribution are constant over the whole data set.

However, consider the scintillation of quasar J1819+3845, analysed by Dennett-Thorpe & de Bruyn (2003). Their Figure 12 shows two years of flux density data after removal of the annual cycle effect in the observed scintillation, and the scintle statistics do not change significantly over the two years. Removal of the annual cycle effects in the scintillation of PKS B1622-253 and PKS B1519-273 is carried out in Chapter 7 with similar results.

An alternative T_{char} error estimation approach is based on examination of the (discrete) ACF. An ACF (e.g. Figure 6.9) often appears smooth with only a small degree of scatter between neighbouring points, which suggests that the error bars associated with each point are also small. But this is incorrect, since errors between neighbouring points in ACFs are highly correlated over a range of lag times roughly equal to the characteristic variability time scale, $T_{\text{char}} \sim T_{\text{period}}$ (see appendix A of Rickett et al., 2002, although they defined $T_{\text{char}} \sim T_{1/e}$).

Another way to see this point is to consider the ACF of a single scintle, with negligible errors in the flux density measurements. This ACF would be smooth, as would the ACF of an adjacent scintle, but in general the two ACFs would give different estimates of $T_{\text{char}} \sim T_{\text{period}}$ because the two adjacent scintles will not have exactly the same period.

Errors in correlation functions are considered by Jenkins & Watts (1968), Rickett et al. (2000), and Rickett et al. (2002). Analysis of a chopped signal is also discussed in Section 4.4.4. The errors result from additive thermal noise, usually only a small effect, and from estimation errors due to observing a stochastic process over a finite period. The error in a normalised ACF at lag time t is approximately given by (Rickett et al., 2002):

$$\varepsilon \approx \left[\frac{3\tau_F}{2 N_{\text{scints}}} \left\{ 1 - \exp\left(-\Psi\right) \right\} \right]^{1/2} \qquad \Psi = 2 \left(\frac{t}{1.2\, T_{\text{char}}} \right)^2$$

where N_{scints} is the number of scintles recorded in the observing period, with $T_{\text{char}} \sim T_{\text{period}}$. From Chapter 2, the scattering strength parameter, $u = L_F / s_o$, is approximately unity in the weak scattering limit, near the transition frequency, with the coherence scale, s_o, comparable to the Fresnel scale, L_F. The corresponding scintillation time scale for a point source is $\tau_F = s_o / V_{rel}$, although the value of s_o depends on the time of year if the scintle pattern is anisotropic, as is the case for both PKS B1622-253 and PKS B1519-273.

The annual cycle analyses presented in Chapter 7 show that nominal mean values of τ_F are ~2.3 days and ~1.3 days for PKS B1622-253 and PKS B1519-273 respectively. The ACF's first peak occurs at lag time $t = T_{\text{char}}$, so $\Psi = 1.39$. For the ACF of an observing period in which only two scintles are recorded, the error in T_{char} is $\varepsilon \sim 1.1$ days for PKS B1622-253 and $\varepsilon \sim 0.9$ days for PKS B1519-273, which correspond to 25% and 30% of the annual mean values of $T_{\text{char}} \sim 4.5$ days and $T_{\text{char}} \sim 3.0$ days for the two sources respectively.

This agrees reasonably well with the conclusion of the next section that assigning a ± 20% error bar to $T_{\text{char}} \sim T_{\text{period}}$ values calculated from two scintles corresponds to a confidence interval of ~95% (i.e. the 2-sigma interval) that the true T_{char} value lies within the error bars. In both approaches, the error bars scale as $\sqrt{N_{\text{scints}}}$, in accord with Gaussian error theory.

Comparison with Monte Carlo predictions

Section 4.4.8 reported on a Monte Carlo investigation of the effect of stochasticity in scintle periods, amplitudes, and phases on the ability to determine a characteristic variability time scale, $T_{\rm period}$. The investigation considered a time series of five scintles, and confirmed that detection of the variability time scale is, unsurprisingly, very sensitive to stochasticity in scintle periods; far less sensitive to stochasticity in scintle phases; and not at all sensitive to stochasticity in scintle heights.

The modelling found that the degree of stochasticity in the scintle periods must be small if the variability time scale is to be detected accurately. For a series of five scintles whose periods have a standard deviation of ~5%, a variability frequency of $f_{\rm o} = 0.62 \pm 0.09$ days^{-1} (mean ± s.d.) was detected, which is reasonable accuracy. When the standard deviation of the scintle periods was increased to ~10%, only an indicative $f_{\rm o}$ value could be determined.

Section 6.4.3 shows that the normalised (to remove the annual cycle effect) scintle period distribution is Gaussian to a good approximation. The 95% confidence interval error bar for $T_{\rm period}$ values calculated from a set of five scintles is estimated to be about $20\sqrt{2/5} = 12.6\%$. This is comparable to the $2\,\sigma \sim 10\%$ upper limit of the stochasticity in $T_{\rm period}$ values that the Monte Carlo modelling found would enable $T_{\rm period}$ to be computed with reasonable accuracy.

6.4.3 Scintle Periods

COSMIC data enable characteristic variability time scales to be determined in terms of the mean scintle periods, $T_{\rm char} \sim T_{\rm period}$, measured as the peak-to-peak or trough-to-trough time. A zero-crossing analysis would provide an alternative measurement method. The use of $T_{\rm char} \sim T_{0.5}$, the time taken for the ACF to fall to a value of 0.5, is not preferred for Ceduna data, for the reasons discussed in Section 4.4.

Consider a given 10-15 day observing period which records N adjacent scintles with periods T_1 to T_N., and a mean scintle period, $T_{\rm char} \sim T_{\rm period}$, calculated from these N values. The $T_{\rm char}$ estimate is associated with the middle of the observing period, with an uncertainty in time equal to the observing period. The deviation of scintle period T_i from $T_{\rm period}$ is:

$$T_{dev}^{i} = \frac{T_i - T_{\rm period}}{T_{\rm period}} \times 100\ \% \quad = \quad \left(\frac{T_i}{T_{\rm period}} - 1 \right) \times 100\ \% \qquad T_{\rm period} = \frac{1}{N} \Sigma\, T_i$$

This calculation approach avoids problems caused by the fact that T_{period} values typically change between observing periods either because of source evolution, or because of the annual cycle expected for scintillation caused by scattering in the ISM, or a combination of these two effects.

The non-dimensionalisation of the deviation of scintle periods with respect to T_{period} results in a distribution of T_{dev} values from different observing periods which are independent of such changes in T_{period}. The underlying assumption that the scintle distribution statistics are constant over the whole data set is discussed in the previous section. The assumption that T_{period} values are constant for the duration of an observing period is weakest during the slow down time(s) of year, notably near day 250. However, the method remains valid for these observing periods since they record only one or two scintles.

Table 6.6 shows PKS B1622-253 scintle periods for those observing periods with multiple scintles. There is good agreement between the direct estimate of $T_{\text{char}} \sim T_{\text{period}}$ and the value determined by the PSD.

Obs.	**Scintle periods (days)**			**Mean**	**PSD**	T_{dev} **(%)**	
Period	**#1**	**#2**	**#3**	T_{period}	T_{period}	**2 scintles**	**3 scintles**
3	4.55	2.62	–	3.6	3.5	27	–
4	2.03	1.99	–	2.0	2.0	1	–
5	4.14	2.21	–	3.2	3.5	30	–
9	2.53	3.37	–	3.0	2.9	14	–
10	3.53	5.33	–	4.4	4.2	20	–
11	2.86	3.85	–	3.4	3.2	15	–
12	2.76	3.95	3.24	3.3	3.6	–	13
15	3.59	4.87	–	4.2	4.6	15	–
16	2.96	5.51	3.78	4.1	4.7	–	23
17	3.30	2.76	3.37	3.2	3.5	–	8
18	3.20	3.88	4.37	3.8	3.6	–	11
19	3.45	4.27	–	3.9	3.9	11	–
21	3.23	3.78	–	3.5	3.9	8	–
22	4.05	3.22	–	3.6	3.5	12	–
23	3.00	2.26	2.46	2.6	2.6	–	11
24	3.05	3.43	4.50	3.7	3.6	–	15
Adjacent scintles							
12	2.76	3.95	–	3.4		18	
	–	3.95	3.24	3.6		10	
16	2.96	5.51	–	4.2		30	
	–	5.51	3.78	4.7		19	
17	3.30	2.76	–	3.0		9	
	–	2.76	3.37	3.1		10	
18	3.20	3.88	–	3.5		10	
	–	3.88	4.37	4.1		6	
23	3.00	2.26	–	2.6		14	
	–	2.26	2.46	2.4		4	
24	3.05	3.43	–	3.2		6	
	–	3.43	4.50	4.0		14	
					Mean	**13.7**	

Table 6.6 PKS B1622-253 scintle period analysis.

The upper panel of Table 6.6 shows T_{dev} values for the ten observing periods with only two complete scintles, and T_{dev} values for the six observing periods with three complete scintles. The lower panel gives additional T_{dev} values for pairs of adjacent scintles, computed from the six observing periods with three scintles. The mean T_{dev} value for adjacent scintle pairs is 13.7% ± 7.9% (mean ± standard deviation). The small number (six) of observing periods with three adjacent scintles does not enable their mean T_{dev} value to be reliably estimated.

Table 6.7 shows the same exercise applied to PKS B1519-273. Since this is a more rapid scintillator than PKS B1622-253, there are generally more scintles recorded in the same observing period. Again, there is good agreement between the direct $T_{\rm char} \sim T_{\rm period}$ estimates, and values determined from the PSD peak.

Obs.	**Scintle periods (days)**				**Mean**	**PSD**	**% Deviation from mean**		
Period	**#1**	**#2**	**#3**	**#4**	$T_{\rm period}$	$T_{\rm period}$	**2 scintles**	**3 scintles**	**4 scintles**
4	2.1	1.6	–	–	1.9	2.0	12	–	–
5	2.7	2.3	3.0	–	2.7	2.7	–	9	–
6	2.9	2.9	–	–	2.9	2.9	1	–	–
10	3.2	2.1	3.7	3.2	3.0	3.0	–	–	16
11	2.1	2.2	2.0	–	2.1	2.1	–	2	–
12	3.4	2.7	–	–	3.0	2.8	12	–	–
14	4.0	4.5	5.9	–	4.8	4.6	–	16	–
15	2.1	2.9	2.0	2.6	2.4	2.4	–	–	15
17	1.6	2.8	2.1	2.6	2.3	2.2	–	–	19
Adjacent scintles									
5	2.7	2.3	–	–	2.5		8		
	–	2.3	3.0	–	2.7		13		
10	3.2	2.1	–	–	2.6		21		
	–	2.1	3.7	–	2.9		29		
	–	–	3.7	3.2	3.5		8		
11	2.1	2.2	–	–	2.1		1		
	–	2.2	2.0	–	2.1		3		
15	2.1	2.9	–	–	2.5		17		
	–	2.9	2.0	–	2.5		19		
	–	–	2.0	2.6	2.3		13		
17	1.6	2.8	–	–	2.2		29		
	–	2.8	2.1	–	2.5		15		
	–	–	2.1	2.6	2.3		10		
						Mean	**12.6**		

Table 6.7 PKS B1519-273 scintle period (days) analysis.

Table 6.7 shows that the mean T_{dev} value for adjacent scintle pairs is 12.6% ± 6.8%, using adjacent scintle pairs from the five observing periods with more than two scintles to obtain sufficient T_{dev} values to compute a credible mean. There are insufficient observing periods with three scintles to enable mean T_{dev} values to be calculated for three adjacent scintles.

Figure 6.11 shows the distribution of T_{dev} values for adjacent scintles in PKS B1622-253 and PKS B1519-273 data. The highest and lowest T_{dev} values are excluded from the data, to avoid the influence of extreme values.

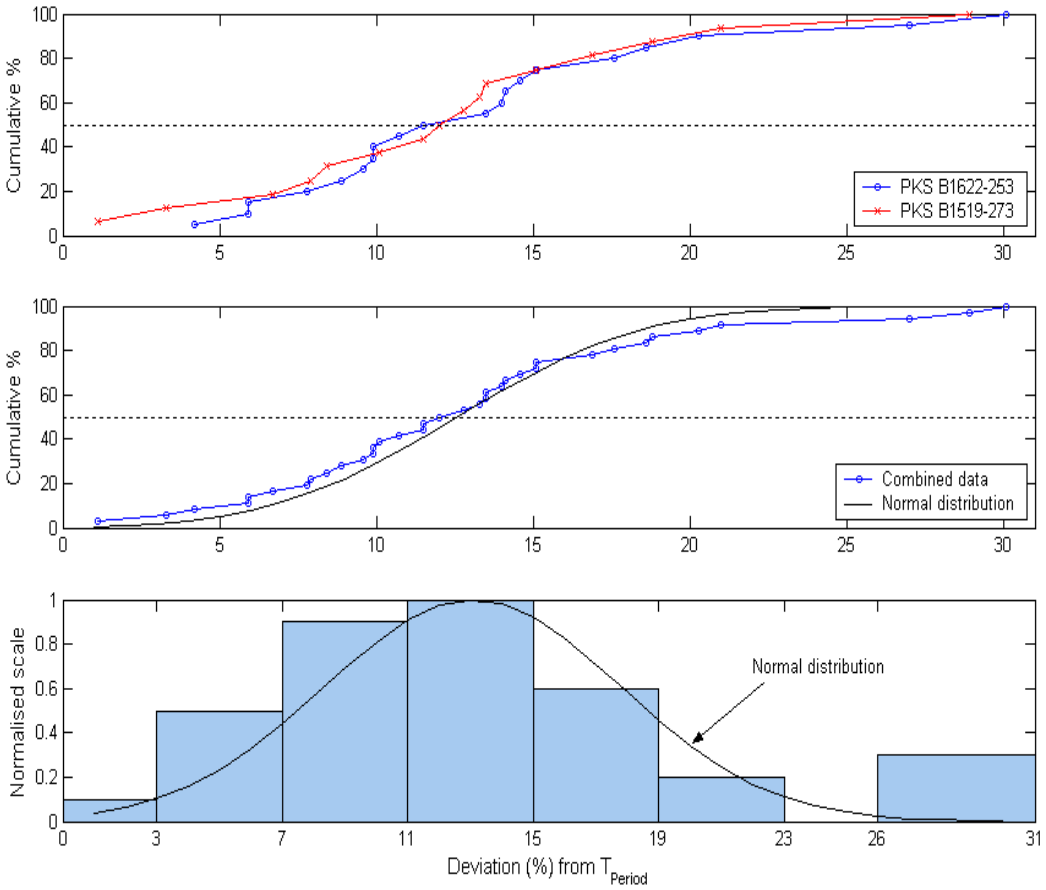

Figure 6.11 Distributions of T_{dev} values calculated from adjacent scintle pairs.

The top plot of Figure 6.11 shows the cumulative frequency plots are very similar for the two sources. The middle and lower plots show the cumulative frequency and the normalised frequency distributions of the combined T_{dev} values for both sources. The black lines in the plots show Gaussian distributions of data with the same mean and standard deviation values.

The distribution of T_{dev} values calculated from two scintles is close to being Gaussian, with a mean ± standard deviation of 13.1% ± 6.7%. In other words, half of all T_{dev} values calculated from two scintles are less than 13.1%, so if an observing period has a $T_{\rm period}$ value calculated from two scintles, an error bar of 0.13 $T_{\rm period}$ corresponds to a confidence interval of ~50% that the true $T_{\rm period}$ value lies within the error bars.

Assigning a ± 20% error bar to $T_{\rm char} \sim T_{\rm period}$ values calculated from two scintles corresponds to a (2-sigma) confidence interval of ~95% that the true $T_{\rm char}$ value lies within the error bars. The corresponding error bars for $T_{\rm period}$ values calculated from 1, 3 and 4 scintles are given by Gauss error theory as $20\sqrt{2/1} = 28\%$, $20\sqrt{2/3} = 16\%$, and $20\sqrt{2/4} = 14\%$ respectively.

The similarity of the PKS B1622-253 and PKS B1519-273 T_{dev} distributions means these T_{char} error bar estimates apply to both sources. However, if a T_{dev} value (given in Table 6.6 and Table 6.7) for an observing period is greater than the error bar estimate, then the T_{dev} value is used as the error bar instead. PKS B1519-273 observing periods 3 and 16 are analysed using the entire data set, and 28% error bars are applied to their T_{char} values.

The similarity of the T_{dev} distributions for the two sources can be explained by considering the power spectrum of temporal flux density variations, $P_{\Delta I}$. As discussed in Section 2.6.1, the power spectrum can be expressed as (e.g. Macquart & de Bruyn, 2006)

$$P_{\Delta I}(\omega) = \frac{1}{V_{rel}} \int_{-\infty}^{+\infty} dq_y \;\; P_{\Delta I}^{\text{Point}} \times \left| V \right|^2$$

where V_{rel} is the relative speed of the ISM with respect to the Earth, taken to be directed along the *x*-component of the 2-dimensional wavenumber vector, $\bar{q}$.

The point source flux density power spectrum, $P_{\Delta I}^{\text{Point}}$, is low-pass filtered by $\left| V \right|^2$, where V is the source visibility. The filter represents the effect of the source size, and these two blazars are large enough that the scintillation process is band-limited in similar ways.

6.4.4 Scintle Heights

Tables 6.8 and 6.9 show PKS B1519-273 and PKS B1622-253 scintle heights respectively, for the same multi-scintle observing periods considered previously. The scintle heights are defined as the mean peak-to-trough flux density differences, and are given in the upper left portions of the tables, in columns #1 to #4. The mean scintle heights are 275 ± 120 mJy and 221 ± 110 mJy for PKS B1622-253 and PKS B1519-273 respectively.

The RMS of the variability in each observing period can be estimated by multiplying the mean of the measured scintle heights by $0.5/\sqrt{2}$, which is the RMS of a sinusoidal plane wave with unit height. These RMS estimates are given in the column labelled "$0.5/\sqrt{2}$". The RMS values can also be computed directly from the flux density time series for each observing period, and these values are given in the columns labelled "RMS".

The two sets of RMS values agree fairly well, giving confidence in the scintle height measurements. Agreement within ~20% is achieved for 16 of the 25 observing periods, evidence that the scintles are quasi-sinusoidal. Better agreement is not expected, since the $0.5/\sqrt{2}$ conversion factor is only correct for a uniformly sampled sinusoidal plane wave, and such sampling is not possible for sources only observed for a fraction of each day.

The distribution of scintle heights can be examined both directly, and in terms of scintle height deviations from the mean height, H_{mean}, for each observing period, paralleling the approach taken in the previous section to analysing the distribution of scintle periods. This distribution is not influenced by changes over time in the scintle height, assuming such changes to be small for the 10-15 days of an observing period. The deviation of scintle height H_i from H_{mean} for an observing period, is:

$$H_{dev}^{i} = \frac{H_i - H_{\text{mean}}}{H_{\text{mean}}} \times 100\,\% \quad = \quad \left(\frac{H_i}{H_{\text{mean}}} - 1 \right) \times 100\,\% \qquad H_{\text{mean}} = \frac{1}{N} \Sigma\, H_i$$

Tables 6.8 and 6.9 show the H_{dev} values computed for PKS B1519-273 and PKS B1622-253 multi-scintle observation periods. The number of H_{dev} values for adjacent scintle pairs are augmented by H_{dev} values computed from adjacent scintle pairs in observing periods with more than two scintles.

Obs.	**Scintle heights (mJy)**					$\times 0.5/\sqrt{2}$	**RMS**	**H_{dev} (%) for N scintles**		
Period	**#1**	**#2**	**#3**	**#4**	**mean**		**(mJy)**	**N=2**	**N=3**	**N=4**
4	236	326	–	–	281	100	116	16	–	–
5	364	131	287	–	261	92	113	–	33	
6	253	182	–	–	217	77	88	16	–	–
10	458	117	219	203	249	88	95	–	–	42
11	124	085	151	–	120	42	83	–	19	
12	303	363	–	–	333	118	118	9	–	–
14	264	266	446	–	325	115	101	–	25	
15	089	184	118	258	162	57	68	–	–	36
17	061	146	063	262	133	47	69	–	–	54
Adjacent scintles										
5	364	131			247	87		47		
	131	287			209	74		37		
10	458	117			288	102		59		
	117	219			168	59		31		
	219	203			211	75		4		
11	124	085			104	37		19		
	085	151			118	42		28		
15	264	266			265	94		1		
	266	446			356	126		25		
	089	184			136	48		35		
17	184	118			151	53		22		
	118	211			165	58		29		
	061	146			103	37		41		
	146	063			104	37		40		
							Mean	**26.9**		

Table 6.8 Scintle height (mJy) analysis for PKS B1519-273.

Obs. Period	Scintle heights (mJy) #1	#2	#3	mean	$\times 0.5/\sqrt{2}$	RMS (mJy)	H_{dev} (%) 2 scintles	3 scintles
3	305	175	–	240	85	140	27	–
4	372	343	–	358	127	191	4	–
5	460	086	–	273	96	95	69	–
9	298	565	–	431	153	170	31	–
10	373	350	–	361	128	148	3	–
11	144	199	–	171	61	61	16	–
12	152	391	308	283	100	182		31
15	439	269	–	354	125	105	24	–
16	271	378	506	385	136	142	–	21
17	320	180	316	272	96	139	–	23
18	470	264	192	309	109	159	–	35
19	286	242	–	264	93	120	8	–
21	167	104	–	136	48	48	23	–
22	242	313	–	278	98	100	13	–
23	266	111	155	177	63	100	–	33
24	082	185	181	149	53	81	–	30
Adjacent scintles								
12	152	391	–	271			44	
	–	391	308	349			12	
16	271	378	–	324			16	
	–	378	506	442			15	
17	320	180	–	250			28	
	–	180	316	248			27	
18	470	264	–	367			28	
	–	264	192	228			16	
23	266	111	–	188			41	
	–	111	155	133			17	
24	082	185	–	133			39	
	–	185	181	183			1	
						Mean	**22.7**	

Table 6.9 Scintle height (mJy) analysis for PKS B1622-253.

Figure 6.12 shows the distribution of scintle heights, which are clearly skewed towards smaller scintle heights. The skews are an expected consequence of scintillation caused by scattering in the ISM, for observations in the vicinity of the transition frequency, since in the weak scattering limit the flux density power density function has a Gaussian form, while in the strong scattering régime it has an exponential form.

The skews may also reflect source evolution. The flux densities of PKS B1622-253 and PKS B1519-273 evolved significantly, especially during 2004 (see Figure 6.4). If the flux density of the scintillating component of a source changes, so will the scintle height, such that the modulation index remains constant.

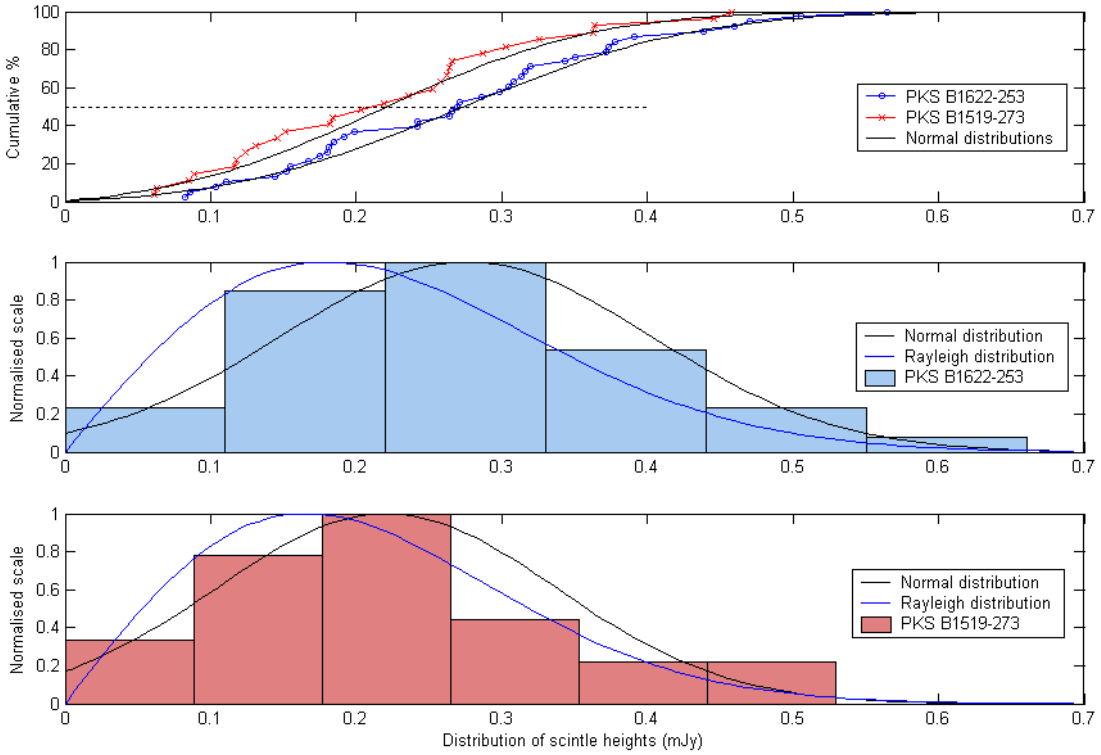

Figure 6.12 Scintle height (mJy) distributions for PKS B1622-253 and PKS B1519-273.

The scintle height distributions shown in Figure 6.12 are poorly defined, and they could be described by any of several distributions. Both Gaussian and Rayleigh distribution fits to the data are shown in Figure 6.12, as examples of alternative (and equally valid) distribution functions. The best Gaussian fits to the data have the same means as the data, but standard deviations of 0.181 mJy and 0.166 mJy, ~1.5 times larger than the data standard deviations.

Although the physics of ISM scattering and ocean waves are quite different, it is interesting that scattering structures in the ISM plasma are sometimes described by analogy to ocean waves, since ocean wave heights follow Rayleigh distributions, with more small waves observed than large waves.

It is also possible that the skews in the scintle height distributions reflect under sampling of large scintle heights. But the counter argument is that the mean scintle heights agree quite well with the data RMS values, as discussed above.

Figure 6.13 shows the two distributions of H_{dev} values for adjacent scintle pairs. The H_{dev} distributions are quite flat. The mean ± standard deviation H_{dev} values computed from adjacent scintle pairs for PKS B1622-253, PKS B1519-273 and the combined data, are 22.7% ± 15.7%, 26.9% ± 15.6% and 24.6% ± 15.6% respectively.

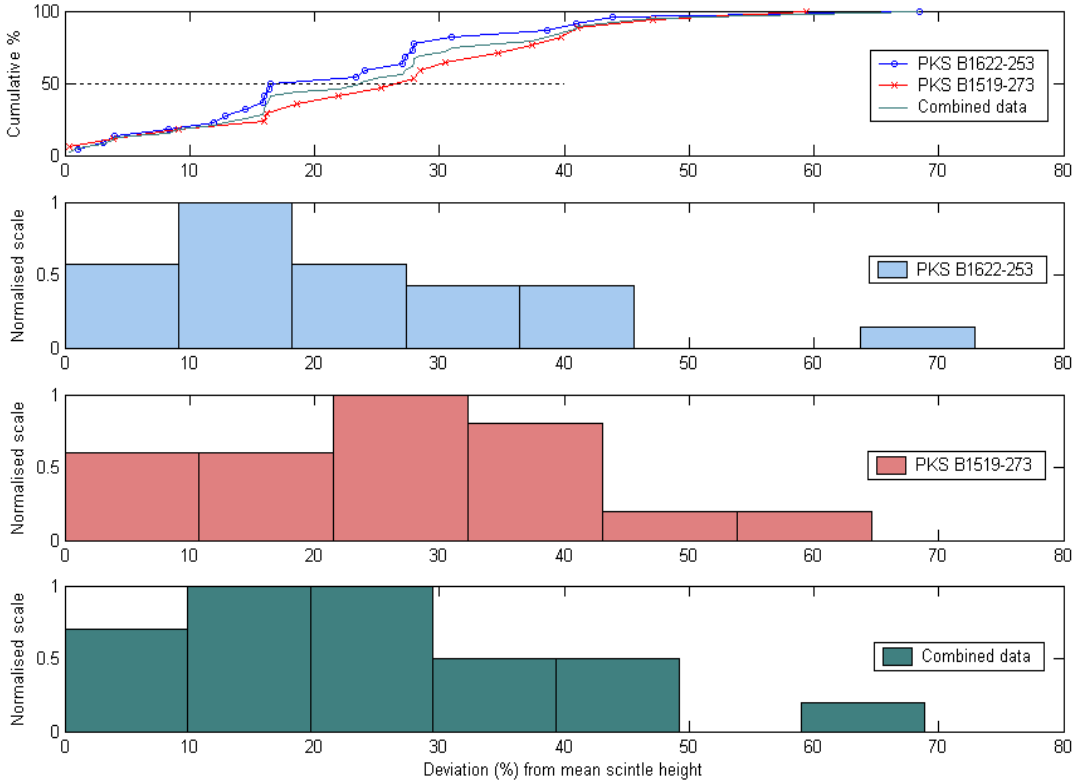

Figure 6.13 Distributions of H_{dev} values calculated from adjacent scintle pairs.

It is estimated from Figure 6.13 that a 40% error bar for H_{dev} values calculated from two adjacent scintles corresponds to a confidence interval of ~80%. Thus, if an H_{mean} value for a given observing period is calculated from two scintles, an error bar of 0.4 H_{mean} corresponds to a confidence interval of ~80% that the true H_{mean} value lies within the error bars (for this non-normal distribution an 80% confidence interval seems more appropriate than a 95% confidence interval). Since H_{mean} values and the data RMS values are correlated under the assumption of quasi-sinusoidal scintles, a 0.4 RMS error bar applied to the RMS value also has a confidence interval of ~80%

The ~80% confidence interval error bars for RMS values calculated from observing periods with 1, 3 and 4 scintles are $40\sqrt{2/1} = 57\%$, $40\sqrt{2/3} = 33\%$, and $40\sqrt{2/4} = 28\%$ respectively, for both PKS B1622-253 and PKS B1519-273. As with scintle periods, if the H_{dev} value for an observing period is greater than the default error bar, then the H_{dev} value is used as the error bar instead. As discussed in Section 6.3.5, the analysis of PKS B1519-273 observing periods 3 and 16 uses the entire data, not just the fast component of the data, and 57% error bars are assumed for these H_{dev} values.

7.0 ANALYSIS OF PKS B1622-253 and PKS B1519-273

7.1 PKS B1622-253 Observations

7.1.1 Source Overview

Blazar PKS B1622-253 is listed in the first Parkes catalogue (Bolton et al., 1975), with flux densities of 2.3 Jy and 2,0 Jy at 2.7 GHz and 5 GHz respectively. It is optically very faint and lies behind the Ophiuchus Cloud, a dense interstellar gas cloud south of ρ Ophiuchus (Hunter et al., 1994). Nearby PKS 1628-268 is also faintly visible, and optical polarisation measurements by Impey & Tapia (1990) may refer to this object (Stickel et al., 1994). It is now established that PKS B1622-253 has a redshift of $z = 0.786$ (di Serego-Alighieri et al., 1994) and an unresolved optical counterpart of magnitude 21.9 (Schlegel et al., 1998).

Gamma ray emissions from PKS B1622-253 were detected by the Energetic Gamma-Ray Experiment Telescope (EGRET) on board the Compton gamma ray observatory (Nolan et al., 1996). From the EGRET observations, Hunter et al. (1994) tentatively determined the gamma ray spectrum of PKS B1622-253 to be described by a power law with spectral index -1.9 ± 0.3. However, PKS B1622-253's gamma ray flux is variable, and changed by a factor of ~2 over the 1991-93 EGRET observation period.

7.1.2 Extended structure

Detailed radio images of PKS B1622-253 were made in June 2002, at 3.6 cm (8.3 GHz) and at 6 cm (4.8 GHz), using the Very Large Array (VLA). Punsly et al. (2005) presents a 6 cm VLA image, reproduced as Figure 7.1. PKS 1628-268 is the nearest radio source to PKS B1622-253, but it does not confuse the VLA image.

Figure 7.1 shows that PKS B1622-253 has an extended radio structure whose main features are a powerful radio core, FR II radio lobes consisting of a diffuse jet-like eastern extension, and a western lobe that is also part of a jet. This structure is consistent with the core-jet morphology of the central engine model. Punsly et al. (2005) estimate the core flux density of PKS B1622-253 to be 1.91 Jy at 8.3 GHz, with western and eastern extended components of 24 and 35 mJy respectively, obtaining the flux densities of the lobes by subtracting a point source with the flux density and position of the core from the (u,v) data. They found that the central engine accretion flow for this blazar is no more than 10^{46} ergs /s, which is weak by quasar standards, although the source is nevertheless associated with a powerful jet with a superluminal speed estimated to be ~14 h^{-1} c (Jorstad et al., 2001). They note that PKS B1622-253 is not unusual in this regard, and that high Doppler factors should be expected for this blazar, especially in flare states.

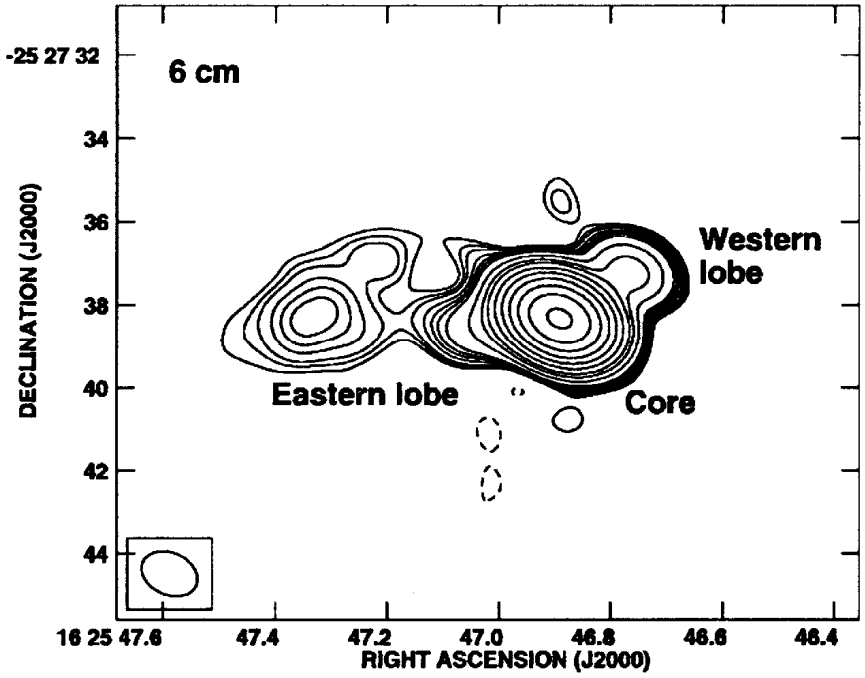

Figure 7.1 VLA 6 cm image of PKS B1622-253 (Punsly et al., 2005).

PKS B1622-253 images provided by the NASA / IPAC Extragalactic Database are cited as having been recorded by the 2 cm (15 GHz) Very Large Baseline Array surveys reported by Kellermann et al. (1998; 2004) and Lister & Homan (2005), and a typical image is given in Chapter 3. However, the source is not actually mentioned in any of the survey reports.

Bignall (2003) presents a 6 cm (4.8 GHz) PKS B1622-253 image made by the Australia Telescope Compact Array, similar to the image shown in Figure 7.1. Tingay et al. (1998) report VLBI observations of PKS B1622-253, with an estimated core size 0.6 x 0.5 mas at 8.4 GHz and an estimated core flux density 0.6 Jy at 8.4 GHz. This does not agree very well with the estimate of Punsly et al. (2005), probably due in part to the variability of this source, and in part because some of the flux density seen in the VLA core is likely resolved out in the VLBI images, which are on milliarcsecond scales.

7.1.3 Radio variability

PKS B1622-253 has pronounced intrinsic radio variability over periods of months. Tingay et al. (1998) note that the Parkes 90 catalogue records its flux density as 2.02 Jy at 5 GHz, but the subsequent Parkes-MIT-NRAO survey records its flux density as 3.5 Jy at 4.85 GHz; and they also note that ATCA observations found its flux density at 8.6 GHz decreased from 2.5 Jy to 0.9 Jy in the 10 months before July 1996. Similarly, 22 GHz observations by the VLBA, reported by Jorstad et al. (2001), found the flux density of the core to vary by a factor of five over the course of a year.

The variability of PKS B1622-253 over periods of months to years is presumed to be intrinsic to the source, and the COSMIC 2003-05 program shows this variability to be a continuing characteristic. Its 6.7 GHz flux density increased from 2.7 Jy in early 2003 to 4.2 Jy a year later, and then decreased to 2.1 Jy by early 2005 (see Figure 6.4).

PKS B1622-253 radio variability on time scales of days was discovered by the ATCA blazar monitoring program from July 1997 to January 2002 (Bignall, 2003). PKS B1622-253 was unfortunately excluded from the earlier 1994 ATCA survey of intraday variables (Kedziora-Chudzer et al., 1997) because it failed to meet a compactness selection criterion. The source also displays circular radio polarisation variability (Tingay et al., 2003), which unfortunately is too weak to be observed by the Ceduna telescope.

Dr Bignall kindly provided the multi-frequency ATCA data from Bignall (2003). The total flux density (Stokes *I*) light curves are re-plotted as Figures 7.2 and 7.3 and have one minute averaging. The lower plot of Figure 7.3 shows the daily means of the 2001-02 observations, highlighting the intrinsic variability of PKS B1622-253 over time scales of months.

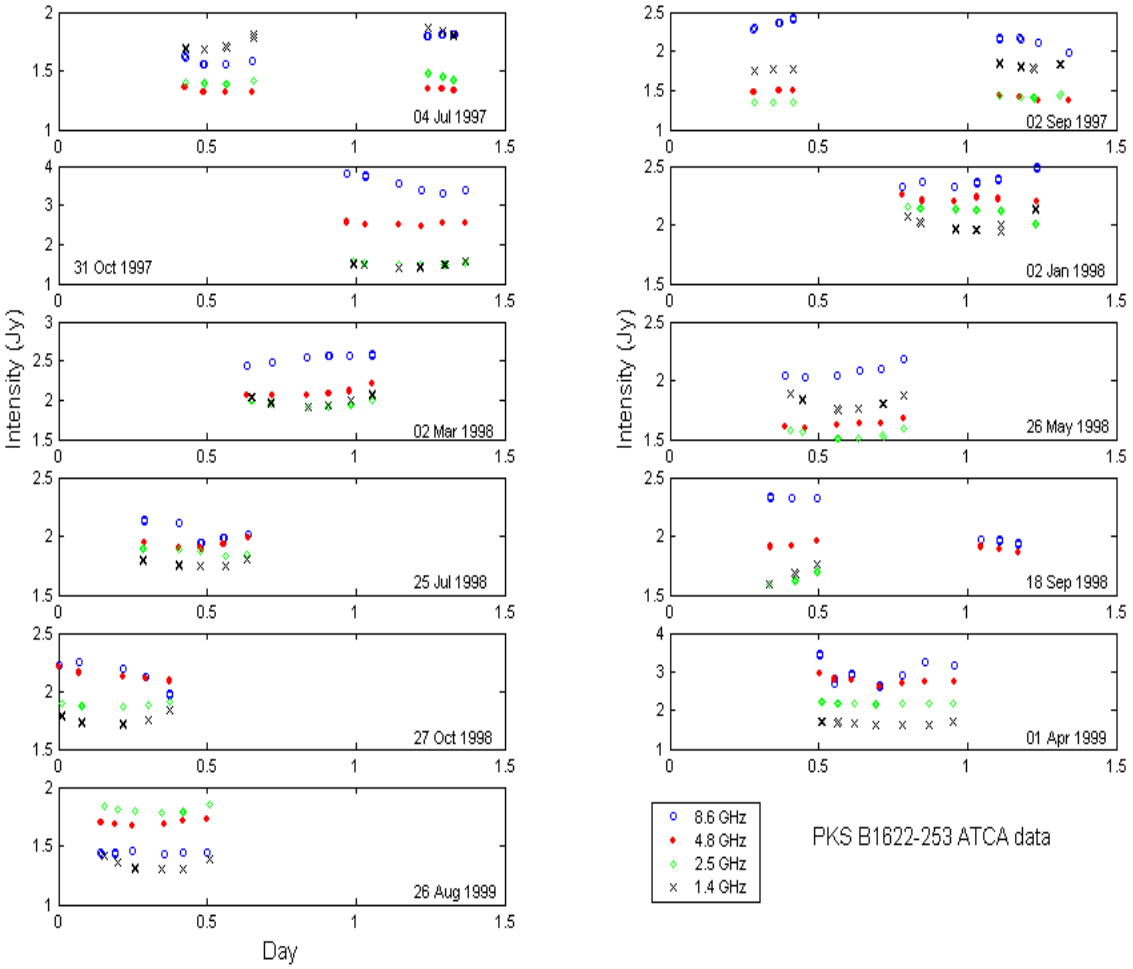

Figure 7.2 Multi-frequency observations of PKS B1622-253 by the ATCA 1997-99.

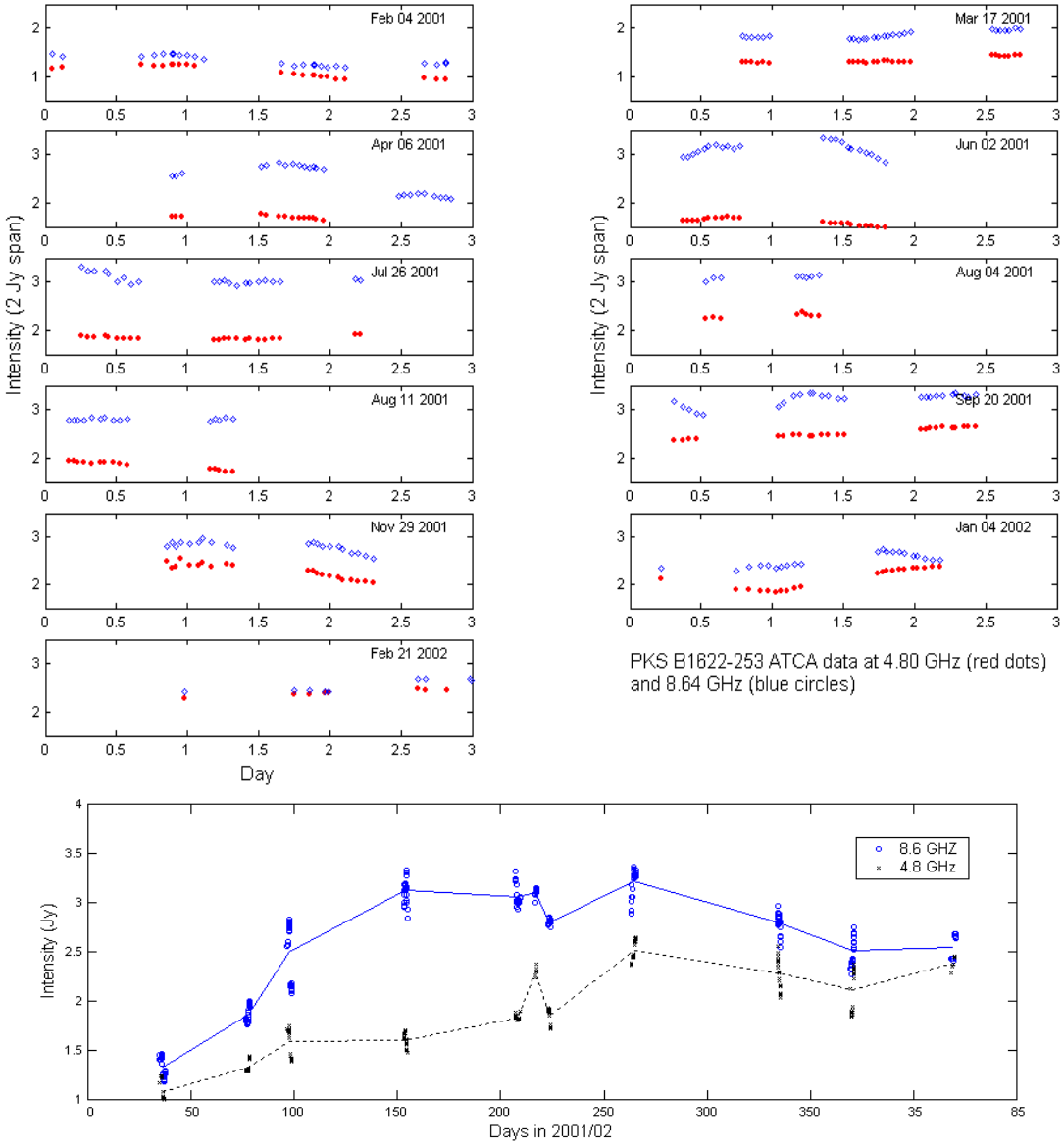

Figure 7.3 ATCA 4.8 and 8.6 GHz observations of PKS B1622-253 in 2001-02. The lower plot shows daily means of the flux densities shown in the upper plot.

The construction of radio images by interferometry must consider variations in flux density due to the changing amount of flux density seen on each baseline as the beam pattern rotates through the sky. One approach is to map the source and subtract its extended components from the data in the (u, v) plane, leaving the point source.

Bignall (2003) applied the extended structure subtraction method outline above to the data from ATCA project C927, shown in Figure 7.3, but not to the earlier data from project C639, shown in Figure 7.2. However, for PKS B1622-253, flux density variations due to extended source structure and confusion are small. Bignall (2003) estimated the percentage flux density in extended components and confusing sources from the closure phases as: 4.1%, 2.7%, 1.5% and 1.2% at 1.4, 2.5, 4.8 and 8.6 GHz respectively, with mean flux densities of 1.80, 1.76, 1.98 and 2.30 Jy at these frequencies.

Defining the spectral index, α, such that $S_\nu = \nu^{-\alpha}$ (see Section 1.3), Tingay et al. (2003) found α = -0.4 between 4.8 and 8.6 GHz, for ATCA observations of PKS B1622-253 over the 10 months to July 1996. Bignall (2003) found α = -0.52 between 4.8 and 8.6 GHz, based on her 2001-02 ATCA observations of PKS B1622-253. Punsly et al. (2005) found that the spectral indices for the core and the (steep-spectrum) west and east lobes shown in the 6 cm VLA map of June 2002 (Figure 7.1), were α = -0.06, +0.64 and +0.66 respectively.

7.1.4 Outbursts

Figure 7.4 shows log-log plots of PKS B1622-253 spectra at 15 observing epochs. The plots combine the ATCA data shown in Figure 7.2, together with 1-22 GHz 1997 data from the RATAN-600 ring telescope (Kovalev et al., 1999).

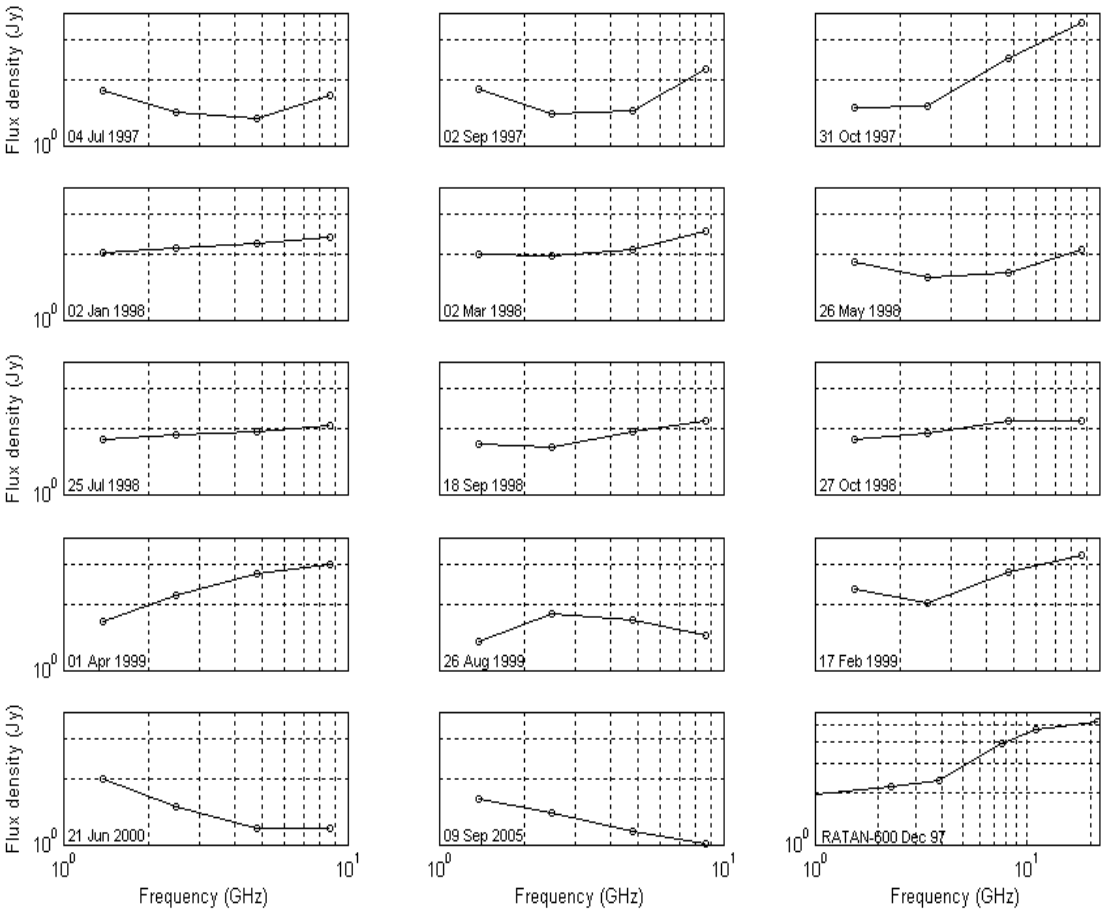

Figure 7.4 Log-log plots of PKS B1622-253 spectra. ATCA & RATAN observations.

The spectra in Figure 7.4 show the highly dynamic nature of the PKS B1622-253 active galactic nucleus. The different spectra across the 1-22 GHz frequency range are interpreted as radio outbursts, associated with superluminal ejecta.

Marscher & Gear (1985) examined outbursts from compact radio sources, particularly a 1983 flare observed in quasar 3C 273, and concluded that the flux density profile of a source during an outburst event is best explained by a shock wave passing through an adiabatic, conical, relativistic jet. According to the shock model of Marscher & Gear (1985), the flux density profile of a source during an outburst event moves through three stages.

i) The source initially brightens at higher frequencies, while the emission region is compact and energy losses are due to the inverse Compton effect (see Section 2.3).

ii) As the emission region expands, the spectral peak moves to lower frequencies, and energy losses are now due to synchrotron processes.

iii) The outburst dies as the emission region expands further, and adiabatic losses occur.

Wu et al. (2002) note that such outbursts are similar to those from microquasars (X-ray binaries) within the Galaxy, although blazars tend to stay in the growth stage longer than microquasars. Flaring events in microquasars have been observed by the VLBA, showing collimated relativistic jets with knot-like features, very similar to features in milliarcsecond-scale VLBI images of 3C 273 and other blazars (e.g. Unwin et al., 1985).

It is interesting that outbursts occur in radio sources that exhibit scintillation over periods of months to years. In addition to PKS B1519-273 and PKS B1622-253, the comparatively rapid scintillators J1819+3845 and PKS 1257-326 are examples of persistent scintillators. However, as discussed in Sections 2.1 to 2.4, rapid radio variability requires a compact emission region irrespective of whether the variability is intrinsic to the source or due to scattering by the interstellar medium. Such compact emission regions would be expected to expand and hence stop scintillating over time scales of months, as is the case with outburst events, and it is therefore puzzling that outbursts are observed but scintillation is nevertheless persistent. Compact radio emissions clearly are able to persist independent of outbursts, at least for some sources, but the reason for this is not known.

7.2 PKS B1519-273 Observation History

The BL Lac object PKS B1519-273 was first listed in the Parkes 2.7 GHz catalogue, with flux densities of 2.0 Jy at 2.7 GHz and 2.3 Jy at 5 GHz (Bolton et al., 1975). It is a point source, with no resolvable structure and no confusing radio sources nearby, and a weak source of soft X-rays (Urry et al., 1996) and possibly of gamma-rays (Fichtel et al., 1994). Optically, PKS B1519-273 is identified as a B filter magnitude 17.7 star-like object with a featureless spectrum (Véron-Cetty & Véron, 2006; Macquart et al., 2000). Visual observations have not identified a host galaxy, because it is obscured by nearby and partly overlapping objects.

PKS B1519-273 was included in high resolution *I*-band studies of 24 BL Lac objects carried out using several telescopes between late 1999 and early 2001, and found to lie at a redshift of $z = 1.294$ based on 4,000 to 10,000 Å low-resolution spectral observations, described by Heidt et al. (2004).

Radio variability in PKS B1519-273 on time scales of days was discovered at 4.8 and 8.6 GHz during the 1994 ATCA survey (Kedziora-Chudzer et al., 1997), and was observed in the 1997-2001 ATCA blazar monitoring program (Bignall, 2003). Dr Bignall has kindly provided the multi-frequency ATCA data for PKS B1519-273 presented in Bignall (2003). The Stokes *I* total flux density light curves are re-plotted in the top plot of Figure 7.5, with one minute averaging.

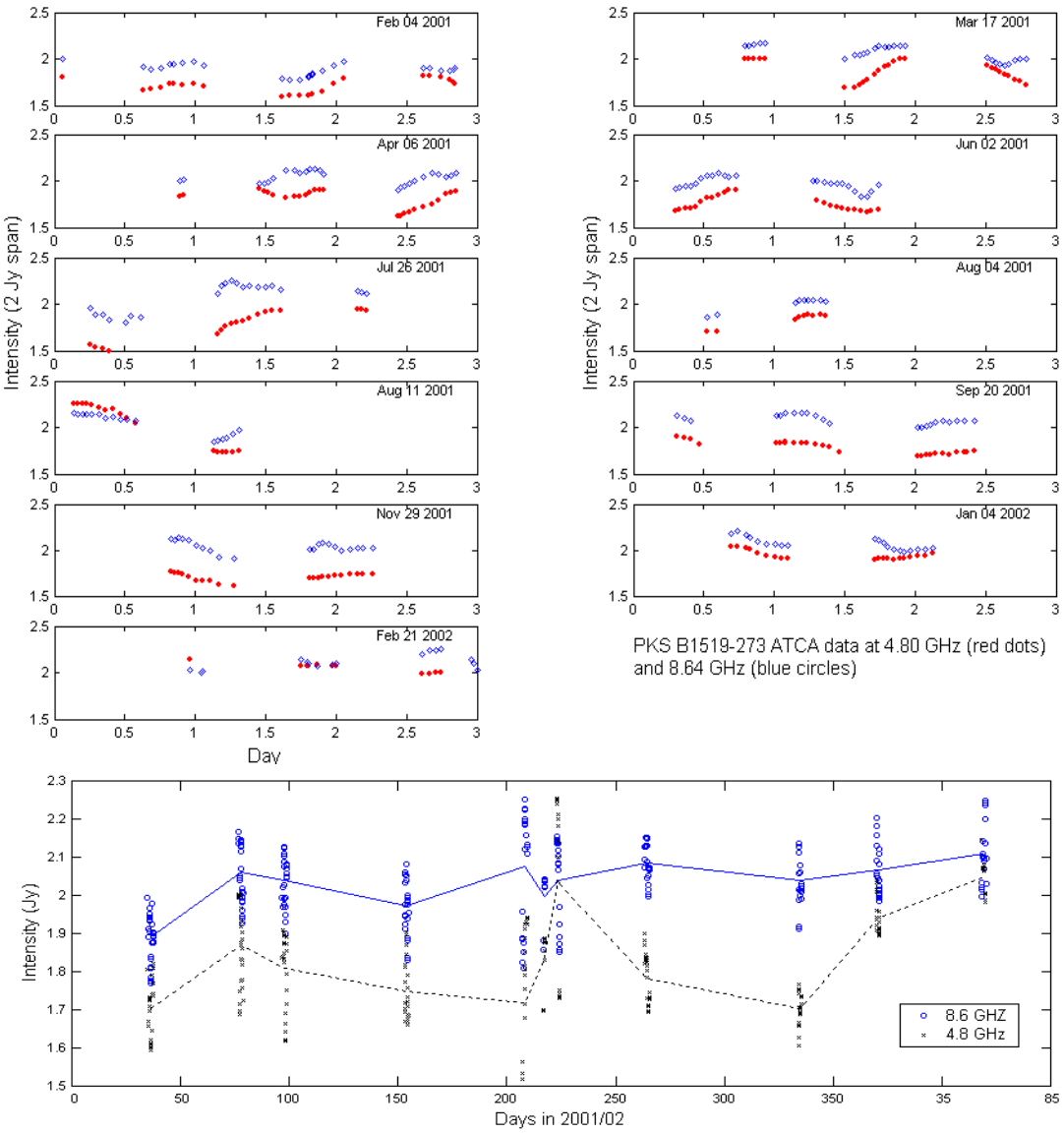

Figure 7.5 **ATCA observations of PKS B1519-273 in 2001-02, at 4.8 and 8.6 GHz. The lower plot shows the daily means of the flux densities.**

PKS B1519-273 also exhibits radio variability on time scales of months that is presumed to be intrinsic to the source. The lower plot of Figure 7.5 shows the daily means of the 2001-02 observations, highlighting the intrinsic variability of PKS B1519-273 over time scales of months. During the COSMIC program, its 6.7 GHz flux density varied from 2.4 Jy in early 2003 to ~1 Jy in early 2005, although its strength occasionally rose before resuming its downward trend (see Figure 6.4).

Since PKS B1519-273 and PKS B1622-253 both vary on time scales of days, a large time commitment is needed from a telescope to observe a series of scintles. This was a prime motivation for the present research, which seeks to establish whether a single 30 m antenna is able to monitor blazars for periods of months. Nevertheless, the ATCA was used to carry out multi-frequency observations of PKS B1519-273, the slightly more rapid scintillator, for five consecutive days starting on 10 June 1996 (Kedziora-Chudczer et al., 1998), and again starting on 9 September 1998 (Macquart et al., 2000). The observed variability was similar on both occasions, and Figure 7.6 reproduces the 1998 observations.

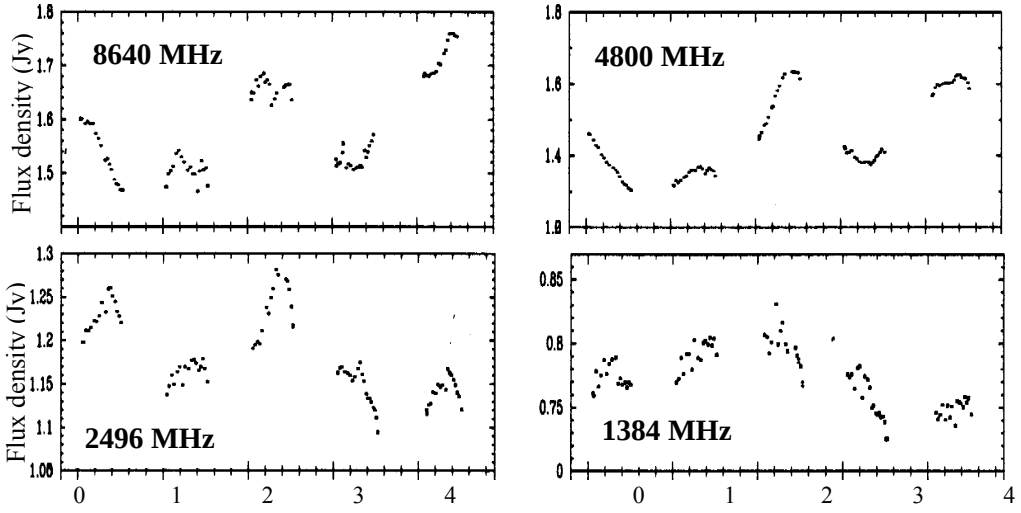

Figure 7.6 Multi-frequency ATCA observations of PKS B1519-273 over 5 days starting on 9 September 1998 (Macquart et al., 2000).

The 4.8 and 8.6 GHz data presented in Figure 7.6 are correlated and span the 6.7 GHz Ceduna observing frequency. Macquart et al. (2000) report the 4.8 GHz flux density RMS to be 0.11 Jy, with a mean flux density of ~1.5 Jy, consistent with the Ceduna data presented in this thesis. PKS B1519-273 exhibits strongly variable circular and linear polarisation at radio frequencies, which is too weak (~1%) to be observed by the Ceduna telescope. Macquart et al. (2000) concluded that the circular polarisation could not be explained by a simple model.

Annual Variability Cycle

Blazar variability intrinsic to the source is often broadband in nature, but PKS B1519-273 does not exhibit day-to-day variability at either optical (Heidt & Wagner, 1996) or at millimetre wavelengths (Steppe et al., 1995). This suggests that day-to-day radio variability is due to scattering by the interstellar medium. The existence of an annual cycle in the characteristic variability time scale of a scintle time series constitutes unarguable proof that the variability is due to ISM scattering, and Jauncey et al. (2003) reported detection of just such an annual cycle in the total flux density of PKS B1519-273.

The data examined by Jauncey et al. (2003) were gathered by the ATCA over ten observing periods, including the five days of 1998 data shown in Figure 7.6; and seven epochs in 2001 shown in Figure 7.5 (4 February, 17 March, 6 April, 2 June, 26 July, 20 September, and 29 November 2001), each with 2-3 days of data. Most of these observing periods were too short to record more than a single scintle, and the characteristic variability of each epoch was thus measured using $T_{\rm char} \sim T_{0.5}$ calculated from the autocorrelation function.

Three of the ten data points span days 120 – 150 of the year, with the $T_{0.5}$ values of ~3 hours (8.6 GHz) and ~5 hours (4.8 GHz). For sinusoidal scintles, $T_{\rm period} \approx 6\ T_{0.5}$ so at the Ceduna observing frequency of 6.7 GHz the expected value of $T_{\rm char} \sim T_{\rm period}$ is 6 x 4 hours = 24 hours during this time of year. This agrees well with the values of $T_{\rm period}$ observed by Ceduna at this time of year (e.g. Figure 7.8).

7.3 Source Size Estimates from Flux Density Spectra

PKS 1519-273 has been classified as a Gigahertz Peaked Spectrum (GPS) source (de Vries et al., 1997; Jauncey et al., 2003), which is unusual given it is a high-amplitude scintillator. GPS sources are hard to place in the Active Galactic Nuclei classification scheme, as discussed in Chapter 1. O'Dea (1998) defines a GPS source to be powerful, compact (< 1 kpc), and with a convex radio spectrum that peaks between 500 MHz and 10 GHz (observer's frame). They are usually not variable, and Section 1.3 noted that PKS B1934-638, the primary calibrator of the ATCA, was the first GPS source discovered, in 1963.

Multi-frequency flux density observations of PKS B1519-273 have been made on several occasions by the RATAN 600 telescope, and Kovalev et al. (1999) describe the 1-22 GHz survey in 1997. Jauncey et al. (2003) present the results of this survey and earlier RATAN observations. Figure 7.7 reproduces these data, and the mean observations (thick blue line) suggest the turnover frequency is in the vicinity of 7 GHz. However, some observations place the turnover at a lower frequency, and Jauncey et al. (2003) suggested a turnover frequency in the vicinity of 5 GHz.

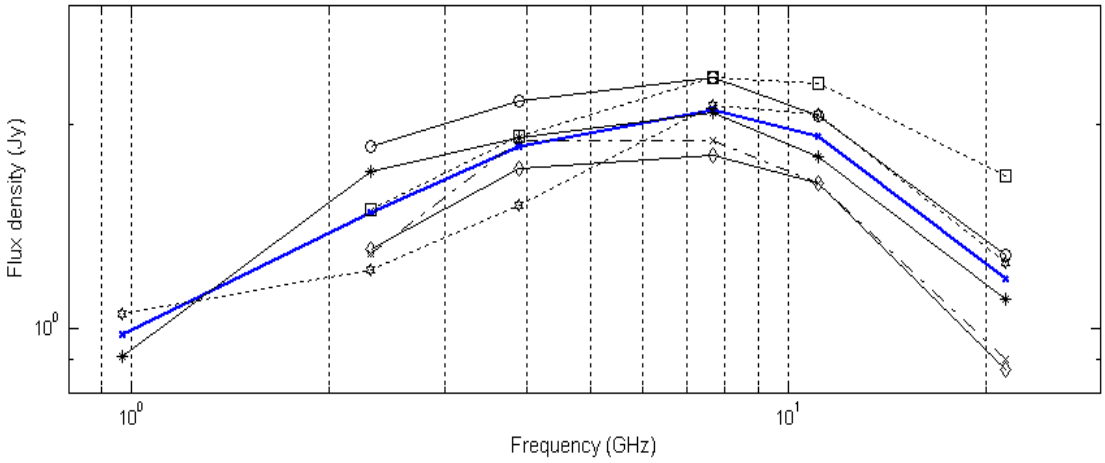

Figure 7.7 PKS B1519-273 spectra. Log-log plot of RATAN 600 observations. The mean spectrum is shown as the thick solid blue line.

More distant GPS sources have relatively high turnover frequencies (de Vries et al., 1997), which suggests the sources are more compact at high redshifts (O'Dea, 1998). Figure 1 of de Vries et al. (1997) shows this relationship for their sample of 72 sources, and a turnover frequency of 5 GHz is quite consistent with the z =1.294 redshift of PKS B1519-273.

As noted in Chapter 1, the frequency turnover is likely due to synchrotron self-absorption, although free-free absorption by an inhomogeneous screen may play a role (O'Dea, 1998), and absorption by induced [not inverse] Compton scattering has also been suggested (Kunic et al., 1998). Kellermann & Pauliny-Toth (1981) showed that, if the frequency turnover is indeed due to the synchrotron self-absorption mechanism, then:

$$\nu_{\text{peak}} \approx 8\, B^{0.2}\, S_{\text{peak}}^{0.4}\, \theta^{-0.8}\, (1+z)^{0.2}$$

where ν_{peak} (GHz) is the spectral peak, S_{peak} (Jy) is the peak flux density, θ (mas) is the angular size of the source, z is the redshift of the blazar, and B (Gauss) is the magnetic field. The dependence of θ on B is very weak, so it is not a critical parameter. If a magnetic field strength of $B \approx 100$ μG is assumed (de Vries et al., 1997), then the angular size of the source can be estimated as:

$$\theta \approx 1.345\, S_{\text{peak}}^{0.5}\, (1+z)^{0.25}\, \nu_{\text{peak}}^{0.8}$$

PKS B1519-273

The turnover of the mean spectrum in Figure 7.7 gives $\nu_{\text{peak}} \sim 7$ GHz and $S_{\text{peak}} \sim 2.1$ Jy, yielding an estimate of θ ~ 0.32 mas. However, this is an overestimate of the angular size of the scintillating component of the blazar, because part of the flux density is due to extended components that, in the case of PKS B1519-273, cannot be resolved.

Macquart et al. (2000) applied interstellar scintillation (ISS) theory to analyse the September 1998 ATCA observations of PKS B1519-273, reproduced in Figure 7.6. They estimated the scintillating component of the source to have a total flux density of 0.93 Jy at 4.8 GHz, and an angular size of $\theta_s \sim 0.035$ mas. The 1998 data are consistent with the turnover frequency of $\nu_{peak} \sim 7$ GHz estimated from the RATAN data presented in Figure 7.7, and assuming that $S_{peak} \sim 1$ Jy gives $\theta_s \sim 0.15$ mas, agreeing to within a factor of four with the Macquart et al. (2000) estimate from ISS theory. However, the extent to which the source total flux density spectrum matches the spectrum of the scintillating (i.e. compact) component of the source adds uncertainty to this calculation.

PKS B1622-253

PKS B1622-253 is not a GPS source, but the above turnover frequency calculation is based on the assumption that synchrotron self-absorption is causing the turnover, an assumption which is also made during the plateau phase of an outburst (Wu et al., 2002). Considering Figure 7.4, the flux density spectrum recorded on 26 August 1999 could be interpreted as a synchrotron self-absorption turnover at $\nu_{peak} \sim 2.5$ GHz, with $S_{peak} \sim 1.8 \times 0.85 = 1.5$ Jy. The factor of 0.85 has been applied on the basis of the estimate by Punsly et al. (2005) that the extended components of PKS B1622-253 are responsible for ~15% of the total emissions.

PKS B1622-253 has a redshift of $z = 0.786$, so the angular size of the core component of the source is $\theta \sim 0.6$ mas. This agrees with the 0.6 x 0.5 mas core size estimated by Tingay et al. (1998), although they also estimated the flux density of the core to be 0.6 Jy at 8.4 GHz, while the total flux density is 1.44 Jy at 8.6 GHz in the flux density spectrum recorded on 26 August 1999.

These calculations are indicative only. PKS B1622-253 is clearly a highly dynamic object, and both measured flux densities and inferred angular sizes of its core are subject to very significant changes between observing epochs. This is highlighted by the work of Jorstad et al. (2001), who constructed 22 GHz images of PKS B1622-253 over a one year period to examine its superluminal motion. They found that during this one year period the flux density of the PKS B1622-253 core changed by a factor of five.

Nevertheless, there is consistency in the fact that PKS B1519-273 and PKS B1622-253 both appear to have sub-milliarcsecond core sizes, and they also display similar scintillation characteristics. This appears to argue against there being yet smaller substructure in these sources that gives rise to the scintillation.

7.4 Scattering Régimes

Considering the multi-frequency ATCA PKS B1519-273 observations shown in Figure 7.6, the transition frequency between strong and weak scattering is in the vicinity of 4.8 GHz. Weak scattering is a broadband effect, and the light curves observed at 8.6 and 4.8 GHz are well correlated. There is some correlation of light curves between 4.8 and 2.5 GHz, but there is clearly a significant change in the nature of the scintillation between 2.5 and 1.4 GHz.

Macquart et al. (2000) found the modulation indices were approximately {0.03, 0.04, 0.08, 0.05} at {1.4, 2.5, 4.8, 8.6} GHz. An increase of the modulation index with frequency to the transition frequency is characteristic of refractive scintillation, and the subsequent fall as the frequency increases further is characteristic of weak scattering. A complicating factor is that the frequency at which the peak intensity modulation occurs can be influenced by the source size. As noted in Section 2.6.2, a larger source pushes the peak frequency of intensity modulations below the true transition frequency. This effect is not likely to be pronounced in the case of PKS B1519-273, since Macquart et al. (2000) have demonstrated that this source has only a small angular size.

PKS B1519-273 flux density variability is therefore associated with the weak scattering régime at the 6.7 GHz Ceduna observing frequency. The transition frequency of 12.5 GHz (see Table 2.4) predicted by the Cordes & Lazio (2006a) model is too high, for reasons discussed in Section 2.5.4.

Determining the scattering régime of PKS B1622-253 at 6.7 GHz is difficult. Table 2.4 shows that the transition frequency predicted by the Cordes & Lazio (2006a) model is slightly higher (17.5 GHz) for PKS B1622-253 than for PKS B1519-273, since it lies at a slightly lower Galactic latitude. However, there is no reason to believe the transition frequency predicted PKS B1622-253 is any more accurate than the incorrect transition frequency predicted for PKS B1519-273.

Chapter 6 shows that the scintillation characteristics of the two sources are very similar, while this chapter will demonstrate that the flux density variability time scales of the two sources follow very similar annual cycles; and that their modulation indices are also similar. It thus is quite reasonable to assume that the flux density variability of PKS B1622-253 is associated with the weak scattering régime at the 6.7 GHz Ceduna observing frequency. Multi-frequency ATCA observations will be required to confirm this conclusion.

7.5 Annual Cycles in Variability Time Scales

Figure 7.8 shows the T_{Period} values for both PKS B1622-253 and PKS B1519-273, including error bars. The time axis spans the 365 days of a normal year, and data gathering started at about days 150 and 100 of 2003 respectively for the two sources. Cycle one refers to data gathered within 12 months of the start date. Cycle two refers to data gathered thereafter.

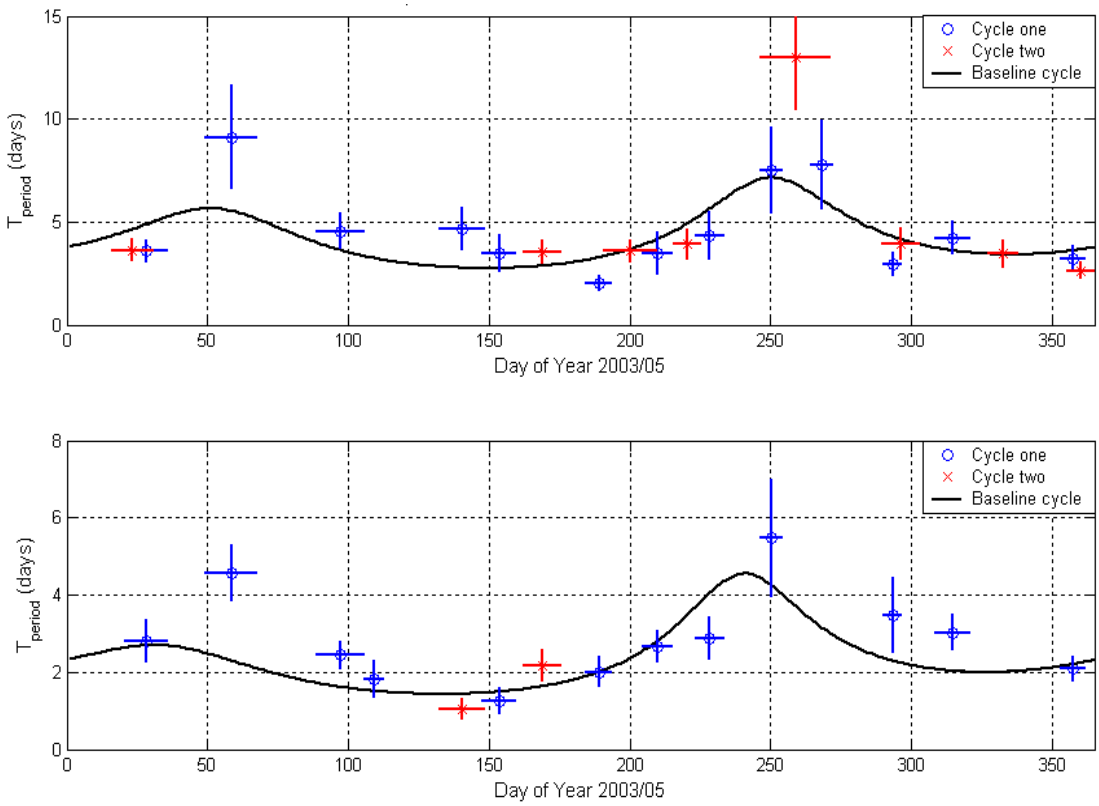

Figure 7.8 ***T_{Period}*** **values for PKS B1622-253 (top) and PKS B1519-273 (bottom), and superimposed annual cycles for baseline parameters (see text).**

Figure 7.8 shows that the variation of T_{Period} values of both sources agree fairly well with the annual cycles expected if scintillation is due to interstellar scattering, as described by the annual cycle model presented in Chapter 2. The model is defined by five parameters:

s_o — Characteristic scintle spatial scale. This is the coherence scale, s_o (km). The characteristic scintillation time scale is $\tau = s_o / V$, where V is the velocity with which the scintillation pattern moves transversely across the line of sight.

R, β — Anisotropy. The spatial pattern of scintles is assumed to form elliptical contours with axial ratio R (this was given the symbol Ω in Chapter 2), and the major axes of the ellipses are inclined at angle β to the direction of the scintillation velocity.

V_α, V_δ — ISM – LSR velocity. The ISM scattering material generally has a velocity offset with respect to the velocity of the Local Standard of Rest, and $\{V_\alpha \;\; V_\delta\}$ are the offset velocity components (km/s) in right ascension and declination.

The baseline annual cycles shown in Figure 7.8 correspond to reasonable values of these parameters, namely: $\{R\ \ \beta\ \ V_\alpha\ \ V_\delta\ \ s_o\}$ = {1, 0 rad, 0 km/s, 0 km/s, q x 10^6 km }, where q = 9 for PKS B1622-253 and q = 5 for PKS B1519-273. Figure 7.9 shows the effect on the annual cycles of small changes to these baseline values in the case of PKS B1622-253.

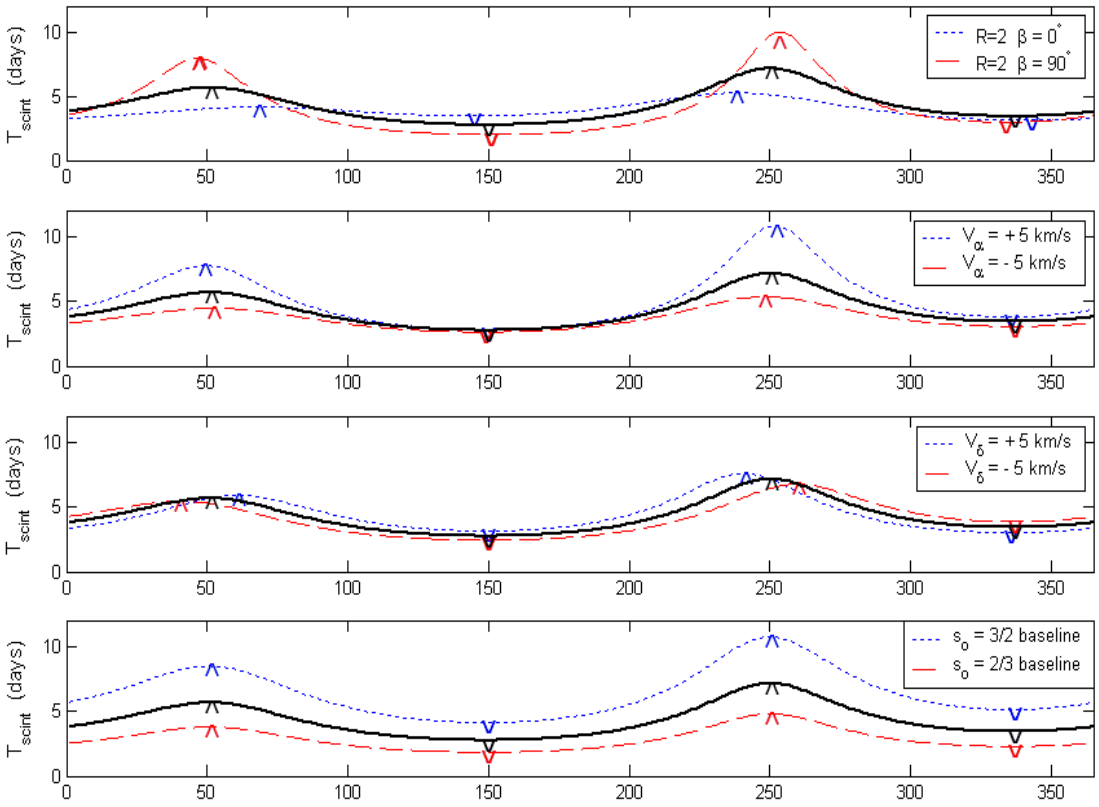

Figure 7.9 **Sensitivity of PKS B1622-253 T_{period} annual cycles to changes in the baseline parameter values (black lines). PKS B1519-273 is similar. The arrows show the location of annual cycle peaks and troughs.**

PKS B1622-253 and PKS B1519-273 lie along similar lines of sight from the Earth, and have similar T_{Period} annual cycles, and sensitivity tests on the PKS B1519-273 annual cycle have similar results to those shown in Figure 7.9. Slow downs (i.e. increases in the T_{Period} values) near days 50 and 250 are robust features of both annual cycles, the slow down near day 250 being the more pronounced of the two.

Characteristic scintle spatial scale. Changes in s_o have a scaling effect: increasing s_o slows down the variability time scale, since $\tau = s_o / V$. The annual cycle is accentuated, with a greater difference between the T_{Period} values in the slow down and speed up times of year, but it does not affect the location of the annual cycle's peaks and troughs.

Anisotropy. The convention used herein to describe anisotropy is that $R \geq 1$, with $\beta = 0°$ denoting the case in which the major axis of the elongated scintle is aligned with the scintillation velocity. The value of β affects the annual cycle as follows (see Section 2.6):

- When $\beta = 0°$, the *major* axis of the elliptical scintles is aligned with the scintillation velocity. The T_{Period} annual cycle is flatter than the $R = 1$ case, as the Earth encounters scintle peaks and troughs more slowly during speed-up times of year, and more quickly during the slow-down times. The locations of the T_{Period} slow down peaks near days 50 and 250 are shifted to slightly later and earlier days respectively. The locations of the T_{Period} speed-up troughs near days 150 and 340 are not much affected.

- When $\beta = 90°$, the *minor* axis of the elliptical scintles is aligned with the scintillation velocity. The T_{Period} annual cycle is accentuated compared to the $R = 1$ case, as the Earth encounters peaks and troughs faster during speed-up times of the year, and more slowly during the slow-down times. The locations of the T_{Period} slow down peaks near days 50 and 250 are shifted to slightly earlier and later days respectively. Again, the location of the speed-up troughs near days 150 and 340 are not much affected.

ISM – LSR velocity offset. For these two sources, a $\{V_\alpha \; V_\delta\}$ velocity offset primarily influences the T_{Period} annual cycles during the slow-down times of year, but hardly affects the speed-up times of year.

- A positive V_α increases T_{Period} at the slow down times of year, accentuating the annual cycle, while a negative V_α reduces T_{Period} at the slow down times of year, flattening the annual cycle. The locations of the slow-down times of year are essentially unchanged.

- Changing V_δ has little effect on the annual cycle for these two sources. A positive V_δ causes the location of the slow-down times of year near days 50 and 250 to shift to slightly later and earlier days respectively, while a negative V_δ causes the reverse effect.

Best fit annual cycles

Figure 7.10 shows the results of multi-parameter optimisation of the annual cycle model fits to the T_{Period} data for PKS B1622-253 and PKS B1519-273, with all five model parameters free to change. The black solid lines are the optimum annual cycle fits. These lie within the error bars of most data points, the error bars being ~95% (i.e. 2-sigma) confidence limits (Section 6.4.2).

Table 7.1 gives the best fit annual cycle parameter values. For both sources the optimum annual cycle is for highly anisotropic scintles and large LSR velocity offsets, particularly V_α. This is unsurprising: significant velocity offsets are expected for scintillation with relatively long variability time scales (days rather than hours), which is associated with more distant scattering screens that typically lie hundreds of parsecs from Earth, and thus are in motion with respect to the LSR.

Anisotropic scintles are associated with other blazar observations, notably PKS 0405-385 (Rickett et al., 2002), and J1819+3845 (Macquart & de Bruyn 2006). Many authors have argued that, for scintillation due to scattering by the ISM, electron density fluctuations are expected to be elongated along the local direction of the magnetic field (e.g. Goldreich & Sridhar 1995; Chandran & Backer 2002). Alternatively, anisotropicity may be due to an anisotropic source structure, instead of the scattering medium, a possibility that is explored later in this chapter.

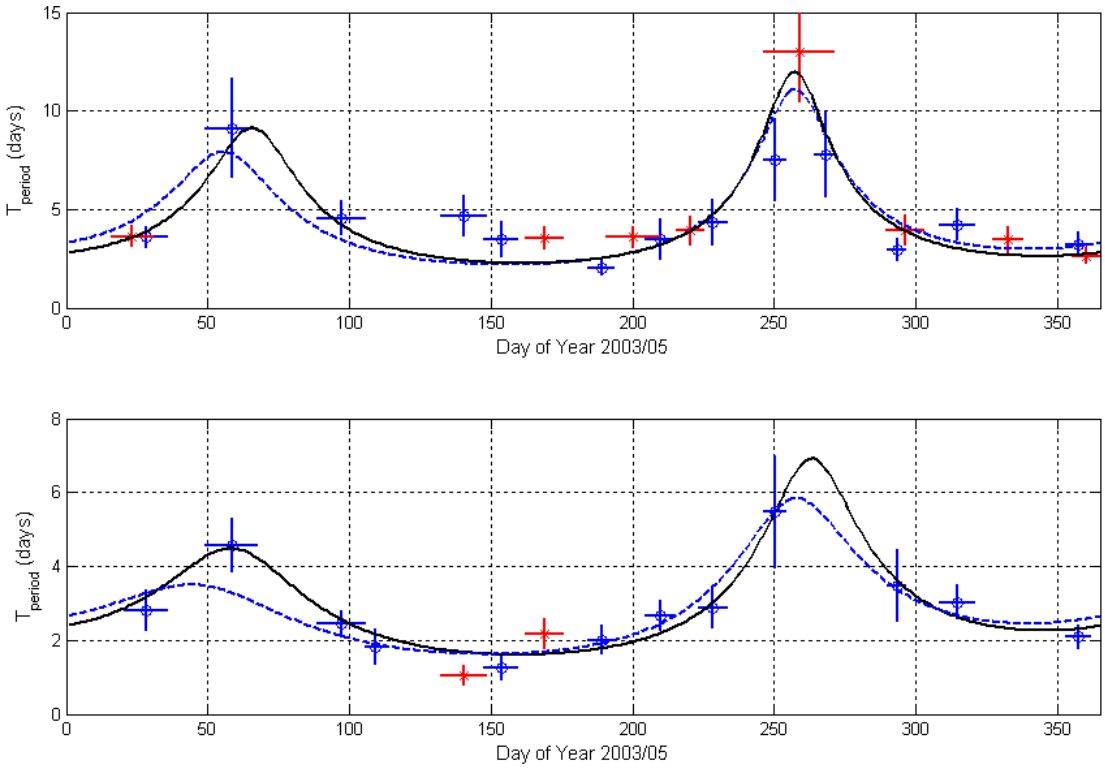

Figure 7.10 **Annual cycle model fits to T_{period} data for PKS B1622-253 (top) and PKS B1519-273 (bottom). Blue circle data points are first year, red cross data points are second year. All-parameter best fits shown as solid black lines. Best fits for R=5 shown as dash blue lines.**

PKS B1622-253	R	β **(rad)**	V_α **(km/s)**	V_δ **(km/s)**	s_o **(10^6 km)**
Optimum	18.0 ± 4.0	0.17 ± 0.02	-37.5 ± 3.0	8.4 ± 0.5	9.2 ± 0.9
$R = 5$	5.0	0.35	-17.1	7.9	7.9
$\{R\ \beta\}$ $\{V_\alpha\ V_\delta\}$ s_o	1.9	1.5	-0.4	3.7	9.9
PKS B1519-273	R	β **(rad)**	V_α **(km/s)**	V_δ **(km/s)**	s_o **(10^6 km)**
Optimum	15.1 ± 3.0	0.07 ± 0.02	-52.0 ± 7.0	12.1 ± 1.0	7.1 ± 0.4
$R = 5$	5.0	0.185	-29.0	8.3	6.1
$\{R\ \beta\}$ $\{V_\alpha\ V_\delta\}$ s_o	1.3	1.9	-4.1	3.6	5.7

Table 7.1 **Annual cycle model best-fit values for a) All parameters; b) R constrained to be ≤5 (best-fit is for R = 5); c) Selected optimisation, as explained in text.**

Anisotropy – velocity offset interplay

The blue dashed lines in Figure 7.10 show the best fit annual cycles when the anisotropy ratio is constrained to $R \leq 5$, with the best-fit values in Table 7.1 being for $R = 5$. Table 7.1 also gives the results of *selected* optimisation exercises: optimisation of $\{R\ \beta\}$ is made with the other parameters fixed at the baseline values associated with Figure 7.8, and similarly for optimisation of $\{V_\alpha\ V_\delta\}$, and optimisation of s_o.

These exercises show the interplay between scintle anisotropy and the LSR velocity offset, particularly V_α. The best fit all-parameter annual cycles to the T_{Period} data are for significant anisotropy and velocity offsets which, as noted, is not surprising. However, the best-fits for the individual parameter optimisations require the anisotropy to be small if the LSR velocity offsets are constrained to be zero; and require the best-fit velocity offsets to be small if the scintles are constrained to be isotropic. This behaviour is also evident in the $R = 5$ best fit annual cycles, which have significantly lower LSR velocity offsets than the optimum fits.

Goodness of Fit and error estimates

The chi-squared statistic, χ^2 , is the sum-squared error of the residuals, weighted by the error bars of the data points, with greater weight given to the model fit through data points with small error bars. The extent to which an annual cycle model fits the data can be assessed using the reduced chi-square statistic, χ^2_{Red} (e.g. Press et al., 1986):

$$\chi^2 = \sum_N \frac{1}{\sigma_i^2}\left(f_i - x_i\right)^2 \qquad 0 < \chi^2 < \infty \qquad\qquad \chi^2_{\text{Red}} = \frac{\chi^2}{N-m}$$

where N is the number of data points, σ_i is the error bar associated with data point x_i , and f_i is the best fit annual cycle model value corresponding to this data point. The annual cycle model has $N - m$ degrees of freedom, where $m = 5$ parameters. The χ^2_{Red} value estimates the ratio of the variance of a model fit, to the variance of the data being modelled. A model is good if $\chi^2_{\text{Red}} \approx 1$. If $\chi^2_{\text{Red}} << 1$, the error bars are probably too large. If $\chi^2_{\text{Red}} >> 1$, either the error bars have been underestimated or the data are not well described by the model.

Evaluating these statistics gives the results in Table 7.2.

	PKS B1622-253	**PKS B1519-273**
N	21	14
χ^2	33.89	7.45
χ^2 / (N-m)	2.12	0.83

Table 7.2 Chi-squared and Reduced Chi-Squared statistics. *N* = data points, *m* = model parameters (5).

which clearly show that the annual cycle models for the two sources both fit the data well; and that the empirically determined error estimates (Chapter 6) are appropriate and neither too large nor too small. A gauge of the significance of the detection of an annual cycle in these sources is the comparison of the χ^2 and $\chi^2_{\rm Red}$ values in Table 7.2 with the values associated with "fitting" the data by a linear model in which T_{Period} = constant. Choosing the constant to be the mean T_{Period} values of 4.68 days and 2.26 days for PKS B1622-253 and PKS B1519-273 respectively gives the following goodness-of-fit values:

PKS B1622-253 $\chi^2 = 334$ $\chi^2_{\rm Red} = 20.9$

PKS B1519-273 $\chi^2 = 90$ $\chi^2_{\rm Red} = 10.0.$

Figures 7.11 and 7.12 show the variation of $\Delta\chi^2 = \chi^2 - \left(\chi^2\right)_{\rm min}$ in the neighbourhood of the optimum model parameters. Constant χ^2 boundaries enable confidence levels (i.e. error bars) to be estimated for model best fit parameters. A change in a parameter with respect to its best-fit value causes a change in chi-square with respect to its minimum value, $\Delta\chi^2 = \chi^2 - (\chi^2)_{\rm min}$, and the confidence level associated with $\Delta\chi^2$ can be determined either analytically or by Monte Carlo simulations. In general it depends on the number of degrees of freedom (DOFs), and Press et al. (1986) tabulate commonly needed results.

If each parameter is considered separately, the one DOF values of $\Delta\chi^2$ are appropriate, and $\Delta\chi^2 = 1.00$ is the 1-sigma (68%) confidence level, while $\Delta\chi^2 = 2.71$ is the 90% confidence level. If two parameters are considered jointly, the two DOF values of $\Delta\chi^2$ are appropriate, and $\Delta\chi^2 = 2.3$ is the 1-sigma (68%) confidence level.

Consider, for example, the top sub-plot of Figure 7.11, which shows $\Delta\chi^2 = 1$ and 2.3 contours for the variation of the velocity offset components, $\{V_\alpha \;\; V_\delta\}$. The 1-sigma error bar for V_α considered separately is found by projecting the $\Delta\chi^2 = 1$ contour limits onto the V_α axis, giving an error bar of ± 2.0 km/s, and a similar projection of the $\Delta\chi^2 = 1$ contour onto the V_δ axis gives an error bar of ± 0.3 km/s. The $\Delta\chi^2 = 2.3$ *ellipse* gives the 1-sigma confidence *region* if the $\{V_\alpha \;\; V_\delta\}$ two parameters are considered jointly (Press et al., 1986).

However, it is <u>not</u> appropriate to set the 1-sigma error bars for the annual cycle model as the parameter changes corresponding to the one DOF values of $\Delta\chi^2$. To see this, consider the best fit annual cycles under the $R = 5$ constraint (dash lines) in Figure 7.10. These are quite similar to the unconstrained best fit annual cycles (solid black lines), and their reduced chi-square values of $\chi^2_{\rm Red} = 2.28$ and 3.18 for PKS 1519-273 and PKS 1622-253 respectively indicate that the $R = 5$ constrained models describe the data fairly well, although not as well as the unconstrained best fit annual cycles.

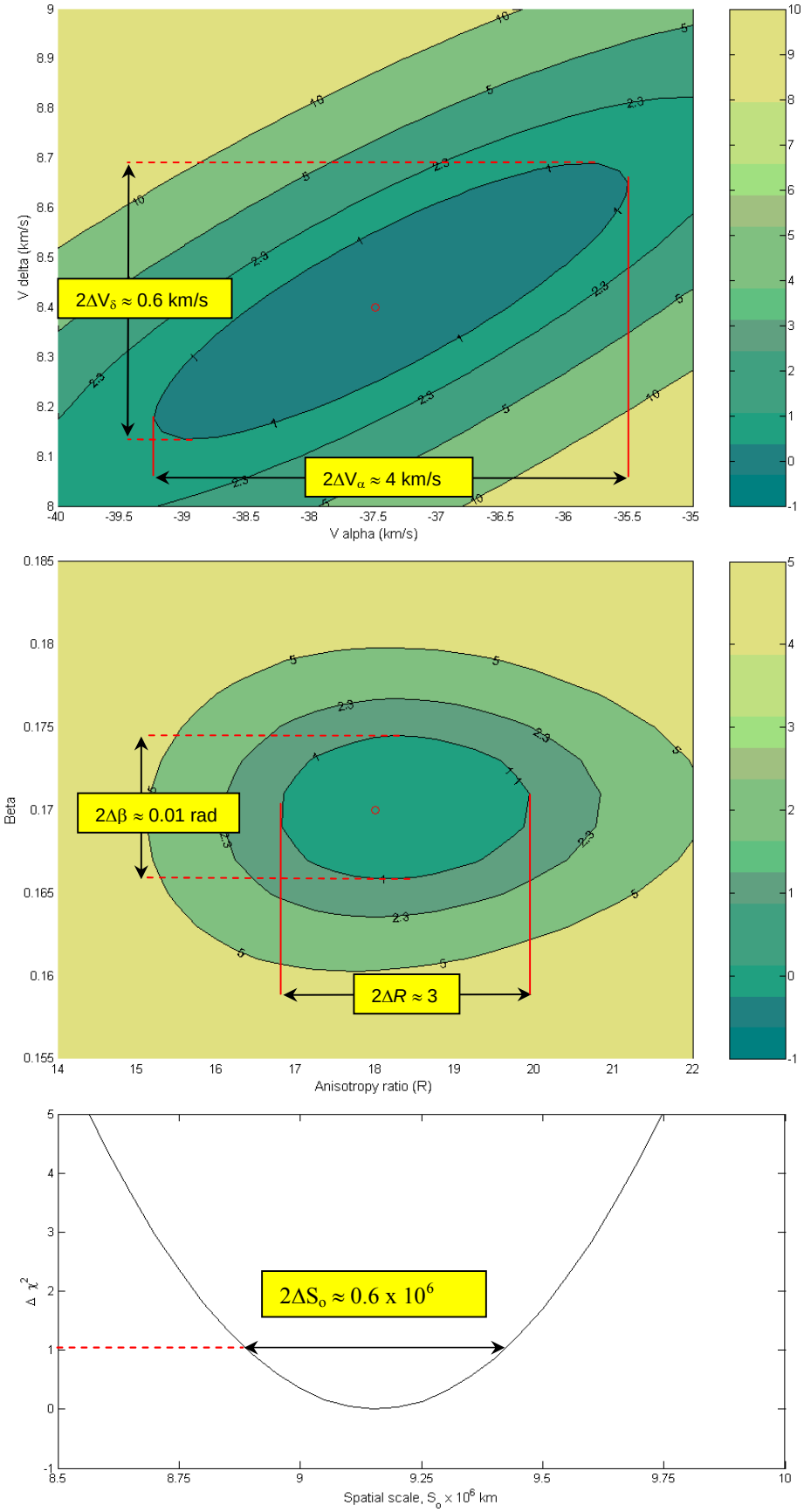

Figure 7.11 **Variation of $\Delta\chi^2 = \chi^2 - (\chi^2)_{min}$ with model parameters in the vicinity of their best-fit annual cycle values, for PKS 1622-253. In each graph, the non-variable model parameters are fixed at their best-fit values.**

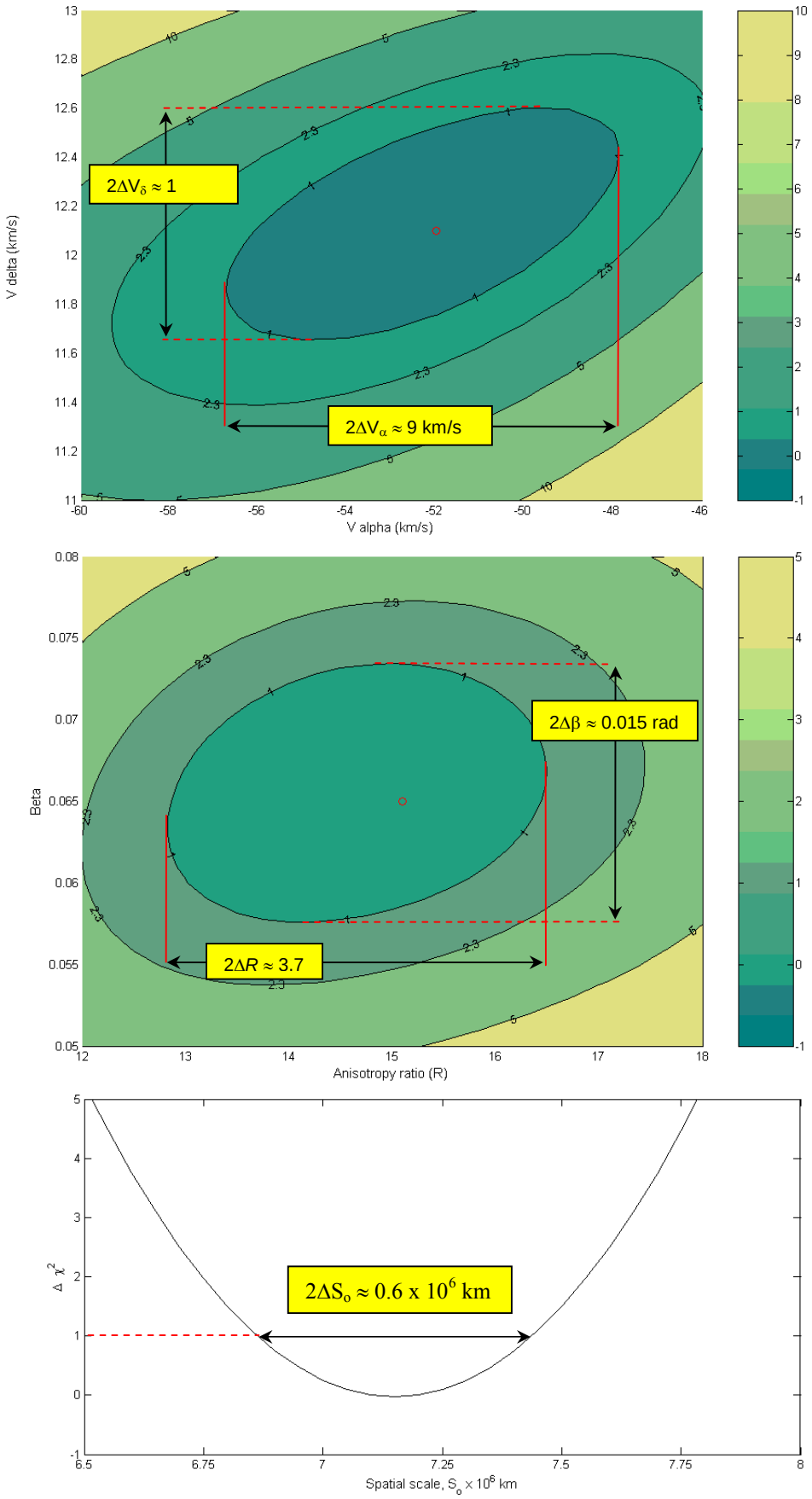

Figure 7.12 **Variation of $\Delta\chi^2 = \chi^2 - (\chi^2)_{min}$ with model parameters in the vicinity of their best-fit annual cycle values, for PKS 1519-273. In each graph, the non-variable model parameters are fixed at their best-fit values.**

This leads to the conclusion that the annual cycle models are not particularly sensitive to the interplay between scintle anisotropy and the LSR velocity offset, and the 1-sigma error bars corresponding to the one DOF value of $\Delta\chi^2 = 1.00$ are too small because this joint variation needs to be considered. Table 7.1 therefore gives 1-sigma (68%) error bars corresponding to parameter changes that result in the two DOF value of $\Delta\chi^2 = 2.30$, including the spatial scale parameter, s_o. These error bars were estimated from $\Delta\chi^2 = 2.30$ contours in $\{R \;\; V_\alpha\}$ plots and $\{R \; V_\delta\}$ plots, and are similar to those obtained from the $\Delta\chi^2 = 2.30$ contour projections in Figures 7.11 and 7.12.

7.6 Removal of Annual Cycle Effects

The annual cycle effect can be removed from a flux density time series by using the best-fit models for annual cycles in T_{period} to correct the data for departures from a specified T_{period} value. This enables examination of the overall pattern of scintillation modulations throughout the 2003/05 observing campaign, without the effects of ISM scattering material motion and anisotropy. This parallels the exercise carried out by Dennett-Thorpe & de Bruyn (2003) for the quasar J1819+3845 data spanning two years of observations.

Figure 7.13 shows all the PKS B1622-253 and PKS B1519-273 data for 2003/05 with the annual cycle effect removed by adjusting the data variability to $T_{\text{char}} \sim T_{\text{period}}$ values of 4.5 and 3.0 days respectively. The reference T_{period} values are close to the mean T_{period} values for the annual cycle, as can be seen from Figure 7.10.

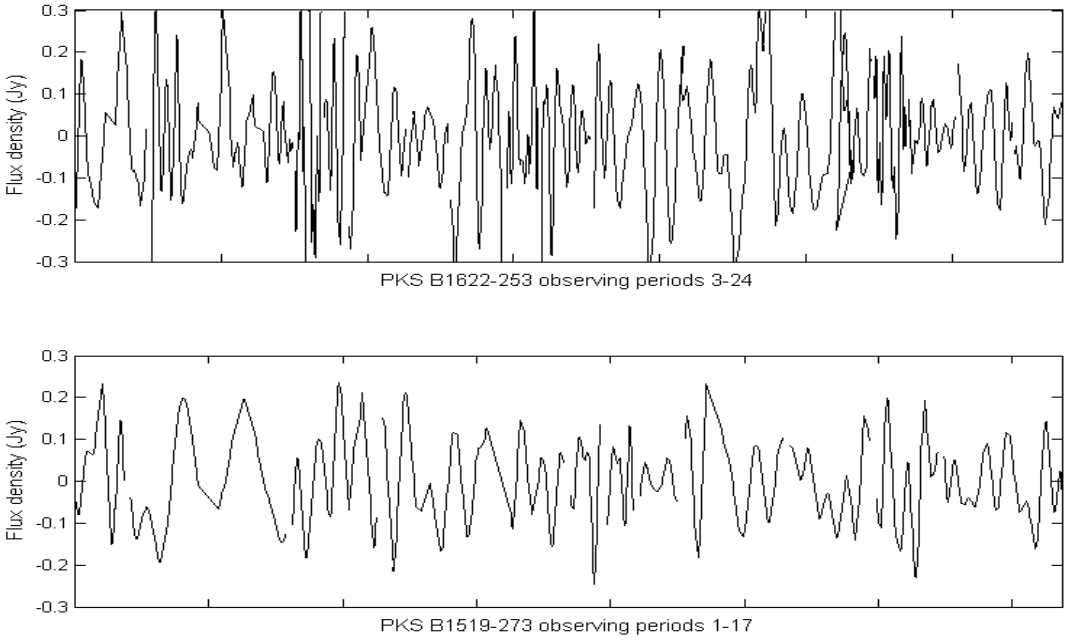

Figure 7.13 PKS B1622-253 and PKS B1519-273 data adjusted by the time scales calculated from the best fit annual cycle models to "constant" variability timescales of 4.5 days and 3.0 days respectively. See text for discussion.

Figure 7.13 is very similar to Figure 12 in Dennett-Thorpe & de Bruyn (2003), for the quasar J1819+3845. As was found for J1819+3845, the variability of both PKS B1622-253 and PKS B1519-273 is, by eye, similar throughout the observing campaign.

Figure 7.14 compares PKS B1519-273 data from observing periods 4 to 10 before and after the time scale correction. The correction is calculated on a daily basis, and the time intervals between flux density data points adjusted by a factor of $T_{period}^{reference} / T_{period}$. The gap between data recorded in adjacent observing periods is set to 1 day.

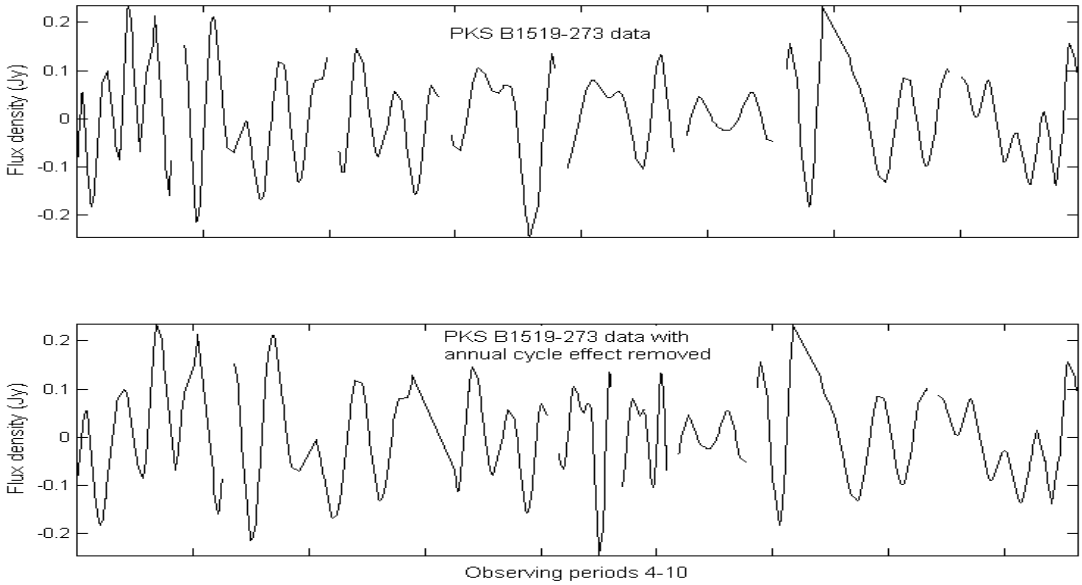

Figure 7.14 PKS B1519-273 observing period 4-10 data before and after adjustment.

Figure 7.15 shows the cumulative PSDs which result from summing the PSDs computed for each observing period for PKS B1622-253 and PKS B1519-273 after adjustment of the data to a single variability timescale, and normalising to unity. Each PSD is determined from an ACF computed at lag increments of 1 hour, with a maximum lag time of 8 days.

The cumulative PKS B1622-253 and PKS B1519-273 PSDs show clear peaks at time scales of about 4.5 days (0.22 days^{-1}) and 3.0 (0.33 days^{-1}) days respectively. These are the mean values of the best-fit annual cycle time scales, $(T_{\text{period}})_{\text{mean}}$, to which the time intervals between flux density data points have been corrected.

A key feature of Figure 7.15 is that there is little or no evidence in either cumulative PSD of additional persistent variability at time scales in the frequency range 0.2 to 0.9 days^{-1}, which corresponds to a scintle period range of about 1.1 days to 5 days.

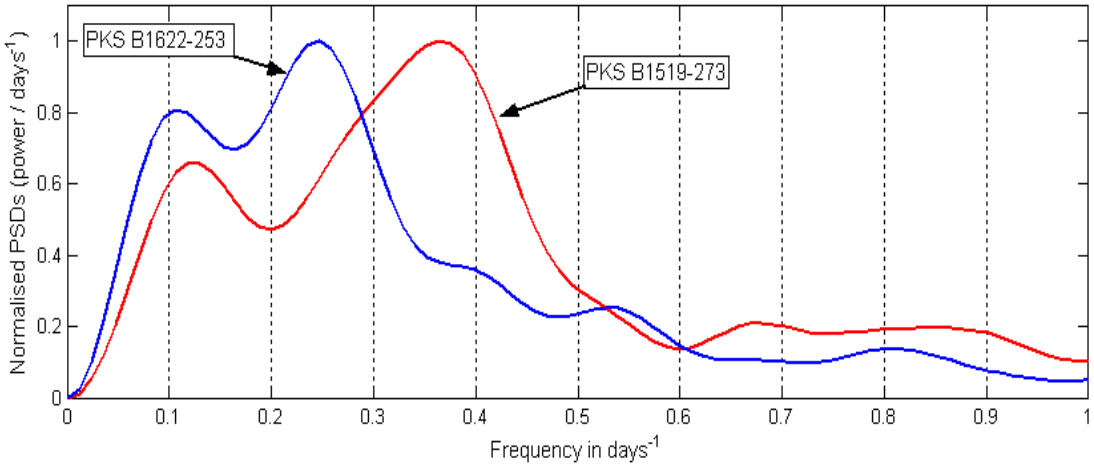

Figure 7.15 Normalised cumulative PSDs for PKS B1622-253 and PKS B1519-273 after time scale adjustment of the data.

As discussed in Chapter 6, the Ceduna data show little or no sign of variability in addition to the variability time scale that follows an annual cycle, as presented above. The data are smoothed to filter out variability on time scales < ~1 day, since these higher frequencies are contaminated by systematic variations, and the PSD thus extends only to 1 days^{-1}. However, Chapter 5 shows that for PKS B1622-253 and PKS B1519-273 there is no evidence of genuine variability at these higher frequencies.

[The exceptions, discussed in Chapter 5, are observing periods 3 and 16 of PKS B1519-273, which span the speed-up time of year and contain some genuine variability near a frequency of 1 days^{-1}. The data for these two observing periods are not smoothed ahead of analysis, at the cost of producing messy PSDs and data folding plots].

Considering lower frequencies, both the cumulative PSDs in Figure 7.15 have spectral peaks at ~0.1 days^{-1} due to residual flux density trends across the observing periods. These trends have largely been removed by the data filtering and correction procedures described in Section 4.5, but even a small residual trend produces a significant low frequency peak in the PSD, which masks the presence of any persistent genuine variability at long time scales. The low frequency peaks in Figure 7.15 are weaker than the high frequency peaks associated with the scintillation variability time scale: it is assumed that any spectral leakage from the low frequency peaks is not sufficient to mask PSD features at higher frequencies.

Figure 7.16 shows this effect for the calibrator, 3C227. A spectral peak at ~0.1 days^{-1} appears in the cumulative PSD if a linear flux density profile is added to each observing period, rising from 0.0 Jy to 0.1 Jy from the start to the end of the observing period.

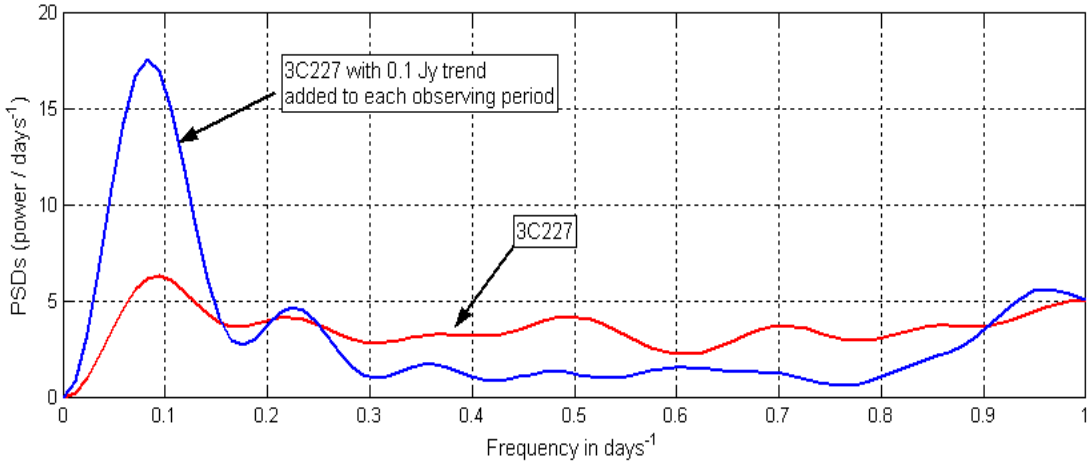

Figure 7.16 **Cumulative PSDs for 3C227 showing the effect of a small linear flux density trend superimposed on the data for each observing period. The PSDs are not normalised, to facilitate comparison of the two PSDs.**

Unlike high frequency variability, any genuine low frequency flux density variability has not been excised from the data. Variability on time scales longer than about 5 days is quite easy to detect when it is present, as is the case for observing periods that span the slow down times of year, particularly for PKS B1622-253. However, the low frequency peak at about ~0.1 days^{-1} in the cumulative PSD has contributions from residual flux density trends in all observing periods, such that any additional variability at long time scales would need to be persistent to be able to compete with this effect.

7.7 Discussion

This research set out to establish whether a small (30 m) radio telescope could monitor blazars well enough to provide data sets spanning years, in which the scintillation was clear enough to estimate variability characteristics and to determine whether variability time scales follow an annual cycle. This research goal has been achieved, and this closing discussion considers the implications of the annual cycle modelling.

Table 7.3 and Figures 7.17 & 7.18 give the mean flux density and the RMS flux density values for each PKS B1622-253 and PKS B1519-273 observing period. These values are quite well correlated in the case of PKS B1519-273, but are far less correlated in the case of PKS B1622-253, with correlation coefficients of 0.72 and 0.44 respectively.

Both sources decreased in strength by a factor of ~2 in 2004. This was accompanied by a similar decrease in the RMS values of the PKS B1519-273 scintillation recorded in each observing period, but the RMS values of the PKS B1622-253 scintillation remained much steadier.

		PKS B1622-253		PKS B1519-273	
Period	**Mean Day**	**Mean Jy**	**RMS mJy**	**Mean Jy**	**RMS mJy**
1	109.2	–	–	2.31	107
2	138.1	–	–	2.40	158
3	153.6	2.80	140	2.44	115
4	189.0	2.93	191	2.64	116
5	209.9	2.93	95	2.34	113
6	228.4	3.20	66	2.19	88
7	250.5	3.68	206	2.04	98
8	268.3	3.48	236	2.04	71
9	293.5	3.09	170	2.13	29
10	314.5	3.26	148	2.02	95
11	357.4	3.53	61	1.92	83
12	393.3	4.02	182	2.18	118
13&14	423.5	4.14	120	2.40	101
15	462.2	3.76	105	2.20	68
16	505.6	3.69	142	2.06	60
17	534.0	3.67	139	2.22	69
18	565.1	3.50	159	1.98	63
19	585.5	3.24	120	1.81	52
20	623.9	2.63	131	1.57	71
21	661.1	2.11	48	1.51	68
22	697.6	2.01	100	1.33	76
23	725.1	2.13	100	1.18	50
24	754.3	2.08	81	1.13	38

Table 7.3 Mean and RMS flux densities for PKS B1622-253 and PKS B1519-273.

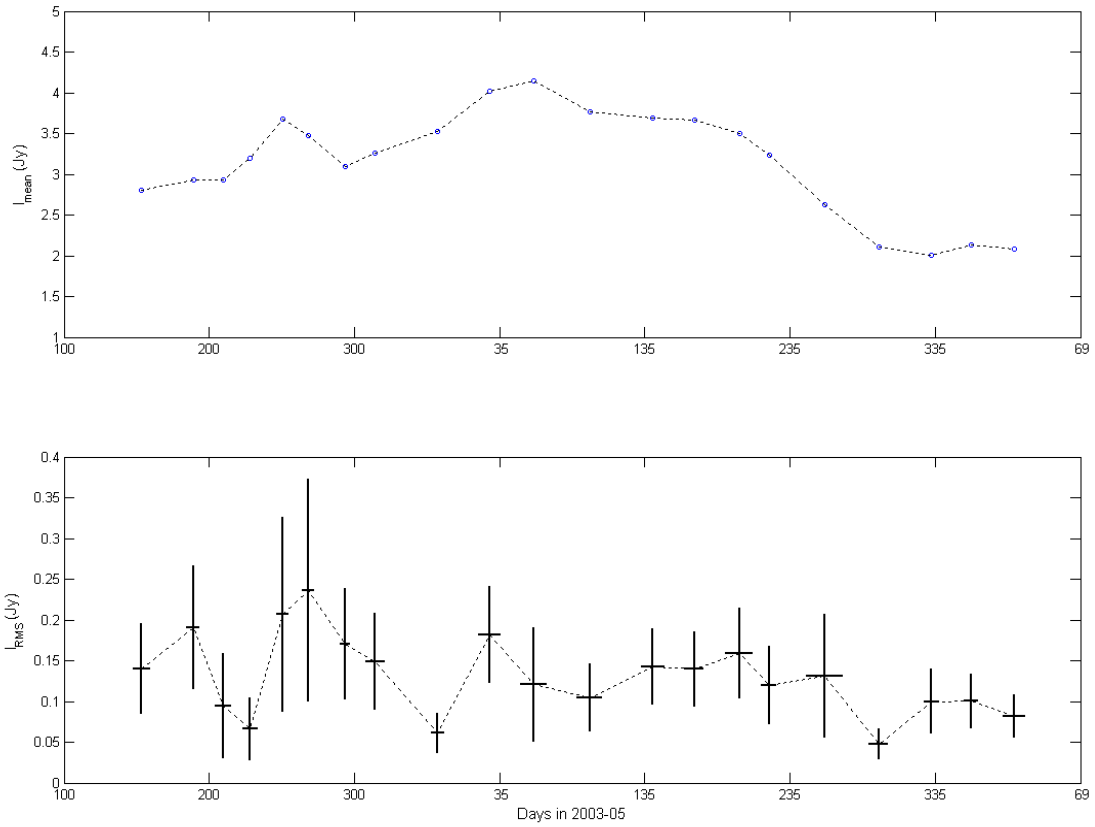

Figure 7.17 Mean and RMS flux densities for PKS B1622-253.

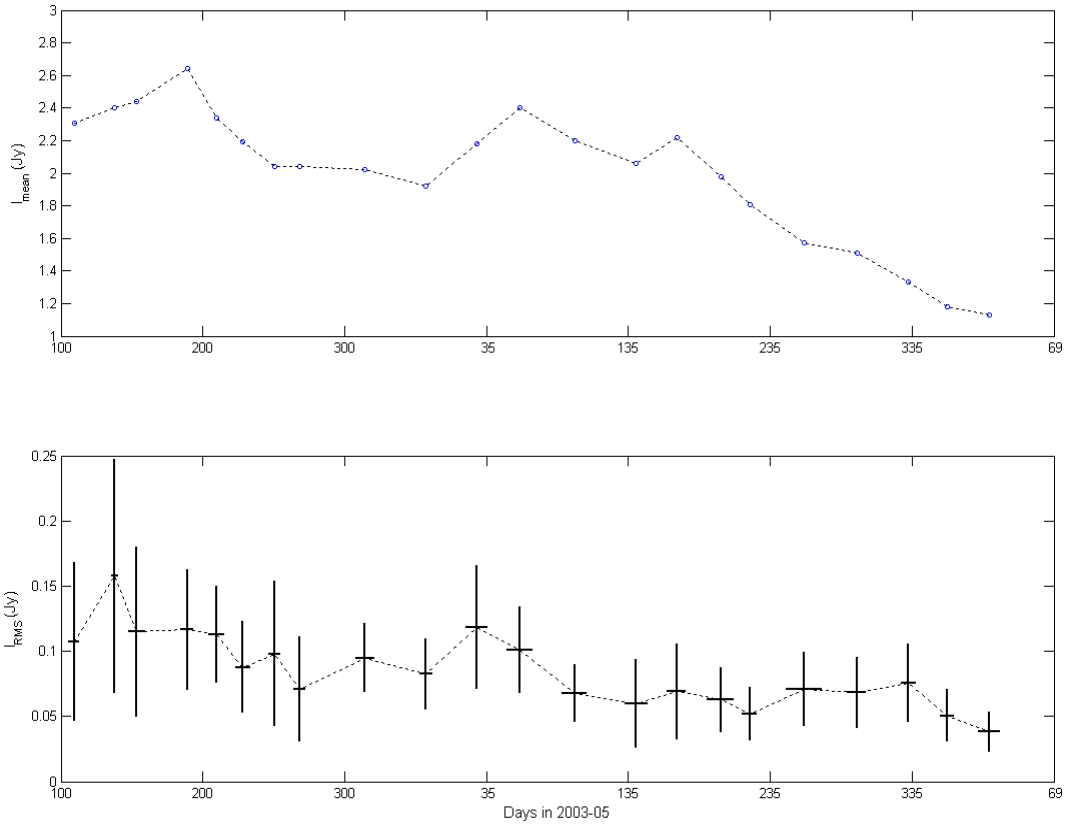

Figure 7.18 Mean and RMS flux densities for PKS B1519-273.

If the modulation indices associated with the scintillating component of each source are constant throughout the COSMIC campaign – an assumption fraught with uncertainty – then the correlations between the mean and the RMS flux densities for each observing period suggests that changes in the mean flux densities over the ~2 year observing campaign are largely due to changes in the scintillating component of the flux density in the case of the PKS B1519-273 emissions, and largely due to changes in the non-scintillating component of the flux density in the case of the PKS B1622-253 emissions.

PKS B1519-273

Section 7.2 found that the variability time scale, T_{period}, of the PKS B1519-273 scintillations, and the annual cycle in the time scale, are fully consistent with the findings of Jauncey et al. (2003), which were based on less data, but data obtained by better telescopes.

Final proof of the validity of the COSMIC results is obtained by comparing them with the findings of Macquart et al. (2000), based on the multi-frequency ATCA observations shown in Figure 7.6. Macquart et al. (2000) argue from study of the variability characteristics at the ATCA observing frequencies (1.4, 2.5, 3.8 & 8.6 GHz) that the 4.8 GHz observations must lie near the transition frequency between the weak and strong scattering régimes, and that the asymptotic results of weak scattering theory are valid at 4.8 GHz.

They note that the source must be partially resolved at 4.8 GHz, given the variability time scale of $\tau_{4.8\,\mathrm{GHz}}$ ~12 h, but its angular size is smaller than 0.3 mas, since it is unresolved by VSOP observations at 1.7 GHz, which places a lower limit on the scattering screen distance. The ATCA observations at 1.4 GHz are interpreted as due to refractive scattering, and in this régime the angular size of the scattering disc in the interstellar medium is comparable to, or larger than, the angular size of the source (see Table 2.2 in Section 2.5.3). This gives a minimum distance to the scattering screen of R = 390 pc through the constraint:

$$\tau_{1.4\,\mathrm{GHz}}\, V_{\mathrm{scint}} / R \quad \leq 0.3 \text{ mas}$$

where $\tau_{1.4\,\mathrm{GHz}} \approx 4$ days is the estimated variability time scale at 1.4 GHz, $V_{\mathrm{scint}} \approx 50$ km /s is the speed at which Macquart et al. (2000) assumed the Earth moves through the scintillation pattern, and the product ($\tau_{1.4\,\mathrm{GHz}}$ x V_{scint}) gives an estimate of the size of the scattering disc.

Near the transition frequency, the source is resolved if its angular diameter, θ_s, is larger than the angular diameter of the first Fresnel zone (again, see Section 2.5.3).

$$\theta_s = (k\,R)^{-1/2}$$

where k is the wavenumber. Assuming that the asymptotic results of weak scattering theory are valid for observations at 6.7 GHz, the scintillation time scale is (Narayan, 1992):

$$\tau_{obs}^{6.7\,\mathrm{GHz}} \approx \theta_s R / V_{\mathrm{scint}}$$

This gives

$$\theta_s \approx 14.44 \left(\frac{\tau_{\mathrm{obs}}}{12\,\mathrm{h}}\right)\left(\frac{V_{\mathrm{scint}}}{50\,\mathrm{km/s}}\right)\left(\frac{R}{1\,\mathrm{kpc}}\right)^{-1} \qquad \mu\mathrm{as}$$

in which the coefficient is (50 x 1000) (12 x 3600) / (1000α β), where the baseline Earth-ISM relative speed of 50 km/s, and the baseline scintillation timescale of 12 h, are converted to meters and seconds respective; α = 3.086 x 10^{16} m/pc, and β = 4.85 x 10^{-12} μas/radian.

Macquart et al. (2000) used $\tau_{4.8\,\mathrm{GHz}} \approx 12$ h, $V_{\mathrm{scint}} \approx 50$ km /s and $R \approx$ 0.39 kpc to estimate the maximum angular diameter of the source at 4.8 GHz to be $\theta_s \sim 37$ μas. Their definition of variability time scale is $T_{1/e}$, and the 4.8 GHz scintles in Figure 7.6 show that a peak-to-peak scintle time of $T_{\mathrm{period}} \sim 2$ days. COSMIC data for PKS B1519-273, presented in Figure 7.8 show that T_{period} values range from ~1 to 5 days over the course of a year, but that a value of $T_{\mathrm{period}} \sim 2$ days is quite in order at the beginning of September, which is when the data examined by Macquart et al. (2000) were recorded.

If the blazar radio emissions are assumed to contain a single scintillating component, then the mean flux density of the scintillating component, I_o, can be estimated from the weak scattering theory presented in Chapter 2, particularly the relationship (Narayan, 1992):

$$\frac{I_{rms}}{I_o} = m(\theta_s) = \left(k\, R\, \theta_s^2\right)^{-7/12}$$

where m is the modulation index expected for a source whose angular diameter is larger than the first Fresnel zone.

The 4.8 GHz PKS B1519-273 observations examined by Macquart et al. (2000), reproduced in Figure 7.6, have an RMS flux density value of I_{rms} = 0.11 Jy. Table 7.3 shows this is very similar to the I_{rms} values of the 6.7 GHz observations of PKS B1519-273 for the first year of the COSMIC campaign, after which the I_{rms} values decreased to about I_{rms} ~ 0.07 Jy.

Chapter 2 discusses the apparent brightness temperature, T_b , of a source with specific intensity I_ν , given by the expression $T_b = c^2 I_\nu \big/ 2 k_B \nu^2$, where k_B = 1.38 x 10^{-23} J/K is the Boltzmann constant. Following Macquart et al. (2000), the value of $I_\nu = I_o$ can be estimated from I_{rms} using the above weak scattering expression, and for 4.8 GHz observations this gives:

$$T_b^{\text{apparent}} \approx 2.0 \text{ x } 10^{14}\ I_{rms} \left(\frac{R}{1\text{ kpc}}\right)^{17/12} \left(\frac{\tau_{obs}^{4.8\text{ GHz}}}{12\text{ h}}\right)^{-5/6} \left(\frac{V_{\text{scint}}}{50\text{ km/s}}\right)^{-5/6} \text{K}$$

For the baseline values of 12 hours, 50 km, and 1 kpc, the coefficient is given as

$$\left(\frac{c^2}{2\pi k_B}\right)\left(\frac{4k^{7/12}}{\nu^2}\right) \quad (12 \text{ x } 3600)^{-5/6}\ (50 \text{ x } 3600)^{-5/6}\ (1000\,\alpha)^{17/12}$$

where α = 3.086 x 10^{16} m/pc, and ν is the observing frequency. Macquart et al. (2000) estimated a minimum brightness temperature of T_b = 5 x 10^{13} K, using $\tau_{4.8\text{ GHz}}$ ~12 h, $V_{\text{scint}} \approx$ 50 km /s and R = 0.39 kpc, consistent with synchrotron emission subject to relativistic beaming.

In summary, there is clear and strong consistency between the variability characteristics of PKS B1519-273 estimated from COSMIC data, and the variability characteristics estimated from ATCA data studied by Macquart et al. (2000). This is very pleasing, and the agreement between this analysis and that ATCA studies of Macquart et al. (2000) provides strong evidence that the calibration, data processing and variability analysis methods developed to handle the Ceduna data are sound and reliable.

Consideration of anisotropy

Full analysis of the PKS B1622-253 and PKS B1519-273 variability requires consideration of anisotropy. Such an analysis is a significant undertaking, but it is a task that must be faced, since it is wrong to assume isotropic scattering in the face of the evidence that the annual cycle in the scintillation time scale for PKS B1519-273 is associated with high anisotropy. Dennett-Thorpe & de Bruyn (2003) also found significant anisotropy in the annual cycle fit to their observations of variability in quasar J1819+3845. They note that anisotropy in scattering structures is generally expected, with potentially very large axial ratios predicted by compressible magnetohydrodynamic turbulence models (Lithwick & Goldreich, 2001).

Anisotropy can, of course, also be due to elongated source structure, or to a mixture of source elongation and scattering structure anisotropy. Scintillation theory suggests that anisotropy due to an elongated source that is larger than the Fresnel angle would dominate anisotropy due to MHD turbulence, but a detailed study is needed to confirm this.

In the case of PKS B1622-253, a detailed variability study should be preceded by multi-frequency observations using the Australia Telescope Compact Array to confirm that this source lies in the weak scattering régime at the 6.7 GHz Ceduna observing frequency.

8.0 CONCLUSIONS AND FUTURE RESEARCH

8.1 Research Summary

The COSMIC project

Conversion of the Ceduna Earth Station antenna for radio astronomy usage was finished in 1997, and greatly enhanced Very Long Baseline Interferometry work in Australia.

The initial COntinuous Single dish Monitoring of Intraday variables at Ceduna (COSMIC) campaign started in March 2003, targeting blazars with flux densities ≥~1 Jy. In 2002, I worked with Dr Simon Ellingsen and others to develop an observing strategy suitable for the Ceduna antenna, and the result was that the blazars were divided into groups lying south and north of the zenith at Ceduna, to avoid excessive telescope slewing, with each group served by a calibrator source. Each group of blazars was observed in turn for periods of 10-15 days.

Establishing that a remotely operated 30 m telescope could achieve the performance needed for long term monitoring of blazars is key outcome of this research. I presented the first COSMIC results at *The Variable Radio Universe* workshop, held in July 2003 at the Parkes radio telescope facility, and subsequently Dr Dave Jauncey presented the same results at the 2003 IAU General Assembly. This work, together with the earlier conversion project, won an Engineering Excellence Award from Engineers Australia in late 2003.

The COSMIC campaign continued until early 2005, when a major maintenance overhaul of the telescope was undertaken. Throughout this ~2 year period, I was responsible for daily monitoring the telescope operation and adjusting it as need be, downloading FITS files and processing the raw data. Several adjustments to the observing strategy were trialed, but in the end the strategy outlined above was continued.

Initial data processing

The Ceduna telescope has remote operation capability, enabling control of the telescope in real-time, including programming it with instructions, starting it, monitoring its operation, stopping it, and stowing it. Chapter 3 provides details of the experimental set-up for the COSMIC project, including a description of the back-end.

The telescope produces a FITS file for each day of operation, containing flux density scans of all the blazar and calibrator radio sources being observed, plus ancillary information. The antenna scans across the source back and forth in right ascension, and then in declination. Each scan takes ~15 seconds at the telescope drive rate of 3º/min, but additional operations of antenna slewing, calibration measurements, data outlier excision, data resampling, and pointing corrections result in a mean scan rate of about one per minute.

I wrote and tested a suite of procedures, using *Matlab* software, to extract and process raw data from the FITS files, to obtain flux density points. These procedures are quite complex, and implement a processing strategy that I designed to be semi-automatic. The procedures include optimisation exercises, display and trouble-shooting routines, pointing corrections (only preliminary pointing corrections are applied during the telescope's operation), gain-elevation corrections that I determined from calibrator data, and quality control tests. The procedures are described in Chapter 3.

Flux density data processing

Preliminary examination in 2003/04 of the quality of data recorded by the Ceduna telescope failed to recognise that ±0.15 Jy flux density fluctuations on diurnal time scales were systematic in nature. These fluctuations are now known to have a thermal origin, and part of the evidence for this is that the flux density time series also exhibit minor fluctuations on time scales of several days (this is best seen by examining the calibrator data), which correspond to the synoptic time scales of weather systems; and also on seasonal time scales.

I developed a data processing method, presented in Chapter 4, which smoothes through the diurnal flux density fluctuations for each 10-15 day observing period, for each blazar being observed, and then uses the calibrator observations to correct for the small weather-related fluctuations on time scales of days. Corrections for minor seasonal effects are also made.

The methodology also removes any flux density trends across an observing period, which result in spurious low-frequency effects (described in Chapter 4), and produces a zero-mean data set for each observing period, suitable for variability analysis. These data are attached in the appendices to this thesis. Somewhat unusually, the data processing is carried out in the time-domain, because visual inspection of the process is reassuring, and because some of the corrections using calibrator data are facilitated by an analysis in the time domain.

Chapter 5 examines the consequences of the systematic fluctuations for variability analysis of the blazars of interest to the present research, PKS B1622-253 and PKS B1519-273. A suite of tests examined the fast (diurnal) component of the blazar variability, comparing the fluctuations and the power spectral density functions of the blazars and the calibrators. The conclusion was that both PKS B1622-253 and PKS B1519-273 vary on time scales of days, and that neither source exhibits genuine variability on diurnal time scales. Of course, an analysis of blazars that do exhibit genuine variability on time scales of hours will first need to remove the systematic fluctuations on these time scales.

In late 2005, PhD candidate Cliff Senkbeil began developing a data processing method to remove the systematic fluctuations in the Ceduna data. A year later he produced a new data processing method that treats flux density measurements made by the two polarisation channels separately, and uses a more sophisticated calibration procedure. Cliff's method is superior to my earlier approach, which combines data from the two polarisation channels and then applies quality control measures that reject poor data based on various consistency tests. My method produces data of comparable quality, but fewer data points.

Unfortunately, the new method does not succeed in removing the systematic fluctuations, and indeed any new method that relies on calibrator data to make corrections can only be applied if sufficient calibrator data are available. Calibrator 3C227 lies north of the equator and is not observed for long enough each day to enable the method to be applied to sources in the northern observing group, which includes PKS B1622-253 and PKS B1519-273.

Data analysis

Analyses of time series recorded over periods of hours to days by major facilities such as the Australia Telescope Compact Array use established analysis software packages. In the case of blazar scintillation studies, spectral analysis based on the use of autocorrelation functions is traditionally used to examine characteristic variability time scales, with $T_{0.5}$ or $T_{1/e}$ being common descriptors of variability.

The time series recorded by the COSMIC project record scintles with peak-to-peak periods of typically several days. These time series have gaps and other characteristics that provide challenges to a variability analysis that do not appear to have been encountered by analyses of more rapid scintillation, or of slow scintillation involving only a few scintles. Chapter 4 demonstrates that determination of $T_{0.5}$ and $T_{1/e}$ is affected by daily observing gaps; by scintles with periods near an integral number of days; and when the above-horizon observing time is shorter than the below-horizon time.

On the other hand, no previous blazar monitoring program has recorded such complete time series of scintles for variability time scales of days. I realised that this enabled a variability analysis in which the characteristic variability time scale is defined to be the scintle peak-to-peak period, T_{period}. Of course, values of $T_{0.5}$ or $T_{1/e}$ can still be estimated for examination of decorrelation timescales, but with the above caveat about the accuracy of these estimates

By mid-2004, I had developed a suite of analysis tools using the *Matlab* software package, appropriate for Ceduna data. The approach, described in Chapter 4, is to determine T_{period} values using spectral analysis, with the power spectral density function preferred to the autocorrelation function; and to use a) empirical scintle counting and b) data folding to cross check the T_{period} values.

Telescope performance

Chapter 5 examines the performance of the Ceduna telescope over the ~2 year period of the COSMIC project, including the thermal and "1/f" ("fractional") noise associated with the Ceduna data, and the deviation of total noise from thermal noise as a function of integrating time. The $1/f$ noise is ~1% of the total flux density, and is probably due to electronic gain fluctuations. It is about 2½ times greater than thermal noise at the integration times relevant to the Ceduna flux density measurements.

The consistency in calibrator observations over the ~2 year period is examined, and clearly shows that the 30 m Ceduna telescope can carry out long term monitoring of sources with strengths ≥ ~1 Jy to the accuracy necessary for the analysis of variability on time scales of days. Better performance is expected in future campaigns, now that the maintenance needs of the telescope are better appreciated; and once the problem of systematic flux density fluctuations on diurnal time scales is addressed.

Data reduction

Chapter 6 sets out the data reduction exercise for PKS B1622-253 and PKS B1519-273, with flux density time series for both blazars, spectral analysis and other plots included in the appendices. The application of the variability analysis tools (spectral analysis, scintle counting, and data folding) to the data is described for each observing period, with estimates of the variability time scale classed as well defined, fairly well defined, and poorly defined, according to criteria set out in the Chapter.

An interesting aspect of the flux density data sets for some observing periods is the presence of small flux density fluctuations, in addition to more distinct fluctuations. Similar small fluctuations have been observed in the scintillation of other blazars, an example being the PKS 1257-326 data reported by Bignall et al. (2003). They are real, but their origin is not known. The likely explanation is that the small fluctuations are genuine scintles which are not well defined compared to adjacent scintles, although explanations such as additional variability time scales are difficult to completely rule out with the present data sets.

Chapter 6 also sets out the statistical properties of the scintle periods and heights. In the case of scintle periods, an approach devised by the author avoids problems caused by the fact that T_{period} values typically change between observing periods either because of source evolution, or because of the annual cycle expected for scintillation caused by scattering in the ISM, or a combination of these two effects.

A knowledge of scintle statistics provides an empirical way to determine error bars for the variability time scale estimated for each 10-15 day observing period. The scintle period distributions are well modelled by Gaussian fits that are very similar for the two blazars, since the sources are large enough to band-limit the scintillation process in similar ways.

Chapter 4 examines the effect of stochasticity in a flux density time series, using Monte Carlo simulations based on synthetic Ceduna data. In Chapter 6, the 95% confidence interval error bars for T_{period} values calculated from a typical set of scintles are found to be comparable to the 2 σ ~ 10% upper limit of the stochasticity in T_{period} values that the Monte Carlo modelling found would enable T_{period} to be computed with fair accuracy.

The Monte Carlo exercise also found, unsurprisingly, that accurate determination of T_{period} values is not sensitive to stochasticity in scintle heights, and this is just as well. Chapter 6 shows that scintle heights for the two blazars vary significantly, and their distributions can be described by any of several distributions. They are skewed towards smaller heights, and possible reasons for this are discussed in the chapter.

Variability analyses

Chapter 7 reviews the observation histories of PKS B1622-253 and PKS B1519-273, and shows that for both these blazars the characteristic variability times scales (the T_{period} values) for each 10-15 day observing period in the COSMIC project exhibit a clear annual cycle.

PKS B1622-253 lies at z = 0.786, and has observed extended radio structure whose main features are a powerful radio core, FR II radio lobes consisting of a diffuse jet-like eastern extension, and a western lobe that is also part of a jet. PKS B1519-273 lies at z = 1.294, and is a point source (< 0.3 mas at 1.7 GHz), with no resolvable structure. Multi-frequency observations of both sources by the Australian Telescope Compact Array and the RATAN-600 ring telescope are presented and rough sub-milliarcsecond source size estimates are made from the flux density spectra.

The COSMIC observations of PKS B1519-273 agree well with previous multi-frequency observations of this source. Its flux density variability is associated with the weak scattering régime at the 6.7 GHz Ceduna observing frequency. The multi-frequency observations to date of PKS B1622-253 are not sufficient to unequivocally define the scattering régime of this source at the 6.7 GHz Ceduna observing frequency, but the similarity of the scintillation record to that of PKS B1519-273 strongly suggests that COSMIC observations of this source also lie in weak scattering régime.

The annual cycles in the variability time scales of the two blazars are modelled using the standard theory of interstellar scintillation of Active Galactic Nuclei radio emissions, described in Chapter 2. T_{period} values for PKS B1622-253 and PKS B1519-273 range over about 2 – 10 days and about 1-5 days respectively. The strength of PKS B1519-273 reduced below 1.5 Jy in mid-2004, precluding accurate determination of T_{period} values in the final half a year or so of the COSMIC project. However, the annual cycle in the variability time scale of this source clearly agrees well with previous observations.

For both sources the optimum annual cycle is for highly anisotropic scintles and for a large velocity offset of the scattering screen with respect to the Local Standard of Rest. This is unsurprising: significant velocity offsets are expected for scintillation with relatively long variability time scales (days rather than hours), which is associated with more distant scattering screens that typically lie hundreds of parsecs from Earth, and thus are in motion with respect to the LSR. Chapter 7 examines a range of annual cycle model sensitivity tests, which highlight the interplay between scintle anisotropy and the LSR velocity offset.

A pleasing outcome of both variability analyses is their reduced chi-square statistics. A model is good if $\chi^2_{\text{Red}} \approx 1$. If $\chi^2_{\text{Red}} << 1$, the error bars are too large. If $\chi^2_{\text{Red}} >> 1$, either the error bars have been underestimated or the data are not well described by the model. The χ^2_{Red} values for PKS B1622-253 and PKS B1519-273 are 2.12 and 0.83 respectively, which confirms that the empirically determined error bar estimates are appropriate, and that the standard annual cycle model credibly describes the variability time scales of both blazars.

A further pleasing outcome of the variability analyses emerges when the annual cycle effects are removed. This exercise parallels that carried out by Dennett-Thorpe & de Bruyn (2003) for the quasar J1819+3845 data, also spanning two years of observations. All three sources display variability that appears to be very similar throughout the observing campaigns, and the cumulative power spectral density functions of the PKS B1622-253 and PKS B1519-273 data over the 2003/05 period, with the annual cycle effect removed, shows little evidence of additional variability in the frequency range of interest for these blazars (0.1 to 0.9 days^{-1}).

Chapter 7 concludes by demonstrating that there is clear and strong consistency between the PKS B1519-273 variability characteristics estimated from COSMIC data, and the variability characteristics estimated from ATCA data studied by Macquart et al. (2000). There is also clear agreement between the PKS B1519-273 variability time scales found by the COSMIC project, and the work reported by Jauncey et al. (2003).

8.2 Future Work

Recommendations for future work break into three groups.

1). Anisotropic variability analysis of PKS B1622-253 and PKS B1519-273.

An analysis of the PKS B1622-253 and PKS B1519-273 variability requires additional consideration of anisotropy to establish whether the anisotropy identified by the annual cycle modelling is due to magnetohydrodynamic turbulence in the interstellar medium (which is significant undertaking), or due to elongated source structure (which is relatively simple), or both. Scintillation theory suggests that anisotropy due to an elongated source that is larger than the Fresnel angle would dominate anisotropy due to MHD turbulence, but a detailed study is needed to confirm this.

In the case of PKS B1622-253, it will first be necessary to carry out multi-frequency observations using the Australia Telescope Compact Array to confirm that variability of this source at the 6.7 GHz Ceduna observing frequency lie in the weak scattering régime.

2). Analysis of other COSMIC sources.

The author carried out an initial analysis of PKS B1144-379 that appeared to show the presence of a persistent 9-11 day variability cycle superimposed on a scintle timeseries similar to the timeseries for PKS B1622-253 and PKS B1519-273. Dr Giuseppe Címò has taken up the task of examining the COSMIC data for this source.

The first scintles identified by the author from the COSMIC project were for J1326-5206, and were very pronounced. The source stopped scintillating for a while, shortly after the start of the COSMIC program in March 2003, but subsequently started scintillating again. Mr Cliff Senkbeil has taken up the task of examining the COSMIC data for this source.

3). Eliminating the systematic fluctuation problem.

Much progress has been made in understanding the nature of the systematic effects identified by the author in 2005, and once this problem is eliminated it is expected that the 30 m Ceduna antenna will be able to examine variability on times scales of hours in sources with flux densities less than ~½ Jy, which is roughly the present limit. Temperature stabilization of as much equipment as possible is recommended.

8.3 Afterword: The Role of Conflict in Research

Debate, controversy, argument. Shades of conflict between people who often hold sharply opposing views: the challenge to prove a theory, to defend a method or an interpretation of observations. Conflict plays an essential role in guiding the path of science, and my past five-plus years of work has given me a clearer insight into the role of conflict in research.

Over 20 years ago, in April 1987, I wrote an essay on the epistemological basis of science, in fulfilment of an assignment set in a University of Toronto philosophy course entitled *Knowledge, Belief & Truth.* The essay, in part, examined the well known "Does God play dice?" debate between Neils Bohr and Albert Einstein over the emerging theory of quantum mechanics, a debate they maintained over a period of decades. It was an excellent example of two scientists seeking to resolve conflict in a professional fashion, and there are many examples of the continuing role that conflict plays in guiding science.

But some conflicts seem to be harder to resolve than they should be if the facts were all that mattered, for the obvious reason that there is a human side to conflict. I find three aspects of this particularly interesting.

First, consider conflict involving many people. Al Gore's movie asserts that climate change is *An Inconvenient Truth*, whereby organisations harbouring vested interests weigh into the conflict alongside scientists. An example closer to the field of astrophysics is the 1986 space shuttle *Challenger* disaster. Richard Feynman's report on the disaster compared the view of shuttle safety held by NASA engineers, that 1 in 100 flights might fail, to the view held by NASA management that 1 in 100,000 flights might fail, such that if a shuttle was to fly every day for 300 years, only one would be lost.

Feynman accused NASA management of ignoring the conflict between the risk level they wanted to be true, and the risk level assessed by the people who had designed, built, and maintained the shuttle. Feynman's message to NASA management was to appreciate that reality must take precedence over public relations, for nature cannot be fooled.

Second, conflict resolution can also suffer from the "inconvenient truth" problem at a more personal level. Paraphrasing Al Gore, it is difficult to make someone change their mind if their reputation and/or funding depends on them not doing so. Peter Woit's book *Not Even Wrong* suggests that the debate over the merits of string theory is an example of this (Woit, 2006). Woit suggests that threats to personal situations underpins some people's entrenched positions on the string theory debate.

An example in the field of astrophysics is provided by Sir Arthur Eddington, whose theories on the fate of stars were in conflict with those of Subramaniam Chandrashekhar, specifically regarding Chandrashekhar's assertion that dying stars with more than ~1.44 solar masses could overcome the electron degeneracy pressure responsible for white dwarfs, and would thus continue to collapse. Eddington, a highly respected scientist, attacked Chandrashekhar in such a fashion that the young scientist abandoned his work in the area. How was his approach to resolving conflict beneficial to science?

And there is a third reason. At the 2006 Texas Symposium on Relativistic Astrophysics, in Melbourne, I was taken aback when some excellent presentations were met by aggressive questioning that bypassed the usual demand of basic people skills of first finding something nice to say about the work being presented. I came away from the symposium thinking that, while the necessary role of conflict in science was alive and well, some scientists likely have difficulty resolving conflict simply because they have atrocious people skills.

My research, while not dealing with impressive subjects such as space shuttles or the fate of stars, has also run the gauntlet of controversy. One conflict was only "resolved" by a change in supervision team, which was a highly unsatisfactory way to move forward.

Conflict is a necessary part of science, but how people go about resolving that conflict is important if science is to progress. I can appreciate the devastation to his confidence that Chandrashekhar must have felt when he was subjected to criticism by Eddington that was not balanced by any praise from the senior scientist for his achievements.

In addition to helping to resolve conflict in a satisfactory fashion, people skills are necessary for effective team work – and science today relies more heavily than ever on team work to achieve results. Some scientists have excellent people skills, of course, but many do not, and some offenders are elevated to positions of leadership because of their academic credentials. I found it almost funny, in a sad way, to watch some people break almost every rule of how to interact with others during breaks at the Texas Symposium. I felt like placing a copy of Dale Carnegie's *How to Win Friends and Influence People* alongside the displays of astrophysics texts.

It is time for scientists to pay more attention to the human side of science and learn the importance of people skills. An ability to work in teams should be an expected attribute of graduates from an undergraduate degree in science. Senior scientists express dismay at younger colleagues who leave the world of science, some as soon as they have earned their degree or higher degree. A common opinion is that the pay is better elsewhere. Well, that might be one reason.

9.0 REFERENCES

A&A	Astronomy & Astrophysics	ESP
AJ	The Astronomical Journal	The American Astronomical Society University of Chicago Press
ApJ	The Astrophysical Journal	The American Astronomical Society University of Chicago Press
Ap&SS	Astrophysics and Space Science	Kluwer Academic Publishers
ASP	Astronomical Society of the Pacific	
MNRAS	Mon. Not. R. Astron. Soc.	Blackwell
PASA	Publications of the Astronomical Society of Australia	CSIRO Publishing
PASP	Publications of the Astronomical Society of the Pacific	University of Chicago Press

Anderson, E.E. 1971. *Modern Physics and Quantum Mechanics.* W.B. Saunders Company, Philadelphia, U.S.

Armstrong, J.W., Rickett., B.J. & Spangler, S.R. 1995, ApJ 443, 209 [*Electron density power spectrum in the local interstellar medium*].

Baars, J.W.M., Genzel, R., Pauliny-Toth, I.I.K. &Witzel, A. 1977, A&A, 61, 99-106. [*The absolute spectrum of CASA - an accurate flux density scale and a set of secondary calibrators]*

Battaner, E. 1996, *Astrophysical Fluid Dynamics*, Cambridge University Press.

Begelman, M.C. & Rees, M.J. 1998. *Gravity's Fatal Attraction: Black Holes in the Universe.* Scientific American Library, New York.

Begelman, M., Rees, M.J. & Sikora, M. 1994, ApJ, 429: L57-60 [*Energetic and radiative constraints on hightly relativistic jets*].

Beckert, T., Fuhrmann, L., Cimò, G., Krichbaum, T.P., Witzel, A. & Zensus, J.A. 2002 In Ros et al. (2002) [*Understanding scintillation of intraday variables*].

Bhat, N.D.R., Gupta, Y. & Rao A.P. 1998, ApJ, 500, 262-279. [*Pulsar scintillation and the local bubble*].

Bignall, H.E. 2003, PhD thesis, University of Adelaide. [*Radio variability and interstellar scintillation of blazars*].

Bignall, H.E., Jauncey, D.L, Lovell, J.E.J., Tzioumis, A.K., Kedziora-Chudzer, L.L., Macquart, J.-P., Tingay, S.J., Rayner, D.P. & Clay, R.W. 2003, ApJ, 585, 653 [*Rapid variability and annual cycles in the characteristic time-scale of the scintillating source PKS 1257-326*].

Birrell, N.D. & Davies, P.C.W. 1982. *Quantum fields in curved space.* Cambridge University Press.

Bland-Hawthorn, B., & Reynolds, R. 2000 *Gas in Galaxies,* in Encyclopedia of Astronomy and Astrophysics, MacMillan and Institute of Physics Publishing.

Blandford, R.D. 1994, ApJ Supp. Series, 90, 515-520. [*Particle Acceleration Mechanisms*].

Blandford, R.D. 2002, luml. conf., 381B. [*To the Lighthouse*]

Blandford, R.D. & Königl, A. 1979, ApJ, 232: 34-48 [*Relativistic Jets as Compact Radio Sources*].

Blandford, R.D., McKee, C.F. & Rees, M. 1977, Nature, 267, 211-216. [*Super-luminal expansion in extragalactic radio sources*].

Blandford, R.D. & Payne, D.G. 1982 MNRAS, 199, 883-903. [*Hydromagnetic flows from accretion discs and the production of radio jets*].

Blandford, R.D. & Znajek, R.L. 1977, MNRAS, 179, 433-456. [*Electromagnetic extraction of energy from Kerr black holes*]

Bolton, J.G., Shimmins, A.J. & Wall, J.V. 1975, AuJPA, 34, 1-32. [*The Parkes 2700 MHz Survey (Seventh Part): Supplementary Catalogue for the Declination zone -4° to -30°*]

Burbidge, G.R., Jones, T.W. & Odell, S. L. 1974, ApJ, 193, 43-54. [*Physics of compact nonthermal sources. III - Energetic considerations*]

Burke, B.F. & Graham-Smith, F. 2002, *An Introduction to Radio Astronomy, 2nd Ed.,* Cambridge University Press, U.K.

Chaisson, E., & McMillan, S. 2002, *Astronomy Today 4th Ed.,* Prentice-Hall Inc., New Jersey, U.S.

Chandran, B.D.G. & D.C. Backer 2002. ApJ, 576, 176. [*Radio wave propoagation through a medium containing electron density fluctuations described by an anisotropic Goldreich-Sridhar spectrum*].

Clements, E. D. 1981, MNRAS, 197, 829 [*Optical positions of Seyfert galaxies*]

Codona, J.L. & Frehlich, R.G. 1987, Radio Sci., 22, 469-480. [*Scintillation from extended incoherent sources*]

Coles, W.A., & Kaufman, J.J. 1978 Radio Science, vol. 13, May-June 1978, pp.591-597. [*Solar wind estimation from multi-station IPS*].

Coles, W. A., Fehlich, R. G., Rickett, B. J. & Codona, J.L. 1987, ApJ, 315, 666-674. [*Refractive scintillation in the interstellar medium*].

Cordes, J.M., & Lazio, T.J.W. 2001, ApJ, 549, 997 [*Anomalous radio-wave scattering from interstellar plasma structures*].

Cordes, J.M. & Lazio, T.J.W. 2006a, draft pre-print 15 May 2006. Astro-ph/0207156. [*NE2001. I. A New Model for the Galactic Distribution of Free Electrons and its Fluctuations*].

Cordes, J.M. & Lazio, T.J.W. 2006b, draft pre-print 24 May 2006. Astro-ph/0301598. [*NE2001. II. Using Radio Propagation Data to Construct a Model for the Galactic Distribution of Free Electrons*].

Cordes, J.M. & Rickett, B.J. 1998, ApJ, 507, 846 [*Diffractive interstellar scintillation timescales and velocities*].

Cox, D.P. 1998, LNP, 506, 121. [*Modeling the Local Bubble*]

Crane, P.C. & Napier, P.J. 1989 In *Synthesis Imaging in Radio Astronomy* eds. R.A. Perley, F.R.Schwab, & A.H. Brindle (San Francisco: ASP conference series), 139-165.

De Bruyn, A.G & Dennett-Thorpe, J. 2001, Ap&SS, 278, 139-142. [*The Microarcsecond Quasar J1819+3845: Polarization Observations and Detailed Lightcurve Analysis*].

Deeming, T.J. 1974, Ap&SS, 36, 137-158. [*Fourier analysis with unequally-spaced data*].

Dennett-Thorpe, J. & de Bruyn, A.G. 2000, ApJ, 529, L65-L68 [*The Discovery of a Microarcsecond Quasar: J1819+3845*]

Dennett-Thorpe, J. & de Bruyn, 2003, A&A., 404, 113-132. [*Annual modulation in the scattering of J1819+3845: Peculiar plasma velocity and anisotropy*].

De Vries, W.H., Barthel, P.D. & O'Dea, C.P. 1997, A&A, 321, 105-110. [*Radio spectra of Gigahertz Peaked Spectrum radio sources.*]

De Young, D.S. 2002, *The Physics of Extragalactic Radio Sources.* Uni. of Chicago Press.

Di Serego-Alighieri, S., Danziger, I.J., Morganti, R. & Tadhunt, C.N. 1994, MNRAS, 269, 998. [*New identifications and redshifts for southren 2-Jy radio sources*].

Eckart, A., Genzel, R., Ott, T. & Schödel, R. 2002, MNRAS, 331, 917-934. [*Stellar orbits near Sagittarius A**].

Edelson, R. A. & Krolik, J. H. 1988, ApJ, 333, 646-659. [*The discrete correlation function - A new method for analyzing unevenly sampled variability data*]

Elmegreen, B.G. & Scalo, J. 2004, Ann. Rev. Astron. Astrophys. 42:211-73 [*Interstellar Turbulence I: Observations and Processes*].

Fanaroff, B. & Riley, J. 1974, MNRAS, 167, 31-35p. [*The morphology of extragalactic radio sources of high and low luminosity*]

Fanti, R., Fanti, C., O'Dea, C., Schilizzi, R.T., Spencer, R.E., Rendong, N., Parma, P., van Breugel, W.J.M. & Venturi, T. 1990, A&A, 231, 333-346. [*On the nature of compact steep spectrum radio sources*]

Ferrière, K.M. 2001, Reviews of Modern Physics, 73, 4 [*The interstellar environment of our Galaxy*].

Fichtel, C.E. {& 25 co-authors} 1994, ApJS, 94, 551-581. [*The first energetic gamma-ray experiment telescope (EGRET) source catalog]*

Fuhrmann, L., Cimò, G., Krichbaum, T.P., Beckert, T., Witzel, A. & Zensus, J.A. In Ros et al. (2002) [*Compact Intraday Variable Radio Cores: New Observational Approaches*].

Gallo, L.C. {& 12 co-authors} 2006, MNRAS, 370, 245-254. [*The spectral energy distribution of PKS 2004-447: a compact steep-spectrum source and possible radio-loud narrow-line Seyfert 1 galaxy*]

Garwood, R.W. 2000. In ASP Conf. Ser., Vol 216, 243. *Astronomical data Analysis Software and Systems IX*, eds. Manset, N., Veillet, C. & Crabtree, D. [*SDFITS: A Standard for Storage and Interchange of Single Dish Data*]

Goldreich, P. & Sridhar, S. 1995, ApJ, 438, 763-775. [*Toward a theory of interstellar turbulence. 2: Strong Alfvenic turbulence*]

Goldreich, P. & Sridhar, S. 1997, ApJ, 485, 680-688. [*Magnetohydrodynamic Turbulence Revisited*]

Gupta, Y. 2001, Ap&SS, 278, 5-10 (IAU Colloq. 182). [*Pulsar scintillation: overview and some recent results*]

Gwinn, C.R., Hirano, C. & Boldyrev, S. 2006, A&A, 453, 595-599. [*Interstellar scintillation of PSR J0437-4715 on two scales*].

Heeschen, D.S. 1984 AJ, 89, 8. [*Flickering of extragalactic radio sources*].

Heidt, J., Troller, M., Nilsson, K., Jager, K., Takalo, L., Rekola, R. & Sillanpaa, A. 2004 A&A, 418, 813. [*Evolution of BL Lacertae host galaxies*].

Heidt, J. & Wagner, S.J. 1996, A&A, 305, 42-52. [*Statistics of optical intraday variability in a complete sample of radio-selected BL Lacertae objects.]*

Hewish, A., Bell, S.J., Pilkington, J.D.H., Scott, P.F. & Collins, R.A. 1968, Nature, 217, 709. [*Observation of a rapidly pulsating radio source*].

Hunter, S. D., Digel, S. W., de Geus, E. J. & Kanbach, G. 1994, ApJ, 436, 216-228. [*Gamma-ray observations of Ophiuchus with EGRET: The diffuse emission and point sources*]

Impey, C. D. & Tapia, S. 1990 ApJ. 354, 124-139. [*The optical polarization properties of quasars*]

Jauncey, D.L., Johnston, H.M.,Bignall, H.E., Lovell, J.E.J., Kedziora-Chudczer, Tzioumis, A.K. & Macquart, J-P. 2003, Ap&SS, 288, 63-68. [*Interstellar scintillation and annual cycles in the BL LAC source PKS 1519-273*].

Jauncey, D.L., King, E.A.,Bignall, H.E., Lovell, J.E.J., Kedziora-Chudczer, Tzioumis, A.K., Tingay, S.J., Macquart, J-P. & McCulloch, P.M. 2003, PASA, 20, 151-155. [*Variability in GPS Sources*].

Jauncey, D.L. & Macquart, J.-P. 2001 A&A, 370, L9 [*Intra-day variability and the interstellar medium towards 0917+624*].

Jenkins, G.M. & Watts, D.G. 1968. *Spectral Analysis and its Applications.* Holden-Day.

Jorstad, S. G., Marscher, A. P., Mattox, J.R., Wehrle, A.E., Bloom, S.D. & Yurchenko, A.V. 2001 ApJ Supp. Series, 134, 181-240. [*Multiepoch Very Long Baseline Array Observations of EGRET-detected Quasars and BL Lacertae Objects: Superluminal Motion of Gamma-Ray Bright Blazars*]

Kaplan, S.A. & Pikelner, S.B. 1970, *The Interstellar Medium,* Harvard University Press.

Kedziora-Chudczer, L., Jauncey, D. L., Wieringa, M. H., Walker, M. A., Nicolson, G. D., Reynolds, J. E. & Tzioumis, A. K. 1997, ApJ, 490, L9-L12. [*PKS 0405-385: The Smallest Radio Quasar?*].

Kedziora-Chudczer, L.L., Jauncey, D.L., Wieringa, M.H., Reynolds J.E. & Tzioumis, A.K. 1998. IAU Colloquium 164, ASP Conference Series, V144. [*Four Southern Intraday Variable Radio sources*]

Kedziora-Chudczer, L., Jauncey, D.L., Wieringa, M.H., Tzioumis, A.K. & Reynolds J.E. 2001 MNRAS, 325, 1411. [*The ATCA intraday variability survey of extragalactic radio sources*]

Kellerman, K.I. & Pauliny-Toth, I.I.K. 1969 ApJ, 155, L71 [*The spectra of opaque radio sources*].

Kellerman, K.I. & Pauliny-Toth, I.I.K. 1981 Ann. Rev. Astron. Astrophys. 19: 373-410 [*Compact Radio Sources*].

Kellerman, K.I., Vermeulen, R.C., Zensus, J.A. & Cohen, M.H. 1998 AJ, 115: 1295-1318 [*Sub-milliarcsecond imaging of quasars and active galactic nuclei*].

Kellerman, K.I., Lister, M.L., Homan, D.C., Vermeulen, R.C., Cohen, M.H., Ros, E., Kadler, M., Zensus, J.A. & Kovalev, Y.Y. 2004 ApJ, 609: 539-563 [*Sub-Milliarcsecond Imaging of Quasars and Active Galactic Nuclei. III. Kinematics of Parsec-scale Radio Jets*].

Kolmogorov, A.N. 1941, Translation from Russian in Proc. Roy. Soc. London Series A (1991) 434, 149-164. [*The local structure of turbulence in incompressible viscous fluid at very large Reynolds number*].

Kovalev, Y. Y., Nizhelsky, N. A., Kovalev, Yu. A., Berlin, A. B., Zhekanis, G. V., Mingaliev, M. G. & Bogdantsov, A. V. 1999, A&AS, 139, 545-554. [*Survey of instantaneous 1-22 GHz spectra of 550 compact extragalactic objects with declinations from -30deg to +43deg*]

Kuncic, Z., Bicknell, G.V. & Dopita, M.A. 1998, ApJ, 495L [*Induced Compton Scattering in Gigahertz Peak Spectrum Radio Sources*]

Lightman, A.P., Press, W.H., Price, R.H. & Teukolsky, S.A. 1975. *Problem Book in Relativity and Gravitation*. Princeton University Press, New Jersey.

Linfield, R. P. {& 14 co-authors}, 1989, ApJ, 336, 1105-1112. [*VLBI using a telescope in Earth orbit. II - Brightness temperatures exceeding the inverse Compton limit*]

Lister, M.L. & Homan, D.C. 2005, AJ, 130, 1389-1417. [*MOJAVE: Monitoring of Jets in Active Galactic Nuclei with VLBA Experiments. I. First-Epoch 15 GHz Linear Polarization Images*]

Lithwick, Y. & Goldreich, P. 2001, AAS, 198. [*Compressible Turbulence in Interstellar Plasmas*]

Lovell, J.E.J., Jauncey, D.L. {& 5 co-authors}, 2003, AJ, 126,1699-1706. [*First Results from MASIV: The Micro-Arcsecond Scintillation-Induced Variability Survey*].

Lovell, J. E. J., Jauncey, D.L., {& 9 co-authors}, 2007, arXiv:astro-ph/0701601. To be published in ASP Conference Series. [*MASIV:The Microarcsecond Scintillation-Induced Variability Survey*]

Luo, Q. & Melrose, D. 2006, MNRAS, 368, 1151-1158. [*Anisotropic weak turbulence of Alfvén waves in collisionless astrophysical plasmas*]

Lyne, A.G. & Graham-Smith, F. 1998. *Pulsar Astronomy*, 2nd Ed., Cambridge Uni. Press.

Ma, C., Arias, E. F. & 7 co-authors 1998 AJ, 116, 516-546. [*The International Celestial Reference Frame as Realized by Very Long Baseline Interferometry*]

Macquart, J.-P. & de Bruyn, A.G. 2006, A&A, 446, 185-200 [*Diffractive interstellar scintillation of the quasar J1819+3845 at λ21* cm]

Macquart, J.-P. & de Bruyn, A.G. 2007, In Prep. To be published in MNRAS, [*Emergence and disappearance of micro-acrsecond structure in the scintillating quasar J1819+3845*]

Macquart, J.-P. & Jauncey, D.L. 2002. ApJ, 572, 786 [*Microarcsecond radio imaging using earth-orbit synthesis*].

Macquart, J.-P., Kedziora-Chudzer, L.L, Rayner, D.P. & Jauncey, D.L. 2000 ApJ, 538, 623. [*Strong, variable circular polarization in PKS 1519-273*].

Madisetti, V.K. & Williams, D.B. (Eds.) 1998. *The Digital Signal Processing Handbook.* CRC Press.

Maíz-Apellániz, J. 2001. ApJ, 560, L83-L86. [*The origin of the local bubble*].

Malkan, M. 2001. *Active Galaxies: Overview.* In Murdin. P. (Ed.). 2001, *Encyclopedia of Astronomy and Astrophysics,* Institute of Physics Publishing, Bristol.

Marion, J.B, & Heald, M.A. 1980. *Classical Electromagnetic Radiation, 2nd Ed.* Academic Press.

Marscher, A.P. & Gear, W.K. 1985, ApJ, 298, 114-127. [*Models for high-frequency radio outbursts in extragalactic sources, with application to the early 1983 millimeter-to-infrared flare of 3C 273*]

Mathworks, 2002. *Signal Processing Toolbox Users Guide Ver. 6.* The Mathworks Inc., MA, USA.

McAdam, W. B. 1978, PASA, 3, 283. [*The time scale of decimetre flux density variations*].

McCulloch, P.M., Ellingsen, S.P., Jauncey, D.L., Carter, S.J.B., Cimò, G., Lovell, J.E.J. & Dodson, R.G. 2005, AJ, 129, 2034-2040. [*COSMIC: Microarcsecond resolution with a 30 meter radio telescope*].

Meier, D.L., Koide, S., & Uchida, Y. 2001, Science 291, 84-92. [*Magnetohydrodynamic Production of Relativistic Jets*].

Meier, D.L. 2003, New Astronomy Reviews 47, 667-672. [*The theory and simulation of relativistic jet formation: towards a unified model for micro- and macroquasars*].

Melrose, D.B. 2002 PASA, 19, 34-38. [*Coherent Emission in AGN: A Critique*].

Misner, C.W., Thorne, K.S. & Wheeler, J.A. 1973 *Gravitation.* W.H. Freeman & Co., San Francisco.

Narayan, R. 1992, Phil. Trans. R. Soc. Lond. A, 341, 151 [*The physics of pulsar scintillation*].

Newland, D.E. 1975. *An Introduction to Rabdom Vibrations and Spectral Analysis.* Longman.

Nolan, P.L. et al. {21 authors listed} 1996 ApJ, 459, 100-108. [*EGRET Observations of Gamma Rays from Point Sources with Galactic Latitude* $+10^{o} < b < +40^{o}$].

Norman, C.A. & Ferrara, A. 1996 ApJ, 467, 280 [*The turbulent interstellar medium: generalizing to a scale-dependent phase continuum*].

O'Dea, C. 1998, PASP, 110: 493-532. [*The Compact Steep-Spectrum and Gigahertz Peaked-Spectrum Radio Sources*]

Padovani, P. & Giommi, P. 1995, MNRAS, 277, 1477-1490. [*A Sample-Oriented Catalogue of Bl-Lacertae Objects*]

Penrose, R. 1969, Rivista del Nuivo Cimento, Numero speciale, 1, 252.

Penrose, R. & Floyd, R. 1971, Nature Physical Science, 229, 177. [*Extraction of rotational energy from a black hole*].

Peterson, B.M. 1997, *An Introduction to Active Galactic Nuclei*. Cambridge University Press.

Pope, S.B. 2000, *Turbulent Flows,* Cambridge University Press.

Press, W.H., Flannery, B.P., Teuskolsky, S.A. & Vetterling, W.T. 1986, *Numerical Recipes: The Art of Scientific Computing*, Cambridge Unievrsity Press.

Punsly, B. 2001, *Black Hole Gravitohydromagnetics.* Springer-Verlag.

Punsly, B. & Coroniti, F.V. 1990, ApJ, 350, 518-534. [*Relativistic winds from pulsar and black hole magnetospheres*]

Punsly, B., Rodríguez, L.F., Tingay, S.J. & Cellone, S.A. 2005, ApJ 633:L93-L96 [*PKS 1622-253: A Weakly Accreting, Powerful Gamma-Ray Source*].

Qian, S.J., Quirrenbach, A., Witzel, A., Krichbaum, T.P., Hummel, C.A. & Zensus, A. 1991 [*A model for the rapid radio variability in the quasar 0917+624*], A&A, 241,15-21.

Readhead, A.C.S. ApJ 1994, 426: 51-59 [*Equipartition Brightness Temperature and the Inverse Compton Catastrophe*]

Rees, M. 2004, In Proc. 17th International Conference on General Relativity and Gravitation, Dublin, 18-23 July 2004. [*Black holes in active galactic nuclei*].

Reynolds, J. 1994 Australia Telescope Compact Array bulletin AT/39.3/040 29 July 1994 (available from ATCA web site). [*A Revised Flux Scale for the AT Compact Array*]

Reynolds, R.J. 1991. In Bloemen, H. (ed) *The Interstellar Disk-Halo Connection in Galaxies.* 67-76, IAU. Printed in the Netherlands.

Reynolds, R.J. 2002, Scientific American, January 2002. [*The gas between the stars*].

Rickett, B.J. 1969, Nature 219:158. [*Frequency Structure of Pulsar Intensity Variations*].

Rickett, B.J. 1977 Ann. Rev. Astron. Astrophys., 15, 479 [*Interstellar scattering and scintillation of radio waves.*].

Rickett, B.J. 1990 Ann. Rev. Astron. Astrophys., 28, 561 [*Radio propagation through the turbulent interstellar plasma*].

Rickett, B.J. 2001 Ap&SS, 278, 5-10 (IAU Colloq. 182) [*Radio Sources and Scintillation*].

Rickett, B.J. 2004, ASTRON/JIVE Workshop on Interstellar Scintillation of Extraglactic Radio Sources, Dwingeloo, The Netherlands. [*Setting the Scintillating Scene*]. Powerpoint presentation available as download from: www.jive.nl/meetings/iss_workshop/presentations/Rickett1.ppt

Rickett, B.J., Kedziora-Chudczer, L. & Jauncey, D.L. 2002, ApJ, 581, 103-126. [*Interstellar Scintillation of the Polarized Flux Density in Quasar PKS 0405-385*]

Rickett, B. J., Quirrenbach, A., Wegner, R., Krichbaum, T. P. & Witzel, A. 1995, A&A, 293, 479-492. [*Interstellar scintillation of the radio source 0917+624*]

Rickett, B. J., Coles, Wm. A. & Markkanen, J. 2000, ApJ, 533, 304-319. [*Interstellar Scintillation of Pulsar B0809+74*]

Rohlfs, K. & Wilson, T.L. 2000. *Tools of Radio Astronomy, 3rd Ed.* Springer-Verlag.

Ros, E., Porcas, R.W. & Zensus, J.A. (eds) 2002, Proc. 6th European VLBI Network Symposium, 25-28 June 2002, Bonn, Germany.

RRFID 2002, TheUnited States Naval Observatory Radio Reference Frame Image Database.

Rybicki, G. B. & Lightman, A.P. 1979. *Radiative Processes in Astrophysics*. John Wiley & Sons.

Ryle, M. & Hewish, A. 1950, MNRAS, 110, 381. [*The effects of the terrestrial ionosphere on the radio waves from discrete sources in the galaxy*]

Scargle, J.D. 1982, ApJ, 263, 835. [*Studies in astronomical time series analysis. ii. statistical aspects of spectral analysis of unevenly spaced data*].

Scheuer, P.A.G. 1968. Nature 218:920. [*Amplitude Variations in Pulsed Radio Sources*].

Schlegel, D.J., Finkbeiner, D.P. & Davis, M. 1998, ApJ, 5005, 525. [*Maps of Dust Infrared Emission for Use in Estimation of Reddening and Cosmic Microwave Background Radiation Foregrounds*]

Shu, F. H. 1992, *The Physics of Astrophysics, Vol 2: Gas Dynamics.* University Science Books, Mill Valley, California.

Snowden, S. L., Egger, R., Finkbeiner, D. P., Freyberg, M. J. & Plucinsky, P. P. 1998, ApJ, 493, 715-729. [*Progress on Establishing the Spatial Distribution of Material Responsible for the 1 4 keV Soft X-Ray Diffuse Background Local and Halo Components*]

Spangler, S.R. 1999, ApJ, 522, 879 [*Two-Dimensional Magnetohydrodynamics and Interstellar Plasma Turbulence*].

Steppe, H., Jeyakumar, S., Saikia, D.J. & Salter, C.J. 1995, Astron. Astrophys. Suppl. Ser., 113, 409-418. [*Millimeter-wavelength observations of compact steep-spectrum sources*.]

Stickel, M., Meisenheimer, K. & Kuehr, H. 1994, Astron. Astrophys. Suppl. Ser., 105, 211-234. [The optical identification status of the 1 Jy radio source catalogue]

Strom, R., Peng B., Walker, M., & Nan R. (Eds.) IAU Colloquium 182: *Sources and Scintillations: Refraction and Scattering in Radio Astronomy*. Ap&SS, 278:1-2.

Taff, L.G. 1981 *Computational Spherical Astronomy.* John Wiley & Sons.

Taylor, J.H. & Cordes, J.M. 1993, ApJ, 411, 674-684. [*Pulsar distances and the galactic distribution of free electrons*].

Tatarskii, V.I. 1961 *Wave Propagation in a Turbulent Medium.* Translated from Russian by R.A. Silverman. McGraw-Hill, New York.

Thompson, A.R., Moran, J.M. & Swenson G.W. 2001 *Interferometry and Synthesis in Radio Astronomy* 2nd Ed., John Wiley, New York.

Thorne, K.S. & Blandford, R.D. 1982, IAUS, 97, 255T. [*Black holes and the origin of radio sources*]

Tingay, S.J., Jauncey, D.L., King, E.A., Tzioumis, A.K., Lovell, J.E.J. & Edwards, P.G. 2003, PASJ, 55, 351. [*ATCA Monitoring Observations of 202 Compact Radio Sources in Support of the VSOP AGN Survey*]

Tingay, S.J., Murphy, D.W. & Edwards, P.G. 1998 ApJ, 500, 673-684. [*VLBI Observations of Southern EGRET Identifications. II. VLBA Observatoins and the Importance of Jet Bending in Gamma-Ray Sources*].

Tornikoski, M., Jussila, I., Johansson, P., Lainele, M. & Valtaoja, E. 2001, AJ 121: 1306-1318. [*Radio Spectra and Variability of Gigahertz-Peaked Spectrum Radio Sources and Candidates*].

Ulrich, M-.H., Maraschi, L. & Urry, C.M. 1997 Ann. Rev. Astron. Astrophys., 35, 445-552 [*Variability of Active Galactic Nuclei*].

Unwin, S.C., Cohen, M.H., Biretta, J.A., Pearson, T.J., Seielstad, G.A., Walker, R.C., Simon, R.S., & Linfield, R.P. 1985 ApJ, 289, 109-119 [*VLBI monitoring of the superluminal quasar 3C 273, 1977-1982*]

Urry, C.M. & Padovani, P. 1995, PASP 107: 803-845. [*Unified Schemes for Radio-Loud Active Galactic Nuclei*].

Urry, C. M., Sambruna, R.M., Worrall, D.M., Kollgaard, R.I., Feigelson, E.D., Perlman, E.S. & Stocke, J.T. 1996, ApJ, 463, 424-443. [*Soft X-Ray Properties of a Complete Sample of Radio-selected BL Lacertae Objects*]

Vermeulen, R.C. & Cohen, M.H. 1994, ApJ, 430, 467-494. [*Superluminal Motion Statistics and Cosmology*].

Véron-Cetty, M.-P.; Véron, P. 2003, A&A, 455, 773-777. [*A catalogue of quasars and active nuclei: 12th edition*]

Wagner, S.J. & Witzel, A. 1995, Annual Rev. Astron. Astrophys. 33: 163-97. [*Intraday variability of Quasars and BL Lac Objects*].

Walker, M.A. 1998 MNRAS, 294, 307 (plus erratum: Walker, M.A. 2001 MNRAS 321, 176) [*Interstellar scintillation of compact extragalactic radio sources*].

Wells, D.C., Greisen, E.W. & Harten, R.H. 1981, Astron. Astrophys. Suppl. Ser. 44, June 1981, 363-370. [*FITS: A Flexible Image Transport System*].

White, G.L., Jauncey, D.L., Wright, A.E., Batty, M.J., Savage, A., Peterson, B.A. & Gulkis, S. 1988, ApJ, 327, 561-569. [*Redshifts of southern radio sources. VII*]

White, R.J. & Peterson, B.M. 1994, PASP, 106, 879-889. [*Comments on cross-correlation methodology in variability studies of active galactic nuclei*]

Woit, P. 2006. *Not Even Wrong.* Jonathan Cape, Random House, London.

Wright, A.E., Griffith, M.R., Burke, B.F. & Ekers, R.D. 1994 ApJS, 91, 111 [*The Parkes-MIT-NRAO (PMN) surveys. 2: Source catalog for the southern survey (delta greater than -87.5 deg and less than -37 deg)*]

Wrobel, J.M. & Walker, R.C. 1999 In *Synthesis Imaging in Radio Astronomy II* eds. G.B. Taylor, C.L. Carilli and R..A. Perley, ASP conference series, Vol. 180, 171-186.

Wu, K., Stevens, J.A. & Hannikainen, D.C. 2002, PASA, 19, 91-99. [*Microquasars: A Galactic-Extragalactic Connection?*]

Yerbury, M.J. 1975, Rev. Sci. Instrum., 46, 169-179. [*A gain-stabilizing detector for use in radio astronomy*].

Zeilik, M. & Gregory, A.S. 1998, *Introductory Astronomy and Astrophysics, 4th Ed.,* Saunders College Publishing, U.S.